Etude du vieillissement des assemblages membrane-électrodes pour piles à combustible basse température

Julien Durst

UNIVERSITÉ DE GRENOBLE

THÈSE

Pour obtenir le grade de

DOCTEUR DE L'UNIVERSITÉ DE GRENOBLE

Spécialité : **Matériaux, Mécanique, Génie Civil, Electrochimie**

Arrêté ministériel : 7 août 2006

Présentée par

Julien DURST

Thèse dirigée par **Frédéric MAILLARD** et par **Marian CHATENET**

préparée au sein du **Laboratoire d'Electrochimie et de Physico-chimie des Matériaux et des Interfaces**
dans **l'École Doctorale Ingénierie – Matériaux, Mécanique, Energétique Environnement Procédés Production**

Etude du vieillissement des assemblages membrane-électrodes pour piles à combustible basse température

Thèse soutenue publiquement le **24 Octobre 2012**,
devant le jury composé de :

Pr. Ricardo P. NOGUEIRA
Professeur, Grenoble INP, Grenoble, Président

Pr. Andrea E. RUSSELL
Professeur, University of Southampton, Southampton (GB), Rapporteur

Pr. Thomas J. SCHMIDT
Professeur, Paul Scherrer Institute, Villigen (CH), Rapporteur

Dr. Frédéric JAOUEN
Chargé de recherche, CNRS, Montpellier, Examinateur

Dr. Frédéric MAILLARD
Chargé de recherche, CNRS, Grenoble, Directeur de thèse

Pr. Marian CHATENET
Professeur, Grenoble INP, Grenoble, Directeur de thèse

« La science est une chose merveilleuse… tant qu'il ne faut pas en vivre. »

Albert Einstein

A ma famille et mes amis qui me donnent tant de plaisir à m'évader de la science.

Table of Contents

Acknowledgments

I would not know who to thank first, since these last three years have been very rewarding from both a scientific and a human aspect. Most of the people I have met during this thesis have contributed to both aspects.

The first people who come into my mind are Frédéric and Marian, my two supervisors. I have not spent one day without learning something from them. It has been exciting working with them. Indeed, it is very frustrating to end this thesis now. They have a passion for their work (but not only) and know how to hand their interest for science on their students.

I would like to thank Pr. Andrea E. Russell and Pr. Thomas J. Schmidt for accepting to review this thesis, Dr. Frédéric Jaouen for examining it and Pr. Ricardo P. Nogueira for chairing this jury. It is a great honour for me that they have accepted to review and judge this work.

All the work carried out and the results obtained and published during these three years belong to the "Durability team", and so to Laetitia, and now Luis. I will miss working in such a friendly and constructive atmosphere.

If I would have to pick up one special moment from this thesis, it would definitely be the one spent at the ESRF for XAS measurements with Frédéric, Yvonne, and with the FAME team: Vincent, Olivier, Denis and Jean-Louis, and those who have helped me during this campaign, Eric, Manuel, Luis and Marian. Among all, I would to thank Yvonne for sharing with me her know-how about XAS in general and EXAFS in particular.

In the frame of the H2E and MDM projects, I have worked with several academic (LEMTA, LMOPS) and industrial (Axane, Air Liquide) institutions, each having special skills and knowledge (from fundamental to applied) on the study of PEMFC. It has been very instructive to benefit from their experience to build a study that tackles multiscale issues. Therefore, I would like to thank Elisabeth, Johan and Nicolas from Axane, Sandrine and Audrey from Air Liquide, Lionel, Corinne, Gilles and Eddy from LMOPS and last but not least at all, I want to give a special thanks to my colleagues from LEMTA: Adrien, Olivier, Gael and Jérôme.

In the frame of the CAPES-COFECUB project, I want to thank Edson, Fabio and their outstanding team of master and PhD students who did kindly welcome me at Sao Carlos during two weeks for on-line DEMS and EC-FTIR measurements. It has been an amazing experience, shared with Benoit, at the "Republica" of Scooby and all of his roommates and friends.

I would like to give a special thanks to Ricardo, current head of the LEPMI. He found the perfect words at the time, three years ago, to convince me to do a thesis. He also gave me the chance to teach corrosion science at his side. I owe him a lot (and I already miss drinking beers with him at Pic'Aglou).

From a technical aspect, I would like to thank the UMEC network ("Réseau des utilisateurs de l'ultramicroélectrode à cavité") from the French National Center for Scientific Research for providing the UMEC, Benoit, Axel Desnoyers de Marbaix and Vincent Vivier for their help in designing and realizing the SSC, Laure (CEA-LITEN), Frédéric, Stéphane, Graziella (CMTC) and Laetitia (LMGP) for their help for STEM-HAADF, SEM, FEG-SEM, FIB-SEM, XRD and TEM measurements.

Of course, although I have travelled all around the world during these three years, I have spent and shared great moment with the master and Ph. D students from LEPMI: Thiago and all of his brazilian students, Marc, Bruno, Zuzhen, Zayang, the two Benoit (one being my Belgium beer body, the other my travelling companion), Pascal, Manu (my PSG friend), Houssem and Thibault (for the too numerous hours spent at the Laboratory Board). I also want to thank the ESME team, the administrative team and the LEPMI laboratory.

My stay in Grenoble comes to its end. After six years spent here, I will leave this city with a lot of great memories in my luggage, but also with a bunch of amazing friends. Thank you Rem'Os, Clairette, CoCo, Djé, Quentin, Sophie, Marine, Paul, David, Gros Yo, Elise, Slag, Manon, Junior, all the former students from ENSEEG' 2008, 2009 and 2010… for making this experience unique.

I would like to thank my parents, my brothers Frédéric and Arnaud, my grandparents Pierre and Cécile and my closest alsatian friends for their long-distance support during these last six years.

I conclude these acknowledgements by thanking Camille, who has been a great support during the last months of this thesis. I owe her a lot…

List of symbols and abbreviations

C_x :	Solubility of x (mol cm^{-3})
D_x :	Diffusion coefficient of x (cm^2 s^{-1})
$\overline{d}_{XRD}$:	Mean crystallite size (nm)
$\overline{d}_N$:	Mean particle size (nm)
$\overline{d}_S$:	Surface averaged particle size (nm)
$\overline{d}_V$:	Volume averaged particle size (nm)
E:	Potential (V)
$E^0_{M^+/M}$:	Standard equilibrium potential of the M^+/M redox couple (V)
E_{ox}:	Potential of oxide formation of an electrode (V)
E_{disk}:	Disk potential (V)
E_{ring}:	Ring potential (V)
F:	Faraday constant charge per mole of electrons (C mol^{-1})
H_{upd}:	Hydrogen under potential deposition
I:	Xurrent (A)
I_f :	Faradaic current (A)
I_k :	Kinetic current (A)
I_{lim} :	Mass diffusion limited current (A)
I/C:	Ionomer to carbon weight ratio
j:	Current density (A cm^{-2})
j_D:	Mass transport limited current density (A cm^{-2})
j_k:	Kinetic current density (A cm^{-2})
N:	Coordination number
n:	Number of exchanged electrons
p_x:	Gas permeability of specie x (mol cm^{-1} s^{-1})
P_x:	Partial pressure of x (mbar)
R:	Half path length (nm)
R_{HF}:	High frequency resistance (Ω cm^2)
$S_{Pt,MEA}$:	Practical electrochemically active surface area of catalyst (cm^2)
$S_{Pt,Cat}$:	Theoretical active surface area of catalyst (cm^2)
T:	Temperature (K)
t:	Time (h)
u_{Pt}:	Utilization factor (%)
u_{eff}:	Effectiveness factor (%)
v:	Linear potential scan rate (V s^{-1})
j_{ad} :	Fractional coverage of an interface by species j
η	Overpotential E-E_{eq} (V)
η_{ORR}:	ORR activation overpotential (V)
η_{HOR}:	HOR activation overpotential (V)
σ:	Debye Waller (Å)
λ:	Number of water molecules per sulfonate groups
γ_{M^+} :	Amount of contamination of an electrolyte for a given metal cation M^+
υ :	Kinematic viscosity (m^2 s^{-1})

$\varepsilon_{ionomer}$:	Volume fraction of ionomer in an electrode (%)
ω :	Angular rotation velocity (rad s^{-1})

BoL:	Beginning of Life
BSE:	Backscattered Electron
CCM:	Catalyst Coated Membrane
CL:	Catalyst Layer
CV:	Cyclic Voltammogram
DEMS:	Differential Electrochemical Mass Spectrometry
DFT:	Density Functional Theory
DoE:	American Department of Energy
ECSA:	Electrochemical Surface Area
EELS:	Electron Energy Loss Spectroscopy
EPR:	Electron Paramagnetic Resonance
EIS:	Electrochemical Impedance Spectroscopy
ESRF:	European Synchrotron Research Facility
EV:	Electric Vehicles
EW:	Equivalent Weight
EXAFS:	Extended X-ray Absorption Fine Structure
FCV:	Fuel Cell Vehicles
FEG:	Field Emission Gun
FIB:	Focused Ion Beam
f.c.c.:	Face Centred Cubic
FWHM:	Full Width at Half Maximum
GDL:	Gas Diffusion Layer
HOR:	Hydrogen Oxidation Reaction
HRSTEM-HAADF:	High Resolution Scanning Transmission Electron Microscopy High-Angle Annular Dark-Field
HSAC:	High Surface Area Carbon
H2E:	Horizon Hydrogen Energy
ICP-AES:	Inductive Coupled Plasma – Atomic Emission Spectroscopy
IEC:	Ion Exchange Capacity
IHP:	Inner Helmholtz Plane
LEIS:	Low-Energy Ion Scattering
MA:	Mass Activity (A g^{-1}_{Pt})
MEA:	Membrane Electrode Assembly
MDM:	Membrane electrode assembly Degradation Mechanisms
MS:	Mass Spectrometer
NHE:	Normal Hydrogen Electrode
OCV:	Open Circuit Voltage
OHP:	Outer Helmholtz Plane
ORR:	Oxygen Reduction Reaction
PEM:	Proton Exchange Membrane
PEMFC:	Proton Exchange Membrane Fuel Cell
PFSA:	Perfluorosulfonic Acid

PSD:	Particle Size Distribution
PZC:	Potential of Zero Charge
PTFE:	Polytetrafluoroethylene
RDE:	Rotating Disk Electrode
RH:	Relative Humidity
RHE:	Reversible Hydrogen Electrode
RHF:	High Frequency Resistance
RRDE:	Rotating Ring Disk Electrode
SA:	Specific Activity (A cm^{-2}_{Pt})
SCE:	Saturated Calomel Electrode
SCV:	Sampled Current Voltammetry
SHE:	Standard Hydrogen Electrode
SSC:	Solid State Cell
SEM:	Scanning Electron Microscopy
STEM:	Scanning Transmission Electron Microscopy
T.K.K. :	Tanaka Kikinzoku Kogyo
TEM:	Transmission Electron Microscopy
UMEC:	Ultra-Microelectrode with Cavity
XANES:	X-ray Absorption Near Edge Structure
XAS:	X-ray Absorption Spectroscopy
XRD:	X-Ray Diffraction
X-EDS:	X-ray Energy Dispersive Spectroscopy

Chapter I.

Overview of PEMFC components, limitations and durability

I. Overview

During the past ten years, solutions have been proposed to mitigate carbon emissions in the atmosphere. The burning of fossil fuels, which still provides more than 75 % of energy worldwide, produces most of these emissions. The rapidly expanding number of automobiles around the globe threatens an even greater escalation in emissions. The need to promote energy-efficiency and renewable resources is obvious. The recent development of electrical powered vehicles (with lithium as an energetic vector and typical energy densities of *ca.* 100 Wh L^{-1} and 100 Wh kg^{-1}) has sparked society awareness about life without oil as an achievable good. However, some issues like the safety of such systems, their long charging time and limited cruising range remain barriers to their wide-spreading. One possibility, already investigated by some vehicle manufacturers, is to develop, in parallel to batteries, fuel cells based on hydrogen as energy vector (energy densities of *ca.* 100 Wh L^{-1} and 10000 Wh kg^{-1}). Applied to transportation, this technology still presents some drawbacks, among which its high cost, its high degradation rate, the hydrogen storage and the lack of infrastructure for refueling. It also offers some advantages, such as a high cruising range and a charging time of less than 5 minutes. Hybrid vehicles using a combined lithium/hydrogen technology have achieved a cruising range of about 560 km without refueling [1].

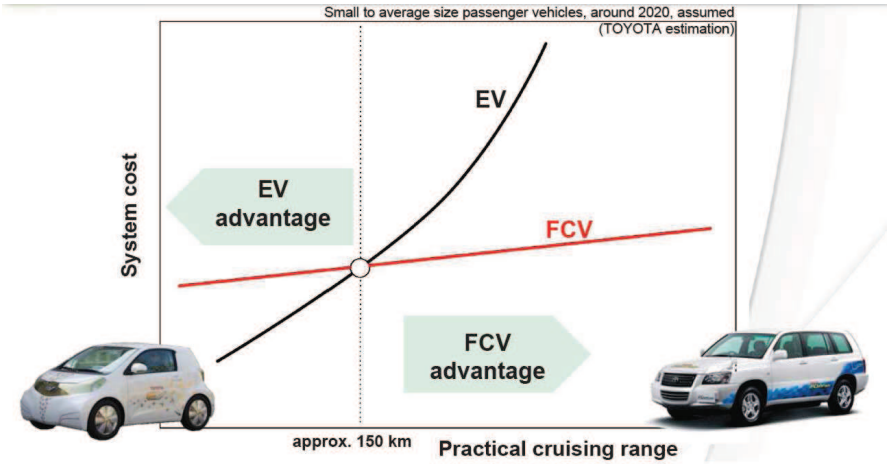

Figure I- 1. System cost of an electrical vehicle (EV) and a fuel cell vehicle (FCV) as a function of the practical cruising range. Reprinted from Cerri [1].

Fuel cells and batteries are both electrochemical galvanic cells that convert chemical energy into electrical energy. They are basically composed of two electrodes, where the electrochemical reactions (*i.e.* an oxidation at the anode and a reduction at the cathode) take place, the electrodes being separated by an electrical insulator, the electrolyte. The fundamental difference between batteries and fuel cell is that the former stores the reactants inside the device (*e.g.* lithium) whereas the latter needs a constant supply of chemicals (an oxidant and a reducer) to operate. Many oxidant/reducer couples can be combined to form a Fuel Cell [2].

In this manuscript, the degradations of the key components of the most commonly used fuel cell (among those working at low temperatures), the proton exchange membrane fuel cell (PEMFC), have been studied. A PEMFC uses hydrogen as reducer and oxygen (or air) as oxidant. At the anode, the hydrogen oxidation reaction (HOR – Equation I-1) produces protons and electrons, which are then used to reduce oxygen into water at the cathode (oxygen reduction reaction, ORR – Equation I-2).

$$H_2 \leftrightarrow 2H^+ + 2e^- \qquad E^0_{H^+/H_2} = 0 \text{ V } \textit{vs.} \text{ NHE} \qquad (T = 298 \text{ K}) \qquad \text{Eq. I-1}$$

$$O_2 + 4H^+ + 4e^- \leftrightarrow 2H_2O \qquad E^0_{O_2/H_2O} = 1.23 \text{ V } \textit{vs.} \text{ NHE} \qquad (T = 298 \text{ K}) \qquad \text{Eq. I-2}$$

Protons are transported from the anode to the cathode via a proton-conducting membrane while electrons flow through an external device where the electrical energy can be utilized. When energy is collected, the two electrodes are polarized, negatively for the cathode and positively for the anode. The detailed mechanism of these reactions as well as their structure sensitivity will be detailed below. By combining these two half-cell reactions, the global reaction of a hydrogen/oxygen PEMFC is:

$$H_2 + \frac{1}{2}O_2 \leftrightarrow H_2O + \text{heat} \qquad \Delta E = 1.23 \text{ V} \quad (T = 298 \text{ K}) \qquad \text{Eq. I-3}$$

II. Electrocatalysis of PEMFC reactions

1. HOR

The hydrogen oxidation reaction, which is among the most extensively studied reactions in electrochemistry, is believed to proceed in a two-step mechanism when catalyzed by platinum. The first step corresponds to the dissociative adsorption of molecular H_2 into H_{ad} following a Heyrovsky (Equation I-4) and/or Tafel step (Equation I-5). In the second step the adsorbed molecular hydrogen H_{ad} is electrooxidized into H^+ following the Volmer step (Equation I-6):

$$H_2 + Pt \leftrightarrow PtH_{ad} + H^+ + e^- \qquad \text{(Heyrovsky)} \qquad \text{Eq. I-4}$$

$$H_2 + 2Pt \leftrightarrow PtH_{ad} + PtH_{ad} \qquad \text{(Tafel)} \qquad \text{Eq. I-5}$$

$$PtH_{ad} \leftrightarrow Pt + H^+ + e^- \qquad \text{(Volmer)} \qquad \text{Eq. I-6}$$

The HOR on platinum is very fast [3] and is therefore under diffusion control for overpotentials as low as 0.1 V. Typical HOR exchange current densities in a PEMFC on a Pt/C catalyst are on the order of 0.2 to 0.6 A cm_{Pt}^{-2} at $T = 353$ K [3].

2. ORR

The oxygen reduction reaction (ORR) has been widely studied as the cathode reaction in a PEMFC but also in the fields of electrosynthesis and corrosion science. From the kinetics viewpoint, Pt is the best electrocatalyst and typical values for the ORR exchange current density are very low and range from 10^{-7} to 10^{-9} A cm^{-2}_{Pt} in typical PEMFC operating conditions at $T = 253$ K [4]. The ORR is a complex 4-electrons reaction involving many reaction intermediates, the most stable being H_2O_2. From a mechanistic viewpoint, the simplified but still ongoing and believed ORR mechanism has been initially proposed by Wroblowa *et al*. [5]. It proceeds either by a direct 4-electron pathway or in a series of consecutive 2-electron pathway. These 2 and 4-electron pathways apparently compete on platinum [6-8].

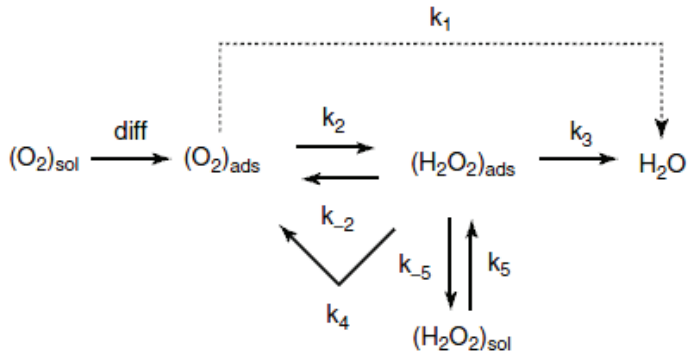

Figure I-2. Simplified scheme of the ORR on Pt surfaces in acid solution proposed by Wroblowa et al. [5]

In any case, the rate determining step is believed to be the first electron and proton transfer to adsorbed O_2:

$$(O_2)_{ad} + H^+ + e^- \rightarrow (O_2H)_{ad} \qquad \text{Eq. I-7}$$

Using the Butler-Volmer approach, the ORR rate can be expressed as [7, 9, 10]:

$$j_k = -nFkC_{O_2}[H^+](1-\theta_{ad})^x \exp\frac{-\alpha FE}{RT}\exp\frac{\Delta G^{\neq}_{\vartheta_{ad}}}{RT} \qquad \text{Eq. I-8}$$

where n is the number of exchanged electrons, k is the rate constant of the *rds*, C_{O2} is the concentration in O_2 in the electrolyte, proportional to the partial pressure in O_2, $[H^+]$ is the concentration of protons near the electrode surface, θ_{ad} is the total coverage by adsorbed species on the modified surface: dioxygen molecules and reaction intermediates $\theta_{Ox,ad}$, anions $\theta_{anions,ad}$ and surface oxides originating from water splitting $\theta_{OH,ad}$, x is the number of sites occupied by the $(O_2H)_{ad}$ adsorbate (x = 1 or 2), α is the apparent transfer coefficient of the ORR, F is the Faraday constant, E is the electrode potential *vs.* a suitable reference such as the RHE, $\Delta G^{\neq}_{\vartheta_{ad}}$ is the coverage-dependent Gibbs free energy of the

reaction. The Gibbs free energy of oxygen adsorption depends on the surface oxide coverage according to Equation I-9:

$$\Delta G_{\vartheta_{ad}}^{\neq} = \Delta G_0^{\neq} - \beta r \theta_{\mathrm{Ox,\,ad}} \qquad \text{Eq. I-9}$$

where $\Delta G_0^{\neq}$ is the Gibbs free energy of oxygen adsorption in the limit of zero coverage, β is a symmetry factor and r is a surface coverage-dependent lateral interaction factor between adsorbed oxygenated species ($r > 0$ for attractive interactions and $r < 0$ for repulsive interactions). Equation I-8 shows that the coverage by adsorbed oxygenated species (θ_{ad}) affects the kinetic current in two ways. First, the adsorbed oxygenated species reduce the number of free Pt surface sites, available for the adsorption of O_2 molecules. Second, they modify the Gibbs free energy of oxygen adsorption [7, 11, 12].

Other electrochemical reactions than the ORR can occur simultaneously at the cathode catalyst surface during PEMFC operation and can increase the θ_{ad} term: (i) hydrogen oxidation (as hydrogen can cross-over the electrolyte from the anodic compartment), (ii) the specific adsorption of sulfonate groups from the ionomer (or any other anionic contaminants such as residual chlorides from the catalyst synthesis) and (ii) the formation of surface hydroxides/oxides. The magnitude of these parasitic reactions in a PEMFC can be evaluated from *in situ* cyclic voltammetry measurements of the PEMFC (using the driven-cell mode [13]) while the cathode is supplied with a non-reacting gas such as Ar (see the "MEA" curve in Figure I-3A) or *ex situ* (using a 3 electrode configuration in liquid electrolyte which has been shown to greatly mimic a PEMFC environment [14], see the "RDE" curve in Figure I-3A). At low cathode potential, *i.e.* $E < 0.3$ V *vs.* RHE, the catalyst surface is the place for the adsorption of atomic hydrogen (H_{ad}) in the negative going sweep. The anodic current recorded in the positive going potential sweep corresponds to the electrochemical desorption of H_{ad}. The specific adsorption of sulfonate groups cannot be evaluated with accuracy using cyclic voltammograms but it is believed to occur mainly for $E > 0.5$ V *vs.* RHE [15]. At higher cathode potentials, *i.e.* $E > 0.6$ V *vs.* RHE, in the cathode potential widow of interest for a PEMFC application, the catalyst surface faces the kinetic irreversible formation of surface oxides in the positive going potential sweep and their reduction in the negative going potential sweep [16]. The formation of surface oxides, which can be seen as the early step of three-dimensional passive film formation in corrosion science, decreases the availability of the platinum surface and inhibits the ORR kinetics. A total coverage of the surface is reached at approximately $E = 0.9$ V *vs.* RHE (Figure I-3B), which roughly corresponds to the open circuit voltage of a PEMFC (discussed hereafter). The formation of surface oxide can be then seen as the main foe for the ORR, as it leads to a high activation overpotential ($\eta_{ORR} > 300$ mV). The ideal catalyst for the ORR should postpone to the highest value the potential of surface hydroxides/oxides formation and reduction. In their recent work, Stephens *et al.* [17] introduced a review of the

electrocatalysis of oxygen reduction with a more theoretical approach based on density functional theory (DFT) calculations. By taking into consideration the adsorption energies of the different intermediates involved in the ORR (and not only H_2O_2) it then becomes possible to calculate the overall free energy pathway for the reaction, as a function of potential. They came to the conclusions that it is not possible to vary the adsorption energies of these intermediates independently of each other by changing the catalyst material. Therefore, a surface that binds $O^{\bullet}$ strongly can also be expected to bind $HO^{\bullet}$ or $HOO^{\bullet}$ strongly, as each adsorbate binds to the surface via the oxygen atom.

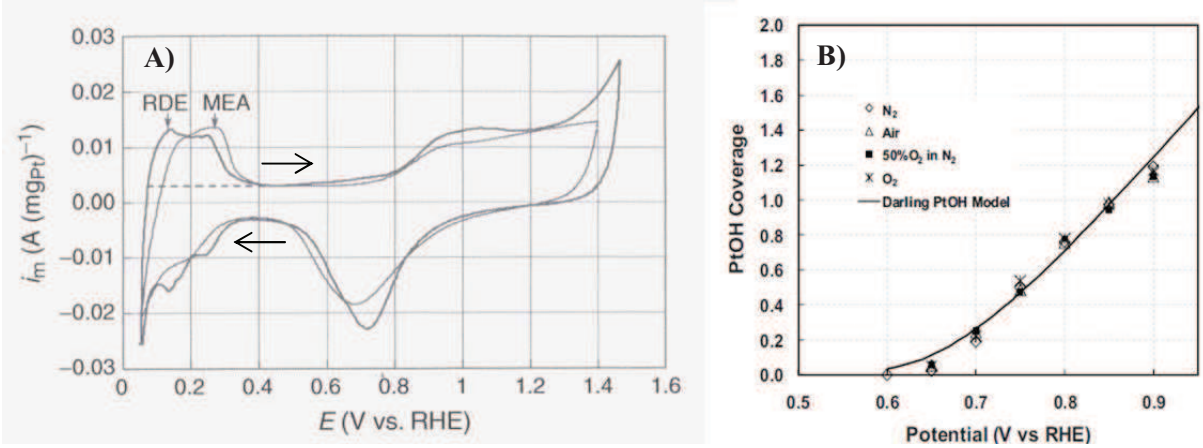

Figure I-3. (A) Cyclic voltammograms on a Pt/C (47 wt. %) recorded in a thin-film rotating disk electrode (0.5 M H_2SO_4) configuration and in a MEA (measured in a driven-cell mode) reprinted from Gasteiger et al. [13]. (B) Predicted PtOH coverages as a function of potential under PEMFC operating conditions for various gas exposures reprinted from Liu et al. [18].

III. Brief description of PEMFC materials

The heart of a PEMFC, where the chemical to electrical conversion occurs, is the Membrane Electrode Assembly (MEA). It is composed of two catalytic layers (CLs), two gas-diffusion layers (GDL), and the proton exchange membrane (PEM). The CLs are composite materials composed of ionomer-bonded carbon-supported Pt-based nanoparticles. The PEM is usually a perfluorosulfonated ionomer, which acts as a transport medium for protons but also as an electron insulator and a gas separator between the hydrogen and oxygen compartments. The two GDL enable the fuel/oxidant transport to/from the CLs, the water management and the electronic/heat conduction. The actual design of this 5 layer structure benefits from almost two centuries of feedbacks since the first hydrogen/air fuel cell structure originally developed by William R. Groove in 1842 (Figure I-4) [19].

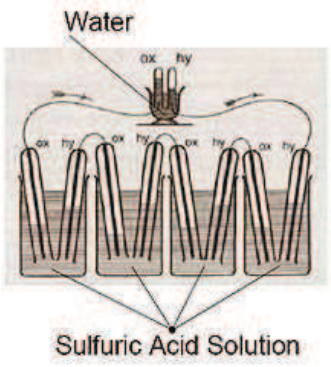

Figure I-4. Grove fuel cell which consisted of the assembly of 4 cells in series connected to an electrolyzer. The electrodes were made of platinum grids. Reprinted from Grove [19].

1. PEMFC electrodes/catalytic layers

Due to the low solubility of hydrogen and oxygen in electrolyte solutions, porous electrodes called gas-diffusion electrodes, with an ideal porosity close to 60 % of the volume (Figure I-5A) [20], are used in PEMFC to electro-oxidize dihydrogen and electro-reduce dioxygen. These two electrochemical reactions, especially the cathodic one, are very complex and involve various types of reactants. Therefore, the electroactive sites must be accessible from a network allowing good gas permeability, low resistance to proton transport, low barrier to water diffusion and sufficient electrical contact with the external circuit, in order to produce water that also should be quickly eliminated. The region where the catalyst phase meets the gas phase and the ionomer phase is called the "three-phase boundary" (Figure I-5B). If one of these points is failing locally, the electrochemical reaction cannot occur. State-of-the-art electrodes are ionomer-bonded carbon-supported Pt-based nanoparticles (ionomer and carbon ensure sufficient proton and electrical conductivities) and are designed to maximize the number of "three-phase boundaries" [21].

The catalyst utilization factor u_{Pt} expresses the fraction of Pt-based nanoparticles that is both in electronic and ionic connection in the catalyst layer. This factor can be defined as the ratio of the practical electrochemically active surface area ($S_{Pt,MEA}$) to the theoretical active surface area of Pt particles ($S_{Pt,Cat}$) as defined by Gasteiger *et al.* [14]. The effectiveness factor u_{eff}, first introduced by Thiele [22] and Wheeler [23] in the field of heterogeneous gas phase catalysis and later adapted to electrocatalysis for PEMFC [24], is defined as the apparent rate of current conversion exhibited by a specific catalyst layer design (current density, expressed per cm^2 of Pt) divided by the ideal rate obtained if all Pt atoms were used ideally, *i.e.* in absence of ohmic and mass-transport limitations. A proper catalyst layer morphology therefore results of a trade-off between sufficient ionomer content to

reach high proton conductivity (and thus high u_{Pt}) and sufficient porosity to enable high reactant/products mass-transport (and thus high u_{eff}) [25-27].

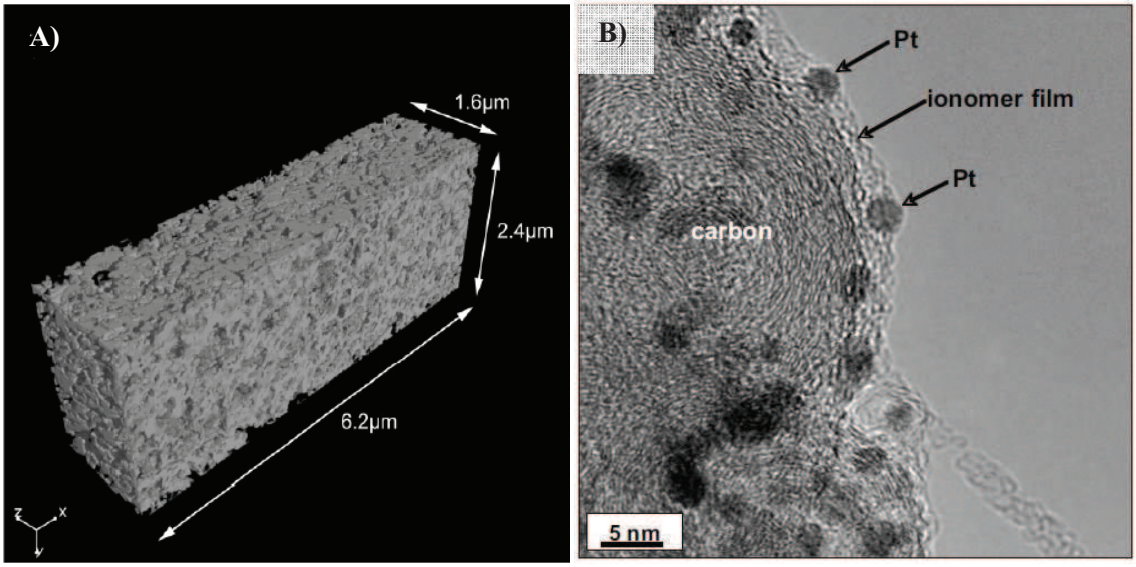

Figure I-5. (A) 3D visualization by FIB nanotomography of a porous electrode reprinted from Zils et al [20]. (B) TEM image showing a model structure of a Pt/C catalyst surrounded by a thin ionomer film reprinted from More et al [28].

a. Platinum-based catalyst nanoparticles

As detailed above, the slow ORR kinetics lowers the performance of a PEMFC compared to thermodynamical predictions. Despite their drawbacks, Platinum-based electrocatalysts remain the best candidates for a successful PEMFC operation, for both the anode and the cathode. Indeed, these materials offer the lowest overpotentials and the highest exchange current densities for the ORR and HOR combined with a high electrochemical stability in acidic media [14]. During the last four decades, only when working on structuring the electrodes, the platinum loading has been reduced by a factor 100, while maintaining a decent ORR activity. This gain has been achieved when switching from Pt black electrodes to nanometer sized Pt nanoparticles, obtained by chemical syntheses or physical techniques [29]. The optimal size, that maximizes the surface specific area and the ORR mass activity (activity per mass of platinum), for a Pt catalyst ranges from 2 to 5 nm (Figure I-5B).

From a thermodynamic point of view, the equilibrium shape of crystallites is determined by the minimization of surface energy per unit area of exposed facets. In the case of Pt, which crystallizes in a face-centered-cubic (f.c.c.) structure, the surface energy of atomic planes with high symmetry follow the order (*111*) > (*100*) > (*110*), where (*hkl*) are the Miller index for planes and directions in crystal lattices, as expected from the surface atomic density [30]. The equilibrium shape of a Pt crystal

at zero temperature is a truncated octahedron consisting of (*111*) and (*100*) facets [31] (Figure I-6A). Clearly, Pt nanometer sized catalyst deviates from this ideal description and possesses numerous surface defects (Figure I-5B). However these nanoparticles, in terms of electrochemical behavior, possess fingerprints of their underlying model surface composition. Therefore we will have many occasions in this manuscript to comment and compare the behaviors/results obtained on Pt-based nanoparticles with those obtained on model surfaces.

From an electrocatalytic viewpoint, the Pt activity for the HOR and ORR (among other electrochemical reactions) is structure sensitive, as nicely summarized by Markovic and Ross [32]. For an ideal particle at equilibrium shape, the contribution of various structural elements is a function of the particle size and can be easily computed. As the particle size decreases, the surface fraction of edges increases whereas that of atoms associated with (111) and (100) facets decreases. For nanocrystals, this translates by the so-called particle size effect that renders small nanoparticles less active for the ORR than extended surfaces [14, 33-35]. Defect sites of lower coordination, edges and kinks bind ORR intermediates strongly leading to an almost negligible contribution from these under-coordinated atoms to the ORR activity (Figure I-6).

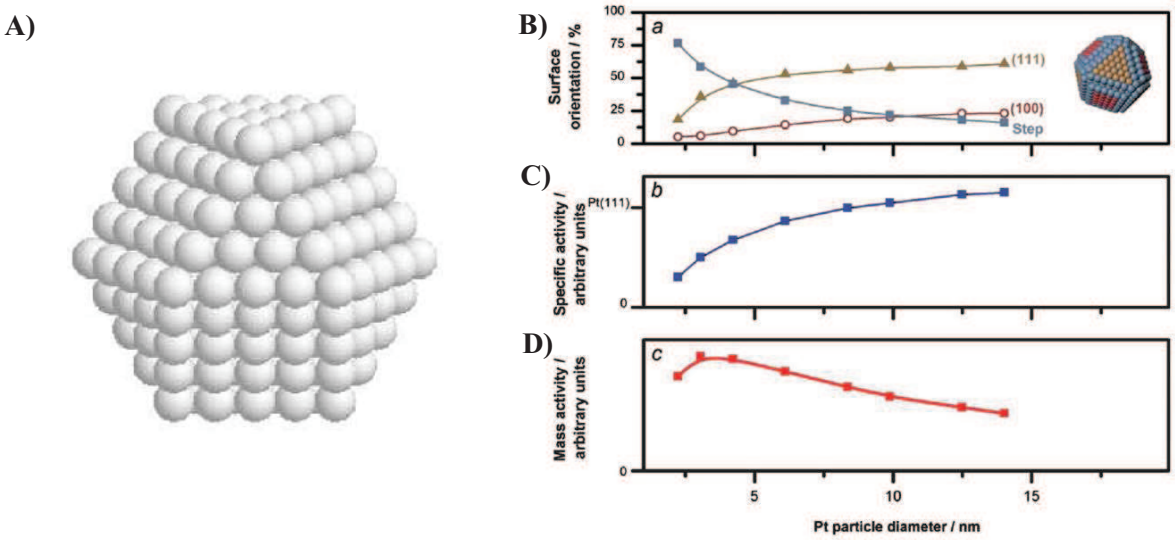

Figure I-6. (A) Atoms distribution for a 309 Pt atoms truncated octahedron under equilibrium shape crystal at T = 0 K based on a modified Wulff construction and reprinted from Mottet [36]. (B) Proportion of surface facets on Pt nanoparticles as a function of their size, based on a modified Wulff construction, as depicted in the inset, (C) theoretical trends in surface specific ORR activity, as a function of particle size, relative to the activity of Pt(111), by taking into account the theoretical activity and the relative proportions of the facets depicted in (B), and (D) theoretical trends in ORR activity, where the current is normalized according to the mass of Pt. (B, C and D) are reprinted from Stephens et al. [17].

With state-of-the-art materials, the Pt loading in a PEMFC is about 0.1 mg cm^{-2} at the anode and 4 times higher at the cathode [14]. Platinum based electrodes represent approximately one half of the cost of a stack and one fourth of the total cost of a PEMFC system [37]. A lot of efforts have to be made to reach the long-term target cost of less than $50 to produce 1 kW. Currently, the average platinum loading needed to produce 100 kW, the requirement for a Fuel Cell Vehicle, is 50 g_{Pt}. Contrary to the cost of the PEM, that can decrease up to a factor 100 if the increase of the annual productions rate maintains in the future [38], with the continuing rise of the platinum cost as primary resource , the current platinum loading in a PEMFC system (0.5 mg_{Pt} cm^{-2} equating to 0.5 g_{Pt} kW^{-1}) has to be divided by at least 5 to reach the long-term cost target.

b. High surface area carbon support

Pt catalyst nanoparticles are supported onto high surface area carbon black, *e.g.* Vulcan XC-72 carbon 250 m^2 g^{-1}_{carbon}. The ensemble Pt catalyst and carbon support is denoted as Pt/C. Thanks to the high carbon surface area, an equal ratio of 1 to 1 of platinum mass per carbon mass can be achieved while keeping the mean platinum particle size at 2 to 5 nm. The role of the carbon support is to ensure the good electrical conductivity between the catalyst nanoparticles and the current collectors of the PEMFC. Typical sizes for carbon primary structures range from 30 to 100 nm (Figure I-5B).

c. Ionomer

In order to ensure sufficient proton conductivity in the two Pt/C electrodes, the latter are partly filled with a proton conducting solid polymer, most of the time the same as the one used in the PEM (detailed below), a perfluorosulfonated polymer. To make the distinction with the polymer in the electrolyte (the PEM), the polymer in the electrodes will be referred to as the ionomer. The ionomer content in an electrode is expressed with the *I*/*C* ratio, which is the mass of ionomer divided by that of carbon. Low *I*/*C* values (< 0.5) induce undesirable high proton conduction resistance, whereas high *I*/*C* values (> 2) induce undesirable high gas diffusion resistances through the electrodes [40]. An *I/C* ratio from 0.5 to 1 is close to the optimum and must be adjusted to the physical and chemical nature of the carbon substrate [41]. When well distributed on the Pt/C catalyst, the average ionomer thickness over the carbon particles is in the range of a few nanometers (Figure I-5B).

2. Proton exchange membrane (PEM)

The large improvements on solid polymer electrolytes brought by Nafion® membranes have resuscitate the interest for PEMFC in the 1980's, with respect to other type of low temperature fuel cells. Typical solid polymer electrolyte materials are perfluorosulfonic acid (PFSA) membranes, such as Nafion® (Du Pont de Nemours & Co.), Flemion® and Aciplex® (Asahi Glass), Dow (Dow Chemical Company), and Aquivion® (Solvay). Structurally, PFSA membranes consist of a polytetrafluoroethylene (PTFE) backbone upon which perfluorovinyl ether and sulfonate groups are bonded (-SO_3H, see Figure I-7A). The sulfonate groups allow the transport of protons (and other cations) in the membrane, which leads to a high acidic environment in/near the electrolyte for the electrodes. The PTFE backbone ensures high mechanical and chemical stability up to T = 393 K (for practical purposes the operating temperature of a PEMFC based on a PFSA PEM is set below T = 353 K). The most important properties of a PEM are:

- the ionic (proton) conductivity (in S m^{-1}), which is strong function of its water uptake (λ, without unity, number of water molecules per sulfonate groups), equivalent weight (EW in $g_{polymer}$ $mol_{SO_3H}^{-1}$ defined as the weight of polymer in molecular mass per mole of sulfonic acid group) or ion exchange capacity (IEC = 1/EW) [42-44], the temperature and the history of the PEM. Typical ionic conductivities at fully humidified conditions are close to 100 mS cm^{-1} .

- the gas permeability of hydrogen and oxygen (p_{H_2} and p_{O_2} respectively in mol cm^{-1} s^{-1}), defined as the product of the gas diffusivity D (in cm^2 s^{-1}) and solubility C (in mol cm^{-3}). Typical diffusion coefficients (and solubilities respectively) of dissolved O_2 and H_2 in Nafion® are in the range of 1.10^{-6} cm^2 s^{-1} (10^{-6} mol cm^{-3} respectively) at T = 353 K [46, 47].

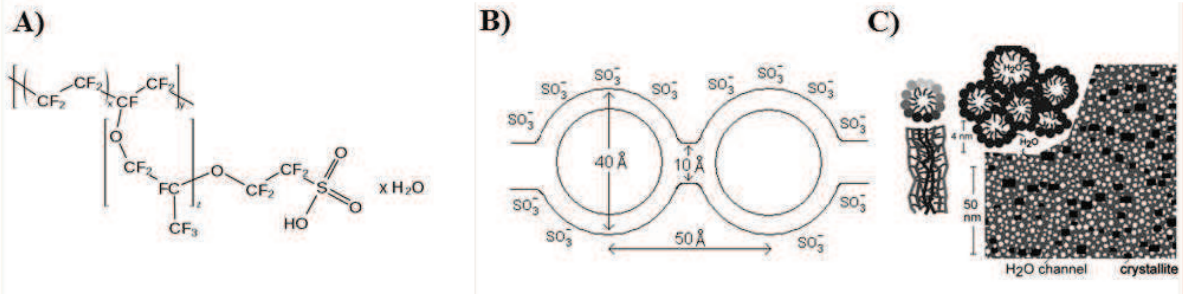

Figure I-7. (A) Chemical structure of Nafion®. (B, C) Two models of transport in Nafion® membranes: the Cluster Network model reprinted from Gierke and Hsu [48] and the Water Channel model reprinted from Schmidt-Rohr and Chen [49]

In a PEMFC, the PEM witnesses different ionic species (protons, impurities, cation contamination), liquid water from electro-osmotic drag and gas. Therefore, it is a still on-going

challenge to understand how such polymers handle these motions. Various models have been built up to describe the structure of Nafion® membranes and its change with the water content [50, 51]. Most of them are based on ionic clusters distributed in a hydrophobic polymeric matrix ("inverse micelles") [48, 50-52]. Upon swelling, the ionic clusters tend to aggregate to form a network where protons can efficiently be transported (Figure I-7). In the cluster-network model, sulfonate ion clusters with a 40 Å diameter are hold within a continuous fluorocarbon lattice while narrow channels of about 10 Å in diameter interconnect the clusters [48]. In the water-channel model, (Figure I-7C), the sulfonic acid functional groups self-organize into arrays of hydrophilic water channels, each of them being ~ 25 Å in diameter, through which small ions can be easily transported [49].

3. Gas diffusion layers (GDL)

Two gas diffusion layers sandwich the electrodes and the PEM to form a membrane-electrode assembly (MEA). These GDL, made of carbon fibers, provide the gaseous reactants and eliminate the produced water at/from the electrodes, through an optimal distribution of both a hydrophilic and a hydrophobic porous structure. These layers also provide a mechanical support to the electrodes (powders) and the PEM (soft polymer). State of the art GDL (e.g. Toray®, Freudenberg®, Sigracet®) are about 250 µm thick, porous at 80% and possess in-plane resistance smaller than 1 Ω. A good adhesion of the GDL to the electrode is necessary to avoid undesirable high electrical contact resistance. A complete datasheet about the GDL preparation techniques, ideal properties and characterizations methods has been given by Mathias *et al*. in Reference [53].

4. From the single galvanic cell to the PEMFC stack and system

The five-layer MEA are sandwiched between two bipolar plates made of stainless steel [54] or graphite-polymer-composite [55] to constitute a PEMFC unit/ single/ elementary cell (Figure I-8a). These bipolar plates are pretreated to show a hydrophilic behavior and stamped with a serpentine flow field design in order to let the gases and produced water droplets diffuse from a gas inlet to a gas outlet [56]. The bipolar plates ensure uniform gas distribution and heat management and collect the current. Bipolar plates represent a significant fraction of the total price of a stack (up to 45%) as well as nearly 80% of its weight. When *x* unit cells are assembled in series, they constitute a *x*-cell stack (Figure I-8b). A complete PEMFC system gathers the PEMFC stack and the required devices to hydrate, heat and supply the gases to the PEMFC stack and to collect the produced electricity. A Mobixane™ system, able to deliver from 0.5 to 2.5 kW under everyday life operating conditions, is shown in Figure I-8c.

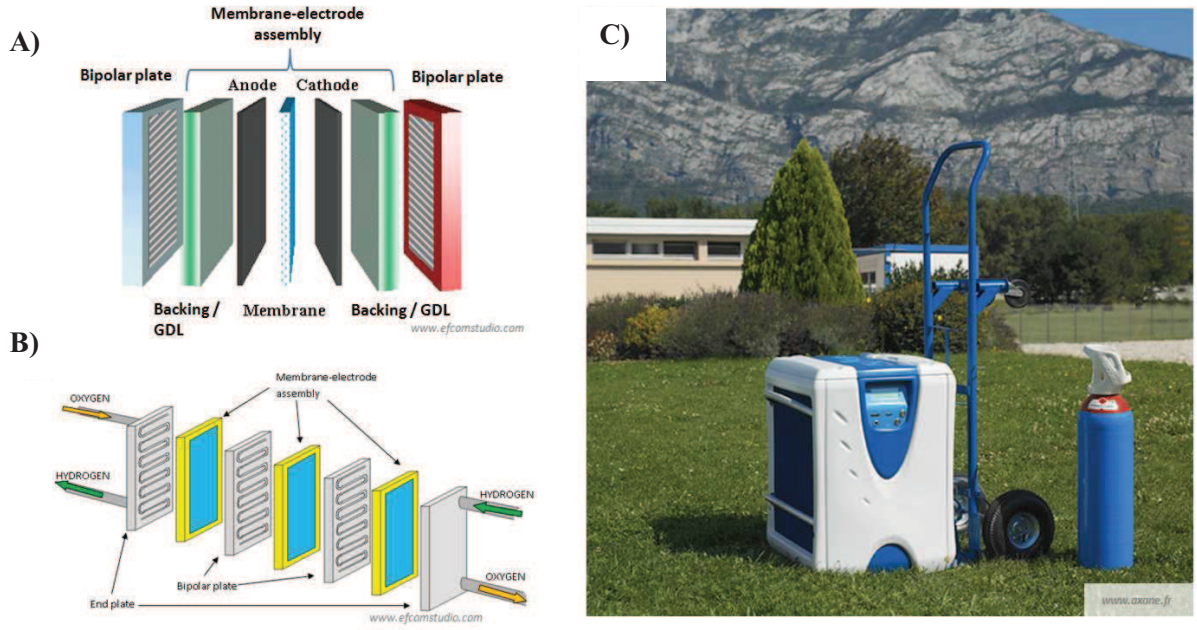

Figure I-8. (A) Simplified composition of a PEMFC unit cell. (B) Simplified composition of a 3-cell PEMFC stack. (C) Picture of a PEMFC system: the Mobixane™.

IV. PEMFC performance under polarization with state-of-the-art materials: from the thermodynamical promises to the first limitations

A PEMFC has an electromotive force of *ca.* E_{eq} (T, P_{O2}, P_{H2}) = 1.169 V, which equates to a standard electric work of *ca.* 237 kJ mol_{H2}^{-1}, under typical PEMFC operating conditions at T = 253 K [14]. During operation, additional voltage losses appear, which are at the origin of the shape of the *I* - E polarization curve (see Figure I-9). As detailed in a series of studies conducted by Gasteiger and coworkers [3, 4, 14, 40, 57, 58], the polarization curve can be deconvoluted into several contributions:

- Activation losses due to the kinetics of the HOR (η_{HOR}) and the ORR (η_{ORR}) on Pt-based materials.
- Ohmic losses (ΔE_{ohmic}) associated with the transport of protons and electrons in the cell. ΔE_{ohmic} is mostly composed of the membrane resistance and of the non-negligible electrical contact resistances between each component of the MEA.
- Mass-transport losses (η_{tx}) due to the proton transport in the polymer phase of the electrodes ($j * R_{H^+,an\&ca(RH)}$) and the oxygen transport in the gas phase of the electrode ($\eta_{tx,O_2(dry)} - \eta_{tx,O_2(wet)}$).

At low current densities the difference between the cell voltage and the thermodynamic equilibrium value is dominated by the cathode overpotential (η_{ORR}) due to the sluggish kinetics of the ORR. At large current densities, mass transport of dioxygen and protons in the cathode CL and in the GDL give significant contribution to the overall losses. For example, at j = 1.5 A cm^{-2}, the ORR losses account for 410 mV, the HOR losses represent 5 mV (75 % of the total voltage losses are attributed to the electrochemical reactions), the ohmic voltage loss ($\Delta E_{ohmic} = j * R_{\Omega(RH)}$) accounts for 90 mV (15 % of the total losses), and the mass transport limitations account for 50 mV (10 % of the total losses). A PEMFC performance can be modeled with equation I-10, where each of these terms are calculated (see [3, 4, 14, 40, 57, 58] for the detailed expression of each term) with physical parameters of the materials used in the PEMFC (*e.g.* the measured kinetics of the electrodes, the transport properties of each species in each phase, etc…).

$$E_{\text{cell}} = E_{\text{rev}} - j * R_{\Omega(\text{RH})} - \eta_{\text{HOR}} - |\eta_{\text{ORR}}| - j * R_{\text{H}^+,\text{an\&ca(RH)}} - \eta_{\text{tx,O}_2\text{(dry)}} - \eta_{\text{tx,O}_2\text{(wet)}} \quad \text{Eq.I-10}$$

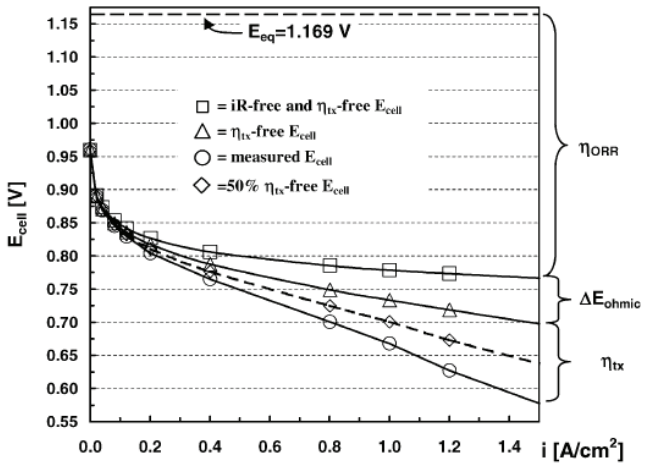

Figure I-9. Circles: 50 cm^2 single-cell H_2/air performance. Squares: E_{cell} vs. i for the mass-transport-free and ohmic corrected (i.e., iR-free) E_{cell}/i-curve shown in (a). (c) Triangles: Addition of the ohmic losses, ΔE_{ohmic}, to the polarization curve shown in (b). (d) Diamonds: E_{cell}/i-curve shown in (a) corrected for 50% of the mass-transport losses. Reprinted from Gasteiger et al. [14].

V. Introduction to the durability issues of state-of-the-art PEMFC components under operation

During the last decade, PEMFCs have witnessed major technology breakthroughs, which for the first time rendered fuel-cell powered applications a practical possibility. However, three major hurdles still need to be overcome to ensure economic viability of the technology: cost, storage/production of hydrogen, and durability. In terms of durability, MEAs must be able to spend at

least 10 years in a vehicle, equating to 5,500 h of operations under transient conditions (including start-stop and freeze-thaw events [38], while keeping a decent electrical performance over time. However PEMFC systems can lose electrical performance (decrease of E_{cell} in equation I-10) due to reversible or irreversible failures of one or more of its materials constituting the MEA [59, 60].

1. Platinum instability under PEMFC operation

The degradation of platinum nanoparticles occurs through their electrochemical dissolution ($E^0_{Pt^{2+}/Pt}$ = 1.18 V *vs*. NHE at T = 298 K), possible at the cathode of a PEMFC under high voltage (and accelerated by potential transient conditions [61-64]) due to the low but finite equilibrium soluble platinum concentration (+II or +IV oxidation state) as shown in Figure I-10A. The dissolution of Pt is believed to proceed either by the direct electrochemical dissolution from the metallic phase [59, 65, 66]:

$$Pt \rightarrow Pt^{2+} + 2e^- \quad \text{Eq. I-11}$$

or *via* the formation of oxidized Pt (in the form of a 2D adsorbate phase or a 3D subsurface oxide) and its subsequent chemical dissolution:

$$Pt + xH_2O \rightarrow PtO_x + 2xH^+ + 2xe^- \quad \text{Eq. I-12}$$

$$PtO_x + 2xH^+ \rightarrow Pt^{2x+} + xH_2O \quad \text{Eq. I-13}$$

or *via* the reduction of the oxide [67]:

$$PtO_2 + 4H^+ + 2e^- \rightarrow Pt^{2+} + 2H_20 \quad \text{Eq. I-14}$$

The reduced stability of the Pt-based nanoparticles compared to bulk Pt is related to the increasing fraction of low-coordinated atoms with the decrease of their size. Indeed, low-coordinated atoms possess higher surface free energy than the atoms contained in the bulk material [61]. The excess surface energy affects the chemical potential per metal atom, as shown by the Gibbs-Thompson relation:

$$\mu(r) = \mu(r = \infty) + \frac{2\gamma_{Pt}V_{Pt}}{r} \quad \text{Eq. I-15}$$

where $\mu(r = \infty)$ is the chemical potential of the bulk Pt phase, r is the radius of the Pt nanoparticle, γ_{Pt} is the surface tension and V_{Pt} is the molar volume of bulk Pt. Equation I-15 shows that the chemical potential of a Pt atom in the smaller grain r is higher than in the bulk and consequently larger grains will grow at the expense of the smaller ones. This phenomenon is known as Ostwald ripening.

In electrochemistry, the Gibbs-Thompson relation translates into a size dependency of the redox potential (M^{z+}/M) for a given metal M [68]:

$$E(r) = E(r=\infty) + \frac{2\gamma_{Pt}V_{Pt}}{zFr} \qquad \text{Eq. I-16}$$

where F is the Faraday constant. Equation I-16 nicely explains the preferential dissolution/redeposition of the smallest platinum nanoparticles observed during PEMFC operation [66]. Once produced at the PEMFC cathode [61-64, 69-71], Pt^{z+} (z = 2 or 4) ions can:

- redeposit electrochemically on larger Pt nanocrystals. This mechanism does not lead to a loss of platinum mass in the electrodes but to the increase of the mean particle size (Figure I-10B) and so to a decrease of the electrochemical surface area. The decreased electrochemical surface area lowers the ORR mass activity (the catalytic activity expressed per gram of Pt) and so increases the η_{ORR} term in equation I-10 (assuming the ECSA loss is not counterbalanced by the positive effect of the nanoparticle growth).

- be transported through the ionomer phase of the cathode/membrane following the electro-osmotic drag or the chemical diffusion, before being chemically reduced by hydrogen crossing over the membrane. It has also been suggested [63] that chloride ions (commonly used for the synthesis of metal nanoparticles), fluoride or sulphate ions (membrane/ ionomer degradation products) may promote the migration from the cathode to the anode of negatively charged Pt complexes. Diffusion/migration of Pt^{z+} ions out of the cathode leads to a decrease of the platinum content and to the formation of the so called "Pt-band" in the PEM (Figure I-10C) [72-74].

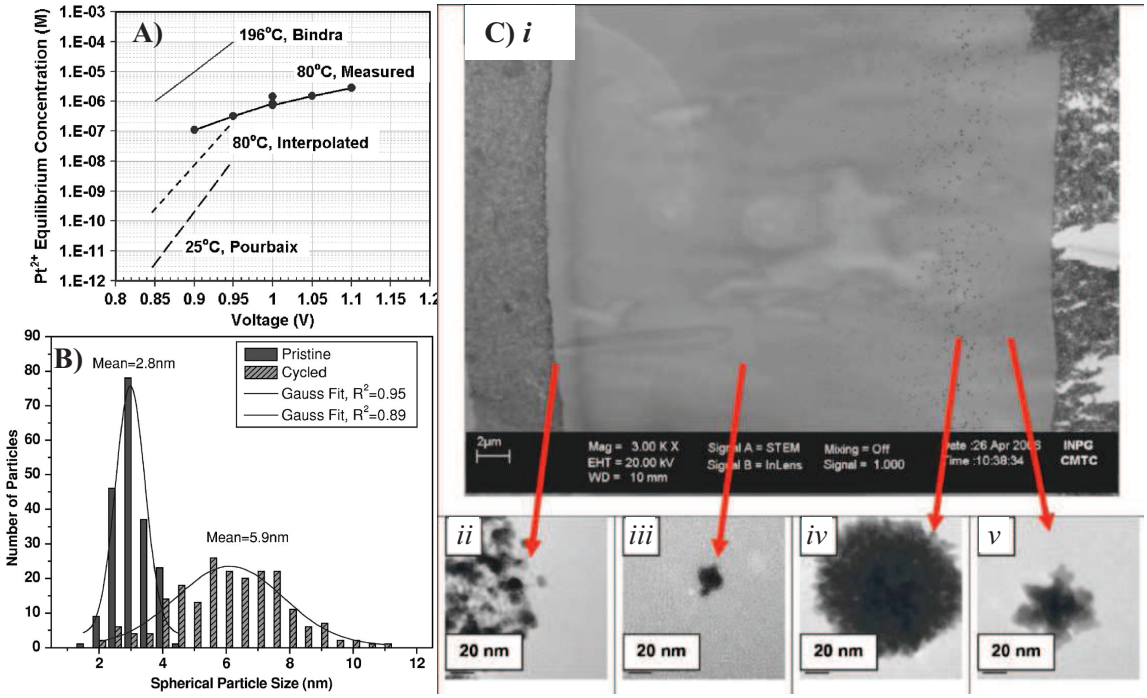

Figure I-10. (A) Equilibrium soluble platinum concentration as a function of the temperature and the cell voltage and (B) size distributions of Pt/Vulcan nanoparticles before/after potential sweeping in a MEA. Reprinted from Ferreira et al. [62]. (C) FEG-SEM images of (i) a cross-sectioned aged PEMFC MEA with (ii – v) higher magnification of Pt nanoparticles inside the PEM imaged by TEM. Reprinted from Guilminot et al. [63].

2. Carbon instability under PEMFC operation

The equilibrium potential of carbon oxidation to carbon dioxide is E^{0}_{C/CO_2} = 0.207 V *vs*. NHE at T = 298 K. This implies that carbon support materials are exposed to conditions which favor their oxidation in PEMFC cathodes: high values of the electrode potential, acidic environment (pH < 1), liquid (water) and oxidizing (dioxygen) environment, elevated temperature but also the presence of electrocatalysts such as (noble) metal nanoparticles. The mechanism of carbon oxidation remains intensively discussed since the early study of Kinoshita and Bett [75]. It has been suggested that carbon oxidizes to CO_2 *via* a dual pathway including the formation of carbon surface oxides (indirect pathway) or the evolution of gaseous CO_2 (direct pathway):

$C + 2H_2O \rightarrow CO_2 + 4H^+ + 4e^-$ $\quad E^0_{CO_2/C}$ = 0.207 V *vs.* NHE $\quad (T = 298\ K)$ Eq. I-17

$C + H_2O \rightarrow CO_{ad} + 2H^+ + 2e^-$ $\quad E^0_{CO/C}$ = 0.518 V *vs.* NHE $\quad (T = 298\ K)$ Eq. I-18

$CO_{ad} + H_2O \rightarrow CO_2 + 2H^+ + 2e^-$ $\quad E^0_{CO_2/CO}$ = - 0.103 V *vs.* NHE $\quad (T = 298\ K)$ Eq. I-19

It is believed that these two processes occur independently on the surface of carbon supports used in PEMFCs [76]. The carbon oxidation kinetics is rather slow at conventional operation potential of a PEMFC cathode, but is significantly increased for E > 1 V *vs*. RHE [76, 77] or during electrode potential transients [78].

At the nanoscale, the oxidation of the carbon support is enhanced at the platinum | carbon interface, because platinum nanoparticles play a role of catalysts. Oxidation of the metal | carbon interface causes the detachment of the platinum nanoparticles. Once disconnected they can either (i) superficially diffuse and further coalesce/agglomerate with other Pt nanoparticles [62, 79-82] or (ii) stay electrically disconnected from the carbon support in the ionomer phase [62, 79, 80, 83, 84]. These phenomena result in a decrease of the ECSA [63, 85]. When occurring at large rates (*e.g.* due to numerous potential transient events), the carbon oxidation through the direct pathway causes a decrease of the cathode catalyst layer thickness (Figure I-11A and B) as well as changes in its porous structure, which in turns affects the transport properties of gas/liquids and increases the mass transport

losses [62, 79, 80, 82, 83, 86-88]. The formation of surface carbon oxides (indirect pathway) complicates water management (the surface becomes more hydrophilic) [89-91].

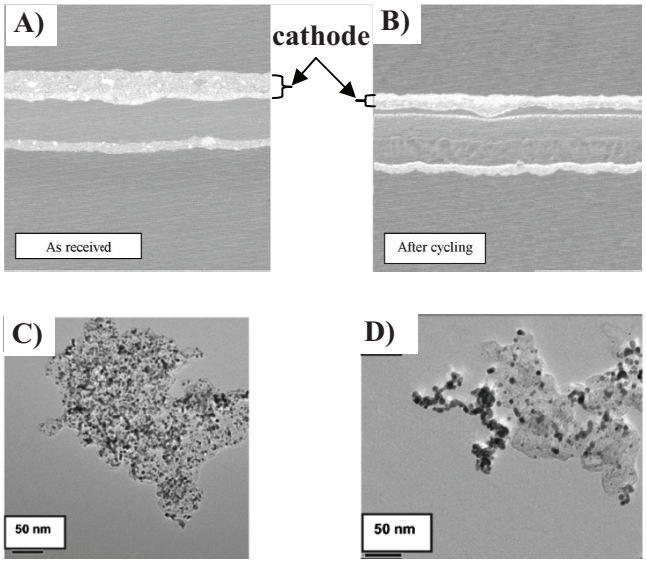

Figure I-11. Electron microprobe images of (A) as-received and (B) post-cycling MEAs reprinted from [92]. Transmission electron microscopy photographs of (C) fresh and (D) aged cathodes catalysts reproduced from [64].

3. Proton Exchange Membrane / Ionomer degradation under PEMFC operation

Nafion®-like polymers can degrade *via* rupture of side-chains or carboxylic end-groups [93] due to the interaction of carbon with strong oxidants (*e.g.* radical species such as hydroxyl $OH^{\bullet}$ and hydroperoxyl $HOO^{\bullet}$ that are generated from H_2O_2 decomposition [94-96]). H_2O_2 can be generated by the oxidation of water and the reduction of oxygen (see Figure I-12) while the thermocatalytic decomposition of H_2O_2 (the Fenton's reaction) is favored in the presence of metal contaminants, such as iron, copper, chromium, cobalt (each present in the PEM as traces [97, 98]) or Pt^{z+} ions produced by the electrochemical oxidation of the Pt nanoparticles [79] at the cathode. These species are also formed at the anode as a consequence of O_2 crossover [97-99]. $OH^{\bullet}$ species have also been detected at the cathode side by electron paramagnetic resonance (EPR) spectrometer via spin trapping [100], although the H_2O_2 production at the cathode is believed to be smaller than at the anode [99]. The main consequence of the PEM degradation is a loss of proton conductivity. High degradation rates yield a significant decrease of the membrane thickness, with even the formation of pineholes [101], adversely affecting the required gas separation between the two electrodes. The degradation of the ionomer in the electrodes is more subtle to observe but is thought to lower the number of "three-phase boundaries" (decrease of ECSA) and increase the proton transport resistance in the electrodes [102].

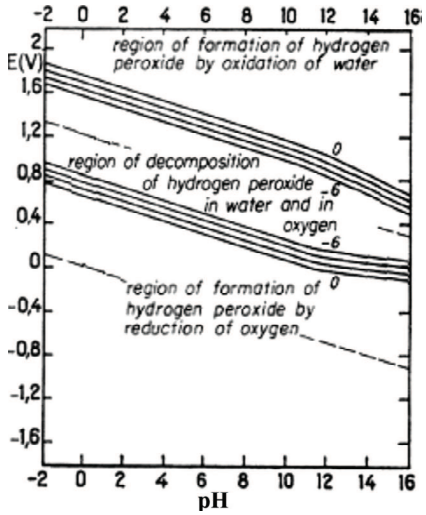

Figure I-12. Pourbaix diagram for H_2O_2 formation and decomposition. Reprinted from Pourbaix [103]

VI. Introduction to the work presented in this thesis

It is clear from the introduction that several hurdles need to be overpassed to ensure the technological and economic viability of the PEMFC technology. One of the major difficulties is the Pt cost of the MEA [14]. The classical cathode (400 μg_{Pt} per geometrical cm^2) and anode (100 μg_{Pt} per geometrical cm^2) Pt loadings must be reduced to meet economic viability. To reach this goal, research and development activities explored two strategies: (i) directly reducing the Pt loading in the CL, (ii) improving the Pt specific activity (SA, activity for the ORR per unit Pt surface area) of the cathodic reaction by a fine tuning of the physical (size, facet distribution and shape) and/or chemical structure (addition of one or more co-elements to platinum) of the metal nanoparticles. However, the question whether "out-of-equilibrium" large Pt nanocrystallites and Pt-alloys maintain their favourable electrocatalytic properties over time still remains opened [14, 38, 73, 104-111]. Unfortunately, most of the works conducted so far investigated the durability of Pt-based/C nanoparticles on short time scales (acid-leaching, voltage cycling in liquid or in solid electrolyte, short PEMFC testing), which are very useful, but do not provide a clear insight into the long-term degradation mechanisms of Pt-based/C catalysts. Also, a detailed picture of how Pt-based/C atomic structures, chemical compositions and morphologies are changing during PEMFC operation and how they influence the surface reactivity is still lacking.

On this basis, in **Chapter III,** we will investigate whether a commercial Pt_3Co-based cathode, which initially performs better for the ORR and present a lower platinum content than a pure Pt cathode, presents the required robustness for wide commercialization in PEMFC systems.

Chapter IV will be devoted to the understanding of the degradation mechanisms of Pt_3Co catalysts in real PEMFC conditions. A special effort will be made to discuss and reconcile the conclusions obtained by different groups on such catalyst aged under accelerated tests or real PEMFC operation.

As briefly evoked in the paragraph describing the durability issues of proton exchange polymers, the presence of metallic cations as traces in a PEM accelerates its chemical degradation. However, their influence on the ORR kinetics at Pt surfaces has only been scarcely studied and is not fully understood from a mechanistic point of view. This will be discussed in **Chapter V** and a special attention will be paid to the influence of Co^{2+} contamination on the ORR kinetics and mechanism.

Finally, although a few studies pointing toward localized degradation phenomena (*e.g.* relative to the PEM or CL) exist, it is striking to note that the PEMFC MEA is generally considered to age homogeneously. Knowing that oxygen is consumed and water produced/accumulated along the gas channel, in-plane heterogeneities *i.e.* from the location where gases are fed in to the position where they exit the MEA, are likely to develop, leading to uneven current distribution within individual MEA. Heterogeneities of ageing of Pt_3Co/C catalysts (structure and composition) within a same MEA will be highlighted in **Chapter VI**.

Before entering the chapter dedicated to results and discussions, **Chapter II** will provide a survey of the main experimental techniques used in the present work.

VII. References

[1] Cerri I., TOYOTA's view of future electromobility. *27th PSI One-Day-Symposium*, (2011).

[2] Sandstede G., Cairns E. J., Bagotsky V. S. and Wiesener K., History of low temperature fuel cells, in *Handbook of Fuel Cells: Fundamentals Technology and Applications*, Vol. 1, Vielstich W., Gasteiger H. and Lamm A. 2003, John Wiley & Sons

[3] Neyerlin K. C., Gu W., Jorne J. and Gasteiger H. A., Study of the exchange current density for the hydrogen oxidation and evolution reactions. *J. Electrochem. Soc.*, 154 (2007).

[4] Neyerlin K. C., Gu W. B., Jorne J. and Gasteiger H. A., Determination of catalyst unique parameters for the oxygen reduction reaction in a PEMFC. *J. Electrochem. Soc.*, 153 (2006) A1955-A1963.

[5] Wroblowa H. S., Pan Y. C. and Razumney G., Electroreduction of oxygen: A new mechanistic criterion. *J. Electroanal. Chem.*, 69 (1976) 195-201.

[6] Adzic R. R., Recent advances in the kinetics of oxygen reduction, in *Electrocatalysis*, Vol. Lipkowski J. and Ross P. N. 1998, Wiley-VCH

[7] Markovic N. M., Schmidt T. J., Stamenkovic V. and Ross P. N., Oxygen reduction reaction on Pt and Pt bimetallic surfaces: A selective review. *Fuel Cells*, 1 (2001) 105-116.

[8] Schneider A., Colmenares L., Seidel Y. E., Jusys Z., Wickman B., Kasemo B. and Behm R. J., Transport effects in the oxygen reduction reaction on nanostructured, planar glassy carbon supported Pt/GC model electrodes. *Phys. Chem. Chem. Phys.*, 10 (2008) 1931-1943.

[9] Chen S. L. and Kucernak A., Electrocatalysis under conditions of high mass transport rate: Oxygen reduction on single submicrometer-sized Pt particles supported on carbon. *J. Phys. Chem. B*, 108 (2004) 3262-3276.

[10] Dubau L., Maillard F., Chatenet M., André J. and Rossinot E., Nanoscale compositional changes and modification of the surface reactivity of Pt_3Co/C nanoparticles during proton-exchange membrane fuel cell operation. *Electrochim. Acta*, 56 (2010) 776-783.

[11] Wang J. X., Markovic N. M. and Adzic R. R., Kinetic analysis of oxygen reduction on Pt(111) in acid solutions: Intrinsic kinetic parameters and anion adsorption effects. *J. Phys. Chem. B*, 108 (2004) 4127-4133.

[12] Stamenkovic V. R., Mun B. S., Arenz M., Mayrhofer K. J. J., Lucas C. A., Wang G. F., Ross P. N. and Markovic N. M., Trends in electrocatalysis on extended and nanoscale Pt-bimetallic alloy surfaces. *Nat. Mater.*, 6 (2007) 241-247.

[13] Gasteiger H. A., Gu W. B., Makharia R., Mathias M. and Sompalli B., Beginning-of-life MEA performance - Efficiency loss contributions, in *Handbook of Fuel Cells: Fundamentals, Technology, and Applications*, Vol. 3, Vielstich W., Gasteiger H. A. and Lamm A. 2003, John Wiley & Sons

[14] Gasteiger H. A., Kocha S. S., Sompalli B. and Wagner F. T., Activity benchmarks and requirements for Pt, Pt-alloy, and non-Pt oxygen reduction catalysts for PEMFCs. *Appl. Catal. B.*, 56 (2005) 9-35.

[15] Subbaraman R., Strmcnik D., Paulikas A. P., Stamenkovic V. R. and Markovic N. M., Oxygen reduction reaction at three-phase interfaces. *Chem. Phys. Chem.*, 11 (2010) 2825-2833.

[16] Conway B. E., Electrochemical oxide film formation at noble-metals as a surface-chemical process. *Prog. Surf. Sci.*, 49 (1995) 331-452.

[17] Stephens I. E. L., Bondarenko A. S., Gronbjerg U., Rossmeisl J. and Chorkendorff I., Understanding the electrocatalysis of oxygen reduction on platinum and its alloys. *Energy Environ. Sci.*, 5 (2012) 6744-6762.

[18] Liu Y. X., Mathias M. and Zhang J. L., Measurement of platinum oxide coverage in a proton exchange membrane fuel cell. *Electrochem. Solid-State Lett.*, 13 (2010) B1-B3.

[19] Grove W. R., On voltaic series and the combination of gases by platinum. *Philos. Mag.*, 14 (1839) 127-130.

[20] Zils S., Timpel M., Arlt T., Wolz A., Manke I. and Roth C., 3D visualisation of PEMFC eectrode structures using FIB nanotomography. *Fuel Cells*, 10 (2010) 966-972.

[21] Kocha S. S., Principles of MEA preparation, in *Handbook of Fuel Cells: Fundamentals, Technology, and Applications*, Vol. 3, Vielstich W., Gasteiger H. A. and Lamm A. 2003, John Wiley & Sons

[22] Thiele E., Relation between catalytic activity and size of particle. *Ind. Eng. Chem.*, 31 (1939) 916.

[23] Wheeler A., Reaction rates and selectivity in catalyst pores. *Adv. Cat.*, 3 (1951) 249.

[24] Gloaguen F., Andolfatto F., Durand R. and Ozil P., Kinetic-study of electrochemical reactions at catalyst-recast ionomer interfaces from thin active layer modeling. *J. Appl. Electrochem.*, 24 (1994) 863-869.

[25] Antolini E., Giorgi L., Pozio A. and Passalacqua E., Influence of Nafion® loading in the catalyst layer of gas-diffusion electrodes for PEFC. *J. Power Sources*, 77 (1999) 136-142.

[26] Song J. M., Cha S. Y. and Lee W. M., Optimal composition of polymer electrolyte fuel cell electrodes determined by the AC impedance method. *J. Power Sources*, 94 (2001) 78-84.

[27] Li G. C. and Pickup P. G., Ionic conductivity of PEMFC electrodes - Effect of Nafion® loading. *J. Electrochem. Soc.*, 150 (2003) C745-C752.

[28] More K., Borup R. and Reeves K., Identifying contributing degradation phenomena in PEM fuel cell membrane electride assemblies *via* electron microscopy. *ECS Trans.*, 3 (2006) 717-733.

[29] Peng Z. and Yang H., Designer platinum nanoparticles: Control of shape, composition in alloy, nanostructure and electrocatalytic property. *Nano Today*, 4 (2009) 143-164.

[30] Skriver H. L. and Rosengaard N. M., Surface energy and work function of elemental metals. *Phys. Rev. B*, 46 (1992) 7157.

[31] Frenken J. W. M. and Stoltze P., Are vicinal metal surfaces stable? *Phys. Rev. Lett.*, 82 (1999) 3500-3503.

[32] Markovic N. M. and Ross P. N., Surface science studies of model fuel cell electrocatalysts. *Surf. Sci. Rep.*, 45 (2002) 117-229.

[33] Mayrhofer K. J. J., Strmcnik D., Blizanac B. B., Stamenkovic V., Arenz M. and Markovic N. M., Measurement of oxygen reduction activities via the rotating disc electrode method: From Pt model surfaces to carbon-supported high surface area catalysts. *Electrochim. Acta*, 53 (2008) 3181-3188.

[34] Maillard F., Pronkin S. and Savinova E. R., Size effects in electrocatalysis of fuel cells reactions on supported metal nanoparticles, in *Fuel Cell Catalysis: a Surface Science Approach*, Vol. Koper M. T. M. 2009, John Wiley & Sons, Inc.

[35] Maillard F., Pronkin S. and Savinova E. R., Influence of size on the electrocatalytic activities of supported metal nanoparticles in fuel cells related reactions, in *Handbook of Fuel Cells: Fundamentals, Technology, and Applications*, Vol. 5, Vielstich W., Gasteiger H. A. and Yokokawa H. 2009, John Wiley & Sons

[36] Mottet C., Étude par simulation numérique d'agrégats libres mono- et bi-métalliques, 1997, Université de la Méditerranée Aix-Marseille II, Marseille.

[37] Rabis A., Rodriguez P. and Schmidt T. J., Electrocatalysis for polymer electrolyte fuel cells: Recent achievements and future challenges. *Acs Catalysis*, 2 (2012) 864-890.

[38] Mathias M. F., Makharia R., Gasteiger H., Conley J. J., Fuller T. J., Gittleman G. J., Kocha S. S., Miller D. P., Mittelsteadt C. K., Xie T., Yan S. G. and Yu P. T., Two fuel cell cars in every garage? *Interface*, 14 (2005) 24-35.

[39] Noble metal price: http://cours-des-metaux.fr/

[40] Liu Y. X., Ji C. X., Gu W. B., Baker D. R., Jorne J. and Gasteiger H. A., Proton conduction in PEM fuel cell cathodes: Effects of electrode thickness and ionomer equivalent weight. *J. Electrochem. Soc.*, 157 (2009) B1154-B1162.

[41] Chatenet M., Dubau L., Job N. and Maillard F., The (electro)catalystmembrane interface in the Proton Exchange Membrane Fuel Cell: Similarities and differences with non-electrochemical Catalytic Membrane Reactors. *Catal. Today*, 156 (2010) 76-86.

[42] Zawodzinski T. A., Derouin C., Radzinski S., Sherman R. J., Smith V. T., Springer T. E. and Gottesfeld S., Water uptake by and transport through Nafion® 117 membranes. *J. Electrochem. Soc.*, 140 (1993) 1041-1047.

[43] Zawodzinski T. A., Springer T. E., Uribe F. and Gottesfeld S., Characterization of polymer electrolytes for fuel-cell applications. *Solid State Ionics*, 60 (1993) 199-211.

[44] Fontanella J. J., Edmondson C. A., Wintersgill M. C., Wu Y. and Greenbaum S. G., High-pressure electrical conductivity and NMR studies in variable equivalent weight Nafion® membranes. *Macromolecules*, 29 (1996) 4944-4951.

[45] Dupont™ Nafion® membranes and dispersions: http://www2.dupont.com

[46] Ogumi Z., Kuroe T. and Takehara Z., Gas permeation in SPE method .2. Oxygen and hydrogen permeation through Nafion®. *J. Electrochem. Soc.*, 132 (1985) 2601-2605.

[47] Yeo R. S. and McBreen J., Transport properties of Nafion® membranes in electrochemically regenerative hydrogen-halogen cells. *J. Electrochem. Soc.*, 126 (1979) 1682-1687.

[48] Gierke T. D. and Hsu W. Y., The cluster-network model of ion clustering in perfluorosulfonated membranes. *ACS Symp. Ser.*, 180 (1982) 283-307.

[49] Schmidt-Rohr K. and Chen Q., Parallel cylindrical water nanochannels in Nafion® fuel-cell membranes. *Nat. Mater.*, 7 (2008) 75-83.

[50] Heitner-Wirguin C., Recent advances in perfluorinated ionomer membranes: Structure, properties and applications. *J. Membr. Sci.*, 120 (1996) 1-33.

[51] Mauritz K. A. and Moore R. B., State of understanding of Nafion®. *Chem. Rev.*, 104 (2004) 4535-4585.

[52] Rubatat L., Rollet A. L., Gebel G. and Diat O., Evidence of elongated polymeric aggregates in Nafion®. *Macromolecules*, 35 (2002) 4050-4055.

[53] Mathias M. F., Roth J., Fleming J. and Lenhert W., Diffusion media materials and caracterisation, in *Handbook of Fuel Cells: Fundamentals, Technology, and Applications*, Vol. 3, Vielstich W., Gasteiger H. A. and Lamm A. 2003, John Wiley & Sons

[54] Wind J., LaCroix A., Braueuninger S., Hendrich P., Heller C. and Schudy M., Metal bipolar plates and coatings, in *Handbook of Fuel Cells: Fundamentals, Technology, and Applications*, Vol. 3, Vielstich W., Gasteiger H. A. and Lamm A. 2003, John Wiley & Sons

[55] Rossberg K. and Trapp V., Graphite-based bipolar plates, in *Handbook of Fuel Cells: Fundamentals, Technology, and Applications*, Vol. 3, Vielstich W., Gasteiger H. A. and Lamm A. 2003, John Wiley & Sons

[56] Wilkinson D. P. and Vanderleeden O., Serpentine flow field design, in *Handbook of Fuel Cells: Fundamentals, Technology, and Applications*, Vol. 3, Vielstich W., Gasteiger H. A. and Lamm A. 2003, John Wiley & Sons

[57] Thompson E. L., Jome J. and Gasteiger H. A., Effects of current density and water content on electrode ice formation and membrane water uptake at -20°C. *ECS Trans.*, 11 (2007) 565-576.

[58] Liu Y., Ji C., Gu W., Jorne J. and Gasteiger H. A., Effects of catalyst carbon support on proton conduction and cathode performance in PEM fuel cells. *J. Electrochem. Soc.*, 158 (2011) B614-B621.

[59] Borup R., Meyers J., Pivovar B., Kim Y. S., Mukundan R., Garland N., Myers D., Wilson M., Garzon F., Wood D., Zelenay P., More K., Stroh K., Zawodzinski T., Boncella J., McGrath J. E., Inaba M., Miyatake K., Hori M., Ota K., Ogumi Z., Miyata S., Nishikata A., Siroma Z., Uchimoto Y., Yasuda K., Kimijima K. I. and Iwashita N., Scientific aspects of polymer electrolyte fuel cell durability and degradation. *Chem. Rev.*, 107 (2007) 3904-3951.

[60] de Bruijn F. A., Dam V. A. T. and Janssen G. J. M., Durability and degradation issues of PEM fuel cell components. *Fuel Cells*, 8 (2008) 3-22.

[61] Shao-Horn Y., Sheng W., Chen S., Ferreira P., Holby E. and Morgan D., Instability of supported platinum nanoparticles in low-temperature fuel cells. *Topics Catal.*, 46 (2007) 285-305.

[62] Ferreira P. J., La O' G. J., Shao-Horn Y., Morgan D., Makharia R., Kocha S. and Gasteiger H. A., Instability of Pt/C electrocatalysts in proton exchange membrane fuel cells. *J. Electrochem. Soc.*, 152 (2005) A2256-A2271.

[63] Guilminot E., Corcella A., Charlot F., Maillard F. and Chatenet M., Detection of Pt^{z+} ions and Pt nanoparticles inside the membrane of a used PEMFC. *J. Electrochem. Soc.*, 154 (2007) B96-B105.

[64] Guilminot E., Corcella A., Chatenet M., Maillard F., Charlot F., Berthome G., Iojoiu C., Sanchez J. Y., Rossinot E. and Claude E., Membrane and active layer degradation upon PEMFC steady-state

operation - I. Platinum dissolution and redistribution within the MEA. *J. Electrochem. Soc.*, 154 (2007) B1106-B1114.

[65] Darling R. M. and Meyers J. P., Kinetic model of platinum dissolution in PEMFCs. *J. Electrochem. Soc.*, 150 (2003) A1523-A1527.

[66] Rinaldo S. G., Stumper J. and Eikerling M., Physical theory of platinum nanoparticle dissolution in polymer electrolyte fuel cells. *J. Phys. Chem. C*, 114 (2010) 5773-5785.

[67] Johnson D. C., Napp D. T. and Bruckenstein S., A ring-disk electrode study of the current/potential behaviour of platinum in 1.0 M sulphuric and 0.1 M perchloric acids. *Electrochim. Acta*, 15 (1970) 1493-1509.

[68] Plieth W. J., Electrochemical properties of small clusters of metal atoms and their role in surface enhanced Raman-scattering. *J. Phys. Chem.*, 86 (1982) 3166-3170.

[69] Shao-Horn Y., Ferreira P. J., G.J. l. O., Morgan D., Gasteiger H. and Makharia R., Coarsening of Pt nanoparticles in proton exchange membrane fuel cells upon potential cycling. *ECS Trans.*, 1 (2006) 185-195.

[70] Shao Y., Yin G. and Gao Y., Understanding and approaches for the durability issues of Pt-based catalysts for PEM fuel cell. *J. Power Sources*, 171 (2007) 558-566.

[71] Shao-Horn Y., Instability of noble metal catalysts in proton exchange membrane fuel cells: Experiments and theory, in *Progress Report for the DOE Hydrogen Program*, Vol. 2007

[72] Okada T., Ayato Y., Yuasa M. and Sekine I., The effect of impurity cations on the transport characteristics of perfluorosulfonated ionomer membranes. *J. Phys. Chem. B*, 103 (1999) 3315-3322.

[73] Ball S. C., Hudson S. L., Thompsett D. and Theobald B., An investigation into factors affecting the stability of carbons and carbon supported platinum and platinum/cobalt alloy catalysts during 1.2 V potentiostatic hold regimes at a range of temperatures. *J. Power Sources*, 171 (2007) 18-25.

[74] Bi W., Gray G. E. and Fuller T. F., PEM fuel cell Pt/C dissolution and deposition in Nafion® electrolyte. *Electrochem. Solid-State Lett.*, 10 (2007) B101-B104.

[75] Kinoshita K. and Bett J., Electrochemical oxydation of carbon black in concentrated phosphoric acid at 135°C. *Carbon*, 11 (1973) 237-247.

[76] Linse N., Gubler L., Scherer G. G. and Wokaun A., The effect of platinum on carbon corrosion behavior in polymer electrolyte fuel cells. *Electrochim. Acta*, 56 (2011) 7541-7549.

[77] Maillard F., Bonnefont A. and Micoud F., An EC-FTIR study on the catalytic role of Pt in carbon corrosion. *Electrochem. Commun.*, 13 (2011) 1109-1111.

[78] Reiser C. A., Bregoli L., Patterson T. W., Yi J. S., Yang J. D. L., Perry M. L. and Jarvi T. D., A reverse-current decay mechanism for fuel cells. *Electrochem. Solid-State Lett.*, 8 (2005) A273-A276.

[79] Chatenet M., Guilminot E., Iojoiu C., Sanchez J.-Y., Rossinot E. and Maillard F., Pt redistribution within PEMFC MEAs and its consequence on their performances. *ECS Trans.*, 11 (2007) 1203-1214.

[80] Guilminot E., Corcella A., Iojoiu C., Berthomé G., Maillard F., Chatenet M. and Sanchez J.-Y., Membrane and active layer degradation upon Proton Exchange Membrane Fuel Cell steady-state operation – Part I: Platinum dissolution and redistribution within the Membrane Electrode Assembly. *J. Electrochem. Soc.*, 154 (2007) B1106-B1114.

[81] Xie J., Wood D. L., More K. L., Atanassov P. and Borup R. L., Microstructural changes of membrane electrode assemblies during PEFC durability testing at high humidity conditions. *J. Electrochem. Soc.*, 152 (2005) A1011-A1020.

[82] Xie J., Wood D. L., Wayne D. M., Zawodzinski T. A., Atanassov P. and Borup R. L., Durability of PEFCs at high humidity conditions. *J. Electrochem. Soc.*, 152 (2005) A104-A113.

[83] Wilson M. S., Garzon F. H., Sickafus K. E. and Gottesfeld S., Surface-Area Loss of Supported Platinum in Polymer Electrolyte Fuel-Cells. *J. Electrochem. Soc.*, 140 (1993) 2872-2877.

[84] Yu J. R., Matsuura T., Yoshikawa Y., Islam M. N. and Hori M., Lifetime behavior of a PEM fuel cell with low humidification of feed stream. *Phys. Chem. Chem. Phys.*, 7 (2005) 373-378.

[85] Asoro M. A., Kovar D., Shao-Horn Y., Allard L. F. and Ferreira P. J., Coalescence and sintering of Pt nanoparticles: *In situ* observation by aberration-corrected HAADF STEM. *Nanotech.*, 21 (2010).

[86] Borup R. L., Davey J. R., Garzon F. H., Wood D. L. and Inbody M. A., PEM fuel cell electrocatalyst durability measurements. *J. Power Sources*, 163 (2006) 76-81.

[87] Xie Z., Navessin T., Shi K., Chow R., Wang Q. P., Song D. T., Andreaus B., Eikerling M., Liu Z. S. and Holdcroft S., Functionally graded cathode catalyst layers for polymer electrolyte fuel cells - II. Experimental study of the effect of Nafion® distribution. *J. Electrochem. Soc.*, 152 (2005) A1171-A1179.

[88] Schulenburg H., Schwanitz B., Linse N., Scherer G. G., Wokaun A., Krbanjevic J., Grothausmann R. and Manke I., 3D imaging of catalyst support corrosion in polymer electrolyte fuel cells. *J. Phys. Chem. C*, 115 (2011) 14236-14243.

[89] Kinoshita K., Carbon, electrochemical and physicochemical properties, Vol. 1988, John Wiley & Sons: New York.

[90] Gallagher K., Darling R. and Fuller T., Carbon-support corrosion mechanisms and models, in *Handbook of Fuel Cells: Fundamentals, Technology, and Applications*, Vol. 6, 2009, John Wiley & Sons

[91] Kangasniemi K. H., Condit D. A. and Jarvi T. D., Characterization of Vulcan electrochemically oxidized under simulated PEM fuel cell conditions. *J. Electrochem. Soc.*, 151 (2004) E125-E132.

[92] Meyers J. P. and Darling R. M., Model of carbon corrosion in PEM fuel cells. *J. Electrochem. Soc.*, 153 (2006) A1432-A1442.

[93] Gubler L., Dockheer S. M. and Koppenol W. H., Radical ($HO^{\bullet}$, $H^{\bullet}$ and $HOO^{\bullet}$) Formation and Ionomer Degradation in Polymer Electrolyte Fuel Cells. *J. Electrochem. Soc.*, 158 (2011) B755.

[94] Endoh E., Terazono S., Widjaja H. and Takimoto Y., Degradation study of MEA for PEMFCs under low humidity conditions. *Electrochem. Solid-State Lett.*, 7 (2004) A209-A211.

[95] Aoki M., Uchida H. and Watanabe M., Decomposition mechanism of perfluorosulfonic acid electrolyte in polymer electrolyte fuel cells. *Electrochem. Commun.*, 8 (2006) 1509-1513.

[96] Mittal V. O., Kunz H. R. and Fenton J. M., Is H_2O_2 involved in the membrane degradation mechanism in PEMFC? *Electrochem. Solid-State Lett.*, 9 (2006) A299-A302.

[97] Healy J., Hayden C., Xie T., Olson K., Waldo R., Brundage A., Gasteiger H. and Abbott J., Aspects of the chemical degradation of PFSA ionomers used in PEM fuel cells. *Fuel Cells*, 5 (2005) 302-308.

[98] Inaba M., Kinumoto T., Kiriake M., Umebayashi R., Tasaka A. and Ogumi Z., Gas crossover and membrane degradation in polymer electrolyte fuel cells. *Electrochim. Acta*, 51 (2006) 5746-5753.

[99] Antoine O. and Durand R., RRDE study of oxygen reduction on Pt nanoparticles inside Nafion®: H_2O_2 production in PEMFC cathode conditions. *J. Appl. Electrochem.*, 30 (2000) 839-844.

[100] Panchenko A., Dilger H., Kerres J., Hein M., Ullrich A., Kaz T. and Roduner E., *In-situ* spin trap electron paramagnetic resonance study of fuel cell processes. *Phys. Chem. Chem. Phys.*, 6 (2004) 2891-2894.

[101] Liu W., Ruth K. and Rusch G., Membrane durability in PEM fuel cells. *J. New Mater. Electrochem. Syst.*, 4 (2001) 227-232.

[102] Young A. P., Stumper J., Knights S. and Gyenge E., Ionomer degradation in polymer electrolyte membrane fuel cells. *J. Electrochem. Soc.*, 157 (2010) B425-B436.

[103] Pourbaix M., Atlas of electrochemical equilibria in aqueous solutions, Vol. 1979, National Association of Corrosion Engineers

[104] Antolini E., Salgado J. R. C. and Gonzalez E. R., The stability of Pt-M (M = first row transition metal) alloy catalysts and its effect on the activity in low temperature fuel cells: A literature review and tests on a Pt-Co catalyst. *J. Power Sources*, 160 (2006) 957-968.

[105] Zignani S. C., Antolini E. and Gonzalez E. R., Evaluation of the stability and durability of Pt and Pt-Co/C catalysts for polymer electrolyte membrane fuel cells. *J. Power Sources*, 182 (2008) 83-90.

[106] Yu P., Pemberton M. and Plasse P., PtCo/C cathode catalyst for improved durability in PEMFCs. *J. Power Sources*, 144 (2005) 11-20.

[107] Colon-Mercado H. R. and Popov B. N., Stability of platinum based alloy cathode catalysts in PEM fuel cells. *J. Power Sources*, 155 (2006) 253-263.

[108] Ball S. C., Hudson S. L., Leung J. H., Russell A. E., Thompsett D. and Theobald B. R., Mechanisms of activity loss in PtCo alloy systems. *ECS Trans.*, 11 (2007) 1247-1257.

[109] Bonakdarpour A., Lobel R., Atanasoski R. T., Vernstrom G. D., Schmoeckel A. K., Debe M. K. and Dahn J. R., Dissolution of transition metals in combinatorially sputtered $Pt_{1-x-y}M_xM'_y$(M, M' = Co, Ni, Mn, Fe) PEMFC electrocatalysts. *J. Electrochem. Soc.*, 153 (2006) A1835-A1846.

[110] Ball S. C., Hudson S. L., Theobald B. R. and Thompsett D., Enhanced stability of PtCo catalysts for PEMFC. *ECS Trans.*, 8 (2006) 141-152.

[111] Chen S., Gasteiger H. A., Hayakawa K., Tada T. and Shao-Horn Y., Platinum-alloy cathode catalyst degradation in proton exchange membrane fuel cells: Nanometer-scale compositional and morphological changes. *J. Electrochem. Soc.*, 157 (2010) A82-A97.

Chapter II.

Experimental section

I. Stack aging

The PEMFC stack aging was performed by Axane at Sassenage (Isère, France). The cells and stacks designs are proprietary informations. However these informations are not necessary to understand the degradation mechanisms of the Pt_3Co/C cathode catalyst. The PEMFC stacks were composed of 16 cells, 85 cm^2 each, made of a Pt/C catalyst at the anode (platinum metal loading over carbon ≈ 50 wt. %; loading in the MEA, ≈ 0.2 mg_{Pt} cm^{-2}_{MEA}) and a Pt_3Co/C catalyst at the cathode (platinum metal loading over carbon ≈ 50 wt. %, and loading in the MEA, ≈ 0.4 mg_{Pt} cm^{-2}_{MEA}). Two stacks were operated at constant current (either I = 20 or 50 A, translating into an average current density of j = 0.24 or 0.60 A cm^{-2}, respectively) and one stack was operated in start/stop conditions (1 h at j = 0.60 A cm^{-2} /1 h of stop), all other conditions being set identical. The cathode was fed with humidified air (65 % RH, 1.1 bar abs., gas stoichiometry of 2.5) and the anode with dry pure dihydrogen (0 % RH, 1.3 bar abs., dead-end mode ~ average H_2 stoichiometry of 1). The gas flow rates were 3.2 and 33.2 NL min^{-1} for dihydrogen and air, respectively and were supplied in a counter flow mode *i.e.* the anode inlet facing the cathode outlet. This last information is essential for the discussion in **Chapter VI** about the aging heterogeneities within each MEA. The relative humidity (RH) was fixed at the gas inlet by an adequate choice of the humidifier and cell temperatures. Air and H_2 purges were performed intermittently to remove the water produced at the cathode or nitrogen/water accumulating at the anode. Before the aging tests, all the MEA underwent a conditioning procedure in the stack, which consists of successive current steps (5 min each at I = 30 A and 45 A). The conditioning was stopped when a stabilization of the electrical performances was recorded (approximately 17 h).

For the stack operated in start/stop mode, during stop conditions, the gas flows were stopped for 1 hour, during which a valve sealed the anode and did forbid any air inlet through the anode gas channels. As the hydrogen permeability through the PEM is fast, the composition of the gases at the cathode changes rapidly from air to a mixture of air and hydrogen. Consequently, the potential of the cathode drops to an undetermined value located between the conventional open-circuit potential (OCV) under air (ca. 1 V *vs.* RHE) and 0 V *vs.* RHE. This process is accompanied by a transient pressure drop across the MEA, the overall pressure at the anode decreasing fast when H_2 diffuses through the PEM; whereas the diffusion of air in the opposite direction is slower.

The stacks were disassembled after different life stages and some MEAs were removed and sent at LEPMI for physical, chemical and electrochemical characterizations. Those MEAs were replaced by fresh ones and the stack was then re-conditioned and re-operated until the next MEA sampling.

II. Single-cell testing

PEMFC single tests were performed in collaboration with Air Liquid CRCD at Sassenage (Isère, France). The 85 cm² MEA were the same as those used for stack aging. Prior to the testing, the MEA underwent a 17 h conditioning procedure in a 6-cell PEMFC short stack, similar as in the stack-aging procedure. The operating parameters (temperature, relative humidities, pressures, etc…) are the same than those used for the stack-aging. Polarization curves were recorded using Air/H_2 reactants. The MEA high frequency resistance (R_{HF}) was measured by electrochemical impedance spectroscopy (EIS) and cyclic voltammograms were recorded, as detailed in **Chapter IV**.

III. *Ex situ* characterization techniques on the fresh/aged MEA cathode catalysts

The MEA used in the study were catalyst-coated membranes (CCM). In this preparation technique, an ink (suspension of the catalyst particles in water and/or organic solvent with addition of ionomer) containing the catalyst of interest is spread on a Teflon support and then transferred to the proton exchange membrane by hot pressing (decal method) or directly dispersed onto the membrane [1]. Then the catalyst coated membrane is sandwiched between 2 porous carbon papers or cloth supports, the gas diffusion layers (GDL) [2, 3]. A five layer MEA is then obtained (configuration A in Figure II-1). MEA prepared by the CCM procedure allow easy post-mortem analysis of the aged catalyst because the two GDL can be easily mechanically removed without detaching the catalyst layers from the membrane (configuration B in Figure II-1). It is also easy to scrap off the catalyst layer from the membrane with a razor blade, and to obtain a catalyst powder blended with the ionomer (configuration C in Figure II-1). The latter can be analyzed by TEM, STEM-HAADF, X-EDS, electrochemical techniques and ICP-AES. The PEM can also be used as a mechanical support to perform XRD and XAS measurements on the catalyst layer (configuration D in Figure II-1). Except when specified, all the characterizations have been performed in the specified region close to the cathode inlet region of the MEA.

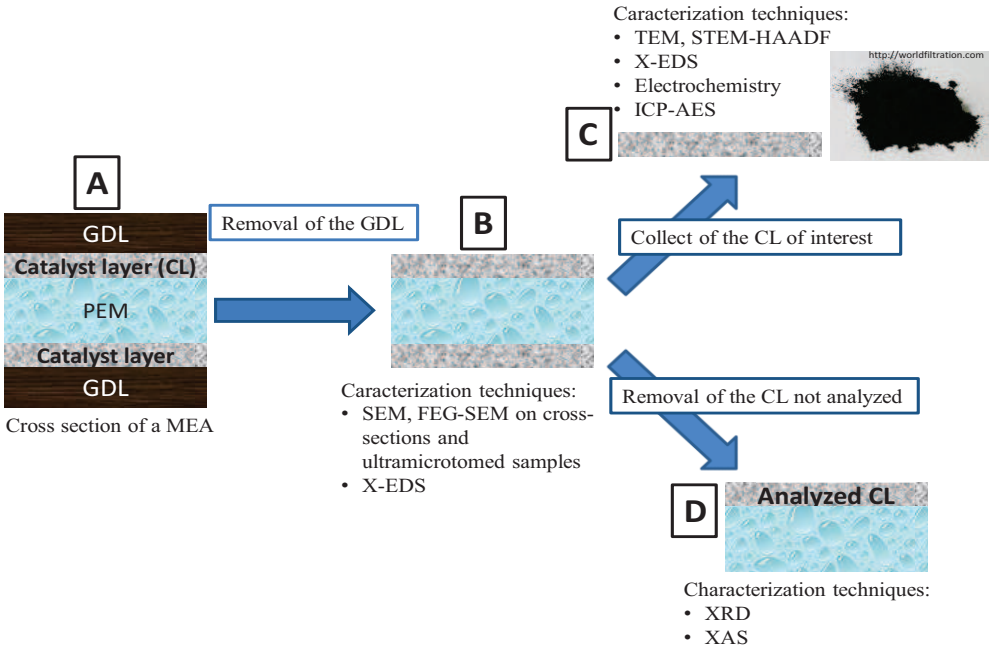

Figure II-1. Schematics of the disassembly procedure used to analyze fresh/aged CCM MEA.

IV. X-Ray Diffraction (XRD)

The X-ray diffraction technique is based on the interactions of X-ray photons with atoms arranged (periodically or not) in a 3 dimension structure. The incident monochromatic X-ray radiation, characterized by its wavelength λ_{XRD}, produces a Bragg peak if its reflections on the various planes interfered constructively, *i.e.* when the phase shift is a multiple of 2π. This condition can be expressed by Bragg's law, which gives the angles for coherent and incoherent scattering from a crystal lattice:

$$n_{XRD}\lambda = 2d_{hkl}\sin\theta \qquad \text{Eq. II-1}$$

where n_{XRD} is the diffraction order, d_{hkl} is the characteristic distance between each (hkl) diffracting planes and θ is the angle between the incident ray and the scattering planes. If crystallites are less than approximately 100 nm in size, appreciable broadening of the diffraction peaks occurs. The quantitative relation between peak broadening by nanocrystals and the crystallite size was deduced by Scherrer in 1918 [4]:

$$\bar{d}_{XRD} = \frac{K\lambda}{B_{2\theta}\cos\theta} \qquad \text{Eq. II-2}$$

where $\bar{d}_{XRD}$ is the crystal dimension normal to the diffracting planes, K the Scherrer constant (K = 0.95), $B_{2\theta}$ the integral breath of the diffraction peak in terms of the 2θ angle in radians (the full width

at half maximum (FWHM) is frequently used), and θ is the angle at the peak maximum. Factors that influence the peak broadening are stress and strain effects, stacking faults, structural disorder and instrumental broadening. The later was measured under identical conditions on a reference sample (Si(111)) and subtracted before determination of the crystallite size of our samples.

A cylinder of *ca.* 1 cm^2 was cut with a punch in the MEA (configuration D in Figure II-1) and analysed using a Philips TW 1730 vertical goniometer/ diffractometer equipped with a diffracted-beam monochromator using Cu ($K_{\alpha 1}$) radiation (λ_{XRD} = 0.15406 nm). The values extracted from the (220) diffraction peak, the only one not overlapping with other diffraction peaks, are reported in the manuscript. This value was confirmed by comparing with three other diffraction peaks ((111), (200), and (311)).

V. Electron Microscopy related techniques

Three types of electron microscopy techniques *i.e.* that use a beam of electrons to illuminate the specimen and produce a magnified image, have been used to characterize the Pt-based catalyst powders: (i) by transmission (Figure II-2A), (ii) by transmission and high angle annular detection (Figure II-2B) and (iii) scanning (Figure II-2C). The following description of these techniques is largely inspired from Chatenet *et al.* [5].

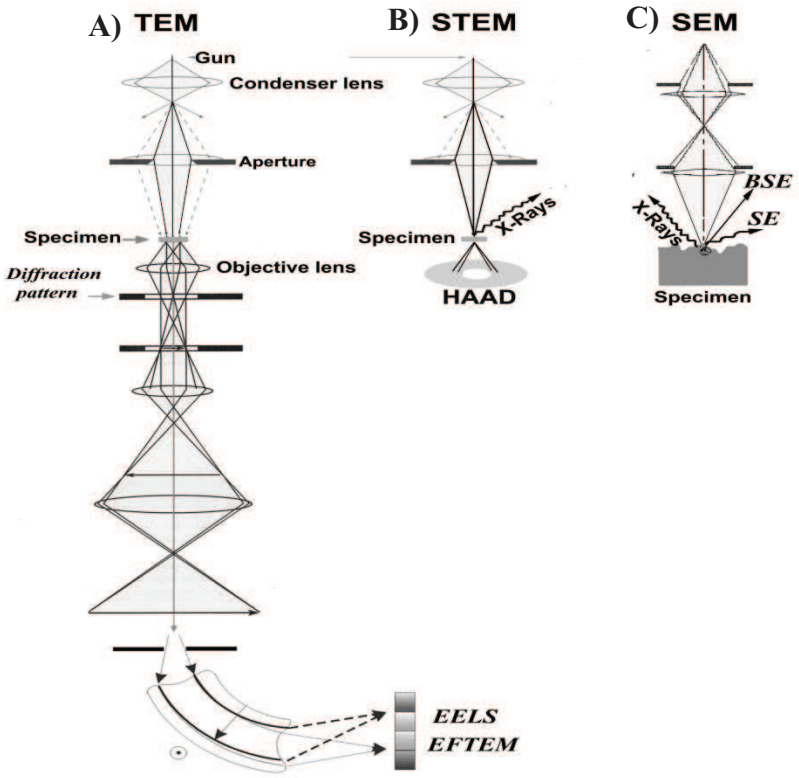

Figure II-2. Scheme of (A) TEM, (B) STEM-HAADF and (C) SEM. Reprinted from Chatenet et al. [5].

1. Transmission Electron Microscopy (TEM)

A TEM (historically the first imaging device based on the use of electrons) is constituted of three main parts: (i) the electrons gun, used to accelerate the electrons at a high voltage (> 100 kV) in order to enable their transmission through a thin sample, (ii) the condenser and (iii) objective lens. The principle of a TEM approaches that of an optical microscope, electrons being used instead of photons and electromagnetic lens instead of optical lens. TEM images (2 dimensions projection of a 3 dimensions sample) result from either a mass/thickness contrast (heavy elements absorb/scatter electrons more efficiently) or a diffraction contrast. The former is most important for non-crystalline materials such as polymers, whereas the latter becomes predominant for crystalline material and strongly depends on the crystallites orientation.

TEM observations were performed with a Jeol 2010 TEM operated at 200 kV with a point to point resolution of 0.19 nm. As TEM analysis is only possible for samples thinner than a few hundred nanometers (electrons have to go through the sample) [6], only catalyst powders and ultramicrotomed membrane-electrode assemblies can be imaged. For the preparation of the ultramicrotomed samples, small pieces (1 cm^3) of the (fresh/aged) membrane electrode assemblies (configuration B in Figure II-1) were first embedded in an Epoxy® resin and dried at T = 333 K for 3 days. Then the samples were sliced with an ultramicrotome (Leica® EM UC6) using a diamond knife (Diatome® ultra 35°) to obtain less than 100 nm-thick slices (between 70 and 90 nm depending on the sample, the thinner the sample the better for the observations). The fresh/ aged cathode catalyst powders were simply deposited on a copper grid baring a lacey carbon membrane for their observation.

The particle size distribution of each catalyst was reconstructed by measuring the diameter of at least 400 individual and round shaped particles from representative TEM images obtained at high magnifications (× 200 000). For each particle size distribution the number-averaged diameter $\overline{d}_{\mathrm{N}}$, the surface-averaged diameter $\overline{d}_{\mathrm{S}}$, and the volume-averaged diameter $\overline{d}_{\mathrm{V}}$ were determined [7]:

$$\overline{d}_{\mathrm{N}} = \frac{\sum_{i=1}^{n} l_i d_i}{\sum_{i=1}^{n} l_i} \qquad \text{Eq. II-3}$$

$$\overline{d}_{\mathrm{S}} = \frac{\sum_{i=1}^{n} l_i d_i^3}{\sum_{i=1}^{n} l_i d_i^2} \qquad \text{Eq. II-4}$$

$$\bar{d}_V = \frac{\sum_{i=1}^{n} l_i d_i^4}{\sum_{i=1}^{n} l_i d_i^3} \qquad \text{Eq. II-5}$$

l_i stands for the number of particles having a diameter d_i. Each diameter does not have the same meaning. The number-averaged diameter $\bar{d}_N$ is the mean diameter, the surface-averaged diameter $\bar{d}_S$ is the diameter reported to the average surface area of the particle and is the most relevant parameter in electrocatalysis (where the surface area dictates the performance) and the volume-averaged diameter $\bar{d}_V$ is the diameter reported to the average volume of the particle; the latter is the most relevant diameter for comparison with $\bar{d}_{XRD}$ (see Equation II-2, for which the volume of the particle is contributing to the overall signal).

2. High Angle Annular Dark Field (HAADF) imaging mode

In a TEM, transmitted electrons can be collected by a HAADF detector (see Figure II-2B), for which the intensity of the signal is a function of the atomic number Z of the observed sample, therefore providing chemical information at the atomic scale (atoms of higher atomic number scatter more electrons at large angle, producing a brighter image). This imaging mode is therefore very powerful to image multi-phasic or multi-atomic structures, such as core/shell nanoparticles used in catalysis [40, 41] or in electrocatalysis [42]. In first approximation, the image intensity at any point is proportional to the product of the number (B) of atoms electrons have gone through and the square of the average atomic number Z of the atoms constituting the column:

$$I = k\, B\, Z^{\alpha} \qquad \text{Eq. II-6}$$

where k is a fixed coefficient ($\alpha \approx 1.8 - 2$). The experimental intensity profiles (determined with Digital Micrograph®) of each particle imaged by STEM-HAADF are then compared with theoretical ones calculated for specific particle structures. Pt-Co/C catalyst powders were observed in HRSTEM-HAADF imaging mode on a FEI-Titan microscope equipped with a Cs probe corrector providing a probe size in the order of 0.1 nm. A 200 kV electron acceleration voltage was chosen in order to minimize the nanoparticle damage under the electron beam.

3. Scanning Electron Microscopy (SEM)

Imaging with SEM consists of sweeping a finely focused electron beam over a conducting sample. The beam energy can be varied between 1 and 40 keV. Upon impingement on the specimen, the electron beam generates different signals, among which are secondary electrons (SE, sensitive to the surface topography), backscattered electrons (BSEs), which are used to observe the global structure of embedded MEA, and X-ray fluorescence. BSEs are electrons of the incident beam which, upon elastic scattering, escape the analyzed surface. The BSE intensity increases with increasing atomic number in the sample, resulting in a compositional contrast image, called *Z* contrast. While the resolution of conventional SEM ranges between 5 and 10 nm, it can reach 1 nm for the newest field-emission gun (FEG)-SEM apparatus, for which the well-defined structure of the LaB_6 cathode that generates the electrons enhances the obtained resolution. The scanning transmission electron microscopy (STEM) mode in a SEM, although of much lower resolution than a conventional TEM, can be used to image ultramicrotomed MEA cross sections (an in-lens detector is placed below the sample) at low magnification, which nicely complements the data originating from TEM.

FEG–SEM images were obtained on a Zeiss Ultra 55 microscope, designed to maximize the imaging resolution at low beam energies. Embedded cross sections of the fresh/aged MEA (configuration B in Figure II-1) were observed to monitor the variations of the components thickness (catalyst layers and PEM) upon aging. For the preparation of the embedded cross sections, the MEA were first embedded in an Epoxy resin (dried under ambient air for 1 day), further polished with SiC polishing disk with small grain size (4000) and finally covered by a thin carbon film. Similar as in TEM, ultramicrotomed samples of the (fresh/aged) membrane electrode assemblies can be observed using the STEM mode in a FEG-SEM. To measure each average thickness of the MEA components, the number of pixels corresponding to each layer was integrated (with ImageJ®) prior to conversion to an equivalent thickness. The presence of platinum or cobalt (metal particles or ions) inside the PEM was first surveyed by observations at high magnification (× 5000) and then by local X-ray energy dispersive spectrometry (X-EDS) analyses.

4. X-Ray Energy Dispersive Spectroscopy (X-EDS)

X-EDS analyses basically consist of analyzing the energy of the X-rays emitted from the sample upon interaction of the electron beam with the inner-shell atomic electrons of the specimen. The spatial resolution of X-EDS is a few micrometers in SEM but can be smaller than 1 nm for TEM using the STEM mode. The FEG-SEM and TEM used in this manuscript were equipped for X-EDS analyses, performed with a Silicon Drift Detector (SDD).

The Co and Pt atomic percentages (Co at. % and Pt at. %) of the Pt-Co/C catalysts were determined by X-EDS. During TEM and FEG-SEM observations, X-EDS acquisitions have been

performed at high primary electron beam energy (200 and 20 keV respectively), so as to excite the Pt Lα and the Co Kα transitions. The analyses were performed for 60 s on a large area of nanoparticles assembly, except when indicated, such as during line scan X-EDS associated with STEM-HAADF.

VI. Inductively Coupled Plasma - Atomic Emission Spectrometry (ICP-AES)

ICP-AES is an analytical technique used for the detection of solubilised trace of metals. It is a type of emission spectroscopy that uses the inductively coupled argon plasma to produce excited atoms and ions that emit electromagnetic radiation at wavelengths characteristic of a particular element. The intensity of this emission is indicative of the concentration of the element within the sample (and has to be calibrated prior to the experiment).

The metal content of the fresh/aged cathode catalyst powders was measured by ICP-AES. 5 mg of the cathode catalyst were first digested in concentrated *aqua regia* (volume ratio HCl/HNO_3 3/1) made from high purity acids (Suprapur®, Merck) at room temperature for at least 5 days. Part of the digestion solution was then pipetted and diluted so as to obtain a working solution containing *ca.* 5 ppm of metal in diluted *aqua regia* (below 1 M HCl). The Pt and Co atomic content were determined by comparing three series of measurements for each working solution and a calibration plot made from standard samples. For that purpose, we used two Pt-related (λ = 265.945, 214.423 nm) and three Co-related (λ = 228.616; 238.892; 230.786 and 236.38 nm) wavelengths.

VII. Electrochemical experiments

1. Electrochemical methods

During cyclic voltammetry measurements, the potential E imposed between the working and the reference electrode is swept linearly at a constant rate $v = \mathrm{d}E/\mathrm{dt}$ between two potential limits, while the current that flows between the working and the counter electrodes is recorded. The total current I recorded during CV is the sum of a faradaic and a capacitive contribution. The faradaic contribution I_f (the algebraic sum of all the faradaic currents) comes from charge transfer reactions (oxidation, reduction) at the working electrode. The capacitive contribution I_dc does not involve any electrochemical reaction (charge transfer) and is caused by accumulation (or removal) of electrical charges on the working electrode and in the electrolyte solution at its vicinity. There is always some capacitive current flowing when the potential of an electrode is changing, and the capacitive current is zero when the potential is constant (provided the transient has elapsed).

$$I = I_\mathrm{f} + I_\mathrm{dc} \qquad \text{Eq. II-7}$$

$$I_{\mathrm{dc}} = C_{\mathrm{dc}} \times S \times \frac{dE}{dt}$$ Eq. II-8

Three types of cyclic voltammetry measurements were surveyed: (i) in supporting electrolyte (hereafter denoted as CV), (ii) during the stripping of one monolayer of CO adsorbed on the catalyst (hereafter denoted as CO stripping) and (iii) during the oxygen reduction reaction in quasi-stationary conditions (hereafter denoted as ORR).

a. Cyclic voltammetry

The electrochemical processes that occur on Pt/C electrodes during a CV were detailed in Chapter I. CV in argon-saturated supporting electrolyte were recorded while the potential of the working electrode was scanned between 0.05 V *vs.* RHE and 1.23 V *vs.* RHE at v = 0.020 V s^{-1}. When no additional informations are provided, the CVs shown in the manuscript were obtained after the complete stabilization of the signal, which normally requires 10 cycles.

b. CO_{ad} stripping voltammograms and measurement of the catalyst active area

For the CO stripping technique, first carbon monoxide was purged in the electrolyte for 6 min at a constant electrode potential E = 0.1 V *vs.* RHE, allowing its adsorption (chemisorption) on the platinum surface (CO_{ad}). This adsorption can be a-top (one CO molecule adsorb on one Pt atom), bridged (one CO molecule adsorb on two Pt atoms) or multifold (the latter is not likely at large CO coverage) [8]. Argon was then purged in the electrolyte during 39 min to remove the CO molecules dissolved in the electrolyte, while keeping the potential constant at E = 0.1 V *vs.* RHE. The electrode potential was then cycled three times between 0.05 V *vs.* RHE and 1.23 V *vs.* RHE at v = 0.020 V s^{-1} (the first potential scan enables the irreversible stripping of CO_{ad} molecules; the second and the third are used to verify that all CO_{ad} species have been oxidized in the first potential cycle). Thermodynamically, CO can be oxidized at low potentials ($E^0_{CO_2/CO}$ = -0.1 V *vs.* NHE), but as seen experimentally, this oxidation only proceeds for E > 0.6 V *vs.* RHE in acidic medium. Therefore, the CO_{ad} monolayer electrooxidation into CO_2 is thought to proceed following a Langmuir-Hinshelwood mechanism involving adsorbed CO_{ad} and adsorbed oxygenated species OH_{ad}:

$$\mathrm{Pt} + \mathrm{H_2O} \leftrightarrow \mathrm{Pt(OH)_{ad}} + \mathrm{H^+} + \mathrm{e^-}$$ Eq. II-9

$$\mathrm{Pt(CO)_{ad}} + \mathrm{Pt(OH)_{ad}} \leftrightarrow 2\mathrm{Pt} + \mathrm{CO_2} + \mathrm{H^+} + \mathrm{e^-}$$ Eq. II-10

Assuming that (i) all CO molecules are adsorbed in an a-top configuration and (ii) a full coverage of the Pt surface by CO molecule is reached, the Pt electrochemical active surface area can be calculated

via the coulometry of the electrochemical CO oxidation reaction. The measurement of this coulometry was achieved by subtracting the third to the first potential cycle [9]. The electrochemically active surface area of Pt-based/C catalysts can be then calculated assuming two electrons exchanged and a charge density of 420 μC per cm^2 for the CO oxidation, a common value for bulk Pt (and assumed to hold true for Pt-Co/C catalysts). This reaction is also widely studied and has strongly advanced the understanding of structural and size effects in fundamental electrocatalysis [8, 10-13].

c. ORR voltammograms and measurement of the catalyst specific activity

When O_2 is purged in the cell and the working electrode polarized (E < 1 V *vs.* RHE) the processes that rule the ORR ($I_f(E)$) are either kinetic (charge transfer limited) at low overpotential or O_2/mass transport related at large overpotential, as described in the Koutecky-Levich model [14]:

$$\frac{1}{I_f(E)} = \frac{1}{I_k(E)} + \frac{1}{I_{lim}} \quad \text{Eq. II-11}$$

For a single step redox reaction where n electrons are exchanged, the potential-dependant kinetic current is given by:

$$R \leftrightarrow O + ne^- \quad \text{Eq. II-12}$$

$$I_k(E) = nFS\left[k_{ox}[R]_{x=0} \exp\left(\frac{n\alpha_{ox}FE}{RT}\right) - k_{red}[O]_{x=0} \exp\left(\frac{n\alpha_{red}FE}{RT}\right)\right] \quad \text{Eq. II-13}$$

where F is the Faraday constant, S the surface of the electrode, k_{ox} and k_{red} the oxidation and reduction kinetic constants, $[O]_{x=0}$ and $[R]_{x=0}$ the oxidant and reductant interfacial concentrations, α_{ox} and α_{red} the symmetry factors ($\alpha_{ox} + \alpha_{red}$ =1), T the temperature (in K) and R the gas constant.

The O_2 mass transport related term is a straightforward function of the O_2 concentration near the electrode: convection and diffusion in solution greatly impact this term. In order to have the control of this term and therefore to access ORR kinetic currents, measurements are always performed in oxygen-saturated environment, usually with rotating disk electrodes, the angular rotation velocity ω (in rad s^{-1}) of which can be controlled to fix the diffusion and convection properties close to the electrode surface. As the disk turns, some of the solution described as the *hydrodynamic boundary layer* is dragged by the spinning disk and the resulting centrifugal force flings the solution away from the centre of the electrode. Solution flows up, perpendicular to the electrode, from the bulk to replace the *boundary layer*. This translates into a laminar flow of solution towards and across the electrode. The region close to the electrode interface (δ_{RDE}) is therefore known to be under diffusion control:

$$\delta_{RDE} = 1.61 \times \nu^{1/6} \times D^{1/3} \times \omega^{-1/2} \quad \text{Eq. II-14}$$

With the law of conservation of mass that links the current to the flux of species, the analytical relation between the O_2 mass-transport-limited current and the angular rotation rate of the RDE (Levich criterion) is:

$$I_{\text{lim}} = 0.62 * nSFD_{O_2}^{2/3} C_{O_2} \upsilon^{-1/6} \omega^{1/2} \quad \text{Eq. II-15}$$

where C_{O_2} (in mol cm^{-3}) is the oxygen solubility in the electrolyte, D_{O_2} the oxygen diffusion coefficient in the electrolyte (in cm^2 s^{-1}) and υ the kinematic viscosity of the electrolyte (in m^2 s^{-1}).

In electrocatalysis it is convenient, when comparing the electrocatalytic properties of two catalysts for a given electrochemical reaction, to look at their specific activities (the kinetic current per real cm^2 of catalyst) or mass activities (the kinetic current per mass of catalyst) at a given potential. For the ORR, the mass and specific activities are usually reported at E = 0.85 or 0.9 V *vs.* RHE. In RDE measurements, the kinetic limited current can be easily extracted from the total current with the following relation:

$$I_k(E) = \frac{I_f(E) \times I_{\text{lim}}}{I_{\text{lim}} - I_f(E)} \quad \text{Eq. II-16}$$

Quasi-stationary ORR voltammograms were recorded in oxygen-saturated solution while the potential was scanned downside between 1.1 and 0.4 V *vs.* RHE at v = 0.001 V s^{-1} (to minimize the contribution of the capacitive current) after the potential was hold 1 min at E = 1.1 V *vs.* RHE (except in **Chapter V** where the potential was scanned positively between 0.4 and 1.05 V *vs.* RHE at v = 0.001 V s^{-1}). After correction from the ohmic drop in solution [15], the ORR kinetic current at E = 0.85 V *vs.* RHE was determined by dividing the measured current by the electrochemically active surface area of the catalyst obtained by the CO stripping technique.

2. Preparation of the inks and of the porous electrodes

Electrochemical characterization was performed in a three-electrode cell thermostated at T = 298 K in 0.1 M H_2SO_4 using an Autolab PGSTAT302N potentiostat. All the glassware was cleaned by immersion in a H_2SO_4:H_2O_2 mixture overnight and thoroughly rinsed with MQ-grade water. Solutions were prepared from ultrapure water (Milli-Q grade, 18.2 MΩ cm, 1-3 ppb TOC) and H_2SO_4 (Suprapur, Merck). In the three electrode configuration the working electrode was either (i) a rotating disk electrode (RDE) composed of the cathode catalyst powder deposited as a thin-film on a glassy carbon disk (Sigradur, 0.196 cm^2), a rotating ring-disk electrode (RRDE) or (iii) a ultra-micro electrode with cavity. The counter-electrode was a flame-annealed Pt foil and the reference electrode was a freshly-prepared reversible hydrogen electrode (RHE).

a. Porous RDE

CO stripping, ORR and cyclic voltammograms were all recorded with the porous RDE technique, except when specified. All porous RDE were prepared according to a home-made procedure first introduced by Gloaguen *et al.* [16, 17]. First, an ink was prepared with 5 mg of the cathode catalyst powder, 54 µL of 5 wt% Nafion® solution, 2.4 mL of MQ-grade water (18.2 MΩ cm^{-1}) and 20 µL of ethanol. After homogenization in an ultrasonic bath, an aliquot of 20 µL was deposited onto the polished glassy carbon disk of the RDE and sintered for 5 minutes at T = 383 K to ensure evaporation of the Nafion® solvents. The optimal catalyst loading that has to be loaded onto the glassy carbon disk (GC) to (i) ensure 100% utilization of the electrocatalyst, (ii) obtain the theoretical diffusion-limited current predicted by the Levich equation on a Pt disk electrode of the same geometrical area, (iii) avoid mass-transport limitations within the thin-film electrodes and (iv) make sure that the specific activity is not depending on the mass of Pt–Co/C loaded onto the electrode, was determined to be 30 $\mu g_{Pt\text{-}Co}$ per cm^{-2} of electrode [18]. Finally the working electrode was immersed in the electrochemical cell at a controlled potential of *ca.* E = 0.10 V vs. RHE.

b. Porous Rotating Ring Disk Electrode (RRDE)

RRDE experiments were performed to determine the number of exchanged electrons in the ORR by quantifying at the ring the amount of dihydrogen peroxide produced at the disk. The ORR takes place on the central disc electrode and the produced H_2O_2 is either oxidized or reduced on the concentric ring electrode, depending on the potential of this electrode [19]. The disc and ring currents (I_D and I_R, respectively) were recorded as a function of the disc electrode potential E_D. The average number of exchanged electrons n_{e^-} (equation II-20) was calculated from the charge (equation II-17 and II-18) and mass (equation II-19) balance equations. The collection efficiency N of the RRDE tip was determined using a standard method with the $[Fe(CN)_6]^{4-}/[Fe(CN)_6]^{3-}$ redox couple (N = 16 %). The two- and four-electron disc currents are I_{2e^-} and I_{4e^-} respectively. In this methodology, the current related to the reduction of dihydrogen peroxide into water is assumed to be negligible, or included in the four-electron disc current:

$$I_{2e^-} = \frac{I_R}{N} \qquad \text{Eq. II-17}$$

$$I_D = I_{2e^-} + I_{4e^-} \qquad \text{Eq. II-18}$$

$$\frac{I_D}{n_{e^-}} = \frac{I_{2e^-}}{2} + \frac{I_{4e^-}}{4} \qquad \text{Eq. II-19}$$

The number of exchanged electrons is then function of the ring and disk currents with:

$$n_{e^-} = \frac{4I_D}{I_D + I_R/N}$$ Eq. II-20

The RRDE was a PINE analytical rotator with a glassy carbon disc (radius r = 5 mm, coated with a catalyst ink as in the porous RDE technique) and a bulk Pt ring (inner radius r = 5.2 mm; outer radius r = 6 mm). The ring potential (E_{ring}) was set at E = 1.23 V *vs.* RHE to oxidize the H_2O_2 species, no other faradaic reaction being possible at this electrode potential.

c. Ultramicroelectrode with cavity (UMEC)

The cavity microelectrode, provided by the ‘‘French CNRS UMEC Network’’, consisted of a gold microelectrode (50 µm in diameter) sealed in a large glass tube (8 mm in diameter). A small cylindrical cavity (35 µm in diameter and 30 µm in depth) was obtained by LASER ablation of the gold wire. Filling the cavity was achieved using the UMEC as a pestle in an agate mortar containing a small amount of Pt/C powder (30 wt. %, E-TEK) without any polymer additives. Compared to the porous RDE technique used to characterize the Pt-based/C electrocatalysts, the use of UMEC allows to work with a low content of material, and suppresses the ohmic and capacitive effects originating both from the large thickness of the composite RDE electrodes [20, 21].

Similar as for RDE configuration, the contribution from the oxygen diffusion in solution must be corrected from the overall current in order to access the ORR kinetic current [14] :

$$j_{k,exp} = \frac{j \times j_{lim}}{j_{lim} - j}$$ Eq. II-21

in which $j_{k,exp}$ stands for the current density corrected from the diffusion in solution, j_{lim} (A m^{-2} geometric) is the limiting current density on the voltammogram and j (A m^{-2} geometric) is the experimental current density. Moreover a correction has to be done in order to take into account the diffusion in the active layer using the macro-homogeneous model [17] (because the depth of the cavity of the UMEC is in the same range as its surface area) :

$$j_{k,exp} = \left(\frac{nFD_{O_2}C_{O_2}}{L}\right)\left[U_L \times j_{k,calc}\right]^{1/2} \tanh\left\{\left[U_L \times j_{k,calc}\right]^{1/2}\right\}$$ Eq. II-22

where $j_{k,exp}$ (A m^{-2} geometric) is the experimental geometric current density given as a function of the electrode potential from Eq. II-21, $j_{k,calc}$ (A m^{-2} geometric) is the true kinetic current density corrected from the oxygen diffusion in the solution and in the active layer, $U_L = \frac{L}{n \times F \times D_{O_2} \times C_{O_2}}$, $L = 29 \times 10^{-6}$m is the active layer depth. The Tafel plot is then calculated by taking into account the roughness factor $\gamma = \frac{m^2 catalyst}{m^2 geometric}$.

d. Solid State Cell (SSC)

A home-made SSC was developed to measure the electrocatalytic activity of Pt-based/C electrocatalyst in contact with a proton conducting membrane. The design and principles of the SSC was inspired from the pioneering works of Parthasarathy *et al.* [22]. The use of this cell is motivated by the idea that the electrocatalytic behaviour of a catalyst in liquid supporting electrolyte differs in some points to its behaviour in a PEMFC environment, mainly due to the strong adsorbing anions in liquid electrolyte that do not perfectly mimic the low adsorbing behaviour of the sulfonate moieties of a PFSA membrane. This SSC consists of a PEM (Nafion® 117, 1100 g mol^{-1} EW), an ultra-micro electrode with cavity pressed on one of its side and a Pt counter electrode and a reference electrode (a RHE) pressed on its other side. The cell was operated under controlled atmosphere, and allows examining the activity of Pt/C for the electrochemical CO oxidation and the ORR. To ensure optimal proton conductivity between the working and the reference electrodes, gases are humidified before being purged in the cell (T = 333 K). Preliminary tests have shown a good concordance between the specific activities for the ORR on a Pt/C catalyst recorded in this cell and in a fuel cell [23].

VIII. X-ray Absorption spectroscopy (XAS)

1. Principles

XAS is a characterization technique, chemically resolved, that enables the determination of the local geometric and electronic structure of a material. In this technique a monochromatic light, characterized by a given energy E in the X-rays domain and intensity I_0, is focused on a material (Figure II-3A). When the energy of the monochromatic light is high enough, the corresponding core electrons of all the atoms having the same Z number will leave their energy level and move up to a state above the Fermi level (Figure II-3B). For a 3d transition metal such as cobalt (electronic configuration [Ar] $3d^7\ 4s^2$,) the core electrons we are talking about are located within the $4s^2$ level and will need an energy of approximately E_0 = 7700 eV, defined as the K absorption edge, to be excited. As the energies used to excite core electrons are high (E = 0.1-100 keV), XAS experiments can only be performed with Synchrotron radiation. However, for atoms with higher Z, such as platinum (electronic configuration [Xe] $4f^{14}\ 5d^9\ 6s^1$), the electrons located at the K edge need too much energy to be excited (E_0 = 78395 eV) and thus it is more common to excite the electrons that are located within the $2p^{3/2}$ level (E_0 = 11560 eV corresponding to the L_3 edge) and to monitor the interactions of these electrons with the surrounding matter. During XAS experiments, the sample is scanned in a range of energy, from close below (-100 eV) to well above (+1000 eV) the absorption edge. We were interested in the interactions of the excited electrons, once located above the Fermi level, with the

neighbours of the absorbing atom, and which lead to a modification of the transmitted photon flux intensity I_t as a function of the photon energy (Figure II-3A).

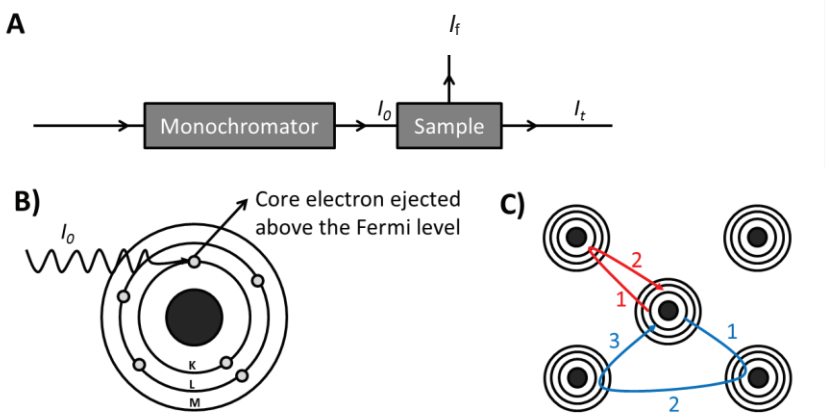

Figure II-3. Simplified scheme of (A) a XAS experiment and (B) a focus at the atomic level of an atom excited by a flux of photons. (C) Simple (in red) and multiple (in blue) scatterings are shown in example of the type of path that can take the photo-electron.

Each absorbing atom in a system is characterized by its absorption coefficient μ(E) function of the incident photon. In a transmission XAS experiment, this absorbing coefficient can be determined with the flux of incident I_0 and transmitted photons through the sample (having a thickness e) I_t:

$$\mu(E)e = \log\left(I_0(E)/I_t(E)\right) \qquad \text{Eq. II-23}$$

In the case of diluted samples, the fluorescence photon flux intensity I_f, measured at 90° of the incident beam, is recorded. This flux of X-ray fluorescence signal originates from the fact that, as soon a core electron is excited above the Fermi level it leaves an empty place in a core level, which has then a strong probability to be filled with an electron located at a higher energy level, accompanied by the emission of a fluorescence photon, whose energy is typical of the absorbing atom. The absorption coefficient measured in fluorescence mode is given by the following expression:

$$\mu(E) \propto I_f(E)/I_0(E) \qquad \text{Eq. II-24}$$

The absorption coefficient μ is calculated following the Fermi's golden rule. It is a general formulation for a system transiting from a fundamental non-excited state to an excited state. With the hypothesis of a uniform electric field at the scale of the atomic orbital, the adsorption coefficient can be written as follow:

$$\mu(E) \propto \sum \left|\langle i \left| \vec{E}.\vec{r} \right| f \rangle\right|^2 \delta(E_\mathrm{i} + \hbar\omega - E_\mathrm{f}) \qquad \text{Eq. II-25}$$

where $\left|\langle i \left| \vec{E}.\vec{r} \right| f \rangle\right|^2$ is a matrix translating the probability of transition between an initial i (before absorption) and a final f atomic state (after absorption), $\vec{E}$ is the vector of the electric field, $\vec{r}$ is a space operator, $\delta(E_i + \hbar\omega - E_f)$ is a Dirac distribution indicating the conservation of the energy of the system, E_i is the absorption energy, E_f is the kinetic energy of the photoelectron.

Practically, each X-ray absorption spectrum ($\mu = \mathrm{f}(E)$), with E the energy of the incident photons, can be divided visually into two regions/regimes (*Figure II-4*A), below and above the absorption edge, but in practical, the two regions of interest are located: (i) near the absorption edge (about ± 100 eV from the absorption edge), referred to as the XANES region (X-ray Absorption Near-Edge Spectroscopy) or (ii) well above the absorption edge (+80 eV from the absorption edge), referred to as the EXAFS region (Extended X-ray Absorption Fine Structure). XANES is strongly sensitive to the oxidation state and coordination chemistry of the absorbing atom, while EXAFS is used to determine distances, coordination number, disorder and chemical environment of the absorbing atom neighbours. The oscillations in the EXAFS region are coming from the constructive and destructive interactions between the waves describing the emitted and the back-diffused photo-electron by the closest neighbours of the absorbing atom (Figure II-3C). In this manuscript we have focused on the EXAFS region/oscillations analysis for the main reason that the electrons ejected right above the absorption edge (XANES) have a long mean free path that enable probing the matter that surrounds the absorbing atom up to + 25 Å. In the case of small nanoparticles, this distance can correspond to the mean particle size, and thus results that are contained within the XANES are too difficult to be discussed quantitatively as they imply to have a good knowledge of the materials within these characteristic distances. In the EXAFS region the electrons have a lower mean free path and they probe the matter down to 5 Å.

In EXAFS, we are modelling the oscillations $\chi(E)$, resulting from the electron-matter interactions, obtained from the experimental absorption spectrum ($\mu(E)$) subtracted from an ideal one ($\mu_0(E)$) corresponding to the absorption of one single isolated atom (Eq. 4). This step is the most critical in the whole EXAFS calculation as the $\mu_0(E)$ term is unique and function of the experimental spectrum. This removal of the background was performed with the Athena software .

$$\chi(E) = \frac{[\mu(E) - \mu_0(E)]}{\mu_0(E)} \qquad \text{Eq. II-26}$$

Typically, EXAFS oscillations are expressed as a function of the *k* wave vector of the photo-electron:

$$k = \sqrt{\frac{2m(E-E_0)}{\hbar^2}} \qquad \text{Eq. II-27}$$

The characteristic EXAFS oscillations are then presented in *Figure II-4*B as a function of *k*. This signal is weighted by a factor k^x (x = 1, 2 or 3, in this work x = 2). This factor is used to exalt the EXAFS oscillations in a specific range of *k* values. The EXAFS signal $\chi(k)$ is the sum of sinusoidal signals. Its mathematic description can be obtained after simplification of Fermi's golden rule. In the case of a K edge, the EXAFS signal simplifies as follows:

$$\chi(k) = -\sum_j \frac{1}{kR_j 2} N_j * e^{-\frac{2R_j}{\lambda}} * e^{-2{\sigma_j}^2 k^2} * \left|f_j(k,\pi)\right| \sin(2kR_j + \Phi_j(k)) \qquad \text{Eq. II-28}$$

This EXAFS equation is the sum over different *j* terms corresponding each to the contribution of one atomic shell. In this sum there are theoretical calculated values $f_j(k,\pi), \Phi_j(k)$ and λ which are respectively, the effective back-scattering amplitude, the effective scattering phase shift and the electronic mean free path respectively and structural parameters that we want to determine (N_j, σ_j, R_j which are the coordination number in the shell *j*, the mean squared displacement or Debye Waller parameter and the interatomic distance between the absorbing atom and any atom in the shell *j* respectively). As this equation is a sum of sinusoidal terms, by taking the Fourier Transform of the EXAFS signal, we obtain a signal in the *R* space where each peak corresponds to the contribution of one shell of interaction (in *Figure II-4*C). These interactions can be simple, an electron ejected interacts with one neighbouring atom and is then retro-diffused to its initial position (see the red path in Figure II-3C that can contribute to the red shell highlighted in *Figure II-4*C), or multiple (see the blue path in Figure II-3C that can contribute to the blue shell highlighted in *Figure II-4*C). The number of equivalent paths corresponds to the number neighbour.

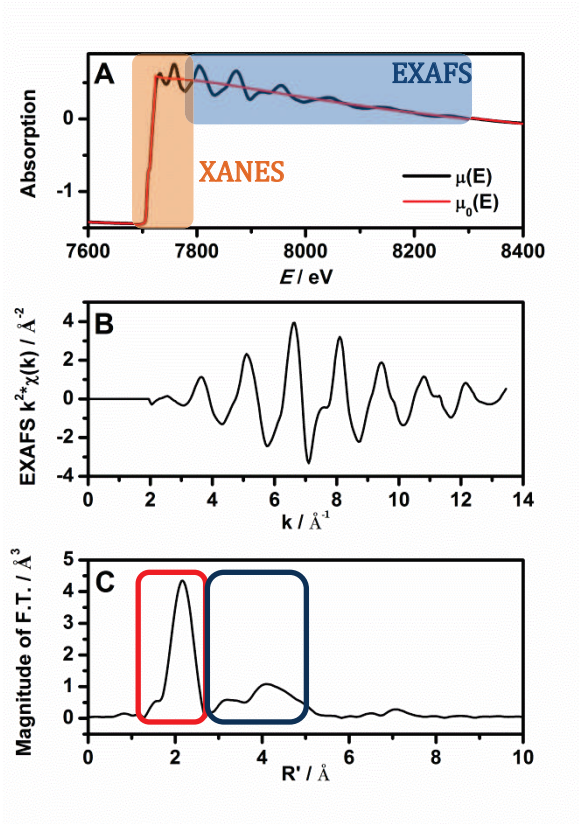

Figure II-4. (A) Absorption spectrum pattern $\mu(E)$ at the K edge of a Co foil (in black). The background function $\mu_0(E)$ representing the absorption of an isolated atom is shown in red. The XANES and EXAFS regions are highlighted in orange and blue respectively. (B) k^2 weighted EXAFS spectrum $\chi(k)$. (C) Fourier transform of the k^2 weighted EXAFS spectrum. The first and following shells of calculation are circled in red and blue respectively.

These peaks are then fitted with the software Artemis to extract the structural parameters cited above corresponding to each shell of interaction. In our case we will limit the calculation of the structural parameters to the first shell of interaction. All the experimental standard deviations have been set at ± 10 % for the coordination numbers and ± 0.01 Å for the lattice parameters. This is the best resolution (function of the optics, detectors, etc.) we can obtain experimentally on this beamline, even though the standard deviation obtained on these parameters with the fitting software was much lower. When the fit indicated a greater standard deviation, this latter value was reported in the manuscript.

More details on the XAS technique can be found in review papers [25, 26]. More information specific to the absorption beamline CRG-BM 30B, which stands for Collaborative Research Group – Bending Magnet) of the European Synchrotron Research Facility (ESRF), such as the type of monochromator (double Si(2 2 0) crystal with an energy resolution $\Delta E/E = 5.6\times10^{-5}$ resulting in a beam size on the sample of about 0.3×0.3 mm^2), or the type of detectors (incident and transmitted

signals were collected by Si diodes, and fluorescence counts by a Canberra™ 30 elements solid-state detector) can be found in Hazemann *et al.* and Proux *et al.* [27-29].

2. *Ex situ* measurements

Fresh/aged Pt_3Co/C catalysts (prepared following configuration D in Figure II-1) were investigated with X-ray absorption spectroscopy at the European Synchrotron Radiation Facility (ESRF) in Grenoble (French CRG beamline BM30B). These tests were performed *ex situ* (*i.e.* without electrode potential control) in the fluorescence mode. The measurements were performed at the Pt L_3 and the Co K edges. The extraction of the atomic background of each signal was performed with the Athena software . The XANES spectrum qualitative analysis (edge energy, jump,…) and the extraction of the EXAFS oscillations were done with the software Athena . The fit of the EXAFS signals were performed with the software Artemis using a f.c.c. Pt_3Co description path .

3. *In situ* measurements

In situ XAS coupled to electrochemical tests were conducted in a home-made cell (Figure II-5). This cell, made of Kel-F (homopolymer of chlorotrifluoroethylene), was designed to minimize the quantity of liquid electrolyte (which absorbs part of the XAS signal) through the path of the X beam. A circular gold current collector is used to connect the probed sample to the working electrode channel of the potentiostat. A platinum wire is used as a counter electrode and a deported saturated calomel electrode (SCE) as the reference electrode. These items, especially the platinum counter electrode, are maintained off the X-ray beams (incident and fluorescence). The cell is showing an angle of 45° with respect to the incident beam, which enables simultaneous recording in transmission and in fluorescence modes (the fluorescence detector is positioned perpendicular to the incident beam, while the transmission detector is in its continuity). The XANES and EXAFS shown in this thesis report have been extracted from the transmitted signal. The fluorescence signal was recorded to confirm the results obtained in the transmitted mode. The samples used in this part of the work were prepared by PaxiTech®. They are made of a Pt_3Co/C (46 wt. % metal loading over high surface area carbon purchased at Tanaka Kikinzoku Kogyo (T.K.K.), as detailed in the following section) catalyst ink deposited as a catalyst layer on a membrane, similar as in a MEA configuration (configuration D in Figure II-1). A theoretical platinum loading in the sample of *ca.* 5 mg_{Pt} cm^{-2} (assuming an atomic ratio Pt/Co in the catalyst nanoparticles of *ca.* 3) was calculated to be the optimized electrode loading to obtain an ideal absorption jump at the cobalt edge ($\ln(I/I_0) = 1$) to perform the observation at both the Pt L_3 and the Co K edges. Experimentally, during operation while the cell is fulfilled with the high absorbing electrolyte, this absorption jump was ten times lower than expected at the cobalt K edge,

which was insufficient to perform *in situ* measurements at the Co K edge. Therefore, all the *in situ* measurements were performed only at the Pt L_3 edge.

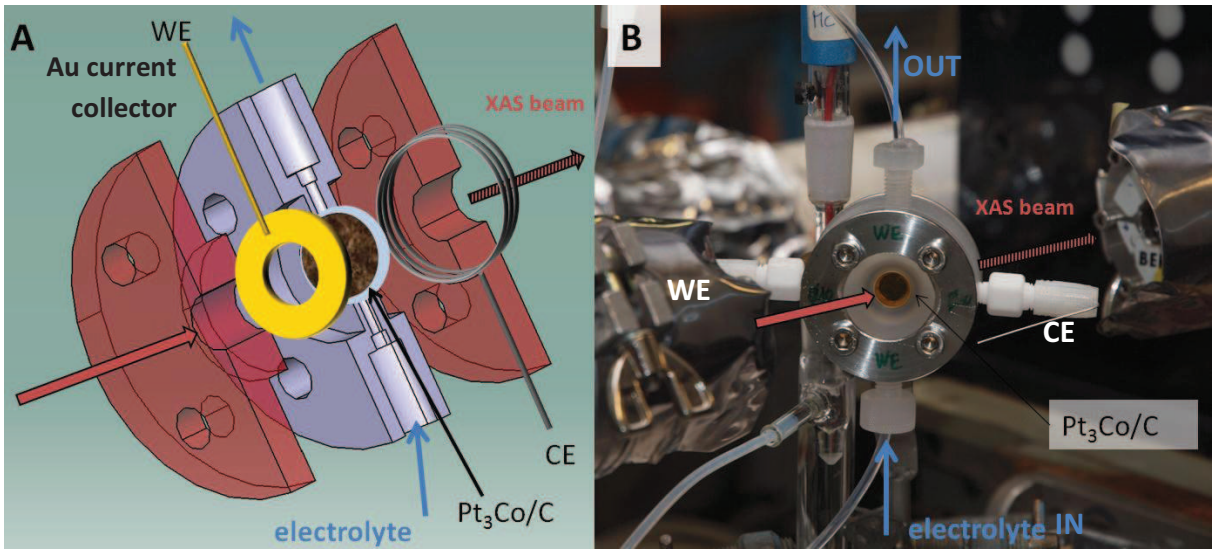

Figure II-5. (A) Scheme of the XAS/electrochemical cell and (B) picture of the cell in operation taken at the beamline BM30B. During the fluorescence acquisition at the Co K edge, the external body of the cell made of stainless steel was removed to avoid any interference of the alloying elements of the stainless steel (Fe and Cr) with the cobalt content of our working electrode.

IX. Preparation of the benchmark Pt_3Co/C-skeleton and Pt_3Co/C-skin catalysts

The Pt_3Co/C-skin and Pt_3Co/C-skeleton used in this work were synthesized using a procedure similar as that used by Wang *et al.* [30]. Pt-Co nanoparticles, having a Pt/Co atomic ratio close to 3/1 and a Pt content of 46 wt. %, supported on high surface area carbon (850 m^2 g_{carbon}) were purchased from T.K.K.. The received catalysts were first immersed overnight in a stirred solution of 1 M H_2SO_4 to obtain a Pt-skeleton catalyst. A fraction of this Pt-skeleton catalyst was then heat treated at T = 673 K under ultra-high vacuum during 4 h to obtain the Pt-skin catalyst.

X. References

[1] Kocha S. S., Principles of MEA preparation, in *Handbook of Fuel Cells: Fundamentals, Technology, and Applications*, Vol. 3, Vielstich W., Gasteiger H. A. and Lamm A. 2003, John Wiley & Sons

[2] Tang H., Wang S., Jiang S. P. and Pan M., A comparative study of CCM and hot-pressed MEAs for PEM fuel cells. *J. Power Sources*, 170 (2007) 140-144.

[3] Wilson M. S. and Gottesfeld S., Thin-film catalyst layers for polymer electrolyte fuel-cell electrodes. *J. Appl. Electrochem.*, 22 (1992) 1-7.

[4] Scherrer P., Bestimmung der Grösse und der inneren Struktur von Kolloidteilchen mittels Röntgenstrahlen. *Nachr. Ges. Wiss*, 2 (1918) 98-100.

[5] Chatenet M., Guétaz L. and Maillard F., Electron microscopy to study MEA materials and structure degradation, in *Handbook of Fuel Cells: Fundamentals, Technology, and Applications*, Vol. 5, Vielstich W., Gasteiger H. A. and Yokokawa H. 2009, John Wiley & Sons

[6] Williams D. B. and Carter C. B., Transmission Electron Microscopy, Vol. I-IV, 1996, Plenum Press

[7] Trasatti S. and Petrii O. A., Real surface-area measurements in electrochemistry. *J. Electroanal. Chem.*, 327 (1992) 353-376.

[8] Maillard F., Savinova E. R., Simonov P. A., Zaikovskii V. I. and Stimming U., Infrared spectroscopic study of CO adsorption and electro-oxidation on carbon-supported Pt nanoparticles: Interparticle versus intraparticle heterogeneity. *J. Phys. Chem. B*, 108 (2004) 17893-17904.

[9] Schmidt T. J., Gasteiger H. A., Stab G. D., Urban P. M., Kolb D. M. and Behm R. J., Characterization of high-surface area electrocatalysts using a rotating disk electrode configuration. *J. Electrochem. Soc.*, 145 (1998) 2354-2358.

[10] Maillard F., Eikerling M., Cherstiouk O. V., Schreier S., Savinova E. and Stimming U., Size effects on reactivity of Pt nanoparticles in CO monolayer oxidation: The role of surface mobility. *Faraday Discuss.*, 125 (2004) 357-377.

[11] Maillard F., Schreier S., Hanzlik M., Savinova E. R., Weinkauf S. and Stimming U., Influence of particle agglomeration on the catalytic activity of carbon-supported Pt nanoparticles in CO monolayer oxidation. *Phys. Chem. Chem. Phys.*, 7 (2005) 385-393.

[12] Andreaus B., Maillard F., Kocylo J., Savinova E. R. and Eikerling M., Kinetic modeling of CO_{ad} monolayer oxidation on carbon-supported platinum nanoparticles. *J. Phys. Chem. B*, 110 (2006) 21028-21040.

[13] Maillard F., Savinova E. R. and Stimming U., CO monolayer oxidation on Pt nanoparticles: Further insights into the particle size effects. *J. Electroanal. Chem.*, 599 (2007) 221-232.

[14] Bard A. J. and Faulkner L. R., Electrochemical methods,(1993), John Wiley & Sons, Inc.

[15] van der Vliet D., Strmcnik D. S., Wang C., Stamenkovic V. R., Markovic N. M. and Koper M. T. M., On the importance of correcting for the uncompensated ohmic resistance in model experiments of the oxygen reduction reaction. *J. Electroanal. Chem.*, 647 (2010) 29-34.

[16] Gamez A., Richard D., Gallezot P., Gloaguen F., Faure R. and Durand R., Oxygen reduction on well-defined platinum nanoparticles inside recast ionomer. *Electrochim. Acta*, 41 (1996) 307-314.

[17] Gloaguen F., Andolfatto F., Durand R. and Ozil P., Kinetic-study of electrochemical reactions at catalyst-recast ionomer interfaces from thin active layer modeling. *J. Appl. Electrochem.*, 24 (1994) 863-869.

[18] Dubau L., Maillard F., Chatenet M., André J. and Rossinot E., Nanoscale compositional changes and modification of the surface reactivity of Pt_3Co/C nanoparticles during proton-exchange membrane fuel cell operation. *Electrochim. Acta*, 56 (2010) 776-783.

[19] Antoine O. and Durand R., RRDE study of oxygen reduction on Pt nanoparticles inside Nafion®: H_2O_2 production in PEMFC cathode conditions. *J. Appl. Electrochem.*, 30 (2000) 839-844.

[20] Cachet-Vivier C., Vivier V., Cha C. S., Nedelec J. Y. and Yu L. T., Electrochemistry of powder material studied by means of the cavity microelectrode (CME). *Electrochim. Acta*, 47 (2001) 181-189.

[21] Guilminot E., Corcella A., Chatenet M. and Maillard F., Comparing the thin-film rotating disk electrode and the ultramicroelectrode with cavity techniques to study carbon-supported platinum for proton exchange membrane fuel cell applications. *J. Electroanal. Chem.*, 599 (2007) 111-120.

[22] Parthasarathy A., Martin C. R. and Srinivasan S., Investigation of the O_2 reduction reaction at the platinum Nafion® interface using a solid-state electrochemical cell. *J. Electrochem. Soc.*, 138 (1991) 916-921.

[23] Vion-Dury B., Mécanismes de vieillissement des électrocatalyseurs de pile à combustible de type PEMFC, 2011, Grenoble INP, Grenoble.

[24] Athena, Artemis, and Hephaestus, XAS Data Analysis Software. *http://cars9.uchicago.edu/ifeffit/BruceRavel/Horae*.

[25] Teo B. K., EXAFS: Basic principles and data analysis,(1986), Springer.

[26] Koningsberger D. C. and Prins R., X-ray absorption: Principles, applications, techniques of EXAFS, SEXAFS and XANES,(1998), Wiley.

[27] Hazemann J.-L., Proux O., Nassif V., Palancher H., Lahera E., Da Silva C., Braillard A., Testemale D., Diot M.-A., Alliot I., Del Net W., Manceau A., Gelebart F., Morand M., Dermigny Q. and Shukla A., High-resolution spectroscopy on an X-ray absorption beamline. *J. Synchrotron Radiat.*, 16 (2009) 283-292.

[28] Proux O., Biquard X., Lahera E., Menthonnex J. J., Prat A., Ulrich O., Soldo Y., Trevisson P., Kapoujyan G., Perroux G., Taunier P., Grand D., Jeantet P., Deleglise M., Roux J. P. and Hazemann J. L., FAME: A new beamline for X-ray absorption investigations of very-diluted systems of environmental, material and biological interests. *Phys. Scripta*, T115 (2005) 970-973.

[29] Proux O., Nassif V., Prat A., Ulrich O., Lahera E., Biquard X., Menthonnex J. J. and Hazemann J. L., Feedback system of a liquid-nitrogen-cooled double-crystal monochromator: Design and performances. *J. Synchrotron Radiat.*, 13 (2006) 59-68.

[30] Wang C., Chi M., Li D., Strmcnik D., van der Vliett D., Wang G., Komanicky V., Chang K.-C., Paulikas A. P., Tripkovic D., Pearson J., More K. L., Markovic N. M. and Stamenkovic V. R., Design and synthesis of bimetallic electrocatalyst with multilayered Pt-skin surfaces. *J. Am. Chem. Soc.*, 133 (2011) 14396-14403.

Chapter III.

Degradations mechanisms of Pt_3Co/C electrocatalysts under real PEMFC operating conditions

Some of the results discussed in this chapter have been published in:

Maillard F., Dubau L., **Durst J.**, Chatenet M., André J., Rossinot E.:
Durability of Pt_3Co/C nanoparticles in a proton-exchange membrane fuel cell: Direct evidence of bulk Co segregation to the surface.
Published in: *Electrochemistry Communications*, 12 (2010), pp. 1161–1164

Dubau L., **Durst J.**, Maillard F., Guétaz L., Chatenet M., André J., Rossinot E.:
Further insights into the durability of Pt_3Co/C electrocatalysts: Formation of "hollow" Pt nanoparticles induced by the Kirkendall effect.
Published in: *Electrochimica Acta*, 56 (2011), pp. 10658-10667

Dubau L., **Durst J.**, Maillard F., Chatenet M., André J., Rossinot E.:
Influence of PEMFC operating conditions on the durability of Pt_3Co/C electrocatalysts.
Published in: *ECS transactions* from the 218th ECS Meeting, 33 (2010), pp. 399-405

I. Why platinum alloys catalysts are used for the ORR?

In the early 70's, platinum alloyed to non-noble (transition) metal were tested for the first time as ORR cathode catalysts in PAFC systems. Binary (PtV and PtCu) and ternary (PtCoCr, PtRhFe, PtIrCr, PtNiCo, PtFeCu, and PtFeCoCu) alloys demonstrated a two- to- threefold gain in both ORR mass and specific activities [1]. In addition, "diluting" Pt conveys undoubtable economic interest. Their implementation in PEMFC systems waited till the early 1990's. The use of such alloys as catalyst for the ORR is however not innocent. At this time it was thought that the rate determining step in the ORR was the dissociation of the oxygen-oxygen bond, which is favoured when decreasing the interatomic distance in the crystallographic structure of the catalyst. In its ordered face centred cubic (f.c.c.) structure, the Pt lattice parameter is 3.93 Å. Pt-M alloys (with M the non-noble metal) present reduced lattice parameters compared to pure Pt. However one cannot get completely rid of the platinum content, because it confers an electrochemical/chemical stability to the alloy (most of the non-noble metals being thermodynamically unstable in the working potential window of a PEMFC cathode). One of the difficulties, from a fundamental point of view, that rose in the 1980's and 1990's was to understand how changes in the atomic composition (the atomic ratio between platinum and non-noble metal atoms) and the method of synthesis (with or without any chemical and/or thermal pre-treatment) of the alloy affect the intrinsic ORR activity of the Pt-based alloys [2, 3]. These difficulties can be summarized into two major questions:

- What is the real effect of a non-noble metal atom underlying a platinum surface on the electrocatalytic properties of the alloy? In other words, is there another effect than the geometric effect (also called strain effect, which originates from the Pt overlayer lateral compression [4, 5]) that rules out the enhancement of the catalytic activity of the alloy?
- What is, at any time, the surface composition of a Pt-alloy?

Answers to these questions came from studies on model surfaces. Indeed, the elucidation of surface composition and structure is more facile for extended surfaces, especially on single crystals. It has been shown that, more than a beneficial geometric effect (smaller bond length in a Pt-alloy than in pure Pt), there is also an electronic effect (also called ligand effect) originating from the decrease of the position of the *d*-band centre relative to the Fermi level [6]. This *d*-band centre is a key parameter in electrocatalysis, since it establishes chemisorption and electrocatalytic trends of metal surfaces. From density functional theory (DFT) studies, based on the assumption that changes in adsorbate chemisorption energies over different metals are related to the metal *d*-band centre, Hammer and Nørskov have shown that the strength of the metal-(hydr-)oxide bond can be evaluated for a given surface [7]. The prediction of the strength of the metal-hydroxide and metal-oxide bonds is of high interest as this cluster plays a crucial role in electrochemical reactions such as the ORR (by acting as a site blocking species and so lowering the rate of the ORR) [8] but also in the metal dissolution [9]. The

lower the *d*-band centre, the weaker the interactions with adsorbates and the better the catalyst for the ORR in PEMFC application. The most optimized configurations are obtained for Pt_3Ni and Pt_3Co surfaces (Figure III-1). The geometric and electronic structures of an alloy are specific to each alloy, as these two parameters strongly depend on the non-noble metal, the composition (atomic ratio Pt/non-noble metal) and the structure (changes of the atomic composition from one atomic layer to another due to surface segregation of one of the element) (Figure III-1A and B) [10].

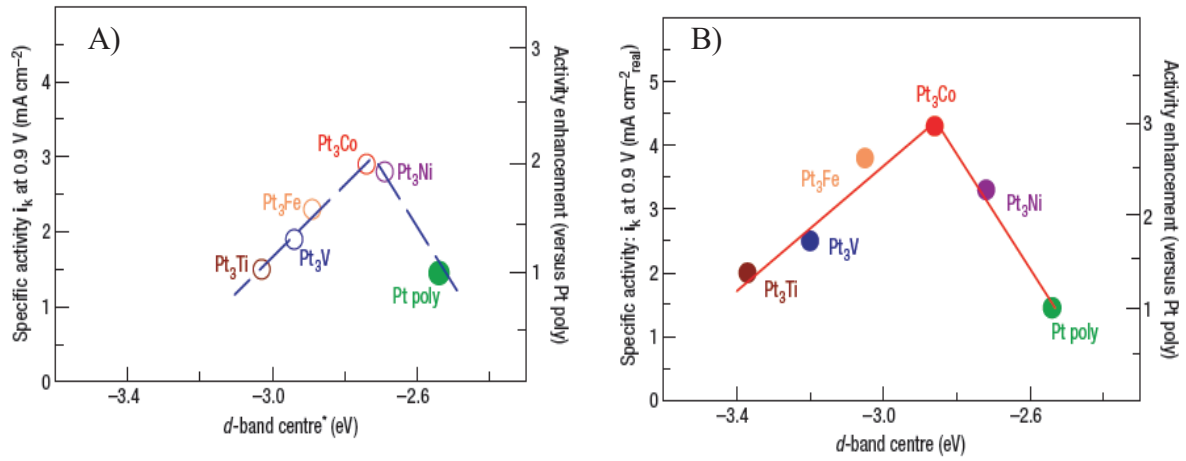

Figure III-1. Relationships between experimentally measured specific activity for the ORR on Pt_3M surfaces in 0.1M $HClO_4$ at T = 333 K versus the position of the d-band centre for Pt-skeleton (A) and Pt-skin (B) surfaces. The Pt-skin is obtained after a thermal annealing of the Pt-skeleton. Reprinted from Stamenkovic et al. [6].

The same reasoning applies for nanometre sized alloy particles, although the control and determination of the structure and composition is more complex than for model single crystals surfaces. It has been experimentally confirmed that there were the same activity enhancement factors for the ORR over corresponding Pt catalyst from model electrodes to nanomaterials [11]. With state-of-the-art Pt-alloy supported catalysts, there is a three-fold enhancement of the ORR specific activity but only a two-fold enhancement of the ORR mass activity, because Pt-alloy/C catalyst exhibit lower specific surface area than Pt/C catalyst [12].

Incommensurable data in the literature concern new synthesis methods, novel alloying elements tested, physical/chemical/electrochemical pre-treatments that enhance the electrocatalytic properties of Pt_3M (with M a first row non-noble metal) nanomaterials [13-15]. Each of these alloys generates unique structures of unique geometric and electronic properties. However, very scarce studies focus on the electrochemical/chemical stability of such platinum alloy in the cathode environment of a PEMFC. A first work published by Antolini *et al.* gathers all the results published at the time regarding the stability of Pt-M/C alloy catalyst [16]. Many adverse results are presented; in particular, negligible [3, 12] and non-negligible non-noble metal dissolution rates are reported. The

dissolution of the non-noble metal atoms can have a positive effect (surface roughening [17, 18], improved electronic effect [2] or presence of cations in the electrolyte [19]), a negative effect (decrease of the ORR activity [20-22], metal cations in the electrolyte [10, 23, 24]) or even no effect [1]. However, even when a decrease of the performance of Pt_xCo_y/C electrocatalysts was monitored, there was still a gain relative to Pt/C [12, 25, 26].

In order to clearly understand this disparity of results, the use of atomic resolved techniques is essential to get more information about the fine structure (local distribution of the alloying elements) of a Pt-alloy and its modification upon aging. Chen *et al*. were the first in 2010 to report the formation of a very few *spongy* particles in the cathode catalyst layer after 24 hours of intensive potential sweeping at 100 mV s^{-1} between 650 and 1050 mV *vs.* RHE, thanks to Scanning Transmission Electron Microscopy – High-Angle Annular Dark-Field (STEM-HAADF) observations [26]. The authors associated the apparition of these spongy particles to the initial presence of cobalt-rich particles $Pt_{<0.5}Co_{>0.5}$/C, for which a great amount of Co is able to dissolve, leading to an almost pure Pt structure. More recently such observations were coupled with a mapping of Pt and Co obtained by electron energy loss spectroscopy (EELS) on tenths of Pt_3Co/C particles [27, 28] and confirmed the heterogeneous redistribution of the platinum and non-noble metal atom within the nanoparticles, depending on the initial size of the particle.

However, most of the studies conducted so far investigated the durability of Pt_xCo_y/C particles on short time scales, with short-duration voltage cycling in liquid electrolyte or PEMFC, which are very useful but do not provide a clear insight into the long-term degradation mechanisms of Pt_3Co/C catalysts.

The aim of this chapter is to confirm whether or not Pt-alloy cathode catalyst meet the requirements in terms of robustness when used as cathode electrocatalyst in a PEMFC. To answer this key question, we will work on a commercial state-of-the-art Pt_3Co/C catalyst. The initial structure of this catalyst will be first determined and compared to that of two model catalysts, the Pt-skeleton and the Pt-skin structures, which will be detailed in the following. Then, the commercial cathode catalyst will be operated in a 16 cell stack under different operating conditions for more than 1000 hours. Physical, chemical and electrochemical techniques will be used to correlate the changes of the surface reactivity of a Pt_3Co/C catalyst with the changes of its fine structure upon degradation.

II. Initial composition and structure of the fresh Pt_3Co/C catalysts

1. First insights by X-ray diffraction

It is essential to determine the structure of the pristine Pt3Co/C cathode catalyst, to be able to discuss its degradation mechanisms upon aging in PEMFC stack. As discussed in the experimental section, the only information that was provided about this alloy cathode catalyst was its platinum to cobalt ratio, its metal loading on the carbon support (≈50 wt. %) and its loading in the MEA (≈ 0.4 mg_{Pt} cm^{-2}_{MEA}). No information was available whether this cathode catalyst underwent any treatments (thermal and/or chemical) post-synthesis, which are believed to greatly influence the surface structure of the catalyst nanoparticles, and therefore its electrocatalytic activity.

Post-synthesis chemical treatments basically consist of washing the fresh Pt_3Co nanoparticles with an acidified H_2SO_4 or $HClO_4$ solution at pH ≤ 1 in order to leach all the cobalt atoms located at the surface of the catalyst. Indeed, the Co/Co^{2+} redox potential is $E^0_{Co^{2+}/Co}$ = -0.28 V *vs.* NHE, which means that Co atoms are instable in a PEMFC environment. In addition, the enthalpy of mixing of Pt–Co alloys [29] is too small to significantly upshift the Co/Co^{2+} redox potential. Assuming that after the synthesis platinum and cobalt atoms are randomly distributed within the nanoparticle (true for some synthesis methods), this *ex situ* pre-operation leaching avoids that a great amount of cobalt atoms leaches in the PEMFC (with harmful consequences, see **Chapter V**) as soon as the catalyst operates at the cathode. Acid-leaching is believed to lead to the formation of a very thin (1 or 2 atomic layers) pure platinum surface with similar structural properties (interatomic distance) than the unmodified Pt_3Co core. The catalyst surface after such acid leaching is atomically rough and composed of low coordinate platinum atoms (having a smaller activity for the ORR and being more prone for a rapid dissolution). The obtained structure is often referred to as the Pt_3Co skeleton (Figure III-2) [2, 4, 30-32].

Post-synthesis thermal treatments can also be carried out in order to (i) reduce the number of low-coordinated Pt atoms and (ii) rearrange the surface layers of the alloy catalyst in terms of structure and composition. Indeed thermal treatments yield surface segregation of the platinum atoms, at the expense of the cobalt atoms, and thus formation of a pure platinum shell (from 1 to 4 monolayers thick [4, 26, 33] equating to 0.277 nm to 1.108 nm, depending on the duration, the atmosphere and the temperature at which the thermal treatment is performed [34]). This surface segregation upon annealing is obtained because, in the case of an initial Pt_3Co alloy, as the heat of mixing is small and the heats of sublimation of the elements are similar, the strain energies become determinant and the surface is thus enriched in the larger atom (here Pt) [35]. DFT calculations of Hirunsit *et al.* confirmed that structures with pure Pt surfaces ($Pt_{100}/Co_{100}/Pt_{50}Co_{50}$ and $Pt_{100}/Pt_{50}Co_{50}/Pt_{75}Co_{25}$) are the most stable configurations in vacuum [36]. The formation of a pure Pt surface upon annealing was confirmed on extended surfaces by low energy ion scattering (LEIS). The resulting surface atoms possess a larger Pt-Pt bond length than in a Pt_3Co system, the latter however remaining smaller than in a bulk Pt nanocatalyst. The obtained structure, often referred to as the Pt_3Co skin (Figure III-2), has

been evidenced to perform better for the ORR in acidic media than the as-synthesized Pt_3Co and the Pt_3Co skeleton structures. This result suggests that the unfavourable changes of the geometric structure of the annealed surface (larger surface bond distance than in a Pt_3Co or Pt_3Co-skeleton system) are largely counterbalanced by favourable modifications of the electronic (Pt-O(H) bond energetics) [32] and geometric structure (smaller proportion of low-coordinated atoms) of the annealed nanoparticle and emphasize some more the difficulty to deconvolute the complex interplay between strain and ligand effects [37-41].

In order to get more information on the initial structure and composition of the commercial Pt_3Co/C catalyst (denoted hereafter as "Pt_3Co/C MDM"), we compare it, by XRD and XAS, to model Pt_3Co/C skeleton and Pt_3Co/C skin structures. A good knowledge of the initial structure is mandatory to unveil the degradation mechanisms.

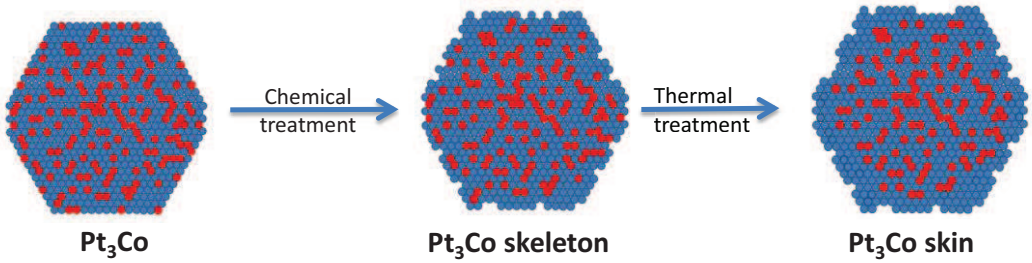

Figure III-2. Cross-sections of a homogeneous cuboctahedral Pt_3Co nanoparticle, a "Pt_3Co skeleton" obtained after a chemical treatment and a "Pt_3Co skin" obtained after a thermal treatment. Colour key: platinum atoms-blue, cobalt atoms-red.

Figure III-3 presents the X-ray diffractograms of the Pt_3Co/C MDM, the Pt_3Co/C skeleton and the Pt_3Co/C skin electrocatalysts. In these diffractograms, each peak corresponds to the diffraction of the X-rays by one of the crystal orientation of the polycrystalline catalysts. Their 2θ position is related to the averaged lattice parameter of the catalyst while their full width at half maximum can serve to calculate the average crystallite size [42]. When comparing the diffractograms of the different catalysts, we notice that the diffraction peaks shift towards smaller 2θ angles for the skin with respect to the skeleton structure, indicating larger average interatomic distance for the former. Assuming that Vegard's law applies to Pt-Co solid solutions, this translates into lower molar fraction of Co alloyed to Pt for the skin *vs*. skeleton structure (Table III-1). The mean crystallite sizes, determined from the Scherrer law using the full width at half maximum of the diffraction peaks, are similar within the error bar of the measurement (see $\bar{d}_{XRD}$ in Table III-1). This indicates that the thermal treatment used to form the skin surface (4 h at T = 673 K) does not lead to any significant coarsening/-agglomeration of the Pt_3Co nanoparticles [43]. On the contrary, larger annealing temperature (T = 1000 K) used by Chen *et al.* [31] causes a severe coarsening/-agglomeration of the nanoparticles and so ECSA loss of

the catalyst (increase from 5.4 nm, equating to 52 m^2 g_{Pt}, to 9.2 nm, equating to 30 m^2 g_{Pt}) [31]. Slight changes of the mean crystallite size are confirmed by the values of the mean particle size estimated by TEM (see $\overline{d}_N$, $\overline{d}_S$ and $\overline{d}_V$ values in Table III-1).

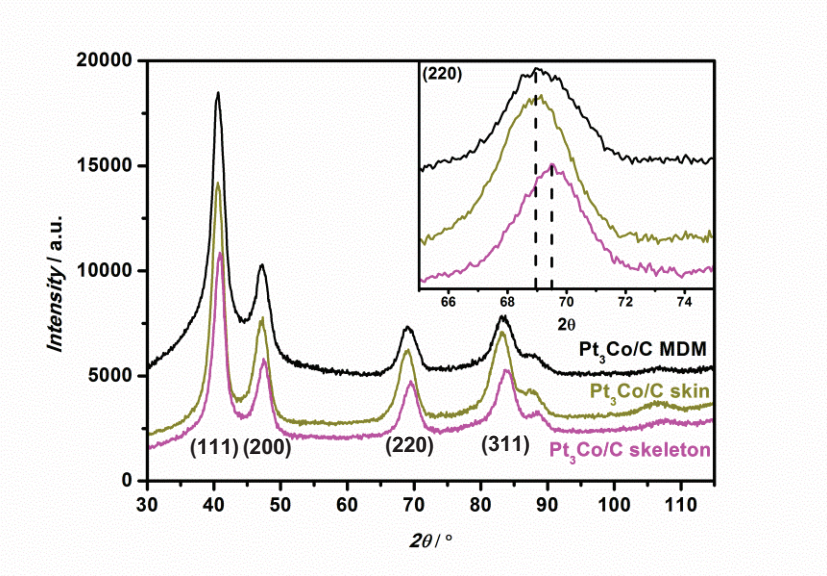

Figure III-3. XRD patterns of the Pt_3Co/C MDM (black), the Pt_3Co/C skeleton (pink) and the Pt_3Co/C skin (khaki) catalysts. The insert is a zoom on the (220) diffraction peak.

Interestingly, the diffraction peaks of the commercial Pt_3Co/C catalyst nearly superpose with those observed for the skin structure, suggesting similar average atom-atom bond length and similar atomic composition (see Table III-1). However, this result does not necessary implies that the Pt_3Co/C MDM and the Pt-skin catalysts possess similar atomic arrangement (and a similar core-shell structure). As we will see later, X-ray absorption fine structure (EXAFS) spectra provide the number, the type and the distance of the backscattering atom surrounding the central absorbing atom and thus provide more information about the fine structure.

Catalysts	XRD			TEM		
	$a_{(220)}$ / nm	$\overline{d}_{XRD}$ / nm	at. comp.	$\overline{d}_N$ / nm	$\overline{d}_S$ / nm	$\overline{d}_V$ / nm
Pt_3Co/C skeleton	0.2706	4.6	Pt_3Co	3.9	4.7	5.2
Pt_3Co/C skin	0.2725	4.3	$Pt_{4.5}Co$	4.0	5.1	5.8
Pt_3Co/C MDM	0.2720	3.5	Pt_4Co	4.2	4.8	5.3

Table III-1. Physical parameters extracted from the XRD diffractograms and the TEM pictures of the Pt_3Co/C MDM, the Pt_3Co/C skeleton and the Pt_3Co/C skin catalysts.

2. X-ray absorption near edge spectroscopy measurements

XANES spectra provide a wealth of information about the oxidation state, the *d*-band density and the electronic environment of the absorbing atoms. To the best of our knowledge, only two groups compared the X-ray absorption behaviours of skin and skeleton structures. The first study, dated 2009, was made by Chen *et al.* [31]. A Pt_3Co/C-skeleton, referred to as "AT-Pt_3Co", and a Pt_3Co/C-skin obtained by annealing "AT-Pt_3Co" at 1000 K for 3 h, referred to as "HT-AT-Pt_3Co", were studied at the Pt L_3 and L_2 edges (which allow the determination of the *d*-band vacancies) but not at the Co edge [31]. In the second study in 2011, Wang *et al*. performed *in situ* X-ray absorption measurements on various PtNi/C catalysts [34]. They tested three catalysts: as-synthesized PtNi/C, acid-treated Pt_3Ni/C, and acid-treated/annealed Pt_3Ni/C. The XANES spectrum were recorded at the Ni K and at the Pt L_3 edges at E = 1.0 V *vs.* RHE (open circuit potential conditions).

In this study, Synchrotron X-ray absorption spectroscopy measurements were performed at the European Synchrotron Radiation Facility for the three catalysts of interest here. The measurements were carried *ex situ* at the Pt L_3 and the Co K edges, which allows reconstructing the fine structure of the catalysts. Figure III-4 presents the normalized X-ray absorption near edge structure (XANES) spectra of the catalysts recorded at the Pt L_3 (Figure III-4.A) and at the Co K edges (Figure III-4.B). The absorption edge E_0 of each sample is defined as the energy at which the second derivative of the XANES spectrum equals zero (the first observed maximum of the first derivative). In the bottom part of the figures are shown the derivatives of the XANES spectrum as a function of the energy, which is more useful to comment the shifts of the absorption peaks (Figure III-4.B and D for the Pt L_3 and Co K edges respectively). Figure III-4 shows no change of the oxidation state of the platinum atoms from one sample to another, in agreement with the observations of Wang *et al*. [34]. The position of the absorption edge for both catalysts is the same than for the Pt foil, E_0 = 11563 eV. The intensity of the white line is smaller for the Pt_3Co-skin than for the Pt_3Co-skeleton catalyst, indicating a reduced amount of platinum oxides in the former structure. However, both alloyed structures are very close to that of the reference Pt foil. The differences between the Pt_3Co-skin and the Pt_3Co-skeleton nanocatalysts are more marked at the Co edge. Although no edge energy shift (same absorption edge E_0 = 7720 eV on the Pt_3Co/C samples and the Co foil) is monitored, there are great changes of the spectrum features, which can be rationalized by a change of the cobalt atomic arrangement in the nanoparticle, when comparing both Pt_3Co/C samples to the Co foil (the Co foil has an hexagonal compact structure, the Pt foil and the Pt_3Co nanoparticles a face centred cubic one), but also when comparing the Pt_3Co-skin to the Pt_3Co-skeleton, similar as in Reference [34]. A higher white line intensity was observed for the skin catalyst, contrary to what was evidenced in [34], for which the authors argued that a small amount of NiO exists underlying the highly corrugated Pt surface morphology in the skeleton catalyst, whereas subsurface Ni in the skin catalyst is well protected [34]. As we will further see from the EXAFS measurements, cobalt atoms do neither have oxygen neighbouring atoms in the skeleton nor in the skin structures.

Similar as for the XRD measurements (Figure III-3), the XANES spectrum of the Pt_3Co/C perfectly superposes with the spectrum of the Pt_3Co/C-skin. This indicates that the atomic arrangements are very similar in the commercial Pt_3Co/C and the Pt_3Co/C-skin catalysts.

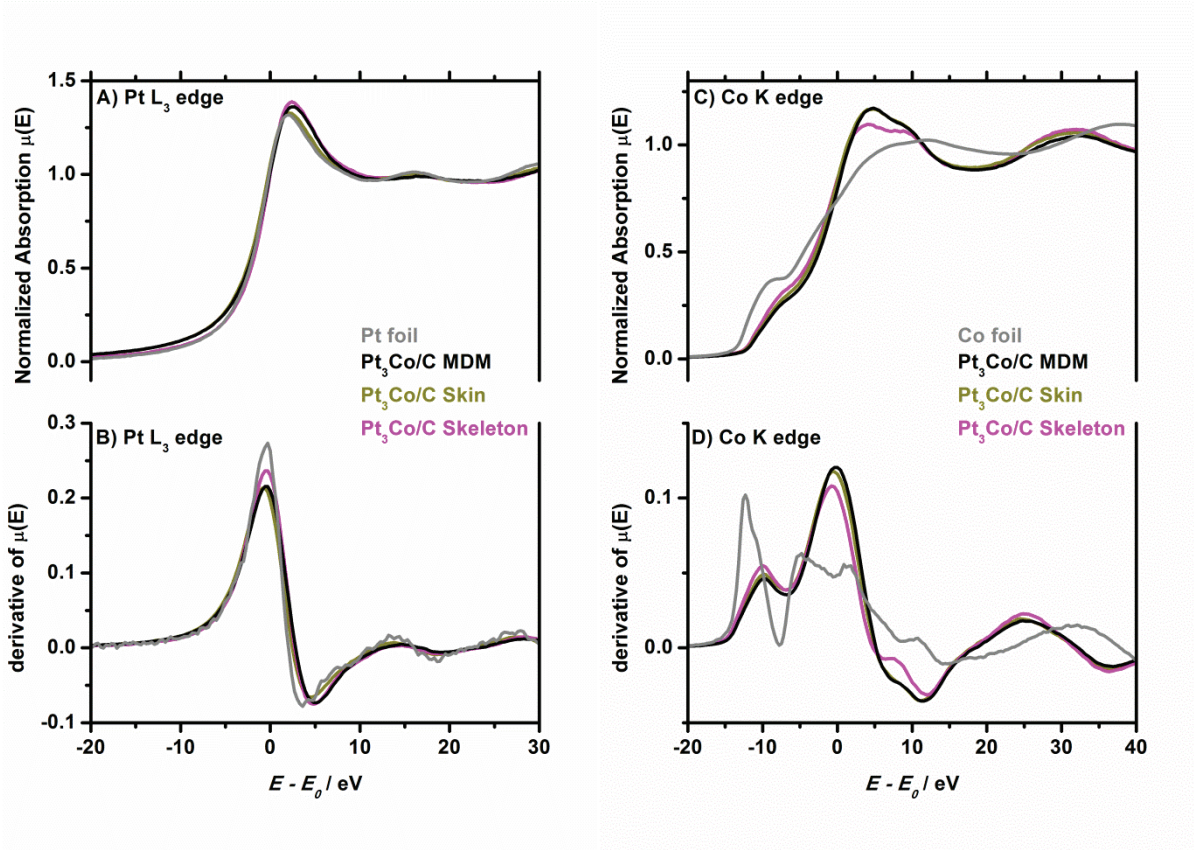

Figure III-4. XANES spectrum of the Pt_3Co/C MDM (in black), the Pt_3Co/C skeleton (in khaki) and the Pt_3Co/C skin (magenta) catalysts recorded at the (A) Pt L_3 and (B) Co K edges. The 0 on the X-axis corresponds to the absorption edge energy of the respective absorbing element E_0. The spectra recorded with Pt and Co foils are shown for comparison (in grey). The derivatives of the XANES spectra are shown in B and D for the Pt L_3 and Co K edges, respectively.

3. Extended X-ray absorption fine structure measurements

We now focus on the EXAFS spectra measured on the three different catalysts. Figure III-5 displays the k^2 weighted EXAFS spectra (k is the wave vector) recorded at the Pt L_3 (Figure III-5A) and at the Co K (Figure III-5B) edges. The EXAFS spectra have been all fitted within the same k-range window (3.5 $Å^{-1} \leq k \leq 11$ $Å^{-1}$). The minimal and maximal values of k were chosen as follows: below k = 3.5, the signals contained too much information from the XANES part of the spectra and, above k = 11, the signals were too noisy. The corresponding Fourier transforms (FT) of the k^2-weighted EXAFS oscillations measured at the Pt L_3 and Co K edges are shown in Figure III-6. The

first shell corresponds to the peaks with radial coordinates comprised between about 1 and 3 Å. The structural parameters extracted from the fitting of these oscillations are separated into the contribution of the several A – B interaction shells, A being the absorbing atom (here Pt or Co) and B the scattering atom (Pt, Co or O). Table III-2 shows structural parameters extracted such as *N* the number of A - B nearest-neighbours, *R* the A – B mean distance, and σ^2 the Debye-Waller factor that delivers information about the ordering of the crystallographic structure from the "absorbing atom point of view".

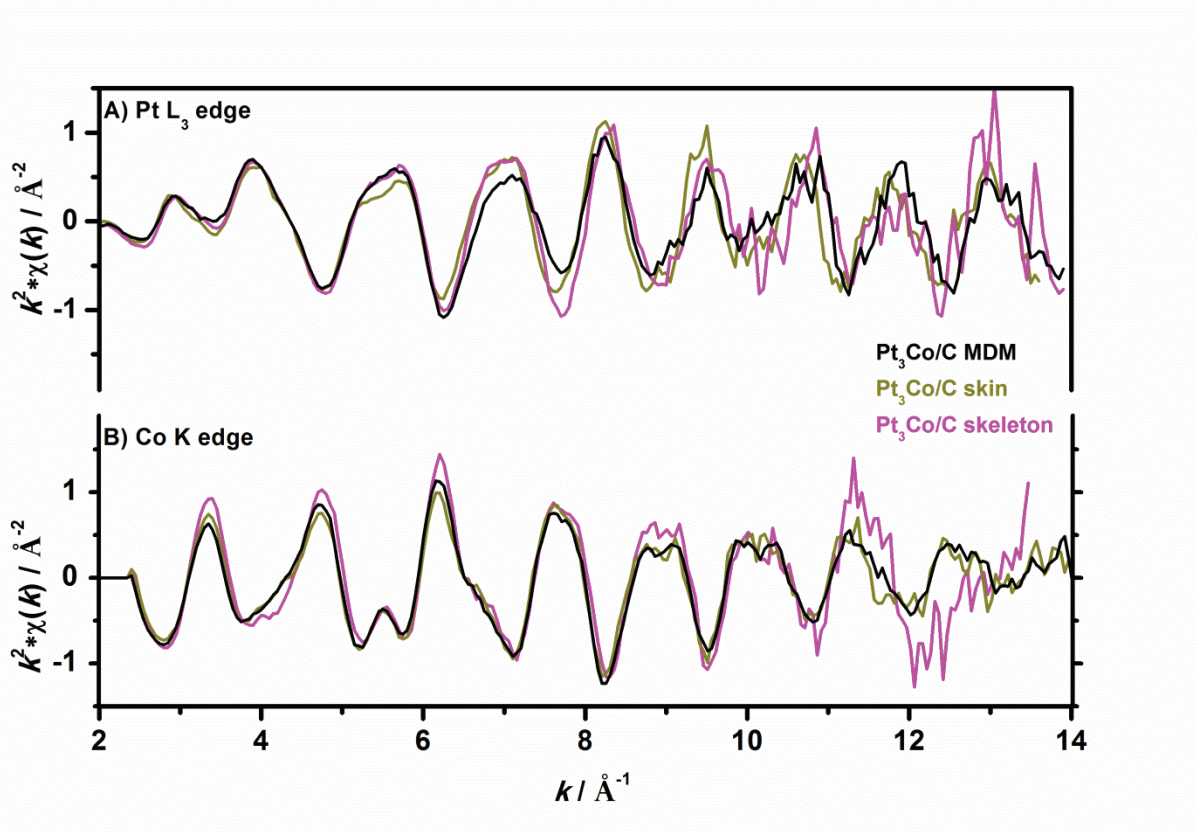

Figure III-5. k^2 weighted EXAFS spectra of the Pt_3Co/C MDM (in black), the Pt_3Co/C skeleton (in purple) and the Pt_3Co/C skin (in khaki) catalysts recorded ex situ at the (A) Pt L_3 and (B) Co K edges.

For the Pt_3Co/C-skeleton, the values of the average first shell coordination number for a platinum atom ($N_{Pt} = N_{Pt\text{-}Pt} + N_{Pt-Co}$)† and cobalt atom ($N_{Co} = N_{Co\text{-}Pt} + N_{Co-Co}$) are very close: N_{Pt} = 9.5 ± 1.0 *vs.* N_{Co} = 9.5 ± 0.9. Those numbers are less than the expected value of 12 for a bulk face centred cubic structure but can easily be rationalized by considering the nanometric dimension of the catalysts. Indeed, these coordination numbers equate to a mean particle of *ca.* 3-4 nm [44], in agreement with what was measured by XRD and TEM (Table III-1). Indeed, the fraction of low coordinated atoms (located at the surface) to the total number of atoms increases with a decrease of the Pt_3Co/C particle size. For example, considering a 3.9 nm f.c.c. particle with cuboctahedral shape, 812 of the 2869 atoms are located at the surface (≈ 30%) [45]. The fact that similar values N_{Pt} and N_{Co} are

† $N_{A\text{-}B}$ being the number of closest A – B neighbors

found indicates that the platinum and the cobalt atoms are randomly and homogeneously distributed within the Pt_3Co/C-skeleton structure (same ratio of surface to bulk atoms for cobalt and platinum). However, considering the accuracy of the measurement, such values do not discard the possibility that a monolayer of pure platinum atoms exists at the extreme surface layer of the Pt_3Co/C-skeleton nanoparticles.

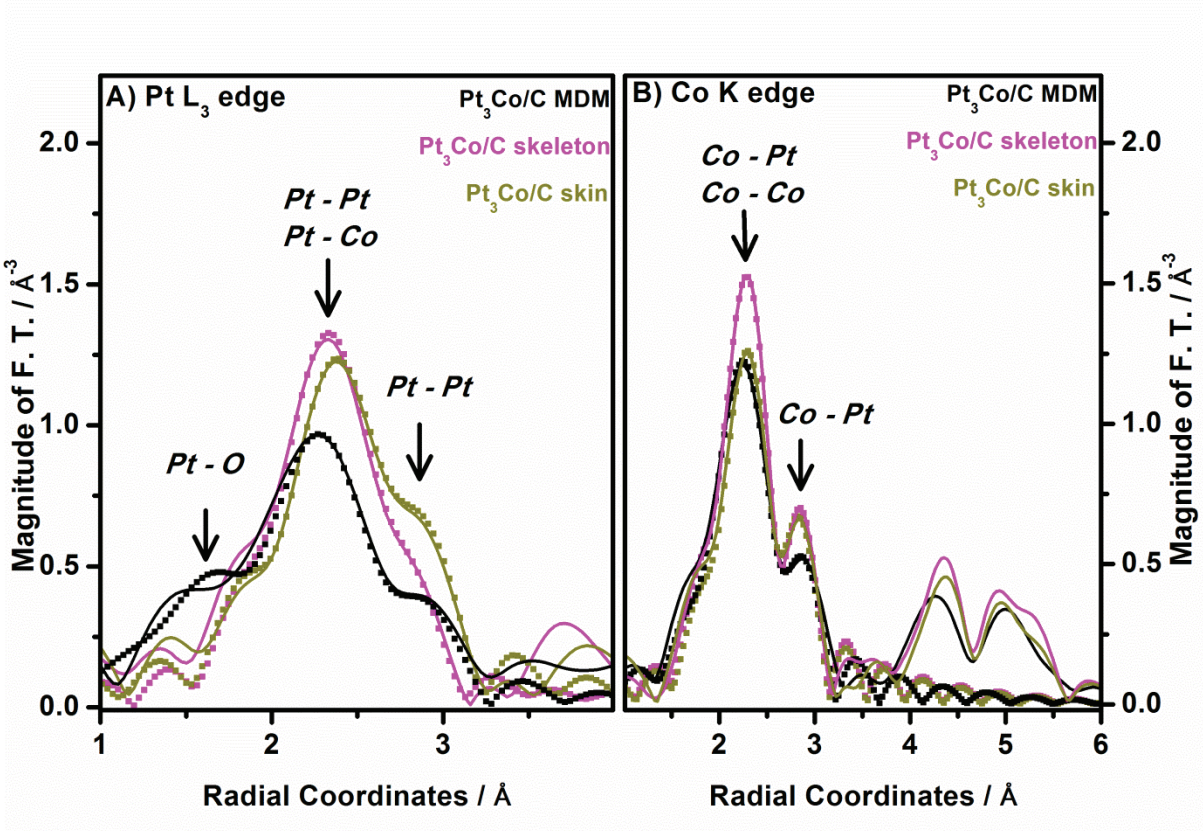

Figure III-6. Fourier Transform magnitudes of $k^2\chi$ (k) EXAFS spectra at (A) the Pt L_3 and (B) the Co K edges for the Pt_3Co/C MDM (in black), the Pt_3Co/C-skeleton (in purple) and the Pt_3Co/C-skin (in khaki) catalysts. The full lines are the experimental data and the dotted lines are the fitted data.

The results obtained for the Pt_3Co/C-skin catalyst differ slightly. The average first shell coordination numbers differ, whether the Pt or Co atomic environment is considered: N_{Pt} = 11.1 ± 1.1 and N_{Co} = 7.4 ± 0.7. Similar observations ($N_{Pt} > N_{Co}$) were derived from the EXAFS analysis on annealed Pt_3Co/C particles by Lai *et al* [46, 47] and on annealed Pd-Co nanoparticles by Kim *et al.* [48]. The lower coordination numbers at the Co edge for the skin with respect to the skeleton structure is confirmed qualitatively when looking at the second shell of neighbours (Figure III-6B). According to Greco *et al*. [49], modifications of the cobalt atoms coordination number (whereas platinum remains unaffected by the thermal treatment) can be accounted for by considering that the EXAFS signals for the Co atoms are extremely sensitive to substitutional disorder, so their intensities can be used as a measurement of the ordering level. Interestingly, the Debye-Waller values (Table III-2) also indicate

that the Co local structure is more disordered (larger Debye-Waller values) than the Pt local structure (smaller Debye-Waller values), which may confirm the hypothesis of Greco *et al*. [49]. In this frame, the smaller cobalt average coordination number observed might sign different structures adopted by the Pt_3Co/C-skin catalyst. For example, it may indicate that (i) cobalt atoms could have segregated toward the surface of the nanoparticle during the annealing procedure, as suggested by Lai *et al*. [46] or (ii) a phase transition from a face centred cubic (lattice constants $a = b = c$ and angles $\alpha = \beta = \gamma = 90°$) to a face centred tetragonal ($a = b \neq c$ and $\alpha = \beta = \gamma = 90°$) crystal structure could have occurred upon annealing, as suggested by Park *et al.* [50]. Such phase transition was also observed by Schulenburg *et al*. [51], but for higher annealing temperatures ($T > 873$ K) than the one used in the preparation of our Pt_3Co/C-skin catalyst. The first scenario is in contradiction with theory and experiments [6, 35]. Regarding the second, a distortion of the lattice crystal induces a decrease of the number of the first closest neighbours, but platinum should have also been impacted by a phase transition, which is experimentally discarded when looking at the value of N_{Pt}. In this case, a lattice mismatch between the Pt-Co core and the pure Pt phase might also explain a decrease of the number of closest neighbours for the atoms located on the top of the core and directly underlying the pure Pt skin surface. Indeed, as the chemical treatment performed to obtain the Pt_3Co-skeleton generates numerous surface vacancies, the thermal treatment, which induces the surface segregation of Pt atoms, might induces a flux of these surface vacancies from the surface to the core, in order to counter balance the flux of Pt atoms. However, this hypothesis could not have been verified in the time-frame of this thesis.

The first-shell interatomic distances estimated from the analyses of EXAFS spectra (Pt-Pt, Pt-Co and Co-Pt but not Co-Co) are found to be less contracted by 1 % in the skin than in the skeleton structure. The fact that the Co-Co bond length remains unaffected by the thermal treatment in the skin catalyst may be an indirect proof that the Co atoms are located in the core of the nanoparticle after the heat treatment (the Co rich core would remain unaffected by the relaxed Pt rich skin surface). It is also interesting to compare the value of the interatomic distances calculated by XRD (Table III-1) and those calculated by EXAFS (Table III-2). The value found by XRD matches the Pt-Pt distance found by EXAFS but is greater than the other interatomic distances (Pt-Co, Co-Pt and Co-Co) by 1 to 4%. Similar effect has been observed but rarely commented in the literature on Pt-alloy nanoparticles with high Pt atomic content of *ca.* ≈75 at. % [31, 52]. The interatomic distances found by XRD are larger than those calculated from the fitting of the XAS signals on Pt-alloy nanoparticles with low Pt atomic content (<50 at. %) [10, 53]. In comparison, the interatomic distances estimated by XRD and XAS agree in the case of pure Pt/C nanoparticles [10]. It is therefore reasonable to wonder if XRD, which is currently the most commonly used technique to measure lattice parameters and further build Volcano plot bridging the activity of faradic reaction to the interatomic distance of a catalyst is the most

appropriate technique to use when working with alloy nanoparticles that can display local heterogeneities of chemical composition/structure.

Interestingly, the structural parameters derived from the analysis of the EXAFS signals on the Pt_3Co/C MDM (Table III-2) are essentially similar to those found on the Pt_3Co/C skin catalyst. From the reasoning on the average coordination number (with $N_{Pt} = 9.9 \pm 0.8$ *vs.* $N_{Co} = 6.9 \pm 0.8$) and the relaxed Pt-Pt bond length, it seems reasonable to think that the Pt_3Co/C MDM catalyst has a core/shell structure, with a Pt-rich shell and a Co-rich core. However, the surface structure (where belong most of the Pt-Pt pairs) is slightly less relaxed than in the Pt_3Co/C-skin while the inner core structure (where belong all the Co-Co pairs) is much more contracted, close to the structural parameters of a pure Co phase ($d_{Co-Co} = 0.257$ nm). These differences might arise from different synthesis routes between these two catalysts or differences in the thermal annealing procedure (duration, temperature).

Summing up, in what follows, it will be considered that the fresh Pt_3Co/C MDM catalyst has a structure similar to that found for the Pt_3Co/C-skin catalyst. We will then comment the degradations of this catalyst in the light of the results found in the literature about core/shell platinum alloy catalysts.

catalyst	Shell	*N*	*R* / Å	σ^2 (x10^{-3}) / Å^2	ΔE_0 / eV	*R*-factor
Pt_3Co/C-skeleton	Pt-Pt	5.8 ± 0.6	2.70 ± 0.01	4.4 ± 1.3	3.7 ± 0.6	0.00520
	Pt-Co	3.7 ± 0.4	2.65 ± 0.01	9.3 ± 1.9	6.3 ± 0.7	0.00520
	Co-Pt	5.1 ± 0.5	2.66 ± 0.01	4.6 ± 0.1	6.5 ± 0.1	0.00003
	Co-Co	4.4 ± 0.4	2.63 ± 0.01	15 ± 0.4	4.4 ± 0.2	0.00003
Pt_3Co/C-skin	Pt-Pt	8.4 ± 0.8	2.73 ± 0.01	4.5 ± 0.6	5.1 ± 0.6	0.00089
	Pt-Co	2.7 ± 0.3	2.68 ± 0.01	15 ± 0.2	8.4 ± 2.4	0.00089
	Co-Pt	4.7 ± 0.4	2.67 ± 0.01	4.5 ± 0.4	5.9 ± 0.4	0.00127
	Co-Co	2.7 ± 0.3	2.63 ± 0.01	14.5 ± 0.8	3.7 ± 1.3	0.00127
Pt_3Co/C MDM	Pt-Pt	5.3 ± 0.4	2.72 ± 0.01	5.0 ± 0.9	6.5 ± 0.8	0.0019
	Pt-Co	3.2 ± 0.2	2.65 ± 0.01	9.5 ± 0.2	7.2 ± 1.3	0.0019
	Pt-O	1.4 ±0.2	2.01 ± 0.02	4.1 ± 5	14 ± 2	0.0019
	Co-Pt	3.8 ± 0.4	2.67 ± 0.01	3.6 ± 0.6	5.1 ± 0.7	0.0079
	Co-Co	3.1 ± 0.4	2.59 ± 0.01	13 ± 1	-0.7 ± 1.2	0.0079

Table III-2. Structural and electronic parameters estimated on the Pt_3Co/C MDM, the Pt_3Co/C skeleton and the Pt_3Co/C skin catalysts from the analysis of the EXAFS signals. The R-factor indicates the quality of the fit from which the data reported in this table are extracted.

III. Evolution of the structure-activity relationship for Pt_3Co/C cathode catalysts upon aging

1. Evolution of the stack performance upon aging

Figure III-7 presents the output cell voltage ΔE_{cell} recorded in the course of the three PEMFC tests realized in this work. ΔE_{cell} comprises the following contributions:

$$\Delta E_{cell} = E_{cathode} - E_{anode} = \Delta E_{eq} - |\eta_{anode}| - |\eta_{cathode}| - \eta_{ohmic} \quad \text{Eq. III-1}$$

where $E_{cathode}$ (respectively E_{anode}) is the potential of the cathode (respectively anode); ΔE_{eq} is the equilibrium voltage; $|\eta_{anode}|$ and $|\eta_{cathode}|$ represent the anodic and cathodic overpotentials, respectively and η_{ohmic} is the sum of the ohmic losses due to the resistance of the proton-exchange membrane (PEM), the catalytic layer (CL), the gas-diffusion layers (GDL) and the contact resistance between the GDL and the flow-field plates. Since the anodic overpotential is small due to the fast kinetics of the hydrogen oxidation reaction (pure hydrogen was fed to the PEMFC stack) and the fast hydrogen mass-transport within the anode, and since the anodic catalyst undergoes no major degradation under operation, the term $|\eta_{anode}|$ is considered to be negligible and constant during the aging procedure [54]. Moreover, since all the MEA components undergo no major degradation at the micro-scale level *i.e.* no thinning of the proton-exchange membrane, the catalyst layers and the GDL due to carbon corrosion (see below), the ohmic losses are believed to be constant during PEMFC operation. Therefore, the variations of the potential of the cathode are believed to follow, in first approximation, those of the average cell voltage: it is thus assumed that the average cathode potential during PEMFC operation varies as $E_{cathode,\ 20\ A\text{-}stat} > E_{cathode,\ 50\ A\text{-}start/stop} > E_{cathode,\ 50\ A\text{-}stat}$ (Figure III-7). As we will see, this assumption is crucial to understand the structural and compositional changes of the Pt_3Co/C nanoparticles over time.

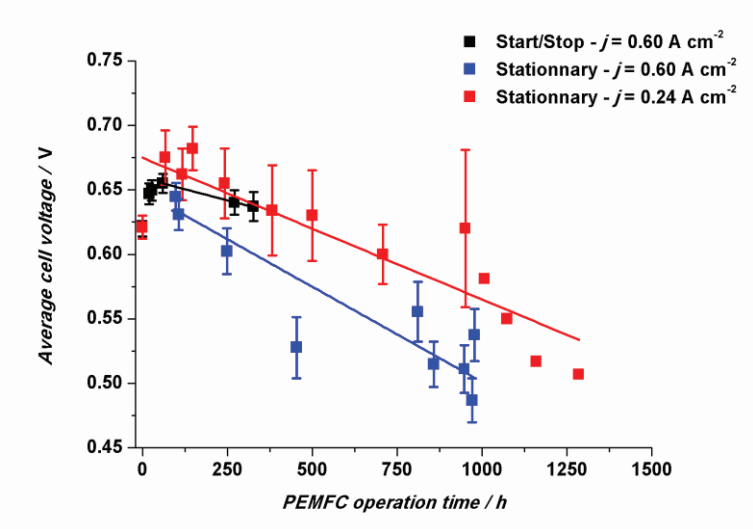

Figure III-7. Output potential difference averaged over 6 cells for the different PEMFC tests as a function of the operation time. Error bars represent the standard deviation. For the test performed at I = 20 A (j = 0.24 A cm^{-2}), only the output cell potential of a single cell was measured after t > 1007 h.

It is interesting to note that the MEAs reach their best electrical performance after $t > 50$ h, which may indicate an incomplete conditioning of the MEA. For longer operation durations, the cell voltage decays at a rate of approximately 130 μV h^{-1} for MEAs operated in constant current load of 0.24 and 0.60 A cm^{-2}. In the start-stop mode, the performance decay is 65 μV h^{-1} over the 327 hours of operation time (disregarding the 327 hours of stop). The performance decay observed in this work agrees with the observations of Xie *et al.* (54 μV h^{-1} under operation at $j = 1.07$ A cm^{-2} with a Pt_3Cr/C cathode catalyst [55]) and Gasteiger *et al.* (60 μV h^{-1} under operation at $j = 0.20$ A cm^{-2} with a multiply leached Pt_3Co/C cathode catalyst [12]) under similar operating conditions. Interestingly, the cell voltage decay is greater for stationary operation mode with respect to intermittent operation mode, the latter being subjected to frequent gas purges. The observed performance decay and the differences between stationary and start/stop aging procedures point towards a beneficial effect of the gas purging in agreement with the observations of Lee *et al.* [56] and indirectly evidence that a large part of the observed voltage degradation is reversible in the constant current tests. This is confirmed by the non-negligible increase of performances after sampling of MEA (Figure III-7). These decays also sign an increase in the ORR overpotential $|\eta_{cathode}|$ over time and so a degradation (loss of catalytic activity) of the Pt-based cathode catalysts.

2. Structural evolution of the cathode catalytic layer upon aging

a. At the micrometer scale

Figure III-8 displays representative FEG-SEM images of the MEAs in their initial state and after $t = 1124$ h of aging at $I = 50$ A. The anode and the cathode have similar thicknesses but can be distinguished in the backscattered electron mode, due to the higher metal loading of the cathode. Operating the PEMFC for $t = 1124$ h does not induce major variations in the thickness of the CLs. In particular, no cracks or cavities are observed, at variance with previous studies on pure Pt/C or Pt_2CoCr/C-based electrodes operated in intermittent [57, 58] or stationary [55] mode, respectively. This result holds true for all the other aged MEAs. Under higher magnification, as observed previously with Pt/C-based cathodes [57, 59-61], metal nanoparticles are detected within the PEM, the density and size distribution of which depend on the distance from the cathode. X-EDS analyses performed locally on the PEM showed that those particles are pure Pt, evidencing that, whereas both Pt and Co elements are corroded from the cathode CL, only Pt can deposit in the PEM following reduction by crossover H_2.

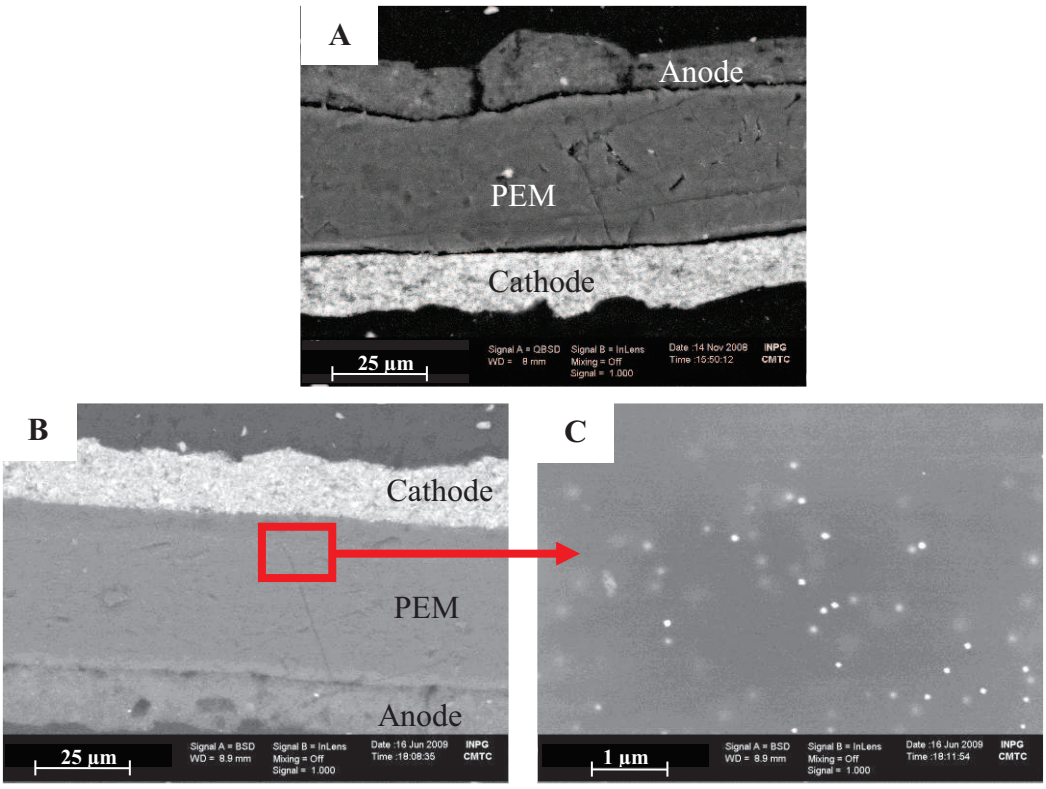

Figure III-8. FEG-SEM images of the (a) fresh MEA and the aged MEA operated for t = 1124 h at I = 50 A in stationary conditions: (b) whole MEA located in the cathode inlet with a special focus (c) in the PEM region facing the cathode.

b. At the nanometre scale

Figure III-9 presents the particle size distribution (PSD), determined from TEM observations, of the cathode catalyst in its native form, after conditioning and after different life stages in various operating conditions. From the particle size distributions, the number, surface and volume-averaged mean particle diameter were calculated (Table III-3). PEMFC operation yields (i) the decrease of the fraction of the smallest nanoparticles, (ii) the increase of the mean particle size and (iii) a significant tailing on the large diameter side of the histogram. These features indicate that, similar than for a Pt/C catalyst [59, 62, 63], 3D electrochemical Ostwald ripening governs the coarsening of the cathodic Pt_3Co/C electrocatalyst. 3D electrochemical Ostwald ripening involves:

i. Preferential dissolution of the smallest nanoparticles (larger Gibbs–Thomson energies).

ii. Formation and redistribution of Pt^{z+} and Co^{y+} ionic species within the cathode CL (discussed in **Chapter V**).

iii. Electrochemical redeposition of Pt^{z+} ions onto the surface of the largest crystallites or chemical reduction by H_2 coming from the anode of the Pt^{z+} ions in the polymer phase (membrane or ionomer) that lead to the formation of the so called Pt-band in the PEM. SEM observations of the fresh/aged MEA confirm the presence of the Pt crystallites in the PEM [64-66]. Conversely, Co^{y+} ionic species can neither be reduced by H_2 in the PEM nor by the electrochemical potential in the catalytic layer. The formation of alloyed Pt-Co particles in the PEM is also thermodynamically unfavourable because the enthalpy of mixing of Pt–Co alloys is low (~ -10 kJ mol^{-1}, see [26]). The influence of Co^{y+} ionic species released by the corrosion of the fresh Pt_3Co/C material on the ORR kinetics will be discussed in **Chapter V**.

Faster PSD broadening (Table III-3) are monitored in intermittent relative to stationary operations, indicating that the extent of degradation of the cathode CL is more pronounced when high/low cathode potentials alternate during start-up/shut-down of the fuel cell, in agreement with the observations of Haas and Davis [67].

A consequence of the increase of the mean particle size is a decrease of the electrochemical surface area (ECSA) of the catalyst. From an electrocatalytic viewpoint, an increase of the mean particle size can lead to a decrease of the mass activity (in A g^{-1}_{Pt}) for the ORR because larger nanoparticles exhibit lower ratio between the number of surface / bulk atoms, meaning that fewer platinum atoms can act as catalytic sites [68]. These two reasons, namely the continuous loss of ECSA and mass activity, qualitatively explain why the ORR overpotentential $|\eta_{cathode}|$ is increasing and the PEMFC performances are decreasing during operation (Figure III-7).

The decreased ECSA over time indicates that Pt_3Co/C catalysts suffer the same durability issues as Pt/C catalysts. This agrees with other results obtained from accelerated ageing tests with either solid [26] or liquid electrolyte [69]. In particular, a recent Identical Location (IL)-TEM study coupled to electrochemical measurements shows that the ECSA of Pt/C and Pt_3Co/C catalysts having initially the same crystallite size and identical carbon supports is decreasing at the same rate, suggesting no beneficial effect of alloying cobalt atoms on the stability of Pt-based nanoparticles [70].

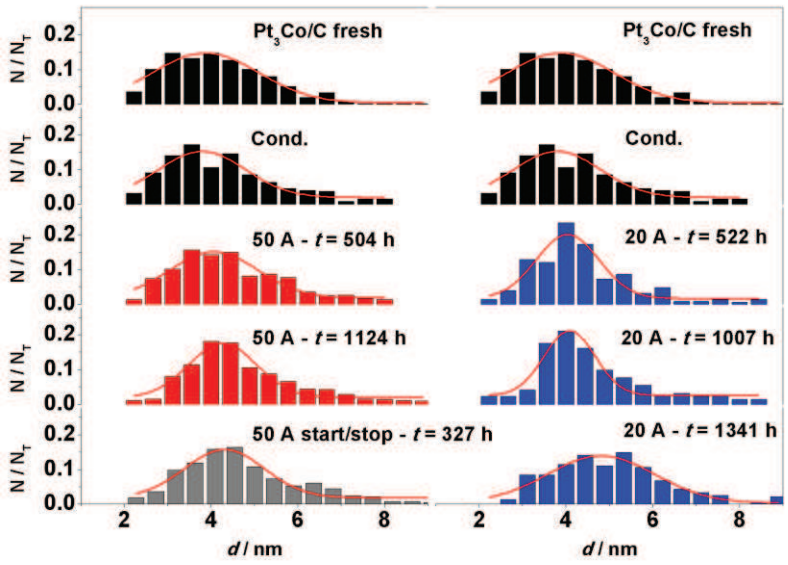

Figure III-9. Particle size distributions of the fresh/aged cathode electrocatalysts after PEMFC operation at constant current density 50 A (j = 0.60 A cm^{-2}), 20 A (j = 0.24 A cm^{-2}) or in start/stop conditions (1 h at j = 0.60 A cm^{-2} /1 h of stop). 400 individual particles (not agglomerated) were measured in each case.

	Fresh	Cond.	50 A		50 A S/S	20 A stat.		
	0 h	17 h	504 h	1124 h	327 h	522	1007	1341
$\bar{d}_N$ / nm	4.2	4.3	4.5	4.7	4.7	4.4	4.6	5.0
$\bar{d}_S$ / nm	4.8	5.1	5.2	5.5	5.5	5.0	5.3	5.7
$\bar{d}_V$ / nm	5.3	5.5	5.5	5.9	5.9	5.4	5.8	6.0
at. % Co (X-	26	24	20	15	24	16	17	14
at. % Co (XRD)	20	18.5	17.5	15	15	16.5	16.5	13 to
at. % Co (ICP)	26.5	20	19	17.5	17.5	19.5	18	---

Table III-3. Physical characteristics of the fresh/aged electrocatalysts: number-averaged $\bar{d}_N$, surface-averaged $\bar{d}_S$ and volume-averaged $\bar{d}_V$ mean particle size and Co atomic percentage evaluated by X-EDS, XRD and ICP-AES.

3. Variation in the chemical composition of Pt_3Co/C particles upon aging

Figure III-10 shows the X-ray diffraction patterns of the fresh/aged cathode catalysts and of a commercial 40 wt. % Pt/Vulcan XC72 (E-TEK) for comparison. The diffraction peaks of the aged catalysts are shifted toward smaller 2θ angles, signing expansion of the lattice parameter of the aged catalysts over time. In Figure III-11, the atomic percentage of Co estimated by ICP-AES and XRD measurements are plotted as a function of different ageing conditions and for different durations. Figure III-11 and Table III-3 show that in all PEMFC operating conditions, the Co atoms are

continuously depleted from the fresh Pt_3Co/C electrocatalyst over time, in agreement with the STM and ICP-OES measurements of Xu *et al*. [71]. The Co atomic content calculated from the shift of the XRD peaks agree with that found by X-EDS and ICP-AES analyses suggesting that the decrease of the lattice contraction may be attributed to the decrease of the cobalt content on the aged nanoparticles, and that most of the Co is indeed present in crystallized phases.

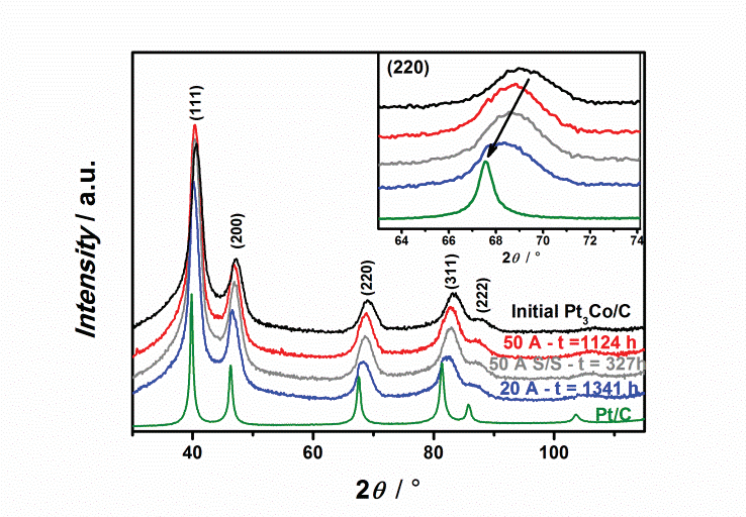

Figure III-10. XRD patterns of the fresh/aged cathode electrocatalysts and of a reference Pt/C catalyst. The inset in A is a zoom on the (220) diffraction peak of each catalyst.

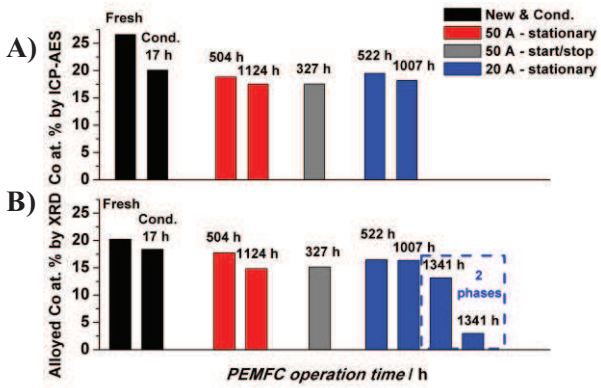

Figure III-11. Compositional changes of the cathode catalyst probed (A) by ICP-AES, giving information on the total Co at. % of the catalytic layer, and (B) by XRD (assuming that Vegard's law applies to Pt-Co solid solutions) providing the fraction of Co alloyed to Pt

Interestingly, the rate of Co depletion is nearly identical for the first 1000 hours of operation at low/high current density. However, after t = 1341 h of operation at a constant load of 20 A, the laboratory X-ray diffraction peaks cannot be fitted by a single composition any more but multiple Pt:Co stoichiometries are detected with a Co content varying from 13 to less than 3 at%. It is also worth mentioning that the Co losses are more pronounced in intermittent relative to stationary operation, confirming the results of the previous section. These results suggest that the cathode

catalyst may age heterogeneously during PEMFC operation (which may be induced by imperfect catalyst utilization in the catalyst layer as it will be discussed in **Chapter IV**).

4. Variation in the fine structure of Pt_3Co/C particles upon aging

a. HRSTEM-HAADF analyses on the aged Pt_3Co/C catalysts

HRSTEM-HAADF observations were performed to unveil the structural/ chemical changes of the Pt-Co/C nanoparticles during PEMFC operation. In this imaging mode, the image intensity (I) of an atomic column is in first approximation, proportional to the product of the number (B) of atoms in the column and the square of the average atomic number Z of the atoms constituting the column:

$$I = k\, B\, Z^{\alpha} \qquad \text{Eq. III-2}$$

where k is a fixed coefficient and $\alpha \sim 1.8 - 2$. Figure III-12A shows a typical aberration-corrected HAADF image of the fresh Pt_3Co/C electrocatalyst. The intensity variations of neighbouring atomic columns indicate that the Pt_3Co structure is chemically disordered (solid solution), which is consistent with a classical description of a Pt_3Co/C alloy nanoparticle. No changes of contrast are detectable from the core to the shell, indicating that Pt and Co atoms are homogeneously disordered within the particle. A core/shell structure, even if present, is difficult to quantify because of the large changes of the nanoparticle thickness close to their border.

The Co composition of this individual particle is close to 30 at. % (Figure III-12B), slightly higher than what was obtained with XRD or ICP-AES measurements (Figure III-10). Figure III-13A shows another particle of the fresh electrocatalyst having a cobalt content close to 20 at. %. In Figure III-13C, the experimental normalized intensity variations in the HAADF image taken across a diameter are compared to the theoretical profile obtained on a spherical homogeneous particle. The theoretical intensity variations result from the variation of the thickness of the sphere along its diameter and not from a variation in chemical composition of the alloy. The agreement between theoretical and experimental profiles indicates that Pt and Co atoms are indeed homogeneously and randomly distributed in the fresh Pt_3Co/C nanoparticle. The experimental profile of the fresh Pt_3Co/C catalyst (Figure III-13C) confirms that the pure Pt surface cannot be distinguished from the Pt-Co core. A better atomic resolution might have been obtained with STEM measurements coupled to energy electron loss spectroscopy (EELS) [27, 33] and would have allowed to calculate the thickness of the Pt shell created during the annealing treatment.

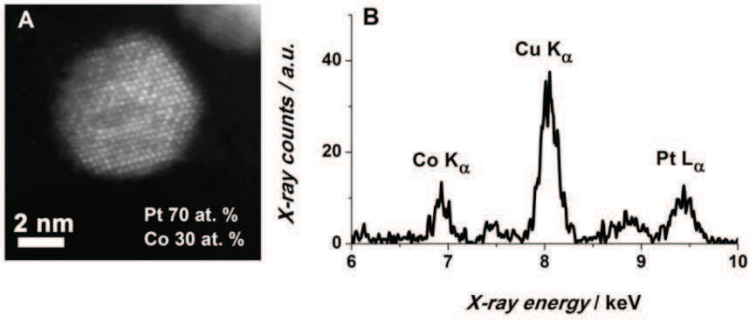

Figure III-12. (A) Aberration-corrected HAADF image of a fresh Pt_3Co/C nanoparticle and (B) the corresponding X-EDS spectrum. The averaged Pt and Co at. % are indicated in (A). The copper signal arises from the copper grid, where the catalyst is deposited for STEM measurements.

Figure III-13B presents a STEM-HAADF image of the Pt_3Co/C electrocatalyst aged for t = 1124 h at I = 50 A. The X-EDS analysis on this particle indicates a Co composition of 7 at. %, slightly lower than what was measured by XRD and ICP-AES (Figure III-10). The comparison between the experimental and the calculated HAADF intensity variations across this particle is presented in Figure III-13D. Interestingly, despite the strong decrease of the cobalt content during PEMFC operation, the agreement between the theoretical and experimental HAADF intensity profiles suggests that the distribution of the Pt and Co atoms of such particles remains homogeneous.

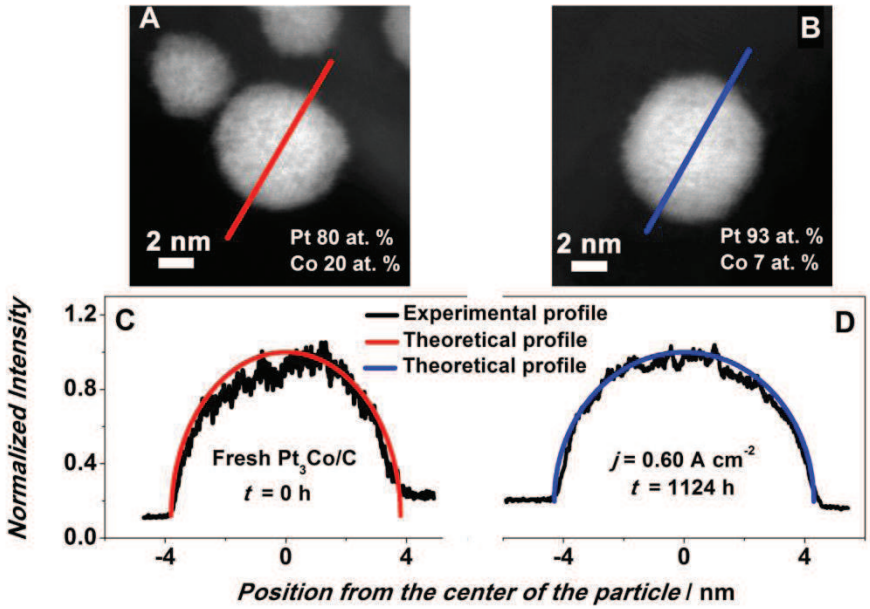

Figure III-13. Aberration-corrected HAADF images of Pt-Co/C nanoparticles (A) before and (B) after operation at 50 A (j = 0.60 A cm^{-2}) for t = 1124 h. The Pt and Co at. % are indicated at the bottom right-hand side of the images. (C) and (D) are normalized HAADF intensity variations of

the particles selected in (A) and (B). The black/coloured curves stand for the experimental/ theoretical intensity profiles, respectively and assume a spherical shape. The image intensity across the particles was measured with Digital Micrograph.

Figure III-14.A shows a typical HAADF image of the Pt-Co/C electrocatalyst aged for t = 327 h under start/stop conditions. Two types of particles coexist: (i) some particles presenting a bright shell covering a darker core, generally with a great difference in intensity between them, suggesting a core/shell structure and (ii) other particles appearing homogeneously contrasted, similar to what was found for the catalyst aged at I = 50 A (see Figure III-13). In order to gain more insights into the chemical structure of the first type of particles cited, we compared the HAADF intensity variations across the particle diameter with different theoretical profiles calculated for: a homogeneous Pt_3Co particle (fit # 1), 8 atomic layers (2 nm) of Pt surrounding a Pt_3Co core particle (fit # 2), 8 atomic layers (2 nm) of Pt surrounding a Co core particle (fit # 3) and a Pt "hollow" particle (8 atomic layers of Pt over an empty core, fit # 4). Obviously, neither the theoretical profile of an homogeneous P3Co nanoparticle (fit # 1) nor that of a nanoparticle containing a Pt_3Co core (fit # 2) do fit the experimental profile. Figure III-14B shows that the best fit between the experimental and the theoretical HAADF intensity profiles is obtained when considering a Pt "hollow" nanoparticle (fit # 4) or a nanoparticle containing a pure Co core (fit # 3). However the last scenario can be discarded because the X-EDS spectrum recorded on this individual particle indicates a chemical composition in Pt of 100 at. %.

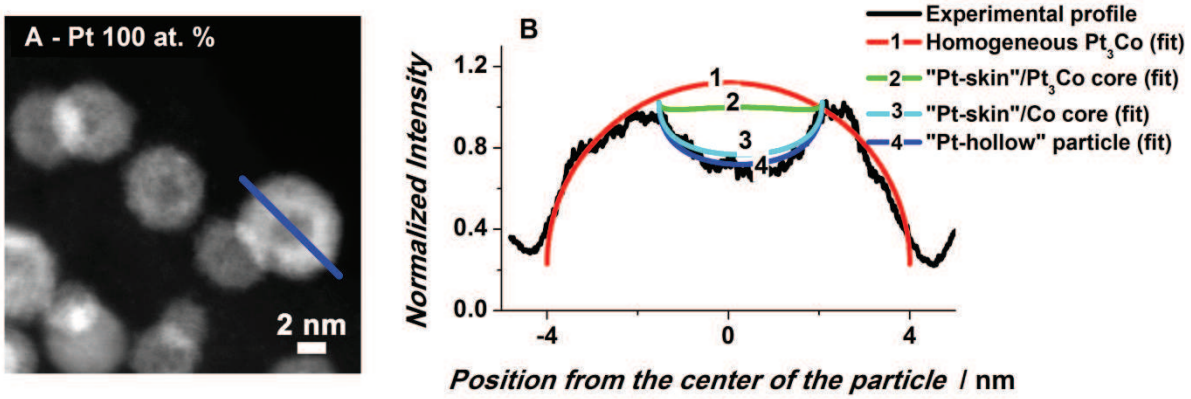

Figure III-14. (A) Aberration-corrected HAADF image of Pt-Co/C nanoparticles aged for t = 327 h in start/stop conditions (327 hours at j = 0.60 A cm^{-2} / 327 hours in stop conditions). (B) Normalized HAADF intensity variations across the particle selected in (A) and theoretical profiles for a homogeneous Pt_3Co particle (fit # 1 - red curve), for a "Pt-skin" /Pt_3Co core particle (fit # 2 - green curve), "Pt-skin" /Co core particle (fit # 3 - cyan curve) and for a "Pt-hollow" particle (fit # 4 - blue curve).

In Figure III-15A and C, we performed similar analyses on the sample aged for t = 1007 h under constant load I = 20 A. In this sample, many of the particles show a uniform contrast in HAADF

and possess a Co content varying between 0 and 10 at. % but, similar to what was found on the sample aged in start-stop conditions, many nanoparticles were found to have a core/shell contrast. Based on STEM-XEDS line-scan analyses along the diameter of individual nanoparticles, we found that the core/shell particles are either pure "Pt-hollow" particles or contain a very small Co at. % in their core (< 5 at. %). The line scan X-EDS analyses recorded at the centre and at the very edge of a particle do not show any Co in the shell, whereas less than 5 at. % of Co is detected in the centre of the nanoparticle (Figure III-15E). Figure III-15B shows a representative HAADF image of the cathode electrocatalyst after t = 1341 h of operation at I = 20 A. Clearly, the fraction of Pt "hollow" particles to the total number of particles greatly increased over time, confirming that the appearance of these structures may be correlated to the aging operation of the PEMFC. The Pt-hollow particles are spherically-shaped, compact with non-porous walls and possess a chemical composition close to 100 at. % Pt, indicating that the Co depletion is completed at the end-of-life of the sample (see Figure III-15F).

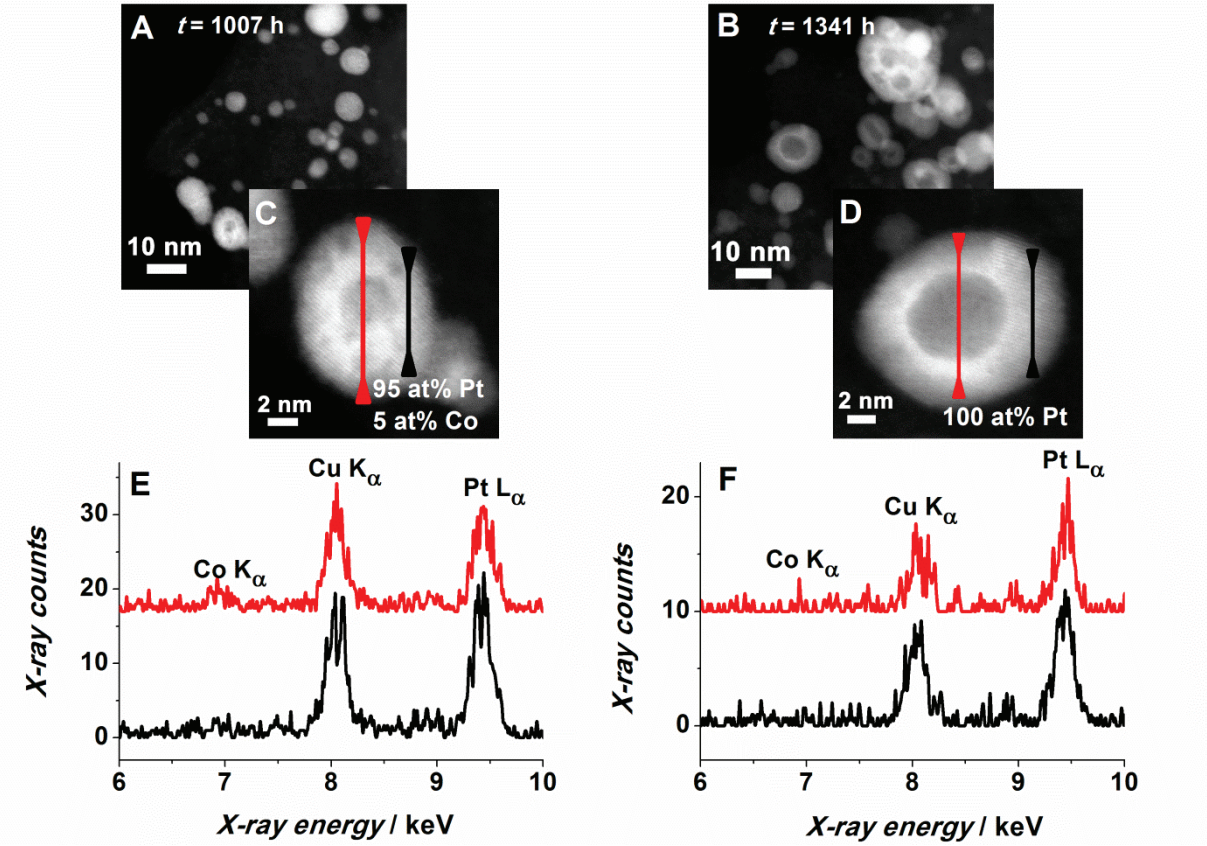

Figure III-15. (A, B) Aberration-corrected HAADF images of Pt-Co/C nanoparticles after operation at 20 A (j = 0.24 A cm^{-2}) for t = 1007 or 1341 h, respectively. (C, D) zoom on a single nanoparticle. The particle-averaged Pt and Co at. % are indicated at the bottom right-hand side of the images. (E, F) X-EDS spectra recorded at the centre and at the very edge of the particle imaged in (C, D) during a line-scan analysis. The lines in the images (C, D) indicate the locations of the

line-scan analysis. The copper signal arises from the copper grid where the catalyst is deposited during TEM measurements.

b. EXAFS analyses of the aged Pt_3Co/C catalysts

To get further insights into their fine nanostructure, the fresh/aged Pt_3Co/C cathode catalysts were also investigated with *ex situ* Synchrotron XAS at the European Synchrotron Radiation Facility. Similar as in the first part of the chapter, only the parameters derived from the fitting of the EXAFS oscillations will be discussed, and the XANES part of the spectra will be used to confirm qualitatively the obtained conclusions.

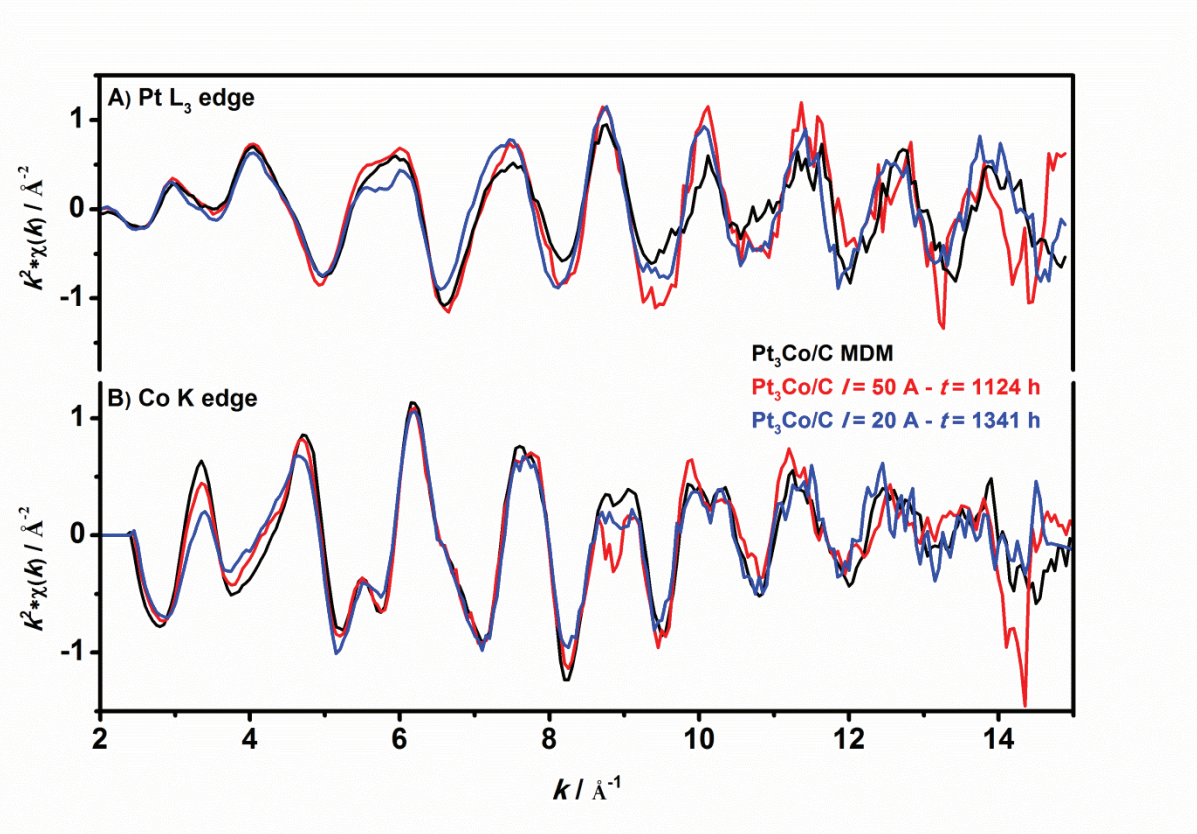

Figure III-16. k^2 weighted EXAFS spectra of the fresh Pt_3Co/C MDM (in black) and the aged catalysts having either homogeneous particles (in red, aged at I = 50 A for t = 1124h) or core-shell/hollow particles (in blue, aged at I = 20 A for t = 1341h) recorded ex situ at the (A) Pt L_3 and (B) Co K edges.

Figure III-16 and Figure III-17 show the k^2-weighted EXAFS and the Fourier transforms of the k^2-weighted EXAFS oscillations recorded on the fresh Pt_3Co/C MDM and on two aged catalysts (the catalyst after t = 1124 h of ageing at I = 50 A, which was found to be partially depleted in cobalt but kept a homogeneous distribution of the atoms (see Figure III-13), and the catalyst aged during t =

1341 h at I = 20 A, for which compact, depleted in Co and spherically shaped "hollow" nanoparticles were found (see Figure III-15). Fitting the Fourier Transform signals enable drawing several conclusions. First, both aged Pt-Co/C catalysts feature an increase of the Pt and Co average coordination numbers (N_{Pt} = 12.2 ± 1.1 and N_{Co} = 7.9 ± 0.9 for the Pt_3Co/ C aged at I = 50 A and N_{Pt} = 10.4 ± 1.4 and N_{Co} = 7.8 ± 0.6 for the Pt_3Co/ C aged at I = 20 A) with respect to the fresh catalyst (N_{Pt} = 9.9 ± 1.0 *vs.* N_{Co} = 6.9 ± 0.7). The rationale for that is believed to be the increase of the mean particle size observed for the aged catalysts (see Figure III-9). Indeed, the average coordination numbers determined at the Pt L_3 edge for the aged Pt-Co/C catalysts are close to those predicted for a 7 nm cuboctahedral f.c.c nanoparticle (calculated average coordination number of $N_{A\text{-}B} \approx 11$) or for a bulk f.c.c. crystal ($N_{A\text{-}B}$ = 12). Two results extracted at the Co edge are interesteing to point out: (i) similar to what was observed for the fresh Pt-Co/C catalyst, the number of Co closest neighbours is much smaller than that of Pt atoms, suggesting that, when cobalt is still present in the particles, it remains confined in the core of the catalyst during the aging process within the same particular structure as discussed in paragraph II.3 (presence of vacancies) and (ii) the number of Co-Co neighbours significantly decreases at the benefit of Co-Pt neighbours. The latter confirms quantitatively that cobalt atoms have been leached out from the catalyst structure during the aging process.

Interestingly, the interatomic distances found on the aged catalysts are very similar to the fresh Pt_3Co/C catalyst (Table III-4), even though an increase of the interatomic distances on the aged catalysts might have been expected from XRD measurements (Figure III-10).

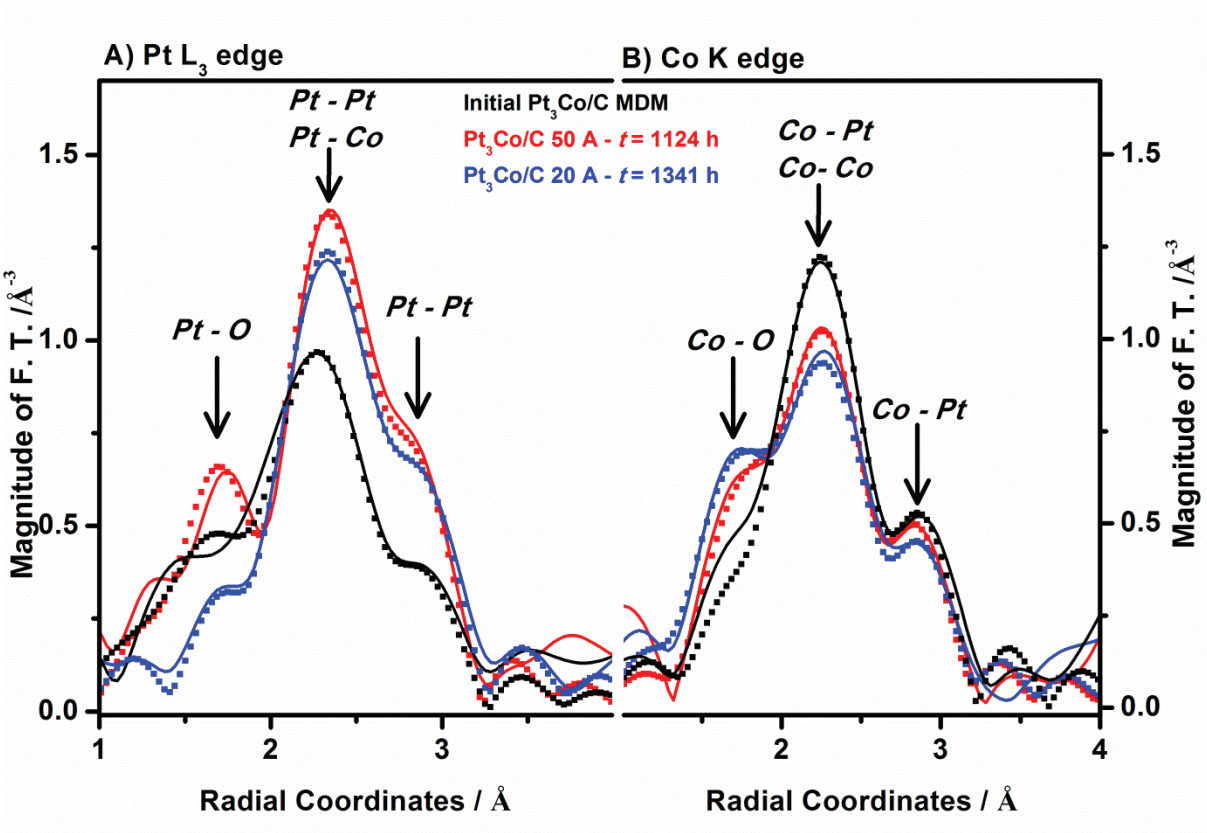

Figure III-17. Fourier transform magnitudes of the fresh Pt_3Co/C MDM (in black) and the aged catalysts having either homogeneous distribution of Pt and Co atom (in red, aged at I = 50 A for t = 1124h) or hollow particles (in blue, aged at I = 20 A for t = 1341h) recorded ex situ at the (A) Pt L_3 and (B) Co K edges. The full lines are the experimental data and dotted lines are the fitted data.

One can also notice that the fits of the EXAFS signals on the aged catalysts greatly improve when Co-O bonds are implemented (see plain and dashed lines in Figure III-17). Actually, fitting reasonably the EXAFS signals at the Co edge without an interaction of the cobalt with a lighter atom such as oxygen (carbon or fluorine would have also fit, but are less likely) would not have been possible. It can be interpreted as the presence of Co-O bonds underlying the Pt surface atoms or oxidized Co atoms located in the ionomer of the cathode catalyst layer (see **Chapter V** for a detailed discussion). For pH ≥ 5, the formation of cobalt oxides is thermodynamically possible [72]. Another explanation for the formation of cobalt – oxide bonds might be that the mechanism of cobalt corrosion involves oxygen adsorption/absorption (discussed in **Chapter IV**).

Catalyst	shell	*N*	*R* / Å	σ^2 ($x10^{-3}$) /	ΔE_0 / eV	*R*-
Pt_3Co/C MDM *t* = 0 h	Pt-Pt	5.3 ± 0.5	2.72 ± 0.01	5.0 ± 0.9	6.5 ± 0.8	0.0019
	Pt-Co	3.2 ± 0.3	2.65 ± 0.01	9.5 ± 0.2	7.2 ± 1.3	0.0019
	Pt-O	1.4 ±0.2	2.01 ± 0.02	4.1 ± 5	14 ± 2	0.0019
	Co-Pt	3.8 ± 0.4	2.67 ± 0.01	3.6 ± 0.6	5.1 ± 0.7	0.0079
	Co-Co	3.1 ± 0.3	2.59 ± 0.01	13 ± 1	-0.7 ±	0.0079
Pt_3Co/C	Pt-Pt	9.7 ± 0.9	2.72 ± 0.01	4.7 ± 0.5	6.0 ± 0.4	0.0010

I = 50 A; *t* = 1124 h	Pt-Co	1.4 ± 0.2	2.68 ± 0.01	5.3 ± 0.3	10.1 ±	0.0010
	Pt-O	1.1 ± 0.1	1.99 ± 0.30	0.5 ± 1.7	3.3 ± 1.8	0.0010
	Co-Pt	4.9 ± 0.5	2.70 ± 0.01	5.6 ± 0.6	8.1 ± 0.3	0.0010
	Co-Co	2.0 ± 0.4	2.59 ± 0.01	10 ± 2	-7.0 ±	0.0010
	Co-O	1.0 ± 0.1	2.04 ± 0.01	3 ± 1	5.7 ± 1.0	0.0010
Pt_3Co/C *I* = 20 A; *t* = 1341 h	Pt-Pt	9.2 ± 0.9	2.72 ± 0.01	4.7 ± 0.3	4.8 ± 0.5	0.0007
	Pt-Co	1.2 ± 0.5	2.68 ± 0.02	5.8 ± 0.2	10.9 ±	0.0007
	Co-Pt	4.7 ± 0.4	2.69 ± 0.01	6.1 ± 0.4	7.2 ± 0.3	0.0008
	Co-Co	1.9 ± 0.2	2.56 ± 0.01	9.5 ± 0.9	-3.3 ±	0.0008
	Co-O	1.0 ± 0.1	2.03 ± 0.01	3 ± 0.5	4.5 ± 0.6	0.0008

Table III-4. Structural parameters obtained by EXAFS analysis at the Pt L_3 and the Co K edges of the fresh Pt_3Co/C MDM and the aged catalysts (I = 50 A for t = 1124h and at I = 20 A for t = 1341h).

5. Changes of surface reactivity and catalytic activity of the catalyst upon aging

a. Cyclic voltammograms in supporting electrolyte

Figure III-18A shows the cyclic voltammograms recorded in 0.1 M H_2SO_4 of the fresh Pt_3Co/C and of a Pt/C used as a reference material. Interestingly, the charge ascribed to the adsorption/desorption of under-potential H (H_{upd}) is developing for the Pt_3Co/C surface with respect to the Pt/C surface. This points towards different H_{upd} coverage/stoichiometry or indicate that the maximum H_{upd} coverage is reached at different potential values for bimetallic and monometallic surfaces. The first point has already been noticed in the literature [31, 32, 73] on bulk or nm-sized Pt_3Co surfaces, although not discussed. Indeed, Stamenkovic *et al*. [32] used charge densities of 200 and 180 μC per cm^2 of Pt to determine the real surface area of "Pt-skeleton" [6, 32] or "Pt-skin"[74] structures, respectively. The primary work of Gauthier *et al*. [74] showed that "Pt-skin" surfaces have a surface enriched in Pt in the first atomic layer, while the next two to three atomic layers are enriched in Co. At variance, Stamenkovic *et al*. [32] evidenced that "Pt-skeleton" structures are alloyed surfaces, which underwent leaching of Co in acidic electrolyte and thus possess a 100% Pt outermost surface layer with subsurface layers having a chemical composition close to that of the mother alloy. Therefore, combining the results obtained by these authors, it is clear that the presence of Co atoms in the near-surface region lowers the H_{upd} charge density. The major consequence of the reduced H_{upd} charge density on aged Pt-Co/C surfaces is that using H_{upd} coulometry yields incorrect values of the real surface area of the fresh/aged electrocatalysts. In view of the above, the current densities of CV and the specific activities for the ORR have been normalized to the Pt real surface area determined by CO_{ad} stripping coulometry. This way of normalizing the CV is used since a long time in our research group [75], and starts now to be used by other research groups [34, 76].

Looking more closely at the CVs, it is interesting to note that not only the charge density but also the intensity of the H_{upd} peaks is changing. Considering similar particle sizes for the two electrocatalysts, the weakly marked H_{upd} features on the fresh Pt_3Co/C indicate that the presence of Co in the near-surface region weakens the chemisorption energy of H_{upd} relative to pure Pt (decreased H_{upd} coverage - ligand effect). It is remarkable to note that the sharpness of the peaks and the H_{upd} charge density are clear fingerprints of the presence/absence of Co in the near-surface region. Second, when looking at the oxide formation potential region at approximately *ca.* E = 0.8 V *vs.* RHE, one notes a shift toward higher potential values for the Pt_3Co/C catalyst comparing to the Pt/C catalyst. Similar for the H_{upd}, the presence of Co in the near-surface region weakens the chemisorption energy of hydroxide/oxide species relative to pure Pt surfaces. The lower affinity to site blocking hydroxide/oxide species is considered to be the reason of the better ORR performance of Pt_3Co/C catalysts with respect to pure Pt/C catalysts.

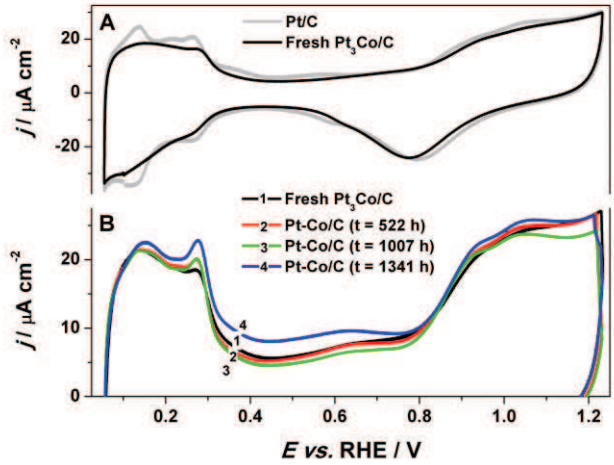

Figure III-18. Base voltammograms of (A) the fresh Pt_3Co/C and the reference Pt/C electrocatalysts and (B) the Pt_3Co/C electrocatalyst in its native form or aged at constant current I = 20 A (j = 0.24 A cm^{-2}) at T = 343K for different life stages. Electrolyte: 0.1 mol dm^{-3} H_2SO_4; v = 0.020 V s^{-1}; T = 298 ± 1K, no RDE rotation. The currents are normalized to the real surface area estimated from CO stripping coulometry. Each voltammogram is the average of at least three measurements.

Interestingly, the voltammograms of Pt_3Co/C electrocatalysts aged at I = 20 A constant load (j ≈ 0.24 A cm^{-2}) are located in-between the curves of the fresh Pt_3Co/C and the Pt/C surfaces (Figure III-18B), confirming that the near-surface region of the catalyst continuously enriches in Pt during PEMFC operation. Similar observations were made at a constant load of 50 A (j ≈ 0.60 A cm^{-2}) [65, 66, 77] and confirm the conclusions derived from physico-chemical techniques: Co atoms are continuously leached from the fresh Pt_3Co/C nanoparticles over time.

Considering the above, the general belief that Pt-alloy/C catalysts are more stable (minor decrease of the ECSA) than Pt/C catalysts should be modulated. Indeed, this statement is usually

based on changes of ECSA estimated from the H_{UPD} coulometry [25, 78-82]. Moreover, the results obtained in this section clearly show that the evolution of the ECSA of a Pt-Co catalyst is a clear function of at least two counterbalancing effects: a positive effect due to the loss of the non-noble metal content (artificial increase of the ECSA) and a negative effect due to the catalyst particles growth/agglomeration (effective decrease of the ECSA). Summing up, CO_{ad} stripping measurements appear a more appropriate technique to draw any conclusion on the robustness (in terms of surface area) of different catalysts. In addition, it should also been pointed out that a fair comparison requires *in situ* measurements (that is with cyclic voltammetry recorded in a PEMFC single cell).

b. ORR activity in liquid electrolyte

Another important requirement of a cathode electrocatalyst for a PEMFC application is its ability to maintain a high ORR activity for the ORR over time. It is specified by the American Department of Energy that the cathode catalyst should never lose more than 60 % of its initial activity [83]. Figure III-19 shows the ORR specific activity (in μA cm^{-2}_{Pt}) of the fresh/aged catalysts in the kinetically limited region of the ORR (E = 0.85 V *vs.* RHE). Interestingly, a Volcano-type behaviour is observed when the ORR activity of fresh/aged catalysts are reported with respect to the interatomic distance determined from the position of the X-ray diffraction peaks. On the descending part of the curve (stationary operation at I = 50 A; j = 0.60 A cm^{-2}), the catalytic activity varies linearly with the Pt-Pt interatomic distance, similarly to what was found by Jalan and Taylor [84]. In these operating conditions, Pt and Co atoms are homogeneously distributed within the individual nanoparticles, as confirmed by STEM-HAADF measurements. The continuous decrease of the Co content during PEMFC operation causes the expansion of the lattice parameter and increases the surface reactivity towards site-blocking oxygenated species (OH/O) [77]. The surface oxide coverage plays a key-role in the ORR kinetics: any decrease of the total number of Pt free sites available for the adsorption of dioxygen and reactive intermediates strongly depreciates the rate of the reaction. Our results are in agreement with the conclusions of the recent X-ray absorption study of Lai *et al.*[47]. The authors found that the ORR activity of Pt_xCo_{1-x} electrocatalysts strongly depends on the chemical dealloying time. For short times close to 15 minutes, the original $Pt_{0.5}Co_{0.5}$/C nanoparticles possess a very thin Pt skin at their surface, and the catalytic performance towards the ORR is significantly enhanced. However, chemical dealloying for 4 hours results in a significant decrease of the Co extent, which depreciates the ORR activity.

We now compare the activity for the ORR of three materials tested in different conditions (50 A for t = 1124 h, 20 A for t = 1341 h and 50 A for t = 327 h of operation in start/stop conditions). Those electrocatalysts exhibit comparable bulk interatomic distance (close to 0.2735 nm) but significant ORR activity variations (by almost a factor of 2). The above results indicate that the ORR

catalytic activity is not only fixed by strain-induced changes in chemisorption energies but that the surface structure plays an essential role [77]. In favourable cell potential conditions *i.e.* catalysts aged under constant load $I \approx 20$ A ($j = 0.24$ A cm^{-2}) or intermittent operation corresponding to an average cell potential higher than 0.60 V, the formation of "Pt-hollow" nanoparticles improves the ORR specific activity with respect to pure Pt/C or even Pt_3Co/C catalysts. The likely reason for that is believed to be (i) the larger particle size of "hollow" Pt particles (diameter above 8 nm), which decreases the contribution of low coordination sites binding oxygenated species very strongly [68, 85, 86] and (ii) the fact that the lattice of the "hollow" Pt nanoparticles is slightly compressed relative to pure Pt/C.

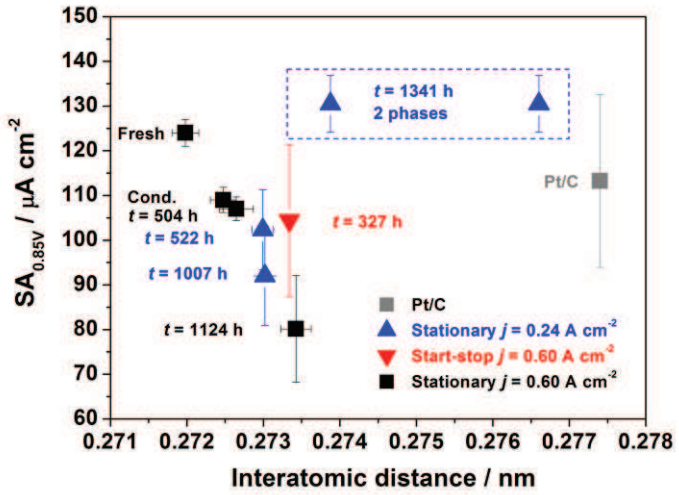

Figure III-19. Specific activities of the fresh/aged Pt_3Co/C electrodes for the ORR reported at E = 0.85 V vs. RHE vs. the Pt-Pt interatomic distance determined from XRD measurements. Porous RDE - Electrolyte: 0.1 M H_2SO_4 - T = 25 ± 1°C - v = 1 mV s^{-1}. The specific activities for the ORR have been normalized to the Pt surface area determined by CO stripping coulometry. Each point is the averaged value of at least three measurements; the error bars represent the standard deviation.

The above hypotheses are strongly reinforced by the results obtained from the XAS study. Indeed, Pt-O bonds have been evidenced on the catalyst aged at $I = 50$ A while none are monitored under the same conditions on the catalyst aged at $I = 20$ A (Figure III-17). Assuming that these bonds are located at the catalyst surface, the Pt-Co/C catalyst aged at $I = 20$ A has then a lower affinity for oxygenated species, which renders it more active for the ORR. These findings on the oxophilicity/oxidized state of the aged catalysts are confirmed by the decrease of the white line intensity on the XANES spectrum at the Pt L_3 edge for the catalyst aged at $I = 20$ A (Figure III-20A). When looking at the XANES spectra obtained at both Pt L_3 and Co K edges, the most significant variations are monitored at the Co K edge with an increase of the white line intensity and a complete

change of the XANES features upon aging (Figure III-20). These changes of the XANES spectra upon aging of the fresh Pt_3Co/C nanoparticles are similar to those observed when comparing the skeleton and the skin structures (Figure III-4). Moreover, these changes are more marked for the catalyst aged at low current I = 20 A than on the catalyst aged at high current I = 50 A.

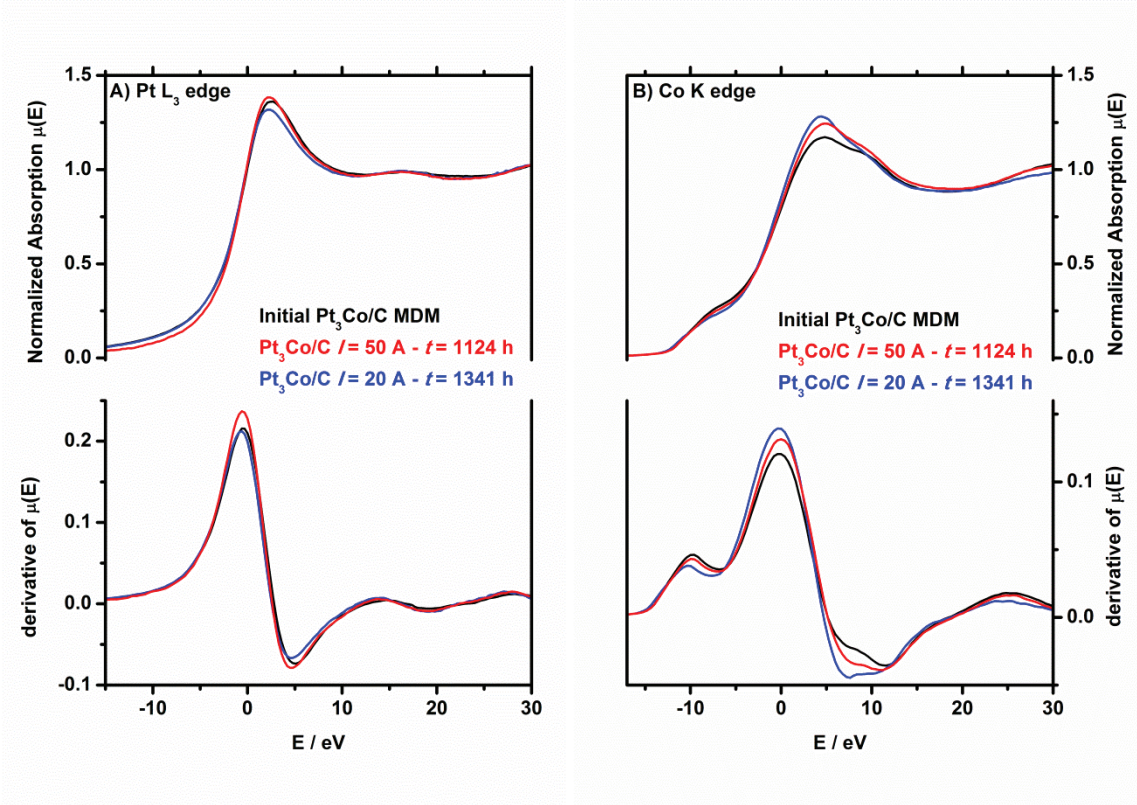

Figure III-20. XANES spectra of the fresh/aged Pt-Co/C catalysts recorded at the European Synchrotron Radiation Facility in Grenoble (beamline BM30B) at the (A) Pt L_3 and the (B) Co K edges. The 0 on the abscissa corresponds to the absorption edge energy of the respective absorbing element

Finally, it should be pointed out that the ORR specific activities presented in Figure III-19 are at least four-fold inferior to those presented in the literature for the same type of materials [12]. Two main reasons may be put forth to account for this disparity. Firstly, in this study, the ORR specific activity of the fresh/aged electrocatalysts was measured in a low pH sulphuric acid electrolyte, because (bi)sulphate ions contained in sulphuric acid electrolyte possess chemical similarities with the sulphonated groups contained in Nafion® type ionomer used in PEMFC cathode catalyst layers [87, 88]. However, even at a low concentration (here 0.1 M), those anions strongly adsorb on Pt-based surfaces, shifting the ORR to more negative potentials with respect to the most commonly used perchloric acid electrolyte [88]. This implies that measurements in sulphuric acid electrolyte "underestimate" the ORR activity of a catalyst in a PEMFC while measurements in perchloric "overestimate" it. Here, it could be argued that *in situ* measurements in a PEMFC single cell remain

the most relevant way of measuring properly the ORR activity of a given cathode catalyst [89]. However, the measurements performed in MEAs remain subjected to criticisms because of severe limitations such (i) catalyst utilization factor below 1, (ii) non-negligible mass transport and Ohmic contributions, (iii) interference of the anode and the cathode (finite permeability of Nafion® membrane to fuel and oxygen), (iv) high cell time-constant.

Another reason that may be evoked is the coverage by oxygenated species. In this study, before the measurements of the ORR activity, the rotating disk electrode was polarized at E = 1.1 V *vs.* RHE for t = 1 min to ensure reproducible state of surface. Such conditions promote the formation of a high coverage with adsorbed species (oxygenated species, anions) that attenuates the reaction rate (see the description of the ORR kinetic current in **Chapter I**). Keeping the same idea in mind, measurements of the ORR activity performed (i) during negative-going potential scans and (ii) at small potential sweep rates severely decrease the availability of the catalytic sites to adsorb and further react O_2 and hence yield poor ORR activities. Those testing conditions were unfortunately used to compare the activity of the fresh/aged Pt-Co/C catalysts with that of other catalysts and may account for the observed large differences in activity observed with reference studies [12, 31, 73].

IV. Conclusion

We have provided in this chapter a body of proof that Pt_3Co/C cathode catalysts, having initially a core/shell structure similar to Pt_3Co/C-skin catalysts, are not stable in their initial structure during long term PEMFC operation. Firstly, they are subjected to 3D Ostwald ripening (similar to what was observed for Pt/C catalysts) yielding changes in the shape and mean particle size. Second, Pt-Co/C nanoparticles undergo irreversible changes of the chemical composition, which largely depend on the cathode potential. At low cathode potential below the onset of surface oxide formation, the Pt-Co/C nanoparticles are depleted in Co but remain homogeneous in chemical composition. The decreased Co content yields a decrease of both the strain and the ligand effect of Co atoms contained in the core and the relaxation of the Pt-Pt bond lengths. Consequently, the ORR activity is depreciated on the aged Pt-Co/C nanoparticles. At high cathode potential, the decrease of the Co content is much faster over time, yielding the formation of compact spherically shaped “hollow” nanoparticles, free of any Co. Such specific structures perform better for the ORR than both Pt/C and the fresh Pt_3Co/C catalysts.

A question also arises to know whether the conclusions drawn from this work on Pt_3Co/C catalysts can be generalized to other Pt-based/C catalysts such as Pt_3Cu/C or Pt_3Ni/C. Regarding the stability toward 3D Ostwald ripening, which is motivated only by the Gibbs-Thomson energy of the particle (dependence on the initial particle size of the catalyst), all types of nanometre sized Pt-alloy seem to be subjected to this degradation mechanism [90]. The small but finite solubility of surface

platinum atoms seems not to be drastically changed, whether non-noble metal atoms are present or not close to the surface. However, regarding the stability toward the subsurface non-noble metal oxidation, which leads to the continuous loss of the non-noble metal content, as this degradation mechanism seems to be potential dependent, the difference in the equilibrium potential of each non-noble metal (cobalt is less noble than nickel and copper) may have an importance.

Therefore, the next chapter is dedicated to the understanding of the mechanism of subsurface cobalt removal from Pt_3Co/C catalysts for at least two reasons: (i) it would help to find a mitigation strategy that could prevent subsurface non-noble metal removal of a Pt-alloy catalyst upon PEMFC operation and (ii) it may be interesting to provoke the removal of subsurface cobalt atoms, as it could be a mean to generate quickly highly performing Pt hollow catalysts.

V. References

[1] Landsman D. A. and Luczak F. J., *US Patent*, 4.316.944 (1982).

[2] Toda T., Igarashi H., Uchida H. and Watanabe M., Enhancement of the electroreduction of oxygen on Pt alloys with Fe, Ni, and Co. *J. Electrochem. Soc.*, 146 (1999) 3750-3756.

[3] Mukerjee S. and Srinivasan S., Enhanced electrocatalysis of oxygen reduction on platinum alloys in proton-exchange membrane fuel-cells. *J. Electroanal. Chem.*, 357 (1993) 201-224.

[4] Strasser P., Koh S., Anniyev T., Greeley J., More K., Yu C., Liu Z., Kaya S., Nordlund D., Ogasawara H., Toney M. F. and Nilsson A., Lattice-strain control of the activity in dealloyed core-shell fuel cell catalysts. *Nat. Chem.*, 2 (2010) 454-460.

[5] Mavrikakis M., Hammer B. and Norskov J. K., Effect of strain on the reactivity of metal surfaces. *Phys. Rev. Lett.*, 81 (1998) 2819-2822.

[6] Stamenkovic V. R., Mun B. S., Arenz M., Mayrhofer K. J. J., Lucas C. A., Wang G. F., Ross P. N. and Markovic N. M., Trends in electrocatalysis on extended and nanoscale Pt-bimetallic alloy surfaces. *Nat. Mater.*, 6 (2007) 241-247.

[7] Hammer B. and Norskov J. K., Electronic factors determining the reactivity of metal surfaces. *Surf. Sci.*, 343 (1995) 211-220.

[8] Markovic N. M. and Ross P. N., Surface science studies of model fuel cell electrocatalysts. *Surf. Sci. Rep.*, 45 (2002) 117-229.

[9] Stamenkovic V. R., Fowler B., Mun B. S., Wang G. F., Ross P. N., Lucas C. A. and Markovic N. M., Improved oxygen reduction activity on Pt_3Ni (111) via increased surface site availability. *Science*, 315 (2007) 493-497.

[10] Mukerjee S., Srinivasan S., Soriaga M. P. and McBreen J., Role of structural and electronic-properties of Pt and Pt alloys on electrocatalysis of oxygen reduction - An *in-situ* XANES and EXAFS investigation. *J. Electrochem. Soc.*, 142 (1995) 1409-1422.

[11] Stamenkovic V. R. and Markovic N. M., Oxygen reduction on platinum bimetallic alloy catalysts, in *Handbook of Fuel Cells: Fundamentals, Technology, and Applications*, Vol. 5, Vielstich W., Yokokawa H. and Gasteiger H. A. 2009, John Wiley & Sons

[12] Gasteiger H. A., Kocha S. S., Sompalli B. and Wagner F. T., Activity benchmarks and requirements for Pt, Pt-alloy, and non-Pt oxygen reduction catalysts for PEMFCs. *Appl. Catal. B.*, 56 (2005) 9-35.

[13] Peng Z. and Yang H., Designer platinum nanoparticles: Control of shape, composition in alloy, nanostructure and electrocatalytic property. *Nano Today*, 4 (2009) 143-164.

[14] Jang J. H., Kim J., Lee Y. H., Kim I. Y., Park M. H., Yang C. W., Hwang S. J. and Kwon Y. U., One-pot synthesis of core shell-like Pt_3Co nanoparticle electrocatalyst with Pt-enriched surface for oxygen reduction reaction in fuel cells. *Energy Environ. Sci.*, 4 (2011) 4947-4953.

[15] Luo J., Wang L., Mott D., Njoki P. N., Lin Y., He T., Xu Z., Wanjana B. N., Lim I. I. S. and Zhong C. J., Core/shell nanoparticles as electrocatalysts for fuel cell reactions. *Adv. Mater.*, 20 (2008) 4342-4347.

[16] Antolini E., Salgado J. R. C. and Gonzalez E. R., The stability of Pt-M (M = first row transition metal) alloy catalysts and its effect on the activity in low temperature fuel cells: A literature review and tests on a Pt-Co catalyst. *J. Power Sources*, 160 (2006) 957-968.

[17] Beard B. C. and Ross P. N., The Structure and Activity of Pt-Co Alloys as Oxygen Reduction Electrocatalysts. *J. Electrochem. Soc.*, 137 (1990) 3368-3374.

[18] Paffett M. T., Beery J. G. and Gottesfeld S., Oxygen Reduction at $Pt_{0.65}Cr_{0.35}$, $Pt_{0.2}Cr_{0.8}$ and Roughened Platinum. *J. Electrochem. Soc.*, 135 (1988) 1431-1436.

[19] Li W. Z., Zhou W. J., Li H. Q., Zhou Z. H., Zhou B., Sun G. Q. and Xin Q., Nano-stuctured Pt-Fe/C as cathode catalyst in direct methanol fuel cell. *Electrochim. Acta*, 49 (2004) 1045-1055.

[20] Watanabe M., Tsurumi K., Mizukami T., Nakamura T. and Stonehart P., Activity and stability of ordered and disordered Co-Pt alloys for phosphoric-acid fuel-cells. *J. Electrochem. Soc.*, 141 (1994) 2659-2668.

[21] Wakabayashi N., Takeichi M., Uchida H. and Watanabe M., Temperature dependence of oxygen reduction activity at Pt-Fe, Pt-Co, and Pt-Ni alloy electrodes. *J. Phys. Chem. B*, 109 (2005) 5836-5841.

[22] Colon-Mercado H. R., Kim H. and Popov B. N., Durability study of Pt_3Ni_1 catalysts as cathode in PEM fuel cells. *Electrochem. Commun.*, 6 (2004) 795-799.

[23] Okada T., Ayato Y., Yuasa M. and Sekine I., The effect of impurity cations on the transport characteristics of perfluorosulfonated ionomer membranes. *J. Phys. Chem. B*, 103 (1999) 3315-3322.

[24] Kelly M. J., Fafilek G., Besenhard J. O., Kronberger H. and Nauer G. E., Contaminant absorption and conductivity in polymer electrolyte membranes. *J. Power Sources*, 145 (2005) 249-252.

[25] Ball S. C., Hudson S. L., Leung J. H., Russell A. E., Thompsett D. and Theobald B. R., Mechanisms of activity loss in PtCo alloy systems. *ECS Trans.*, 11 (2007) 1247-1257.

[26] Chen S., Gasteiger H. A., Hayakawa K., Tada T. and Shao-Horn Y., Platinum-alloy cathode catalyst degradation in proton exchange membrane fuel cells: Nanometer-scale compositional and morphological changes. *J. Electrochem. Soc.*, 157 (2010) A82-A97.

[27] Xin H. L. L., Mundy J. A., Liu Z. Y., Cabezas R., Hovden R., Kourkoutis L. F., Zhang J. L., Subramanian N. P., Makharia R., Wagner F. T. and Muller D. A., Atomic-resolution spectroscopic imaging of ensembles of nanocatalyst particles across the life of a fuel cell. *Nano Lett.*, 12 (2012) 490-497.

[28] Carlton C. E., Chen S., Ferreira P. J., Allard L. F. and Shao-Horn Y., Sub-nanometer-resolution elemental mapping of "Pt_3Co" nanoparticle catalyst degradation in proton-exchange membrane fuel cells. *J. Phys. Chem. Lett.*, 3 (2012) 161-166.

[29] Niessen A. K., Miedema A. R., Deboer F. R. and Boom R., Enthalpies of formation of liquid and solid binary-alloys based on 3D metals. 4. Alloys of cobalt. *Physica B & C*, 151 (1988) 401-432.

[30] Stephens I. E. L., Bondarenko A. S., Bech L. and Chorkendorff I., Oxygen electroreduction activity and X-ray photoelectron spectroscopy of platinum and early transition metal alloys. *Chem. Cat. Chem*, 4 (2012) 341-349.

[31] Chen S., Sheng W. C., Yabuuchi N., Ferreira P. J., Allard L. F. and Shao-Horn Y., Origin of oxygen reduction reaction activity on "Pt_3Co" nanoparticles: Atomically resolved chemical compositions and structures. *J. Phys. Chem. C*, 113 (2009) 1109-1125.

[32] Stamenkovic V. R., Mun B. S., Mayrhofer K. J. J., Ross P. N. and Markovic N. M., Effect of surface composition on electronic structure, stability, and electrocatalytic properties of Pt-transition metal alloys: Pt-skin versus Pt-skeleton surfaces. *J. Am. Chem. Soc.*, 128 (2006) 8813-8819.

[33] Dutta I., Carpenter M. K., Balogh M. P., Ziegelbauer J. M., Moylan T. E., Atwan M. H. and Irish N. P., Electrochemical and structural study of a chemically dealloyed PtCu oxygen reduction catalyst. *J. Phys. Chem. C*, 114 (2010) 16309-16320.

[34] Wang C., Chi M., Li D., Strmcnik D., van der Vliett D., Wang G., Komanicky V., Chang K.-C., Paulikas A. P., Tripkovic D., Pearson J., More K. L., Markovic N. M. and Stamenkovic V. R., Design and synthesis of bimetallic electrocatalyst with multilayered Pt-Skin surfaces. *J. Am. Chem. Soc.*, 133 (2011) 14396-14403.

[35] Campbell C. T., Bimetallic surface chemistry. *Annu. Rev. Phys. Chem.*, 41 (1990) 775-837.

[36] Hirunsit P. and Balbuena P. B., Surface atomic distribution and water adsorption on Pt-Co alloys. *Surf. Sci.*, 603 (2009) 912-920.

[37] Stamenkovic V., Mun B. S., Mayrhofer K. J. J., Ross P. N., Markovic N. M., Rossmeisl J., Greeley J. and Norskov J. K., Changing the activity of electrocatalysts for oxygen reduction by tuning the surface electronic structure. *Angew. Chem.-Int. Edit.*, 45 (2006) 2897-2901.

[38] Zhang J. L., Vukmirovic M. B., Xu Y., Mavrikakis M. and Adzic R. R., Controlling the catalytic activity of platinum-monolayer electrocatalysts for oxygen reduction with different substrates. *Angew. Chem.-Int. Edit.*, 44 (2005) 2132-2135.

[39] Zhou W. P., Yang X. F., Vukmirovic M. B., Koel B. E., Jiao J., Peng G. W., Mavrikakis M. and Adzic R. R., Improving electrocatalysts for O_2 reduction by fine-tuning the Pt-support interaction: Pt monolayer on the surfaces of a $Pd_3Fe(111)$ single-crystal alloy. *J. Am. Chem. Soc.*, 131 (2009) 12755-12762.

[40] Fowler B., Lucas C. A., Omer A., Wang G., Stamenkovic V. R. and Markovic N. M., Segregation and stability at $Pt_3Ni(111)$ surfaces and $Pt_{75}Ni_{25}$ nanoparticles. *Electrochim. Acta*, 53 (2008) 6076-6080.

[41] Bardi U., Beard B. C. and Ross P. N., CO chemisorption on the [111] and [100] oriented single crystal surfaces of the alloy $CoPt_3$. *J. Catal.*, 124 (1990) 22-29.

[42] Schulenburg H., Durst J., Müller E., Wokaun A. and Scherer G. G., Real surface area measurements of Pt_3Co/C catalysts. *J. Electroanal. Chem.*, 642 (2010) 52-60.

[43] Oezaslan M., Hasche F. and Strasser P., *In situ* Observation of Bimetallic Alloy Nanoparticle Formation and Growth Using High-Temperature XRD. *Chem. Mater.*, 23 (2011) 2159-2165.

[44] Witkowska A., Di Cicco A. and Principi E., Local ordering of nanostructured Pt probed by multiple-scattering XAFS. *Phys. Rev. B*, 76 (2007).

[45] Borodzinski A. and Bonarowska M., Relation between crystallite size and dispersion on supported metal catalysts. *Langmuir*, 13 (1997) 5613-5620.

[46] Lai F. J., Sarma L. S., Chou H. L., Liu D. G., Hsieh C. A., Lee J. F. and Hwang B. J., Architecture of bimetallic Pt_xCo_{1-x} electrocatalysts for oxygen reduction reaction as investigated by X-ray absorption spectroscopy. *J. Phys. Chem. C*, 113 (2009) 12674-12681.

[47] Lai F. J., Su W. N., Sarma L. S., Liu D. G., Hsieh C. A., Lee J. F. and Hwang B. J., Chemical dealloying mechanism of bimetallic Pt-Co nanoparticles and enhancement of catalytic activity toward oxygen reduction. *Chem.-Eur. J.*, 16 (2010) 4602-4611.

[48] Kim D. S., Kim J. H., Jeong I. K., Choi J. K. and Kim Y. T., Phase change of bimetallic PdCo electrocatalysts caused by different heat-treatment temperatures: Effect on oxygen reduction reaction activity. *J. Catal.*, 290 (2012) 65 - 78.

[49] Greco G., Witkowska A., Principi E., Minicucci M. and Di Cicco A., Local structural and chemical ordering of nanosized $Pt_{3+/-\delta}Co$ probed by multiple-scattering x-ray absorption spectroscopy. *Phys. Rev. B*, 83 (2011).

[50] Park J. I., Kim M. G., Jun Y. W., Lee J. S., Lee W. R. and Cheon J., Characterization of superpararnagnetic "core-shell" nanoparticles and monitoring their anisotropic phase transition to ferromagnetic "solid solution" nanoalloyse. *J. Am. Chem. Soc.*, 126 (2004) 9072-9078.

[51] Schulenburg H., Muller E., Khelashvili G., Roser T., Bonnemann H., Wokaun A. and Scherer G. G., Heat-treated $PtCo_3$ nanoparticles as oxygen reduction catalysts. *J. Phys. Chem. C*, 113 (2009) 4069-4077.

[52] Witkowska A., Dsoke S., Principi E., Marassi R., Di Cicco A. and Rossi Albertini V., Pt-Co cathode electrocatalyst behaviour viewed by *in situ* XAFS fuel cell measurements. *J. Power Sources*, 178 (2008) 603-609.

[53] Min M.-K., Cho J., Cho K. and Kim H., Particle size and alloying effects of Pt-based alloy catalysts for fuel cell applications. *Electrochim. Acta*, 45 (2000) 4211-4217.

[54] Neyerlin K. C., Gu W., Jorne J. and Gasteiger H. A., Study of the exchange current density for the hydrogen oxidation and evolution reactions. *J. Electrochem. Soc.*, 154 (2007).

[55] Xie J., Wood D. L., Wayne D. M., Zawodzinski T. A., Atanassov P. and Borup R. L., Durability of PEFCs at high humidity conditions. *J. Electrochem. Soc.*, 152 (2005) A104-A113.

[56] Lee S.-Y., Cho E., Lee J.-H., Kim H.-J., Lim T.-H., Oh I.-H. and Won J., Effects of purging on the degradation of PEMFCs operating with repetitive on/off Cycles. *J. Electrochem. Soc.*, 154 (2007) B194-B200.

[57] Guilminot E., Corcella A., Charlot F., Maillard F. and Chatenet M., Detection of Pt^{z+} ions and Pt nanoparticles inside the membrane of a used PEMFC. *J. Electrochem. Soc.*, 154 (2007) B96-B105.

[58] Guilminot E., Corcella A., Iojoiu C., Berthomé G., Maillard F., Chatenet M. and Sanchez J.-Y., Membrane and active layer degradation upon proton exchange membrane fuel cell steady-state operation – Part I: Platinum dissolution and redistribution within the membrane electrode assembly. *J. Electrochem. Soc.*, 154 (2007) B1106-B1114.

[59] Guilminot E., Corcella A., Chatenet M., Maillard F., Charlot F., Berthome G., Iojoiu C., Sanchez J. Y., Rossinot E. and Claude E., Membrane and active layer degradation upon PEMFC steady-state operation - I. Platinum dissolution and redistribution within the MEA. *J. Electrochem. Soc.*, 154 (2007) B1106-B1114.

[60] Zhang J., Litteer B. A., Gu W., Liu H. and Gasteiger H. A., Effect of hydrogen and oxygen partial pressure on Pt precipitation within the membrane of PEMFCs. *J. Electrochem. Soc.*, 154 (2007).

[61] Akita T., Taniguchi A., Maekawa J., Siroma Z., Tanaka K., Kohyama M. and Yasuda K., Analytical TEM study of Pt particle deposition in the proton-exchange membrane of a membrane-electrode-assembly. *J. Power Sources*, 159 (2006) 461-467.

[62] Shao-Horn Y., Sheng W., Chen S., Ferreira P., Holby E. and Morgan D., Instability of supported platinum nanoparticles in low-temperature fuel cells. *Topics Catal.*, 46 (2007) 285-305.

[63] Shao Y. Y., Yin G. P., Gao Y. Z. and Shi P. F., Durability study of Pt/C and Pt/CNTs catalysts under simulated PEM fuel cell conditions. *J. Electrochem. Soc.*, 153 (2006) A1093-A1097.

[64] Dubau L., Durst J., Maillard F., Chatenet M., André J. and Rossinot E., Heterogeneities of aging within a PEMFC MEA. *Fuel Cells*, 12 (2012) 188-198.

[65] Dubau L., Maillard F., Chatenet M., Guétaz L., André J. and Rossinot E., Durability of Pt_3Co/C cathodes in a 16 cell PEMFC stack: Macro/microstructural changes and degradation mechanisms. *J. Electrochem. Soc.*, 157 (2010) B1887-B1895.

[66] Maillard F., Dubau L., Durst J., Chatenet M., André J. and Rossinot E., Durability of Pt_3Co/C nanoparticles in a proton-exchange membrane fuel cell: Direct evidence of bulk Co segregation to the surface. *Electrochem. Commun.*, 12 (2010) 1161-1164.

[67] Haas H. R. and Davis M. T., Electrode and catalyst durability requirements in automotive PEM applications:Technology status of a recent MEA design and next generation challenges. *ECS Trans.*, 25 (2009) 1623-1631.

[68] Maillard F., Pronkin S. and Savinova E. R., Influence of size on the electrocatalytic activities of supported metal nanoparticles in fuel cells related reactions, in *Handbook of Fuel Cells: Fundamentals, Technology, and Applications*, Vol. 5, Vielstich W., Gasteiger H. A. and Yokokawa H. 2009, John Wiley & Sons

[69] Schlogl K., Mayrhofer K. J. J., Hanzlik M. and Arenz M., Identical-location TEM investigations of Pt/C electrocatalyst degradation at elevated temperatures. *J. Electroanal. Chem.*, 662 (2011) 355-360.

[70] Schlogl K., Hanzlik M. and Arenz M., Comparative IL-TEM Study Concerning the Degradation of Carbon Supported Pt-Based Electrocatalysts. *J. Electrochem. Soc.*, 159 (2012) B677-B682.

[71] Xu Q. M., Kreidler E. and He T., Performance and durability of PtCo alloy catalysts for oxygen electroreduction in acidic environments. *Electrochim. Acta*, 55 (2010) 7551-7557.

[72] Greszler A., Moylan T. and Gasteiger H. A., Modeling the impact of cation contamination in a polymer electrolyte membrane fuel cell, in *Handbook of Fuel Cells: Fundamentals, Technology, and Applications*, Vol. 4, Vielstich W., Gasteiger H. A. and Yokokawa H. 2009, John Wiley & Sons

[73] Chen S., Ferreira P. J., Sheng W. C., Yabuuchi N., Allard L. F. and Shao-Horn Y., Enhanced activity for oxygen reduction reaction on "Pt_3Co" nanoparticles: Direct evidence of percolated and sandwich-segregation structures. *J. Am. Chem. Soc.*, 130 (2008) 13818-13819.

[74] Gauthier Y., Joly Y., Baudoing R. and Rundgren J., Surface-sandwich segregation on nondilute bimetallic alloys: $Pt_{50}Ni_{50}$ and $Pt_{78}Ni_{22}$ probed by low-energy electron diffraction. *Phys. Rev. B*, 31 (1985) 6216.

[75] Guilminot E., Corcella A., Chatenet M. and Maillard F., Comparing the thin-film rotating disk electrode and the ultramicroelectrode with cavity techniques to study carbon-supported platinum for proton exchange membrane fuel cell applications. *J. Electroanal. Chem.*, 599 (2007) 111-120.

[76] Stephens I. E. L., Bondarenko A. S., Gronbjerg U., Rossmeisl J. and Chorkendorff I., Understanding the electrocatalysis of oxygen reduction on platinum and its alloys. *Energy Environ. Sci.*, 5 (2012) 6744-6762.

[77] Dubau L., Maillard F., Chatenet M., André J. and Rossinot E., Nanoscale compositional changes and modification of the surface reactivity of Pt_3Co/C nanoparticles during proton-exchange membrane fuel cell operation. *Electrochim. Acta*, 56 (2010) 776-783.

[78] Yu P., Pemberton M. and Plasse P., PtCo/C cathode catalyst for improved durability in PEMFCs. *J. Power Sources*, 144 (2005) 11-20.

[79] Ball S. C., Hudson S. L., Theobald B. R. and Thompsett D., PtCo, a durable catalyst for automotive PEMFC? *ECS Trans.*, 11 (2007) 1267-1278.

[80] Ball S. C., Hudson S. L., Theobald B. R. and Thompsett D., Enhanced stability of PtCo catalysts for PEMFC. *ECS Trans.*, 8 (2006) 141-152.

[81] Mathias M. F., Makharia R., Gasteiger H., Conley J. J., Fuller T. J., Gittleman G. J., Kocha S. S., Miller D. P., Mittelsteadt C. K., Xie T., Yan S. G. and Yu P. T., Two fuel cell cars in every garage? *Interface*, 14 (2005) 24-35.

[82] Wagner F. T., Gasteiger H. A., Makharia R., Neyerlin K. C., Thompson E. L. and Yan S. G., Catalyst development needs and pathways for automotive PEM fuel cells. *ECS Trans.*, 3 (2006) 19-29.

[83] U.S. DoE Technical Plan - Fuel Cells -: http://www1.eere.energy.gov/hydrogenandfuelcells/mypp/pdfs/fuel_cells.pdf

[84] Jalan V. and Taylor E. J., Importance of interatomic spacing in catalytic reduction of oxygen in phosphoric acid. *J. Electrochem. Soc.*, 130 (1983) 2299-2302.

[85] Wang C., van der Vliet D., Chang K.-C., You H., Strmcnik D., Schlueter J. A., Markovic N. M. and Stamenkovic V. R., Monodisperse Pt_3Co nanoparticles as a catalyst for the oxygen reduction reaction: Size-dependent activity. *J. Phys. Chem. C*, 113 (2009) 19365-19368.

[86] Mukerjee S. and McBreen J., Effect of particle size on the electrocatalysis by carbon-supported Pt electrocatalysts: An *in situ* XAS investigation. *J. Electroanal. Chem.*, 448 (1998) 163-171.

[87] Subbaraman R., Strmcnik D., Paulikas A. P., Stamenkovic V. R. and Markovic N. M., Oxygen reduction reaction at three-phase interfaces. *Chem. Phys. Chem.*, 11 (2010) 2825-2833.

[88] Takahashi I. and Kocha S. S., Examination of the activity and durability of PEMFC catalysts in liquid electrolytes. *J. Power Sources*, 195 (2010) 6312-6322.

[89] Gasteiger H. A., Gu W. B., Makharia R., Mathias M. and Sompalli B., Beginning-of-life MEA performance - Efficiency loss contributions, in *Handbook of Fuel Cells: Fundamentals, Technology, and Applications*, Vol. 3, Vielstich W., Gasteiger H. A. and Lamm A. 2003, John Wiley & Sons

[90] Colon-Mercado H. R. and Popov B. N., Stability of platinum based alloy cathode catalysts in PEM fuel cells. *J. Power Sources*, 155 (2006) 253-263.

Chapter V.

Impact of metal cations on the electrocatalytic properties of Pt/C electrocatalysts at multiple-phase interfaces

The results discussed in this chapter have been published in:

Durst J., Chatenet M., Maillard F.:
Impact of metal cations on the electrocatalytic properties of Pt/C electrocatalysts at multiple phase interfaces
Published in: *Physical Chemistry Chemical Physics*, 14 (2012), pp. 13000-13009

I. Origins of a contamination by metal cations at the cathode of a PEMFC

The instability of the PEMFC cathode catalyst in operation yields partial dissolution of the alloy nanoparticles and formation of Pt^{z+} and Co^{y+} ($y = 2$ is the most likely) ionic species (**Chapter III** and **IV)** [1, 2]. As detailed in **Chapter I**, mobile Pt^{z+} produced at the cathode are known to (i) redeposit electrochemically on Pt particles *via* a 3D Ostwald ripening mechanism and/or (ii) cross over the membrane following the electro-osmotic drag or the chemical diffusion before being chemically reduced by hydrogen. The behaviour of the Co^{2+} species has been scarcely studied in the literature. Contrary to Pt^{z+} species, Co^{2+} can neither redeposit in the cathode catalyst layer nor be reduced by H_2. Therefore, they remain ion-exchanged in the ionomer, at least momentarily [3, 4]. It is thus interesting to investigate how these cobalt ions behave in a PEMFC environment once leached, and answer the following questions. How do they interact with the other components? What is their mechanism of contamination? Does Co^{2+} contamination induces reversible or irreversible loss of electrical performances? To which extent does it affect the degradation rates of the MEA materials and is there any mitigation strategy? The understanding of these interactions is crucial since polluting cations can be produced *in situ* by the corrosion of the cathodic electrocatalysts during PEMFC operation, but also by the corrosion of metal bipolar plates [5].

The amount of Co^{2+} leached from the cathode catalyst may not be negligible. Indeed, with a Pt_3Co/C (40 wt. %) cathode loaded at *ca.* 0.4 mg_{Pt3Co} cm^{-2}, a Nafion® 900 EW ionomer and a ionomer to carbon ratio *I*/*C* of 1/1 in the cathode catalyst layer (these are standard values), the total amount of cobalt ions that can be leached is $n_{Co^{2+}} = 6.2 \times 10^{-7}$ mol cm^{-2}, while the total number of sulfonate groups available in the ionomer is $n_{SO_3^-} = \frac{m_{polymer}}{EW} = \frac{0.6 \times 10^{-3}}{900} = 6.7 \times 10^{-7}$ mol cm^{-2}. Assuming that one cobalt ion occupies two sulfonate sites of the cathode ionomer, the complete cobalt dealloying of the Pt_3Co catalyst is not even necessary to pollute all sulfonate groups of the cathode ionomer and so to completely inhibit its proton transport properties. The key question is then how these ionic species will behave: will they accumulate in the cathode catalyst layer and pollute the ionomer, redistribute in the whole MEA, like Pt^{z+} ions do, or be washed out in the exhaust water produced at the cathode?

The transport of Pt^{z+} ions from the cathode to the anode is believed to proceed *via* a combination of (i) chemical diffusion due to the increasing concentration gradient [1, 6-10] , (ii) electro-osmotic drag [6] and (iii) migration, due to the formation of negatively charged platinum complexes (*e.g.* with halide species provided by the chemical degradation of the ionomer/membrane). If the concentration gradient rules the transport of ionic species in the PEMFC, it is interesting to compare the amount of Pt^{z+} and Co^{2+} produced during the degradation of the cathode catalyst. Chen *et al.* calculated that roughly 25% of the overall platinum mass from an initial Pt_3Co/C cathode catalyst loaded at 0.5 mg_{Pt} cm^{-2} was lost in the ionomer phase after a 24 h intensive voltage cycling [1]. In the

meantime the overall cobalt concentration in the cathode catalyst decreased from 17 to 12.5 at. %. Therefore the amount of platinum ($\Delta n_{Pt^{z+}}$) and cobalt ($\Delta n_{Co^{y+}}$) ions produced from the degradation of the cathode catalyst is $\Delta n_{Pt^{z+}} = 6.4 \times 10^{-7} mol\ cm_{MEA}^{-2}$ and $\Delta n_{Co^{y+}} = 2.5 \times 10^{-7} mol\ cm_{MEA}^{-2}$. These values are close enough to suggest that, if a concentration gradient rules the transport of ionic species in the PEM, Co^{2+} could be redistributed such as Pt^{z+} are.

The dynamic of transport also plays a significant role in the redistribution Pt^{z+} species. From the work of Ferreira *et al.* [11], the diffusion coefficient of platinum and cobalt ions ($D_{Pt^{z+}}$and $D_{Co^{y+}}$) in the ionomer phase can be estimated with the following equation:

$$D_{ion} \approx D_{ion,H_2O} \varepsilon_{ionomer} \chi_{H_2O} \qquad \text{Eq. V-1}$$

where D_{ion,H_2O} is the diffusion coefficient of the ion in water ($D_{Pt^{z+},H_2O} = 1 \times 10^{-5}$ cm² s^{-1} and $D_{Co^{y+},H_2O} = 0.7 \times 10^{-5}$cm² s^{-1}), $\varepsilon_{ionomer}$ is the volume fraction of ionomer in the electrode and χ_{H_2O} is the volume fraction of water in the ionomer phase. The comparable values of diffusivities ($D_{Co^{y+}} \approx 0.7\ D_{Pt^{z+}}$) should allow the redistribution of cobalt ions at roughly the same rate as platinum ions.

In order to overcome the migration forces imposed by the potential gradient between the two electrodes when current flows (and so to be redistributed out of the cathode), Co^{2+} and Pt^{z+} have to form neutral or negatively charged compounds. The main thermodynamic data relative to the formation of Pt-based and Co-based complexes with negatively charged ions that can possibly be found within a PEMFC are listed in Table V-1. Whereas it is energetically favourable ($\Delta_r G^\circ << 0$) for platinum ions to form stable negatively charged (or neutral) complexes, it is clearly not the case for cobalt ions, except with F^- species that are known to form when the Nafion® PEM is chemically attacked [12] (we did not find any thermodynamic data relative to the formation of PtF_2). These results suggest that, under operation, cobalt ions most likely remain trapped in the cathode catalyst layer, which was confirmed experimentally by Kienitz *et al.* [13]. In the light of this result, the need to study the impact of cobalt ions on the electrocatalytic properties of cathode catalyst appears obvious.

Formed species	$\Delta_r H^\circ$ / kJ mol^{-1}	$\Delta_r G^\circ$ / kJ mol^{-1}
$PtSO_4$	2.5	-17.0
$Pt(SO_4)_2^{2-}$	11.2	-27.8
$Pt(SO_4)_3^{4-}$	10.4	-35.6
$PtCl_2$	-92.6	-88.5
$PtCl_4^{2-}$	-177.1	-114.5
$CoCl_2$	-8.4	14.5
$CoSO_4$	0.1	-0.7
$Co(OH)_4^{2-}$	215	264
CoF_2	36.7	-29

Table V-1. Main thermodynamic data relative to the formation of complex with Pt^{z+} or Co^{y+} and some negatively charged ions that can be found within a PEMFC at T = 298 K [14].

From an applied viewpoint, two approaches have been developed to quantify the impact of cation contamination on the PEMFC performance: either the cation is injected into the air stream of the PEMFC, [15, 16] or the MEA is soaked in a solution containing the metallic salt prior being mounted and tested in the cell [13, 17, 18]. Whatever the way the contaminant is brought to the system, the PEM resistance, the ORR charge transfer resistance and the mass transport resistance are significantly increasing. While an increase in the PEM resistance in cation-contaminated PEMFC is commonly attributed to the higher affinity of the sulfonic acid groups of the perfluorosulfonated PEM to metal cations [19-23], the mechanisms leading to the increase in the ORR charge transfer and mass transport resistances remain poorly understood and require systematic work with model electrodes.

From a most fundamental point of view, the interactions between the so-called spectator species (such as solvated anions/cations, which can be electrochemicaly stable in their ionic form in the potential window of interest), and platinum electrocatalysts have been recently brought to light by Strmcnik *et al.* in alkaline electrolyte [24]. The authors evidenced that hydrated alkali metal cations form quasi-adsorbed clusters on Pt (111) surfaces and tailor the catalytic activity for reactions such as the ORR, the methanol oxidation and the hydrogen oxidation reaction. In a study on stepped platinum electrodes in alkaline electrolyte, Stoffelsma *et al.* showed that small cations with high hydration energies promote the CO electrooxidation kinetics, which they relate to the easier formation of hydroxide species OH_{ad} on these surfaces [25]. Nevertheless, the role of spectator cations has only been seldom explored in acidic media [26-28], in particular for nanometre-sized particles of interest for proton-exchange membrane fuel cells (PEMFC).

The purpose of this chapter is to provide new insights of how such spectator cations do influence reactions of interest for PEMFC. We investigated the effect of several solvated metal cations (having different hydration energies and being electro-inactive in the potential range of interest for this study) on the surface reactivity and the electrocatalytic activity of Pt/C nanoparticles. These nanoparticles were coated or not with a perfluorosulfonated ionomer in order to simulate two-phase and three-phase interfaces (Pt | liquid and Pt | polymer | liquid interfaces depicted in Figure V-1). The ORR and the CO monolayer electrooxidation were particularly surveyed. In the second part of the chapter, Pt/C nanoparticles were contacted with membranes contaminated with known amounts of metal cations, and their ORR activity was determined using an ultramicroelectrode with cavity and a solid state cell (SSC), especially developed for this study (Pt | polymer interface depicted in Figure V-1).

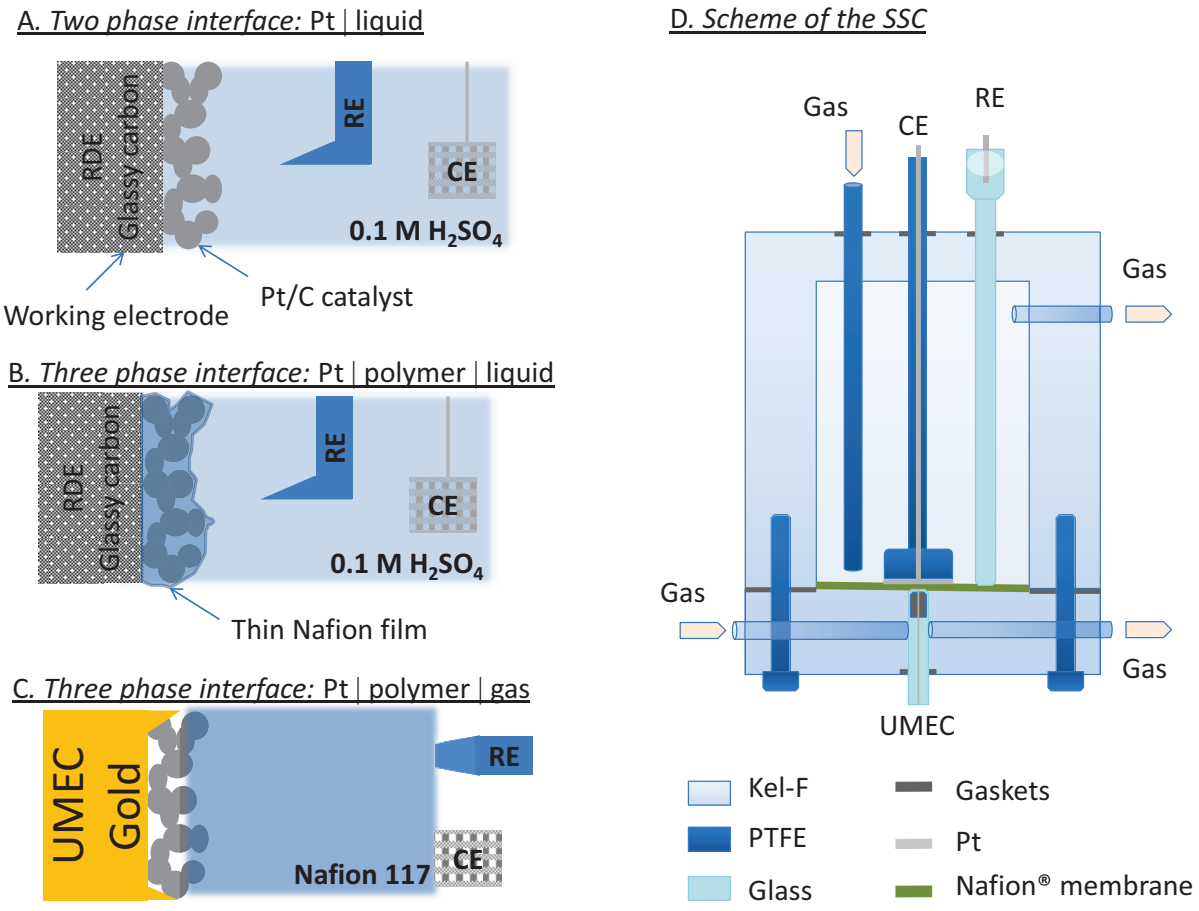

Figure V-1. Schematics of the three electrochemical setup used in this study A) two-phase Pt /liquid interface, B) three-phase Pt /polymer /liquid interface and C) three-phase Pt /polymer / gas interface. The schematics of the SSC (D) are reprinted from Ref. [29] with permission of the author.

II. Effect of mono- and multivalent cations at the Pt | liquid electrolyte two-phase interface

In the first part of this study, a rotating disk electrode (RDE) composed of Pt/C (30 wt. %, E-TEK) loaded at 9 $\mu g_{Pt}\ cm^{-2}_{geo}$ and without addition of Nafion® ionomer (Figure V-1a) was used as working electrode in a three-electrode cell configuration (Pt | liquid interface in Figure V-1A). The same single RDE tip was first tested in 0.1 M H_2SO_4 and then in each cation-containing solution, so as to directly monitor the impact of metal cations on the Pt/C surface reactivity (ORR and CO electrooxidation kinetics). The metal salts added to the supporting electrolyte were K_2SO_4 H_2O (Organics, 99%), Li_2SO_4 H_2O (Merck, 99%), $CoSO_4$ 7 H_2O (Prolabo, 99%) and $Al_2(SO_4)_3$ 18 H_2O (Merck, 99%). The amount of contamination of the liquid electrolyte for a given metal cation M^+ is expressed by:

$$\gamma_{M^+} = \frac{c_{M^+}}{c_{H^+} + c_{M^+}} \qquad \text{Eq. V-2}$$

where c_{H^+} is the proton concentration and c_{M^+} the M^+ concentration in the electrolyte solution.

Figure V-2 displays the modifications of the cyclic voltammetry (CV) in supporting electrolyte (Figure V-2A) and the CO_{ad} stripping voltammogram (Figure V-2B) induced by the addition of monovalent (K^+ and Li^+), divalent (Co^{2+}) and trivalent (Al^{3+}) cations to the base 0.1 M H_2SO_4 electrolyte. In the low potential region of the CV, the positions and the intensities of the peaks are associated with the adsorption/desorption of H_{upd} on/from the different facets of the platinum nanoparticles. The H_{upd} features remain largely unaffected by the presence of metal cations, which suggests that the latter are not specifically adsorbed on the Pt/C surface. The small variations of the electrochemically active surface area determined from the H_{upd} coulometry (A_{Hupd}) remain in the error bar of this measurement (Table V-3). The case of Co^{2+} ions however differs, since underpotential deposition is observed on the Pt/C surface at $0.2 < E < 0.4$ V *vs.* RHE, which agrees with the literature [30]. At higher potential, where currents are associated to the formation/reduction of surface oxides on platinum, the CV is also barely modified except in the presence of aluminium cations, for which the onset of Pt-oxide formation is shifted towards positive potential. This observation is not in line with experiments conducted on single crystals in alkaline electrolyte, which evidenced that the growth of the hydroxide layer is promoted and shifted toward lower potential values in the presence of metal cations with high hydration enthalpies [24].

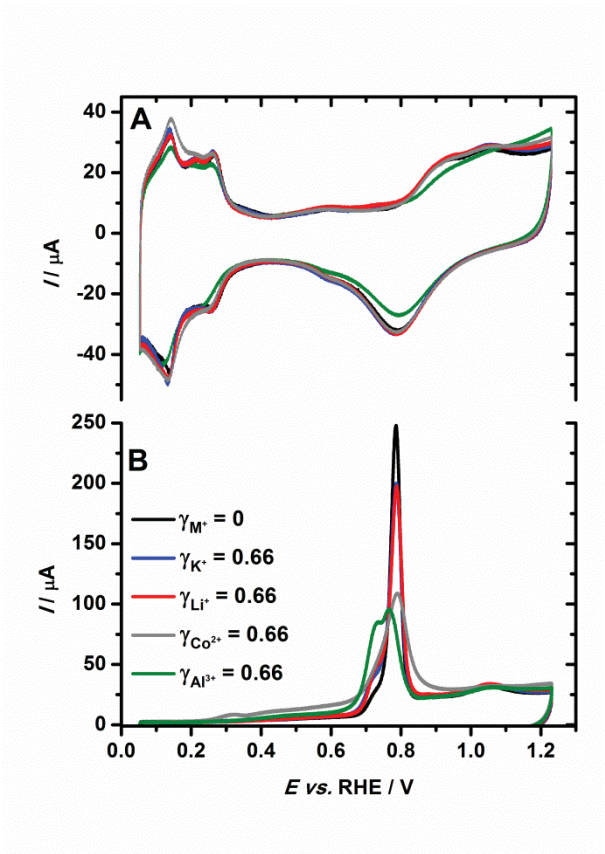

Figure V-2 (A) Cyclic voltammograms and (B) CO_{ad} stripping voltammograms for Pt/C electrodes in 0.1 M H_2SO_4 (black) modified by the addition of 0.1 M K^+ (blue), 0.1 M Li^+ (red), 0.1 M Co^{2+} (grey) or 0.1 M Al^{3+} (green). T = 298 ± 1 K, sweep rate = 0.020 V s^{-1}. As the same single RDE tip was probed in 0.1 M H_2SO_4 and in each of the four cation-containing solution, the I vs. E curves allow a direct monitoring of the impact of cations on the electrochemical surface area.

Figure V-2B features the CO_{ad} stripping voltammograms recorded for different electrolyte compositions. As for H_{upd}, the charge of the CO monolayer oxidation is not depreciated in the presence of cations (see A_{CO} in Table V-3). The CO_{ad} stripping voltammogram in 0.1 M H_2SO_4 features both a main oxidation peak at $E \approx 0.76$ V *vs.* RHE, ascribed to the electrochemical oxidation of CO molecules adsorbed on isolated particles, and a prepeak at $E \approx 0.70$ V *vs.* RHE, ascribed to the more facile CO oxidation on grain boundaries interconnecting Pt crystallites, such as agglomerated particles [31, 32]. Interestingly, the oxidation of the CO_{ad} monolayer initiates at lower potential values compared to 0.1 M H_2SO_4 in the presence of metal cations in solution, both for the main electrooxidation peak and the prepeak. It is also instructive to note that the coulometry of the main oxidation peak decreases at the expense of the prepeak in the presence of metal cations, this feature being more pronounced for Co^{2+} and Al^{3+} with respect to K^+ and Li^+ ions. Additional CV, CO_{ad} stripping and ORR voltammograms were also performed in 0.1 M H_2SO_4 after the measurements in solutions containing metal cations. In each case, the final electrochemical characterizations overlapped with the initial ones, showing that metal cations only reversibly impact the electrocatalyst, therefore asserting that the structure of the Pt/C nanoparticles did not change during the electrocatalytic measurements. These findings indirectly mean that the formation of active oxygen-containing adsorbate species on the platinum surface is promoted in the presence of metal cations in solution. The greater the hydration enthalpy of the cation (Table V-3), the higher the negative shift of the onset of the CO_{ad} monolayer oxidation (the reaction onset is even slightly above the potential of zero charge for aluminium ions), which agrees with the results obtained in alkaline media [25]. The authors successfully showed that alkali metal cations with high hydration energies stabilize adsorption of OH_{ad} molecules at the Pt surface. Consequently, the reaction kinetics of the methanol oxidation reaction or the oxygen reduction reaction are enhanced/depreciated depending if the oxygen-containing species are required by the reaction or rather poison the Pt surfaces sites respectively.

In agreement with the above, Figure V-3A shows that the Pt/C catalyst performs better for the ORR in 0.1 M H_2SO_4 than in the presence of any of the metal cations used in this study. A negative shift in potential of both the kinetic and the mass-transport limiting regions of the ORR curves is observed, the intensity of which scales as $Al^{3+} > Co^{2+} > K^+ \approx Li^+$. This shift translates by a decrease of both the ORR specific activity measured at $E = 0.85$ V *vs.* RHE and the diffusion limiting current (see $SA_{0.85V}$ and j_D in Table V-3). As detailed in **Chapter I**, the current for the ORR in the kinetic region can be expressed as:

$$j_k = -nFkC_{O_2}\left[H^+\right](1-\theta_{ad})^x \exp\frac{-\alpha FE}{RT}\exp\frac{\Delta G^{\neq}_{g_{ad}}}{RT} \qquad \text{Eq. V-3}$$

Consequently, a decrease in the kinetic current for the ORR may be ascribed to (i) an increased coverage by sulphate anions, resulting from the addition of cations in solution, (ii) a decrease in the number of exchanged electrons, (iii) an increased coverage by oxygenated species due to an easier platinum surface oxidation, (iv) an increase of the local pH (the pH of the solution was kept at the same value), (v) a decrease in the oxygen solubility, or (vi) a change in the rate determining step of the ORR. To check the first hypothesis, experiments were performed in electrolytes where the sulphate concentration was adjusted to the same concentration as the experiment with the metallic salt and quantified the resulting variation of specific activity and number of exchanged electrons. It is obvious from Table V-3 that the increase in sulphate concentration contributes only to a minor extent to the changes of both the specific activity and the number of exchanged electrons. To check the second hypothesis, RRDE measurements were performed and, from the disk and ring currents and the collection efficiency of the setup, the number of exchanged electrons *n* for the ORR was calculated in the presence/absence of the metal cations (Figure V-3). Table V-3 reports the number of exchanged electrons at E = 0.4 V vs. RHE (see $n_{E=0.4\,V}$), in the mass transport limited region. The impact of the presence of metal cations on the overall number of exchanged electrons is in the same range than the results presented by Li *et al.* [33]. No clear explanations can rationalize why the H_2O_2 production increases with cation addition, which could be important for membrane health in PEMFC. It was speculated that the effect of weakly adsorbed Co^{2+} on the ORR mechanism may occur mainly through Co^{2+} reacting with the intermediate Pt-$O_2H_{2(ad)}$ generating [Co-H_2O_2]$^{2+}$ complexes in solution [33]. However, the small decrease of the number of exchanged electrons can also be attributed to (i) a small increase of the local pH in the close vicinity of the electrode in each cation-containing solution [34] or (ii) to steric hindrances induced by the oxide coverage increase, which leaves less place available for O_2 molecules adsorption in the bridge configuration; the O_2 molecules will then preferentially adsorb on top (only one oxygen bonded to platinum), a less favourable configuration to break the oxygen – oxygen bond that may account for the higher release of hydrogen peroxide as discussed by Roche *et al.* for MnO_x/C-based ORR electrocatalysts [35]. As it is obvious from Figure V-3 and Table V-3 that the decrease in the number of exchanged electrons is negligible, we can therefore correlate the decrease of the kinetic current to an increase of the coverage by site-blocking species on platinum. Since cations are not specifically adsorbed at potentials above the potential of zero charge, this observed effect may be rationalized by considering more facile formation of (hydr)oxide species on the catalyst surface, or smaller C_{O_2} in solution. To go beyond, one must consider the diffusion-convection limited current.

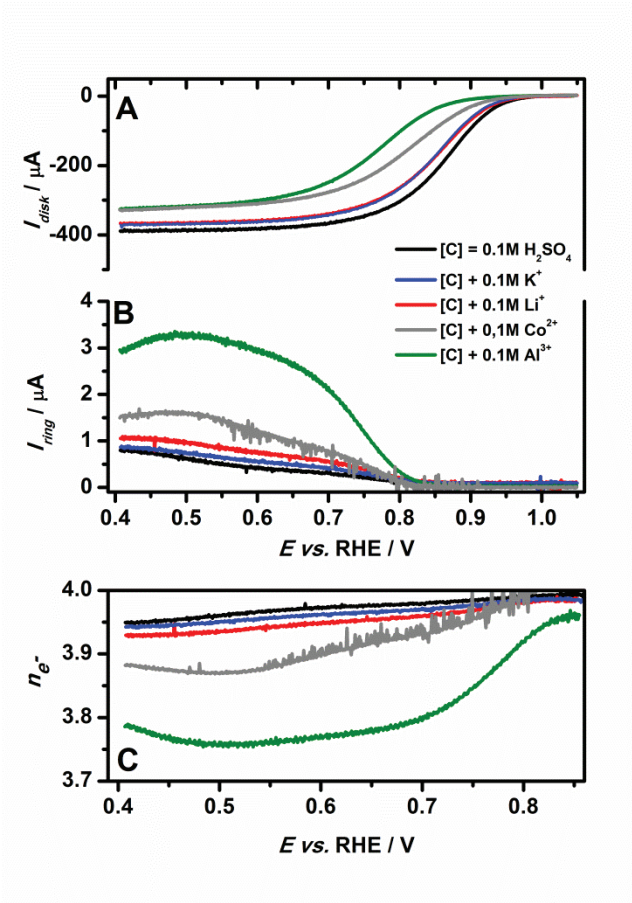

Figure V-3. (A) Disk and (B) ring currents (E_{ring} = 1.23 V vs. RHE) for the ORR, corrected from the Ohmic drop (the ohmic resistances range from 17 Ω cm² in 0.1 M H_2SO_4 to 19 Ω cm² in the most heavily cation polluted solution), recorded in oxygen saturated 0.1 M H_2SO_4 (black) modified by the addition of 0.1 M K^+ (blue), 0.1 M Li^+ (red), 0.1 M Co^{2+} (grey), or 0.1 M Al^{3+} (green). ω = 200 rpm, collection efficiency N = 16 %, T = 298 ± 1 K, v = 0.001 V s^{-1}. The effective number of electrons is reported in (C).

Understanding the observed decrease in the diffusion limited current with increasing concentrations in metal cations in solution requires considering the analytic expression of the Levich equation:

$$j_D = 0.62 * nFD_{O_2}^{2/3} C_{O_2} \upsilon^{-1/6} \omega^{1/2} \qquad \text{Eq. V-4}$$

where D_{O_2} the oxygen diffusion coefficient in the media (in $m^2\ s^{-1}$), υ the kinematic viscosity (in $cm^2\ s^{-1}$) and ω the angular rotation velocity of the electrode (in rad s^{-1}). A decrease of the limited current densities in the contaminated solutions can be ascribed either to (i) a decrease of the number of exchanged electrons and so to a change of the ORR pathway (H_2O_2 production) or to (ii) changes of the oxygen transport properties (D_{O_2}, C_{O_2} and υ) in the bulk electrolyte. Even if the number of exchanged electrons decreases in presence of the metallic ions, its magnitude only contributes to a

minor extent to the overall decrease of j_D. In the particular case of the cobalt-containing solution, the number of exchanged electrons decreases by 1%, while the limited current density decreases by 17%, with respect to the measurement performed in 0.1 M H_2SO_4. Consequently, we argue that the O_2 transport properties *i.e.* D_{O_2}, C_{O_2} and υ values must be greatly affected by the presence of foreign metal cations in the base electrolyte.

In order to verify this last assertion, these parameters were calculated in 0.1 M H_2SO_4 and in 0.1 M H_2SO_4 + 0.1 M $CoSO_4$ electrolyte solutions. The oxygen diffusion coefficient D_{O_2} was determined from Cottrell-like chronoamperometry experiments, performed on an ultramicroelectrode with cavity (UMEC) filled with a Pt/C powder (30 wt. %, E-TEK). In this technique, first published by Denuault *et al.*[36] for a gold microdisk and later on optimized by Wang *et al.*[37] for a gold microsphere, the ultramicroelectrode is polarized first at a potential where the ORR does not occur (here E = 1.1 V vs. RHE for t = 30 s) and then in a potential region where the oxygen reduction is diffusion limited (here E = 0.4 V *vs.* RHE for t = 10 s). The current transient during the potential step is recorded every t = 10 ms. From the slope S and the intercept A of the $I = f(t^{-1/2})$ plot (Figure V-4), the oxygen diffusion coefficient can be determined with:

$$D_{O_2} = \frac{r^2 \times A^2}{\pi \times S^2} \qquad \text{Eq. V-5}$$

with r is the radius of the microelectrode (r = 17 µm). The oxygen coefficient calculated in 0.1 M H_2SO_4, D_{O_2}= 1.9 $\times 10^{-5}$ cm^2 s^{-1}, is in agreement with the value given by Dubau *et al.* [38] for the same electrolyte (see Table V-2). In presence of cobalt ions, the oxygen diffusion coefficient is decreased by *ca.* 16% to D_{O_2}= 1.6 $\times 10^{-5}$ cm^2 s^{-1}. With the calculated values of the oxygen diffusion coefficient, the kinematic viscosity of both solutions can be determined with the oxygen diffusivity transient method on a rotating ring disk electrode introduced by Gan and Chin [39] and Lozar *et al.* [40] according to the Bruckenstein and Feldman method [41]. In this transient method, a potential step from E_{disk} = 1.1 V *vs.* RHE to E_{disk} = 0.4 V *vs.* RHE is applied on the disk to reduce oxygen while in the same time the ring is maintained at a potential enabling oxygen reduction (E_{ring} = 0.4 V *vs.* RHE). Stepping the potential step at the disk generates a depletion of oxygen, which reaches the vicinity of the ring after a transit time t_s (s). This time t_s can be expressed as follows:

$$t_s = \frac{2\pi K}{60} \times \left(\frac{\upsilon}{D_{O_2}}\right)^{1/3} \times \omega^{-1} \qquad \text{Eq. V-6}$$

where K is a coefficient characteristic of the geometry of the RRDE. For an ideal RRDE it can be calculated with:

$$K = 43.1 \times \left(\log\left[\frac{r_2}{r_1}\right]\right)^{2/3} \qquad \text{Eq. V-7}$$

r_2 is the inner radius of the ring electrode (in cm) and r_1 the radius of the disk electrode (in cm). Here K = 7.94. Therefore, from the slope of the $I = f(t^{-1/2})$ plot (Figure V-5), the kinematic viscosities in both electrolytes can be calculated. Similar as for the oxygen diffusion coefficient, the presence of solvated cations such as Co^{2+} induces non-negligible decrease of the kinematic viscosity (Table V-2). Finally, with the measured value of j_D, n, D_{O_2} and ν in each electrolyte, the oxygen solubility C_{O_2} in presence/ absence of solvated cobalt cations can be calculated with the Levich equation and is reported in Table V-2. The oxygen solubility is also decreased in a cobalt contaminated electrolyte. Similar changes were found by Okada *et al.* [28, 42] on Nafion®-covered Pt surfaces in solutions containing Fe^{3+}, Ni^{2+} and Cu^{2+}.

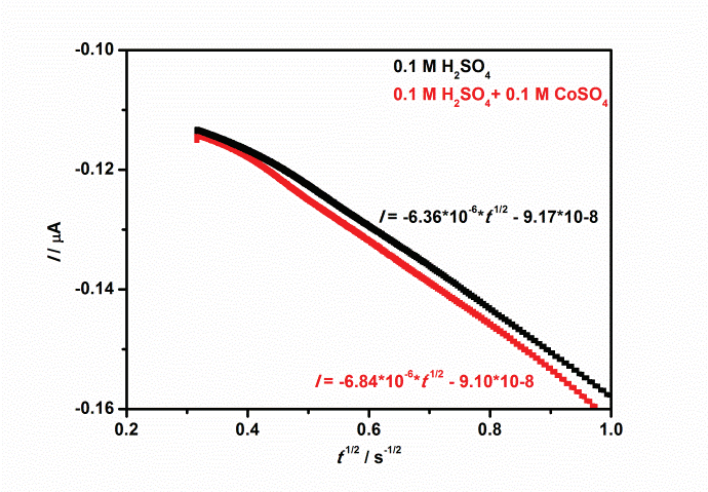

Figure V-4. Cottrell lines relative to a potential step from E = 1.1 V vs. RHE to E = 0.4 V vs. RHE in oxygen saturated 0.1 M H_2SO_4 (black square symbols) and 0.1 M H_2SO_4 + 0.1 M $CoSO_4$ (red square symbols). Sampling time = 10 ms. Three repetitions of the measurement confirmed the results. The linear regression of the corresponding curves are given.

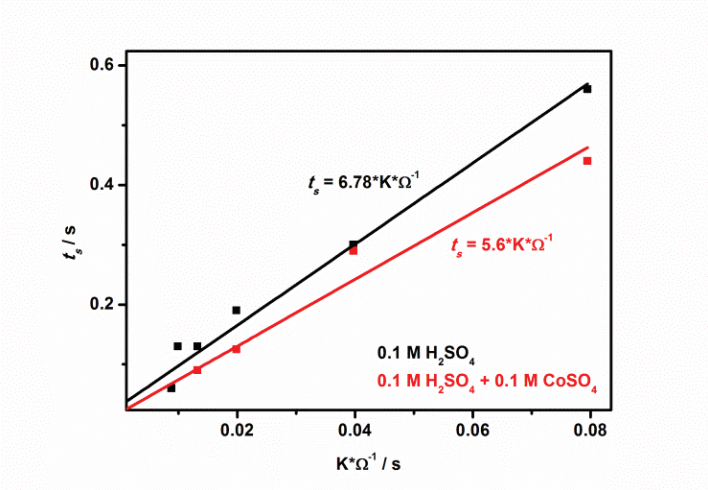

Figure V-5. Transit time versus K*Ω^{-1} recorded in oxygen saturated 0.1 M H_2SO_4 (black square symbols) and 0.1 M H_2SO_4 + 0.1 M $CoSO_4$ (red square symbols). Three repetitions of the measurement confirmed the results. The linear regressions are also given.

	j_D / mA cm^{-2}_{geo}	n	D_{O_2} / cm^2 s^{-1}	ν / cm^2 s^{-1}	C_{O_2} / mol cm^{-3}
0.1 M H_2SO_4	4.14	3.94	1.9×10^{-5}	0.60×10^{-2}	2.3×10^{-6}
0.1 M H_2SO_4 + 0.1 M Co^{2+} (γ_{Co2+} = 0.66)	3.42	3.88	1.6×10^{-5}	0.30×10^{-2}	1.9×10^{-6}

Table V-2. ORR limiting current densities j_D (from Table V-2), number of exchanged electrons n (from Table V-2), kinematic viscosities ν, oxygen diffusion coefficients D_{O_2} and solubilities C_{O_2} in 0.1 M H_2SO_4 and in presence or absence of 0.1 M $CoSO_4$.

To summarize this first part, it is worth mentioning that the H_{upd} process on Pt seems to be poorly affected by the presence of cations in solution, which agrees with previous works on Pt single crystal surfaces in acidic [27] and alkaline [24] supporting electrolyte. More interesting are the subtle effects of these cations on the hydroxide/oxide layer formed during CV experiments in 0.1 M H_2SO_4, while the kinetics and thermodynamics of the CO_{ad} oxidation and the ORR, two reactions closely related to this hydroxide/oxide layer formation, are strongly but reversibly affected by the presence of metal cations in solution.

	0.1 M H_2SO_4 ($\gamma_{M^+} = 0$)	0.15 M H_2SO_4	0.2 M H_2SO_4	0.25 M H_2SO_4	0.1 M H_2SO_4 + 0.1 M K^+ ($\gamma_{K^+} = 0.66$)	0.1 M H_2SO_4 + 0.1 M Li^+ ($\gamma_{Li^+} = 0.66$)	0.1 M H_2SO_4 + 0.1 M Co^{2+} ($\gamma_{Co^{2+}} = 0.66$)	0.1 M H_2SO_4 + 0.1 M Al^{3+} ($\gamma_{Al^{3+}} = 0.66$)
Hydrated radii in pm	-----	-----	-----	-----	331 for K^+	238 for Li^+	423 for Co^{2+}	475 for Al^{3+}
Hydration energy in kJ mol^{-1}	-----	-----	-----	-----	-322 for K^+	-520 for Li^+	-1996 for Co^{2+}	-4430 for Al^{3+}
$A_{H_{upd}}$ in cm^2_{Pt}	1.06	1.08	1.07	1.01	1.12	1.05	1.20	1.03
A_{CO} in cm^2_{Pt}	1.28	-----	-----	-----	1.39	1.37	1.26	1.33
$SA_{0.85V}$ in µA cm^{-2}_{Pt}	360	310	283	277	230	245	104	36
$\lvert j_D \rvert$ in mA cm^{-2}_{geo} @ E = 0.4 V	4.14	3.90	3.83	3.75	3.93 (-5%)	3.88 (-6%)	3.42 (-17%)	3.37 (-19%)
$\theta_{ad,(x=1)}$ @ E = 0.85 V	0.65	0.67	0.69	0.69	0.71	0.72	0.83	0.93
$\theta_{ad,(x=2)}$ @ E = 0.85 V	0.65	0.67	0.68	0.68	0.70	0.70	0.78	0.86
$n_{E = 0.4\ V}$	3.94	3.91	3.90	3.90	3.93 (-0.3%)	3.93 (-0.3%)	3.88 (-1%)	3.78 (-4%)

Table V-3. Hydrated radii and hydration energies given for the metal cations of interest in this study. The real Pt surface area determined from the H_{upd} $A_{H_{upd}}$ and the CO_{ad} stripping coulometry A_{CO} were determined assuming 210 and 420 µA cm^{-2}_{Pt}, respectively. The ORR specific activity, the ORR diffusion limited current and the number of exchanged electrons were determined on Pt/C electrocatalysts in O_2-saturated 0.1M H_2SO_4 solutions in the presence/absence of metallic cations. Sweep rate = 0.001 V s^{-1}; positive-going potential sweep from 0.4 to 1.05 V vs. RHE; rotation rate = 200 rpm, collection efficiency N = 16 %, T = 298 ± 1 K.

III. Effect of Co^{2+} cations at the Pt | polymer | liquid three-phase interface

In both the anode and cathode catalytic layers of a PEMFC, the electrochemical reactions take place at a three-phase interface composed of Pt/C nanoparticles, gas/fluid and a proton-conducting ionomer that forms a proton conducting network. The conventional ionomer in PEMFCs is Nafion®. It is well-established that the sulfonic acid groups of the proton-conducting ionomer possesses stronger affinity for metal cations (other than Li^+) than for protons, [43] which favours protons replacement and formation of metal cations-sulfonate ion pairs (M^{z+}….SO_3^-) as in normal ion exchange processes [24, 44, 45]. Therefore, the rate of the CO electrooxidation and of the ORR are expected to differ significantly at the Pt | polymer | liquid three-phase interface and at the Pt | liquid two-phase interface. For the sake of better describing the transition from a two-phase to a three-phase interface, porous RDE were prepared with 3 ionomer to carbon weight (*I/C*) ratio: *I/C* = 0, *I/C* = 0.6 and *I/C* = 1. The experiments at *I/C* = 0.6 and *I/C* = 1 are close to the optimal ionomer loading required in a PEMFC [46] and serve to reconstitute Pt | polymer | liquid interfaces with variable diffusion properties (Figure V-1B). The average ionomer thickness over the carbon support can be calculated by dividing the surface area of carbon (250 $m^2\ g^{-1}_{carbon}$ for Vulcan XC-72) by the volume of Nafion® (calculated with its density 0.924 $g_{Nafion}\ m^{-3}$ and its loading in the electrode). For the experiment at *I*/*C* = 0.6, the average ionomer thickness over the carbon support is approximately 1 nm (assuming homogeneous and complete coverage of the carbon surface by the Nafion® ionomer), while at *I*/*C* = 1 it is approximately 2 nm. Such calculations fairly agree with the experimental values of the thickness of the recast ionomer measured by More et *al.* [47].

Figure V-6 presents the CV and the CO_{ad} stripping voltammograms recorded at the Pt | polymer | liquid interface in the presence of increasing amounts of $CoSO_4$ (2, 10 and 100 mM corresponding to γ_{Co}^{2+} = 0.04, 0.17 and 0.66, respectively) and in the absence of Nafion® (*I/C* = 0). The addition of Co^{2+} cations to the base electrolyte does not modify the shape of the CV but strongly affects the CO_{ad} stripping voltammograms. Indeed, the latter becomes highly asymmetric for increased Co^{2+} concentration in solution (Figure V-6B). Also, a shift towards negative potential of the onset potential of the CO_{ad} monolayer oxidation is observed at high Co^{2+} concentrations. These features can easily be rationalized by considering more facile (hydr)oxide formation at the Pt surface in the presence of Co^{2+} ions in solution. Interestingly, the effect of Co^{2+} ions is almost vanishing with increasing values of the *I/C* ratio (Figure V-6A, C, E).

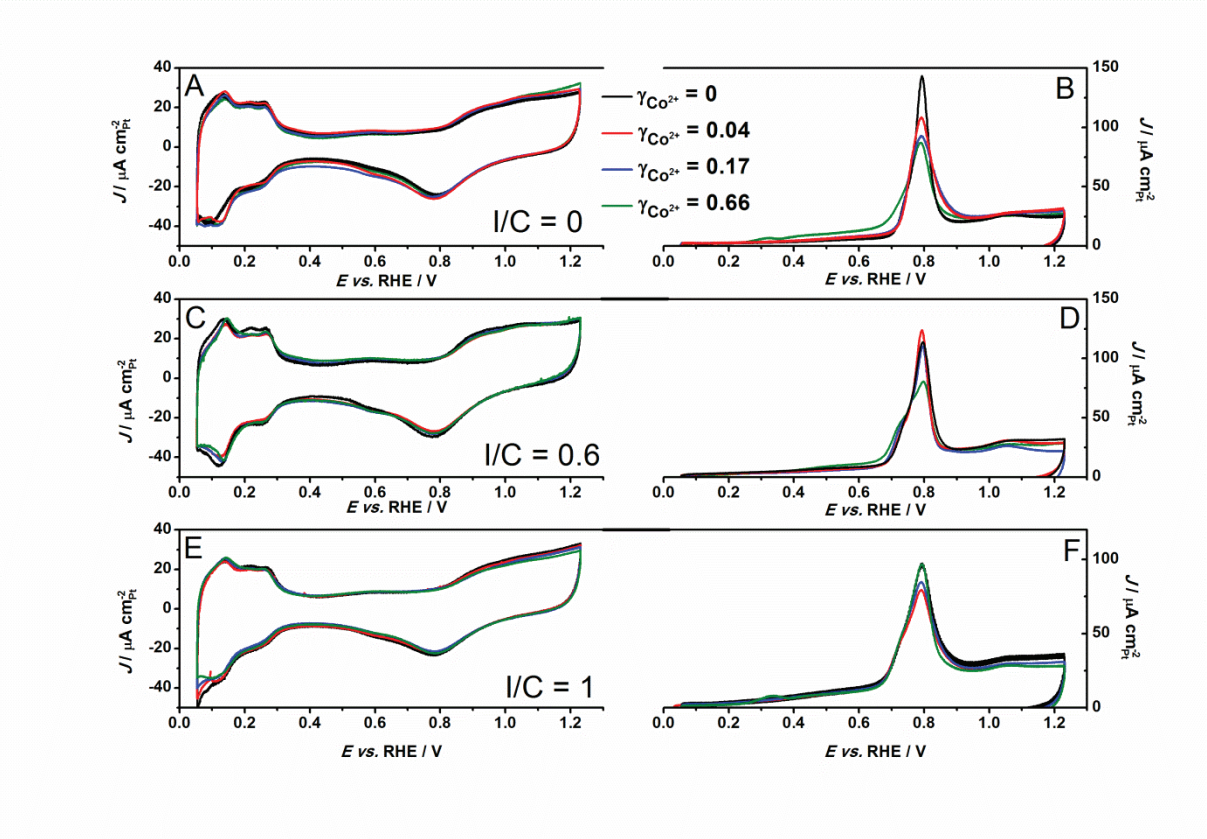

Figure V-6. Cyclic voltammetries in supporting electrolyte and CO_{ad} stripping voltammograms for Pt/C in 0.1 M H_2SO_4 (black curves) and in Co^{2+} containing solution: γ_{Co}^{2+} = 0.04 (red curves), γ_{Co}^{2+} = 0.17 (blue curves) and γ_{Co}^{2+} = 0.66 (green curves) with different amounts of Nafion® added to the ink during the preparation of the porous RDE: I/C = 0 (A and B), I/C = 0.6 (C and D) and I/C = 1 (E and F). T = 298 ± 1 K, v = 0.020 V s^{-1}. The currents are normalized with the area determined from CO_{ad} stripping experiments.

The ORR voltammograms recorded for different *I*/*C* ratio in Co^{2+} containing solutions are presented in Figure V-6. Whatever the value of *I*/*C*, the presence of Co^{2+} ions in solution depreciates the rate of the ORR in both the kinetic and the diffusion limited region of the voltammogram. As for CO_{ad} stripping voltammograms, the impact of Co^{2+} ions on the ORR voltammograms is depressed at high *I*/*C* ratio (Figure V-6B and C). For instance, the ORR specific activity decrease in heavily Co^{2+} contaminated solutions (γ_{Co}^{2+} = 0.66), amounts 20 % at *I*/*C* = 1 and *ca.* 70 % at *I*/*C* = 0 (Figure V-8). The increasing effect of the I/C ratio on the ORR kinetics is believed to reflect different degree of coverage of the Pt/C with Nafion® at *I*/*C* = 0.6 and I/C = 1 (in the case *I*/*C* = 0.6 and 1, some Pt/C nanoparticles may still experience a Pt | liquid electrolyte environment).

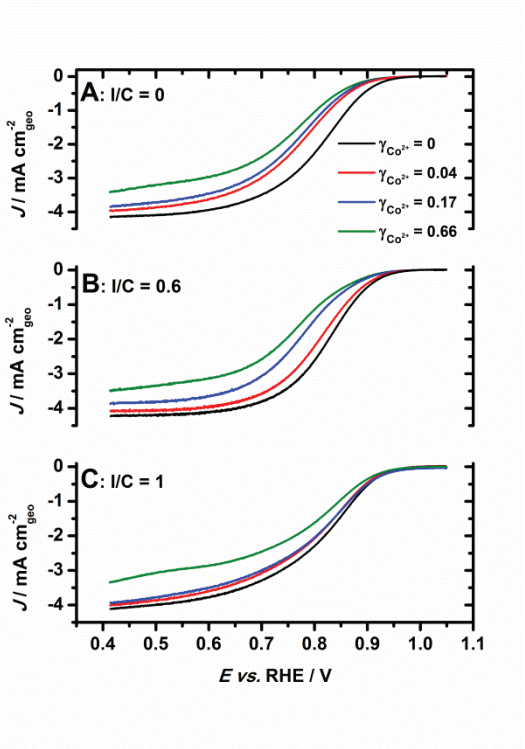

Figure V-7. Linear sweep ORR voltammograms, corrected from ohmic drop (the ohmic resistances range from 17 Ω cm^2 in 0.1 M H_2SO_4 to 19 Ω cm^2 in the most heavily cobalt polluted solution), for Pt/C in 0.1 M H_2SO_4 (γ_{Co}^{2+} = 0, black curves) and in Co^{2+} containing solution: γ_{Co}^{2+} = 0.04 (red curves), γ_{Co}^{2+} = 0.17 (blue curves) and γ_{Co}^{2+} = 0.66 (green curves). Several amount of Nafion® were added to the ink for the preparation of the porous RDE: (A) I/C = 0, (B) I/C = 0.6 and (C) I/C = 1. T = 298 ± 1 K, v = 0.001 V s^{-1}, ω = 900 rpm.

Electrochemical measurements were also performed to show whether any "recovery" was possible after contamination of the porous RDEs by Co^{2+} ions. For that purpose, the porous RDEs were transferred back from the most-concentrated Co^{2+} containing solution to the base 0.1 M H_2SO_4 solution after the ORR measurements. Figure V-8 shows that the ORR kinetic parameters of the aged RDEs nicely superpose with those measured on the "fresh" electrode. This result suggests that the observed changes of the rates of CO electrooxidation or ORR in Co^{2+}-containing solution are essentially linked to a modification of the double-layer structure, which will be discussed in Section 3.4. Also, the recovery of the intrinsic catalytic activity of the Pt/C surface agrees with the results reported by Kienitz *et al.* [13] on Cs contaminated MEAs.

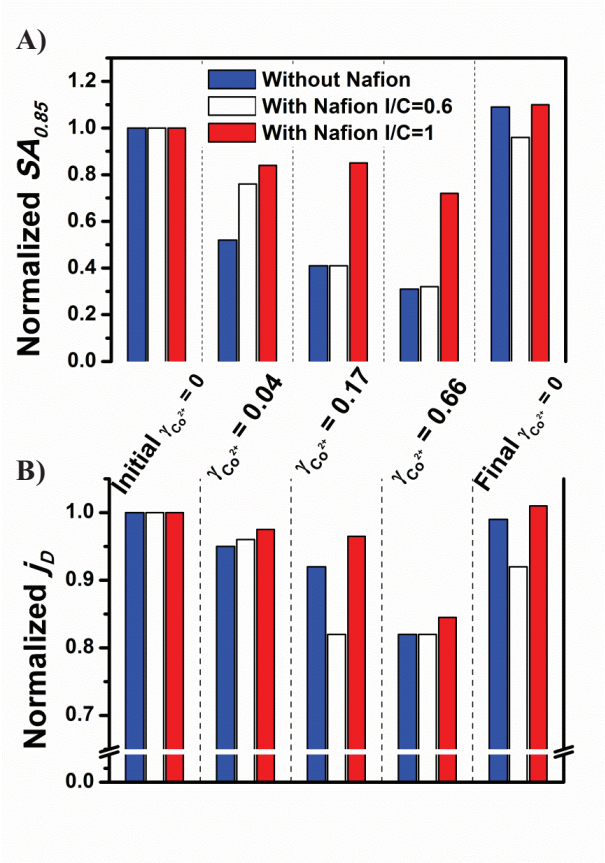

Figure V-8. (A) Normalized specific activities at E = 0.85 V vs. RHE ($SA_{0.85}$) and (B) normalized current densities (j_D) with respect to the "Initial γ_{Co}^{2+}=0" value in several cobalt containing solutions and with several amount of Nafion® added to the ink for the preparation of the porous RDE: (blue columns) I/C = 0, (white columns) I/C = 0.6 and (red columns) I/C = 1. T = 298 ± 1 K, v = 0.001 V s^{-1}, ω = 900 rpm.

IV. Effect of Co^{2+} ions at the 3-phase Pt | polymer | gas interface using a solid state cell (SSC)

1. Description of the SSC setup

A home-made SSC was developed to measure the electrocatalytic activity of Pt/C catalyst powders in contact with a proton conducting membrane which should mimic the Pt | polymer interface in a PEMFC (Figure V-1C). The use of such cells is motivated by the idea that the electrocatalytic behaviour of a catalyst in liquid supporting electrolyte differs in some points to its behaviour in a PEMFC environment. This SSC consists of a PEM (Nafion® 117, 1100 g mol^{-1} EW), a ultra-micro electrode with a cavity pressed on one of its side and a Pt counter electrode and a reference electrode (a RHE) pressed on its other side (see Figure V-1d). The cell is operated under controlled atmosphere, and allows examining the activity of Pt/C for the electrochemical CO_{ad} oxidation and the ORR. More information about the SSC can be found in the experimental section of this manuscript and in reference [29].

2. Preparation and quantification of the cobalt-contaminated membranes

The amount of contamination of the membrane is defined similarly as the amount of pollution of the liquid electrolyte (equation V-1), which allows comparing the experiments in both type of electrolyte (liquid and solid). Nafion® membranes were contaminated by replacing a fraction of the H^+ associated with the sulfonic acid groups with Co^{2+} ions, as detailed in Reference [18]. Nafion® 117 membranes were first acidified in 1 M H_2SO_4 for 2 two days at ambient temperature, then soaked in stirred solutions of 1 M H_2SO_4 with several amount of $CoSO_4$ over 1 week. To ensure that all $CoSO_4$ salt was removed from the PEM, the latter was rinsed in ultra-pure water (18.2 MΩ cm, < 3 ppb total organic carbon) over one week, the water being replaced every two days. The amount of contamination of the PEM was determined with X-ray energy dispersive spectroscopy measurements. Figure V-9 gives the isotherm of equilibrium of a cobalt doped-Nafion® 117 membrane with a cobalt-doped 0.1 M H_2SO_4 solution. This plot perfectly translates the higher affinity of the sulfonate groups of the Nafion® membrane towards cobalt ions than towards protons (at a given $\gamma_{Co^{2+},solution}$, $\gamma_{Co^{2+},membrane} > \gamma_{Co^{2+},solution}$). The trend of this curve agrees with the results obtained by Okada *et al.* [20] with Nafion® 117 membranes contaminated by other divalent cations (Fe^{2+}, Ni^{2+}, Cu^{2+}).

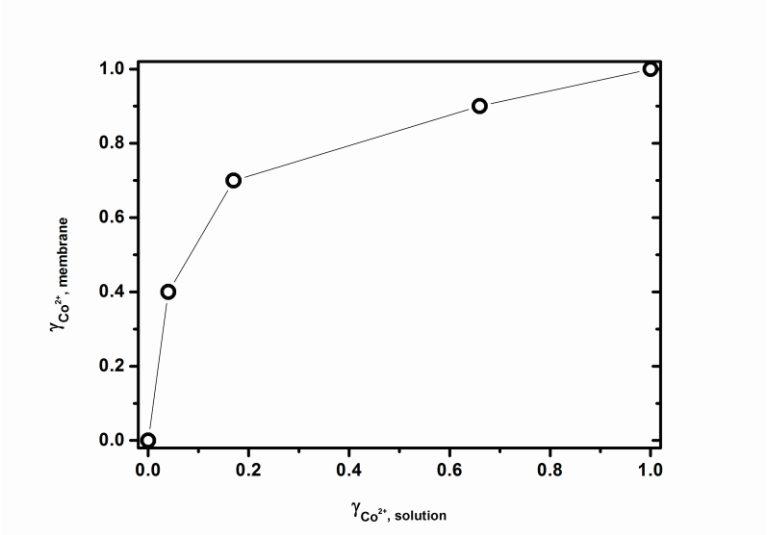

Figure V-9. Measured equilibrium contamination fraction of the membrane ($\gamma_{Co^{2+},membrane}$) as a function of the contamination fraction of the liquid solution the membranes were soaked in ($\gamma_{Co^{2+},solution}$).

3. CV and CO_{ad} stripping measurements in the SSC

Having convincingly shown that Co^{2+} ions modify the Pt surface reactivity both at the Pt | liquid and the Pt | polymer | liquid interfaces, we now focus on a pure Pt | solid electrolyte interface,

the structure of which is very similar to that observed in a MEA. Figure V-10 displays the cyclic voltammograms and the CO_{ad} monolayer oxidation voltammograms recorded in the SSC with a UMEC in contact with a Nafion® 117 in its H^+ form or with a cobalt-polluted Nafion® 117 membrane ($\gamma_{Co^{2+}} = 0.9$). The CV is greatly affected by the presence of Co^{2+} ions bounded to sulfonate sites: (i) the charge in the H_{upd} region is increased and (ii) the hydroxide/oxide layer formation on Pt is favoured when cobalt ions are present in the membrane.

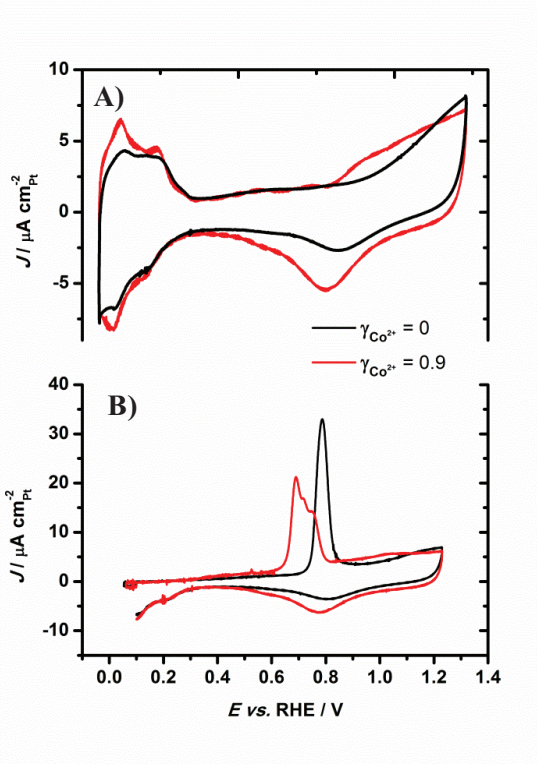

Figure V-10. Base (A) and CO_{ad} stripping voltammograms (B) for Pt/C in contact with a cobalt free Nafion® 117 ($\gamma_{Co^{2+}} = 0$) and a cobalt contaminated Nafion® 117 ($\gamma_{Co^{2+}} = 0.9$). T = 295 ± 3 K, v = 0.005 V s^{-1}.

4. ORR measurement in the SSC

Figure V-11A shows a marked decrease of the ORR rate both in the diffusion limited and in the kinetically controlled region of the CV with increasing values of $\gamma_{Co^{2+}}$. In the SSC, the changes induced on the kinetics of the CO_{ad} stripping oxidation (Figure V-10B) and the ORR can be easily rationalized by the favoured hydroxide/oxide layer formation on Pt observed on the CV. In the Tafel cathodic plots given in Figure V-11 for several cobalt-contaminated membranes, the ORR curves are gradually depreciated when the extent of contamination of the membrane increases. The decrease in the ORR kinetic currents in cobalt-contaminated membrane agrees with results obtained on caesium-polluted MEA during fuel cell experiments [13]. The ORR limiting current density (j_D) are greatly affected by the presence of cobalt in the membrane (Figure V-11A). These values are showing almost

a linear decrease with the extent of contamination of the membrane $\gamma_{M^{y+}}$ (with here $M^{y+} = Co^{2+}$) (Figure V-11C). Other data, collected from liquid electrolyte experiments (Figure V-8) and from caesium-polluted MEA fuel cell experiments [13], are added to Figure V-11C for the sake of comparison. Clearly, the values collected from the SSC experiments are exhibiting an intermediate behaviour between those collected in liquid electrolyte experiments, where the presence of solvated cobalt affects mainly the oxygen diffusion related parameters, and those collected in single cell tests, where the presence of caesium bounded to sulfonate sites are believed to decrease the availability of protons in the cathode catalyst layer.

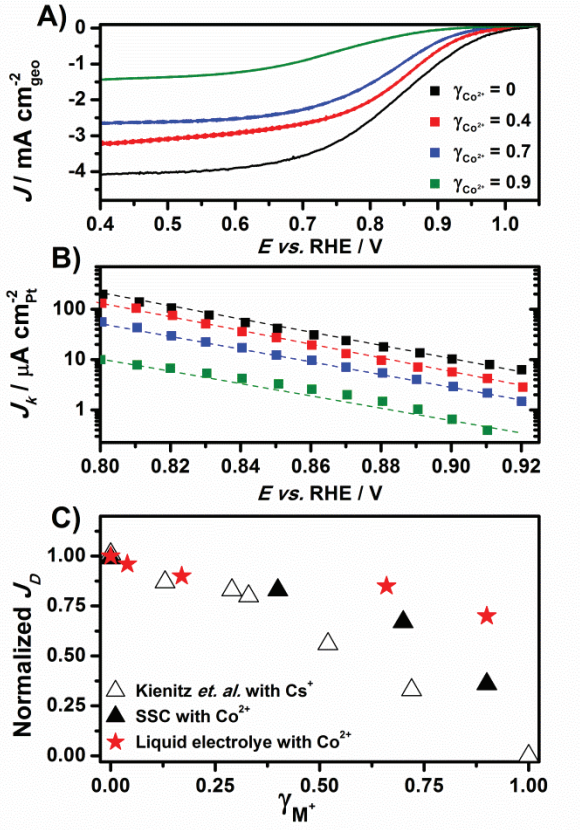

Figure V-11. (A) linear sweep ORR voltammograms for Pt/C in contact with cobalt-free ($\gamma_{Co^{2+}} = 0$) or cobalt-contaminated Nafion® 117 PEMs, (B) Tafel plots of the mass-transport corrected kinetic current obtained from the steady-state I-U curves at a rotation rate = 900 rpm, (C) normalized diffusion limited current for cobalt-free and cobalt-contaminated Nafion® 117 PEMs. Temperature = 22 ± 1°C, sweep rate = 0.001 V s^{-1}.

To determine the mechanism that limits the ORR in the mass transport limited region *i.e.* to settle which one from the protons or oxygen mass-transport is limiting in this SSC experiment, additional experiments were carried out. First, in Figure V-12A, a mild potential sweeping was performed in the hydrogen evolution region with a cobalt-free and a cobalt-contaminated Nafion® 117 PEM. The amount of H_2 generated from the reduction of H^+, largely superior to the amount of H_2O released during the ORR, suggests that the ORR kinetics in the SSC is not limited by the concentration

of H^+, even in heavily Co^{2+} contaminated PEMs. A sampled-current voltammetry was also performed in the same conditions (Figure V-12). In this technique [48], the electrode potential continuously alternates between an electrode potential where the faradic reaction proceeds *(*E_1 = 0.4, 0.5, 0.6, 0.7, 0.8, 0.85, 0.9 or 0.95 V *vs.* RHE) and a potential where the faradic reaction does not occur (E_2 = 1 V *vs.* RHE). During the rest period at E_2 *(*t = 1 minute), the solution is purged by O_2 so as to restore the O_2 concentration at the vicinity of the Pt/C surface. At the electrode potential E_1, O_2 purging is stopped to avoid any transport by convection, and the ORR current is measured after different sampling times (t = 0.2 s (square symbols) or t = 10 s (triangle symbols)). For the longer sampling time (t = 10 s), the SCVs feature three distinct zones: (i) a kinetic region above 0.90 V *vs.* RHE, (ii) a mixed diffusion-kinetic limitation region (0.75 < E < 0.90 V), and (iii) a diffusion controlled region (E < 0.75V), similarly to the experiments performed in the porous RDE or SSC configuration. Clearly, the rate of the ORR is slightly varying between the fresh and Co^{2+} contaminated Nafion® 117 PEM. More interesting are the ORR currents measured after t = 0.2 s. When the Pt/C surface is in contact with a cobalt-free Nafion® 117 PEM, the larger values of the measured current indicate that more oxygen molecules are able to diffuse through the ionomer within this timeframe to be further reduced at the Pt/C surface, with respect to a Co^{2+} contaminated Nafion® membrane. In the light of these results, one can conclude that the O_2 transport properties limit the ORR performance in the SSC configuration and that on the contrary protons are not limiting the ORR in our experimental conditions. This result could also have been predicted from the work of Greszler *et. al.* [18] with the following equation:

$$i_{\mathrm{protonlimited}} = \frac{K_{\mathrm{limited}}\kappa^0_{\mathrm{H+}}RT}{Ft_{\mathrm{membrane}}} \qquad \text{Eq. V-8}$$

where $i_{\mathrm{protonlimited}}$, the maximum ORR current in a PEMFC in the case of a proton limiting mechanism, is given for any average cation fraction in a membrane. K_{limited} is a dimensionless factor related to the average cation fractional occupancy in the membrane, κ^0_{H+} is the conductivity of the membrane (in S cm^{-1}) and t_{membrane} is the membrane thickness (in cm). The other parameters have their usual meanings. In the case of the most heavily cobalt polluted ($\gamma_{Co^{2+}} = 0.9$, $K_{\mathrm{limited}} \approx 0.5$) Nafion® 117 membrane ($\kappa^0_{H+} \approx$ 0.1 S cm^{-1}, t_{membrane} = 0.0175 cm) [49] one obtains $i_{\mathrm{protonlimited}} \approx$ 70 mA cm^{-2}_{geo}, which is almost 50 times greater than the present experimental ORR limiting current (Figure V-11A).

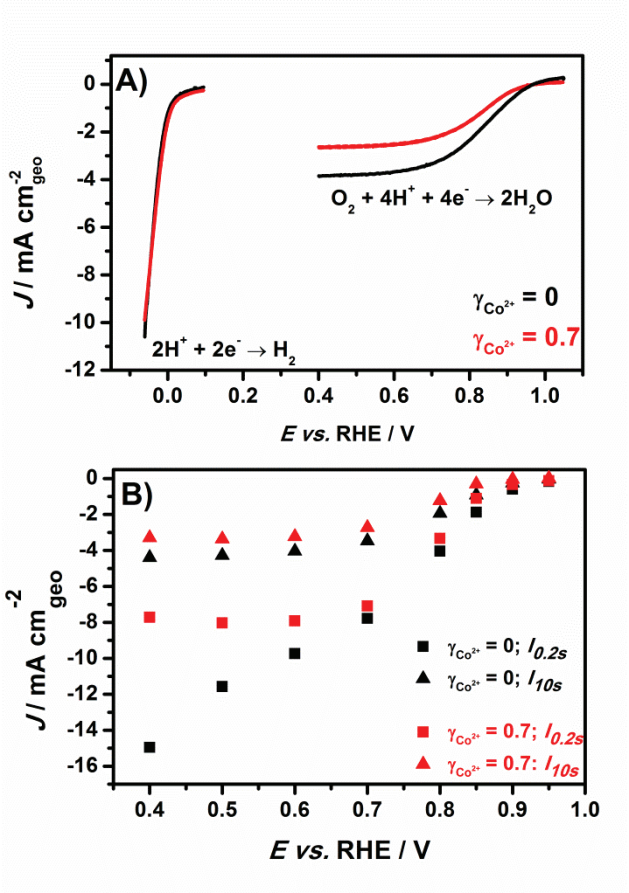

Figure V-12. (A) Linear sweep ORR voltammograms for Pt/C in contact with a pure Nafion® 117 ($\gamma_{Co^{2+}}$= 0, black curves) and a Co-contaminated Nafion® 117 ($\gamma_{Co^{2+}}$= 0.7, red curves) and linear sweep voltammograms in argon saturated solution in the hydrogen formation region, (B) sampled-current voltammetry in an oxygen saturated SSC with a pure Nafion® 117 ($\gamma_{Co^{2+}}$= 0, black symbols) and a Co-contaminated Nafion® 117 ($\gamma_{Co^{2+}}$= 0.7, red symbols). The current is sampled after 0.2 s (square symbols) and after 10 s (triangle symbols).

Summing up, contrary to the common belief, it is the oxygen transport that mainly limits the ORR in the SSC experiments and not that of protons, even for Co^{2+}-contaminated membranes. Similar to the results obtained in liquid electrolyte, we assumed that the ORR mechanism remains largely unchanged for the cobalt-free and the cobalt-contaminated PEMs [28]. As argued in the experimental section, in the SSC configuration, O_2 molecules have to cross over the Nafion® 117 PEM before reacting on the Pt/C surface. Various models have been used in the literature to describe the structure of the Nafion® PEMs but most of them proposed that ionic clusters are distributed in a hydrophobic polymeric matrix ("inverse micelles") [50-53]. Upon swelling, the ionic clusters then aggregate to form a network where protons can efficiently be transported. In the SSC configuration, it is believed that O_2 molecules diffuse through this network from the gas atmosphere to the Pt/C surface, where they are reduced. The decrease of j_D with the increase of $\gamma_{Co^{2+}}$ suggests that the size of the hydrophilic channels connecting the ionic clusters is severely decreasing upon pollution with Co^{2+}

[54]. This is in line with previous observations, [20, 42, 55] which have shown reduced water uptake as the contamination level increases. Therefore, it can be postulated that the fast decrease of the diffusion limited current in the SSC configuration mainly reflects the changes in the size/connection of the hydrophilic domains of the PEM.

V. Representations of the nano-scale interactions of solvated cations with a platinum surface

From all our results we are now able to answer, or at least give some lead, how cations interact with platinum interfaces in simple two phase interfaces or in more complicated three-phase interfaces, such as in a PEMFC active layer. The results obtained are graphically summarized in Figure V-13. At the Pt | liquid interface - at electrode potential above the point of zero charge (PZC) - water molecules, dissociated water molecules (OH_{ad}) and sulphate anions are chemisorbed in the inner Helmholtz plane (IHP). The centre of the electrical charge of the solvated counter cations is located in the outer Helmholtz plane (OHP). As suggested by Strmcnik *et al*. [24], some of the solvated counter cations partially lose their hydration shell and come closer to the Pt surface, yielding increased OH_{ad} coverage ("non-covalent" interactions). The more facile OH_{ad} formation on Pt in the presence of Co^{2+} ions enhances the CO_{ad} electrooxidation kinetics and depreciates the rate of the ORR in the kinetically-controlled region of the ORR curves ("site blocking" effect). Changes in the diffusion limited region of the ORR curves are rationalized on the basis of reduced values of the O_2 mass-transport.

At the Pt | polymer | liquid interface, the impact of Co^{2+} cations is modulated, which can be accounted for by considering different double layer structures on a Nafion®-free and on a Nafion®-covered Pt/C surface. Indeed, at the latter and at electrode potential above the PZC, the positive charge carried by the Pt surface may cause the adsorption of the sulfonic acid groups or electrostatic interactions with the fluorinated backbone of the perfluorosulfonated ionomer. Consequently, the Co^{2+} ions interacting with the sulfonate groups of the ionomer (they have replaced H^+) are repelled from the surface further from the OHP.

Finally, the experiments performed at the Pt | polymer | gas interface unambiguously show that the O_2 transport properties limit the ORR performance in a configuration that is close to that encountered in a PEMFC environment. These changes are tentatively explained by the reduced water uptake at saturation, which we believe translates by a decrease in the size of the channels connecting the hydrophilic domains of the Nafion® PEM/ionomer, that adversely affects O_2 transport.

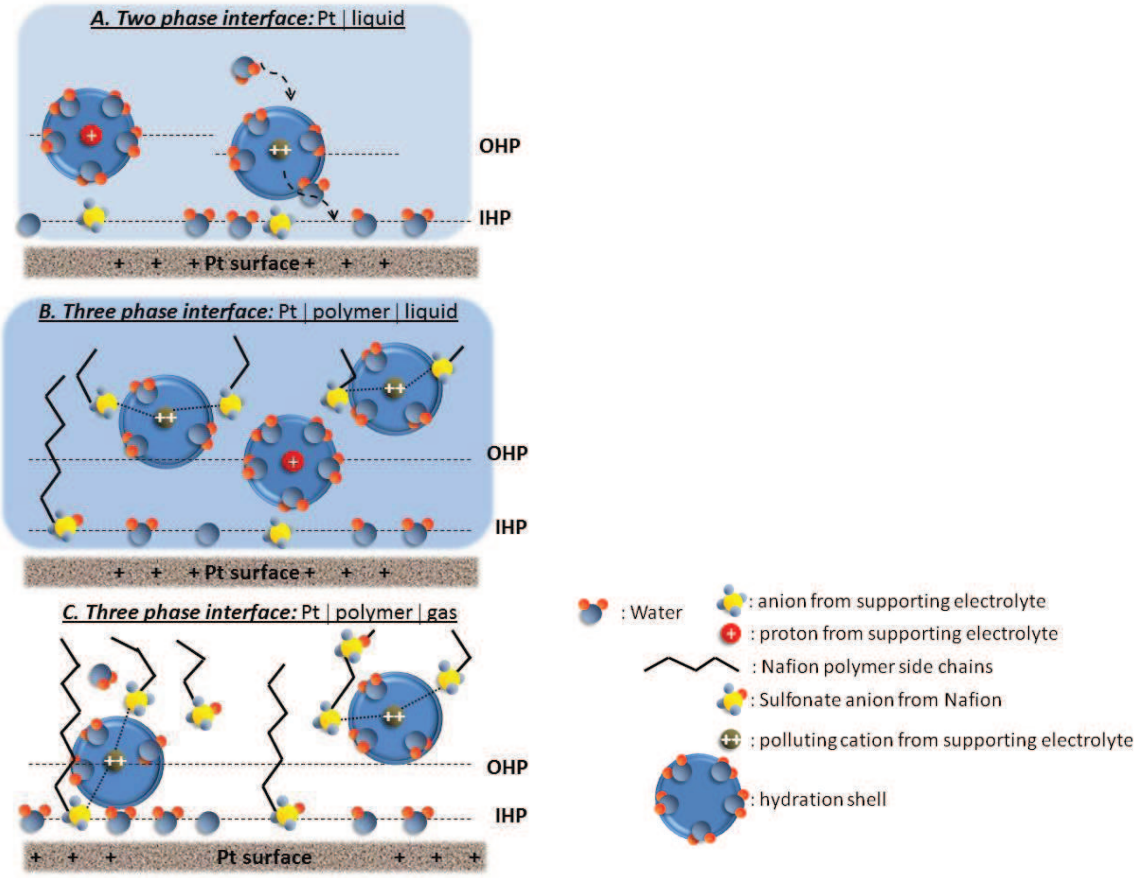

Figure V-13. Sketches of (A) two-phase Pt /liquid interface, (B) three-phase Pt /polymer /liquid interface and (C) three-phase Pt /polymer /gas interface in the presence of solvated metal cations.

VI. Conclusion

Metal/alloy nanoparticles dissolution upon PEMFC long-term operation is a well-known issue at the cathode of a PEMFC, especially when state-of-the-art Pt-M/C electrocatalysts are used (M being a 3d transition metal). While it is commonly admitted that the metal cations generated upon the cathode electrocatalyst corrosion do contaminate the ionomer and hinder the ORR kinetics, little is known about the mechanisms at stake in these processes. In this chapter, model Pt/C nanoparticles coated or not with a perfluorosulfonated ionomer, were studied for the CO electrooxidation reaction and the ORR in the presence of metal cations in the electrolyte phase(s). The study was performed for three electrode-electrolyte configurations: (i) Pt/C RDE | liquid electrolyte interface, (ii) Pt/C RDE | polymer | liquid electrolyte interface and Pt/C UMEC | polymer electrolyte | gas phase. The results assert that metal cations enhance the adsorption of oxygen species (water) at the Pt surface and therefore do negatively impact the ORR kinetics, whatever the nature of the Pt/C | electrolyte interface. In addition, we provide indubitable evidence that the electrolyte contamination heightens the

mass-transport resistance of molecular oxygen more than the proton resistance, even for solid polymer electrolytes, a configuration mimicking that encountered in real PEMFC conditions.

VII. References

[1] Chen S., Gasteiger H. A., Hayakawa K., Tada T. and Shao-Horn Y., Platinum-alloy cathode catalyst degradation in proton exchange membrane fuel cells: Nanometer-scale compositional and morphological changes. *J. Electrochem. Soc.*, 157 (2010) A82-A97.

[2] Dubau L., Durst J., Maillard F., Guétaz L., Chatenet M., André J. and Rossinot E., Further insights into the durability of Pt_3Co/C electrocatalysts: Formation of "hollow" Pt nanoparticles induced by the Kirkendall effect. *Electrochim. Acta*, 56 (2011) 10658-10667.

[3] Ball S. C., Hudson S. L., Theobald B. R. and Thompsett D., Enhanced stability of PtCo catalysts for PEMFC. *ECS Trans.*, 8 (2006) 141-152.

[4] Ball S. C., Hudson S. L., Theobald B. R. and Thompsett D., PtCo, a durable catalyst for automotive PEMFC? *ECS Trans.*, 11 (2007) 1267-1278.

[5] Zamel N. and Li X., Effect of contaminants on polymer electrolyte membrane fuel cells. *Prog. Energ. Comb. Sci.*, 37 (2011) 292-329.

[6] Guilminot E., Corcella A., Charlot F., Maillard F. and Chatenet M., Detection of Pt^{z+} ions and Pt nanoparticles inside the membrane of a used PEMFC. *J. Electrochem. Soc.*, 154 (2007) B96-B105.

[7] Ferreira P. J., la O' G. J., Shao-Horn Y., Morgan D., Makharia R., Kocha S. and Gasteiger H. A., Instability of Pt/C electrocatalysts in proton exchange membrane fuel cells - A mechanistic investigation. *J. Electrochem. Soc.*, 152 (2005) A2256-A2271.

[8] Burlatsky S. F., Gummalla M., Atrazhev V. V., Dmitriev D. V., Kuzminyh N. Y. and Erikhman N. S., The Dynamics of Platinum Precipitation in an Ion Exchange Membrane. *J. Electrochem. Soc.*, 158 (2011) B322-B330.

[9] Ettingshausen F., Kleemann J., Marcu A., Toth G., Fuess H. and Roth C., Dissolution and migration of platinum in PEMFCs investigated for start/stop cycling and high potential degradation. *Fuel Cells*, 11 (2011) 238-245.

[10] Yasuda K., Taniguchi A., Akita T., Ioroi T. and Siroma Z., Platinum dissolution and deposition in the polymer electrolyte membrane of a PEM fuel cell as studied by potential cycling. *Phys. Chem. Chem. Phys.*, 8 (2006) 746-752.

[11] Ferreira P. J., La O' G. J., Shao-Horn Y., Morgan D., Makharia R., Kocha S. and Gasteiger H. A., Instability of Pt/C electrocatalysts in proton exchange membrane fuel cells. *J. Electrochem. Soc.*, 152 (2005) A2256-A2271.

[12] Xie J., Wood D. L., Wayne D. M., Zawodzinski T. A., Atanassov P. and Borup R. L., Durability of PEFCs at high humidity conditions. *J. Electrochem. Soc.*, 152 (2005) A104-A113.

[13] Kienitz B., Pivovar B., Zawodzinski T. and Garzon F. H., Cationic contamination effects on polymer electrolyte membrane fuel cell performance. *J. Electrochem. Soc.*, 158 (2011) B1175-B1183.

[14] Common Thermodynamic Databse Project: http://www.ctdp.org

[15] Li H., Gazzarri J., Tsay K., Wu S. H., Wang H. J., Zhang J. J., Wessel S., Abouatallah R., Joos N. and Schrooten J., PEM fuel cell cathode contamination in the presence of cobalt ion (Co^{2+}). *Electrochim. Acta*, 55 (2010) 5823-5830.

[16] Li H., Tsay K., Wang H. J., Shen J., Wu S. H., Zhang J. J., Jia N. Y., Wessel S., Abouatallah R., Joos N. and Schrooten J., Durability of PEM fuel cell cathode in the presence of Fe^{3+} and Al^{3+}. *J. Power Sources*, 195 (2010) 8089-8093.

[17] Mikkola M. S., Rockward T., Uribe F. A. and Pivovar B. S., The effect of NaCl in the cathode air stream on PEMFC performance. *Fuel Cells*, 7 (2007) 153-158.

[18] Greszler A., Moylan T. and Gasteiger H. A., Modeling the impact of cation contamination in a polymer electrolyte membrane fuel cell, in *Handbook of Fuel Cells: Fundamentals, Technology, and Applications*, Vol. 4, Vielstich W., Gasteiger H. A. and Yokokawa H. 2009, John Wiley & Sons

[19] Cipollini N. E., Chemical aspects of membrane degradation. *ECS Trans.*, 11 (2007) 1071-1082.

[20] Okada T., Ayato Y., Yuasa M. and Sekine I., The effect of impurity cations on the transport characteristics of perfluorosulfonated ionomer membranes. *J. Phys. Chem. B*, 103 (1999) 3315-3322.

[21] Kelly M. J., Fafilek G., Besenhard J. O., Kronberger H. and Nauer G. E., Contaminant absorption and conductivity in polymer electrolyte membranes. *J. Power Sources*, 145 (2005) 249-252.

[22] Iojoiu C., Guilminot E., Maillard F., Chatenet M., Sanchez J. Y., Claude E. and Rossinot E., Membrane and active layer degradation following PEMFC steady-state operation. *J. Electrochem. Soc.*, 154 (2007) B1115-B1120.

[23] Luo Z., Li D., Tang H., Pan M. and Ruan R., Degradation behavior of membrane-electrode-assembly materials in 10-cell PEMFC stack. *Int. J. Hydrog. Energy*, 31 (2006) 1831-1837.

[24] Strmcnik D., Kodama K., van der Vliet D., Greeley J., Stamenkovic V. R. and Markovic N. M., The role of non-covalent interactions in electrocatalytic fuel-cell reactions on platinum. *Nat. Chem.*, 1 (2009) 466-472.

[25] Stoffelsma C., Rodriguez P., Garcia G., Garcia-Araez N., Strmcnik D., Markovic N. M. and Koper M. T. M., Promotion of the oxidation of carbon monoxide at stepped platinum single-crystal electrodes in alkaline media by lithium and beryllium cations. *J. Am. Chem. Soc.*, 132 (2010) 16127-16133.

[26] Garcia N., Climent V., Orts J. M., Feliu J. M. and Aldaz A., Effect of pH and alkaline metal cations on the voltammetry of Pt(111) single crystal electrodes in sulfuric acid solution. *Chem. Phys. Chem.*, 5 (2004) 1221-1227.

[27] Garcia-Araez N., Climent V., Rodriguez P. and Feliu J. M., Thermodynamic evidence for K^+-SO_4^{2-} ion pair formation on Pt(111). New insight into cation specific adsorption. *Phys. Chem. Chem. Phys.*, 12 (2010) 12146-12152.

[28] Okada T., Ayato Y., Dale J., Yuasa M., Sekine I. and Asbjornsen O. A., Oxygen reduction kinetics at platinum electrodes covered with perfluorinated ionomer in the presence of impurity cations Fe^{3+}, Ni^{2+} and Cu^{2+}. *Phys. Chem. Chem. Phys.*, 2 (2000) 3255-3261.

[29] Vion-Dury B., Mécanismes de vieillissement des électrocatalyseurs de pile à combustible de type PEMFC, 2011, Grenoble INP, Grenoble.

[30] Herrero E., Li J. and Abruna H. D., Electrochemical, *in-situ* surface EXAFS and CTR studies of Co monolayers irreversibly adsorbed onto Pt(111). *Electrochim. Acta*, 44 (1999) 2385-2396.

[31] Maillard F., Schreier S., Hanzlik M., Savinova E. R., Weinkauf S. and Stimming U., Influence of particle agglomeration on the catalytic activity of carbon-supported Pt nanoparticles in CO monolayer oxidation. *Phys. Chem. Chem. Phys.*, 7 (2005) 385-393.

[32] Cherstiouk O. V., Gavrilov A. N., Plyasova L. M., Molina I. Y., Tsirlina G. A. and Savinova E. R., Influence of structural defects on the electrocatalytic activity of platinum. *J. Solid State Electrochem.*, 12 (2008) 497-509.

[33] Li H., Tsay K., Wang H. J., Wu S. H., Zhang J. J., Jia N. Y., Wessel S., Abouatallah R., Joos N. and Schrooten J., Effect of Co^{2+} on oxygen reduction reaction catalyzed by Pt catalyst, and its implications for fuel cell contamination. *Electrochim. Acta*, 55 (2010) 2622-2628.

[34] Strbac S., The effect of pH on oxygen and hydrogen peroxide reduction on polycrystalline Pt electrode. *Electrochim. Acta*, 56 (2011) 1597-1604.

[35] Roche I., Chainet E., Chatenet M. and Vondrak J., Carbon-supported manganese oxide nanoparticles as electrocatalysts for the Oxygen Reduction Reaction (ORR) in alkaline medium: Physical characterizations and ORR mechanism. *J. Phys. Chem. C*, 111 (2007) 1434-1443.

[36] Denuault G., Mirkin M. V. and Bard A. J., Direct determination of diffusion-coefficients by chronoamperometry at microdisk electrodes. *J. Electroanal. Chem.*, 308 (1991) 27-38.

[37] Wang K. L., Lu J. T. and Zhuang L., Direct determination of diffusion coefficient for borohydride anions in alkaline solutions using chronoamperometry with spherical Au electrodes. *J. Electroanal. Chem.*, 585 (2005) 191-196.

[38] Dubau L., Maillard F., Chatenet M., André J. and Rossinot E., Nanoscale compositional changes and modification of the surface reactivity of Pt_3Co/C nanoparticles during proton-exchange membrane fuel cell operation. *Electrochim. Acta*, 56 (2010) 776-783.

[39] Gan F. and Chin D. T., Determination of diffusivity and solubility of oxygen phosphoric-acid using a transit-time on a rotating ring disc electrode. *J. Appl. Electrochem.*, 23 (1993) 452-455.

[40] Lozar J., Bachelot B., Falgayrac G. and Savall A., Diffusivity and solubility measurement of oxygen in water acetic acid sodium acetate solutions on a rotating ring disc electrode. *Electrochim. Acta*, 43 (1998) 3293-3296.

[41] Bruckenstein S. and Feldman G. A., Radial transport times at rotating ring-disk electrodes. Limitations on the detection of electrode intermediates undergoing homogeneous chemical reactions. *J. Electroanal. Chem.*, 9 (1965) 395.

[42] Okada T., Ayato Y., Satou H., Yuasa M. and Sekine I., The effect of impurity cations on the oxygen reduction kinetics at platinum electrodes covered with perfluorinated ionomer. *J. Phys. Chem. B*, 105 (2001) 6980-6986.

[43] Okada T., Effect of ionic contaminants, in *Handbook of Fuel Cells: Fundamentals, Technology, and Applications*, Vol. 3, Vielstich W., Gasteiger H. A. and Lamm A. 2003, John Wiley & Sons

[44] Subbaraman R., Strmcnik D., Paulikas A. P., Stamenkovic V. R. and Markovic N. M., Oxygen reduction reaction at three-phase interfaces. *Chem. Phys. Chem.*, 11 (2010) 2825-2833.

[45] Subbaraman R., Strmcnik D., Stamenkovic V. and Markovic N. M., Three phase interfaces at electrified metal-solid electrolyte systems 1. Study of the Pt(hkl)-Nafion® interface. *J. Phys. Chem. C*, 114 (2010) 8414-8422.

[46] Liu Y. X., Ji C. X., Gu W. B., Baker D. R., Jorne J. and Gasteiger H. A., Proton conduction in PEM fuel cell cathodes: Effects of electrode thickness and ionomer equivalent weight. *J. Electrochem. Soc.*, 157 (2009) B1154-B1162.

[47] More K., Borup R. and Reeves K., Identifying contributing degradation phenomena in PEM fuel cell membrane electride assemblies *via* electron microscopy. *ECS Trans.*, 3 (2006) 717-733.

[48] Bard A. J. and Faulkner L. R., Electrochemical methods,(1993), John Wiley & Sons, Inc.

[49] Slade S., Campbell S. A., Ralph T. R. and Walsh F. C., Ionic conductivity of an extruded Nafion® 1100 EW series of membranes. *J. Electrochem. Soc.*, 149 (2002) A1556-A1564.

[50] Heitner-Wirguin C., Recent advances in perfluorinated ionomer membranes: Structure, properties and applications. *J. Membr. Sci.*, 120 (1996) 1-33.

[51] Gierke T. D. and Hsu W. Y., The cluster-network model of ion clustering in perfluorosulfonated membranes. *ACS Symp. Ser.*, 180 (1982) 283-307.

[52] Mauritz K. A. and Moore R. B., State of understanding of Nafion®. *Chem. Rev.*, 104 (2004) 4535-4585.

[53] Rubatat L., Rollet A. L., Gebel G. and Diat O., Evidence of elongated polymeric aggregates in Nafion®. *Macromolecules*, 35 (2002) 4050-4055.

[54] Mani A. and Holdcroft S., Highly temperature dependent mass-transport parameters for ORR in Nafion® 211. *J. Electroanal. Chem.*, 651 (2011) 211-215.

[55] Okada T., Satou H., Okuno M. and Yuasa M., Ion and water transport characteristics of perfluorosulfonated ionomer membranes with H^+ and alkali metal cations. *J. Phys. Chem. B*, 106 (2002) 1267-1273.

Chapter VI.

"In-the-plane" and "Through-the-plane" heterogeneities of aging within a PEMFC MEA

The results discussed in this chapter have been published in:

Dubau L., **Durst J.**, Maillard F., Chatenet M., André J., Rossinot E.:
Heterogeneities of aging within a PEMFC MEA.
Published in: *Fuel Cells*, 12 (2012), pp. 188-198

I. Origins of “In-the-plane” and “Through-the-plane” aging heterogeneities

Despite some (mere) studies pointing towards localized phenomena (*e.g.* relative to the PEM [1-4] or CL [4-6] degradation), it is striking to note that PEMFC membrane-electrode assembly (MEA) is generally considered to age homogeneously. Considering that oxygen and hydrogen are consumed and water produced/accumulated along the gas channel, this fact cannot be taken as granted: it should indeed yield in-the-plane heterogeneities, as demonstrated by local measurements of the heterogeneous current distribution within individual MEA [7-10]. Also, it is now well-established that the part of the CL located close to the membrane works more efficiently than that located close to the gas-diffusion layer (GDL), because the ionic path there is much smaller; this should drive through-the-plane heterogeneities, yielding different aging rates and/or mechanisms at the GDL | CL and CL | PEM interfaces [5, 6, 11]. Obviously, such heterogeneous aging within individual MEA is very prone to be accentuated by the operating conditions: current density, stoichiometry, relative humidity, temperature etc. but very few studies have focused on this issue so far. Two scales of heterogeneities appearing during PEMFC operation that can directly impact the degradation of the cathode catalyst layer have been identified (Figure VI-1), and will be explored in the present chapter.

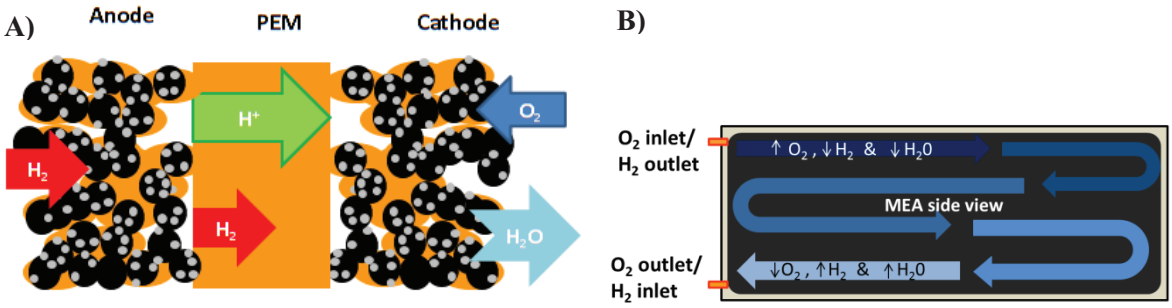

Figure VI-1. Scheme of the two levels of heterogeneities that can be found within a single MEA: (A) through-the-plane, i.e. from the anode to the cathode and especially from PEM | Cathode to the Cathode | GDL interface, and (B) in-the-plane, i.e. from the cathode inlet (facing the anode outlet) to the cathode outlet (facing the anode inlet) in a counter-flow configuration.

We will first try to unveil through-the-plane (from the GDL | CL to the CL | PEM interface of the cathode CL, Figure VI-1A) heterogeneities of aging. For that purpose, ultramicrotomed thin slices of MEAs operated in various operating conditions were prepared and thoroughly analyzed in field-emission gun scanning electron microscopy (FEG-SEM) and transmission electron microscopy (TEM). These tools were used to isolate the catalyst morphology changes (density over the carbon substrate, size, shape, extent of agglomeration) within the CL thickness.

In the second part of this chapter, we will investigate in-the-plane (along the gas channel, *i.e.* from the cathode inlet to the cathode outlet, Figure VI-1B) degradation heterogeneities of the cathode

catalyst that appear upon long-term PEMFC aging. It is worth to point out that the MEA were operated in counter-flow mode, meaning that the cathode inlet faces the anode outlet and the cathode outlet faces the anode inlet. As concerned with this second type of heterogeneities, never reported so far in the literature to the best of our knowledge, the cathode inlet and outlet regions of the MEA were thoroughly and quantitatively surveyed on a comparative basis. For that purpose, aging markers such as the presence/absence of Pt nanoparticles in the PEM (from FEG-SEM analyses on ultramicrotomed MEA), the mean particle size, particle density and morphology (isolated *vs.* agglomerated) (all determined from TEM), the mean crystallite size (from X-ray diffraction, XRD) and the chemical composition (either relative to the crystalline particles: XRD, or to the whole population of particles on a global (ICP-AES) or local (X-ray energy dispersive spectroscopy, TEM/X-EDS) were compared for the cathode electrocatalysts at the inlet (IN) or outlet (OUT) regions of the cathode. All these characterization techniques were performed very locally, close to each inlet/outlet, as depicted in Figure VI-2.

To give more strength to this study, additional experiments using a segmented cell approach (with the cathode being segmented in 20 segments along the gas flow channel, and having the same cell geometry than that use to age the MEA by Axane) will be presented at the end of the chapter.

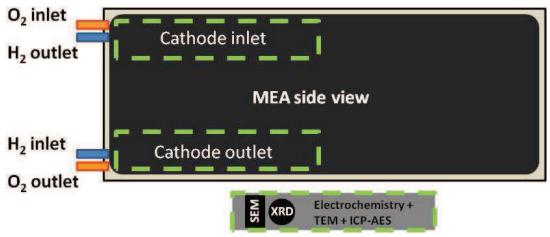

Figure VI-2: Schematic representation of the localization of the regions investigated with physico-chemical analyses.

II. Through the plane heterogeneities

Through-the-plane heterogeneities at the cathode were studied for samples taken from the cathode inlet of the aged MEA (see Figure VI-1), where the operating conditions regarding liquid and gas mass transport are better managed than at the cathode outlet (unlikely accumulation of liquid water). Experiments were performed on the same MEAs (with initially a Pt_3Co/C cathode) that underwent the same aging procedures (stationary aging at I = 20 A for t = 1341 h and I = 50 A for t = 1024 h) than in **Chapter III**. For the sake of convenience, we present in this chapter the results obtained only on the MEA aged at I = 20 A for t = 1341 h. Indeed, the data obtained on the MEA aged

at I = 50 A for t = 1024 h, published by Dubau *et al.* [12], are similar regarding most of the points detailed hereafter.

TEM images of the aged ultramicrotomed MEA, with a special focus at different positions of the cathode catalyst, are given in Figure VI-3. The particle size distributions (PSD) of the cathode electrocatalyst were evaluated at the two interfaces (Figure VI-4). In agreement with [12], Figure VI-4 evidences (i) a decrease of the fraction of the smallest particles, (ii) an increase of the mean particle size, (iii) a significant tailing on the large diameter side of the particle size distribution after PEMFC operation. Those nm-scale changes of the particle morphology agree with an Ostwald ripening mechanism, as discussed in **Chapter III**. Of particular interest in Figure VI-4 is that the changes are function of the “through-the-plane” position within the cathode CL. In particular, the loss of the smallest particles and the increased fraction of agglomerated large particles (the size of which ranges between 10 to 15 nm) is more important at the CL | PEM interface relative to the GDL | CL interface. Those features translate into an increased mean particle size close to the PEM relative to the GDL. In a PEMFC, Ostwald ripening is believed to occur in three dimensions and the inter-particle transport is ensured by the diffusion of Pt^{z+} ionic species, while the growth of the particles follows the electrochemical/chemical redeposition of these ions. In the present study, the increased mean particle size and the increased fraction of agglomerated particles at the CL | PEM interface is likely a consequence of the higher probability for Pt^{z+} to be reduced by H_2 crossing over the PEM (the concentration of H_2 coming from the anode side is obviously higher at this interface). Conversely, Pt^{z+} ionic species produced close to the GDL are more prone to be washed by water and to leave the cell.

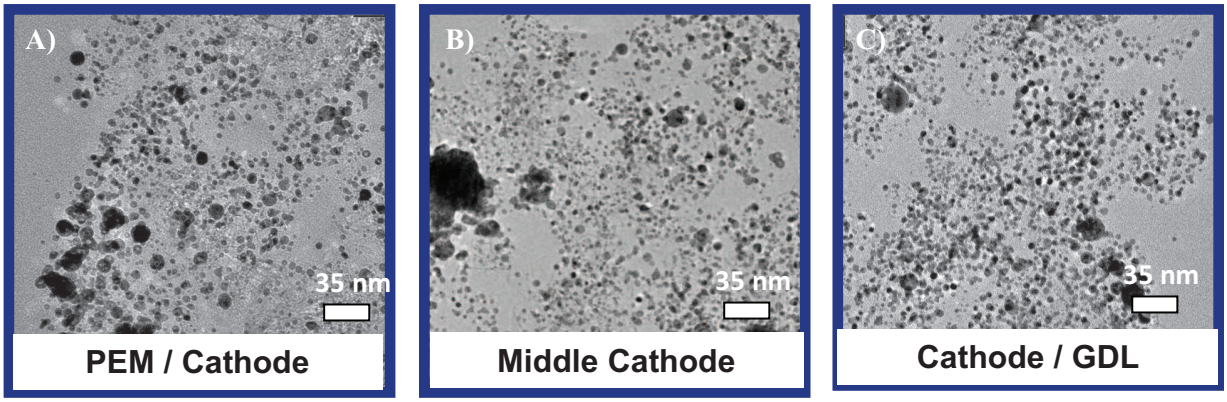

Figure VI-3. Characteristic TEM images of the cathode catalyst aged at I = 20 A for t = 1341 h relative to (A) the PEM/ Cathode interface, (B) the middle of the cathode and (C) the Cathode/ GDL.

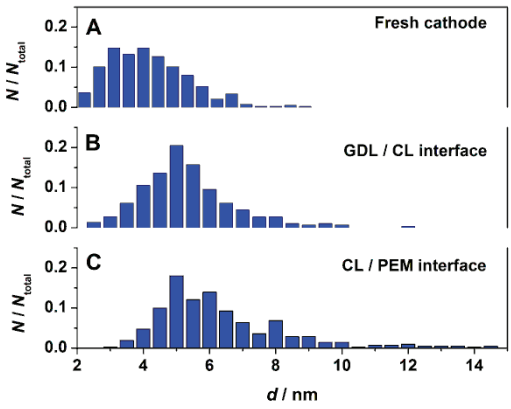

Figure VI-4. Particle size distribution of (A) the fresh and the 1341h aged Pt-Co/C electrocatalyst (B) at the GDL │CL interface and (C) at the CL │PEM interface evaluated from TEM images on ultramicrotomed MEAs.

In Figure VI-5, the fraction of isolated and agglomerated particles estimated from TEM images of the fresh/aged cathode electrocatalyst is presented. In agreement with [12], a pronounced increase of the fraction of agglomerated particles is observed at the expanse of the fraction of isolated particles (the density of isolated/agglomerated nanoparticles amounts to 14350/650 particles per μm^2 of carbon, respectively). These features are classical in durability studies of PEMFC materials and can be accounted for by the occurrence of Ostwald ripening and crystallite migration [13, 14]. Interestingly, the total number of particles (isolated + agglomerated) is larger at the GDL | CL interface relative to the CL | PEM interface. Combined with the larger decrease of the amount of isolated particles, these features point towards more pronounced degradation of the CL | PEM region of the cathode.

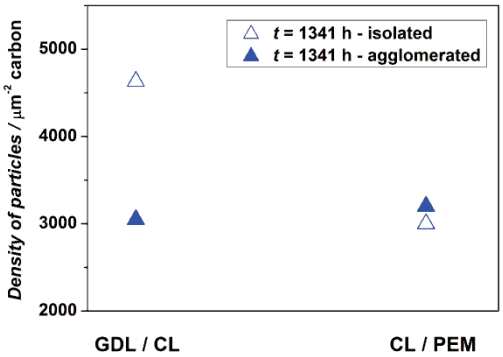

Figure VI-5. Density of isolated particles (open triangles) and agglomerated particles (filled triangles) for the 1341 h aged cathode catalyst

Figure VI-6C shows the FEG-SEM image of an ultramicrotomed slice of the MEA operated during t = 1341 h at I = 20 A (the GDL/CL interface being located at the left and the CL/PEM interface at the right). X-EDS analyses were performed on ten identical rectangles (L = 29 µm, l = µm, e = 90 nm (the thickness of the ultramicrotomed sample) equating to a volume analyzed of *ca.* V = 2 μm^3) defined “through-the-plane” in the cathode catalyst layer. Performing X-EDS on an ultramicrotomed slice allows a great spatial resolution of the analysis (due to the limited depth/sphere of interaction of the X-ray fluorescence zone) *i.e.* much greater than on a classical non-ultramicrotomed sample. The large volume analyzed (V = 1.8 μm^3) also gives statistical relevance to this measurement.

First, the Pt:Co atomic ratio (Figure VI-6A) shows little variations from the PEM to the GDL, in agreement with [12, 15]. As the Pt:Co atomic ratio is stable as one move from the PEM/cathode to the cathode/GDL interfaces, this result suggest that the path taken for the production/removal of the Pt and Co ionic species might be closely linked. Looking now at the platinum and cobalt individual weight per cent, a trend is discernible: a gradual much lower weight content in platinum is depicted at both interfaces with respect to the middle of the cathode CL. This indicates that the Pt^{z+} ionic species, produced by corrosion of the Pt-Co/C particles, can be removed either through the PEM or through the GDL (along the gas flow channel). At the CL | PEM interface, these results may be rationalized by considering that crossover H_2 favours the precipitation of Pt^{z+} species in the ion-conducting phase, yielding the “Pt-band” in the PEM. The chemical reduction of Pt^{z+} ions by H_2 forces the diffusion of Pt ionic species towards the “Pt-band” and activates Pt mass losses at the CL | PEM interface. The above arguments agree with the theoretical model of Pt surface area/mass losses developed by Holby *et al.* [16]. The formation of a Pt-band in the PEM is monitored at a distance of *ca.* 5-6 µm away from the interface with the cathode inlet (Figure VI-7A). While the FEG-SEM resolution enables the monitoring of the formation of the Pt-band due to almost micrometre size of the particles in this region, TEM observations on the ultramicrotomed samples demonstrated that the redistribution and redeposition of the Pt^{z+} occurs in the whole PEM (Figure VI-7A), with however a decreasing size of the Pt particles when moving from the Pt-band to the anode interface [13]. Figure 2 in [12] depicts similar phenomenon at the cathode inlet region of the stack aged for t = 1124 h at I = 50 A. For the longest duration *i.e.* 1341 h at the lowest current density I = 20 A, where the Pt dissolution is exacerbated (highest cathode potential), a clear Pt excess is monitored at the anode CL | PEM interface facing the cathode inlet region (Figure VI-7B). The rationale for the presence of Pt redeposition onto the anode facing the cathode-inlet region is once again the combination of a strong flux of Pt^{z+} species originating from the corrosion of the cathode-inlet electrocatalyst and the small flux of H_2 in the anode-outlet; both enable Pt^{z+} species to diffuse in greater extent down to the anode interface, where they electrochemically redeposit into Pt metal at the anode potential [13, 17, 18].

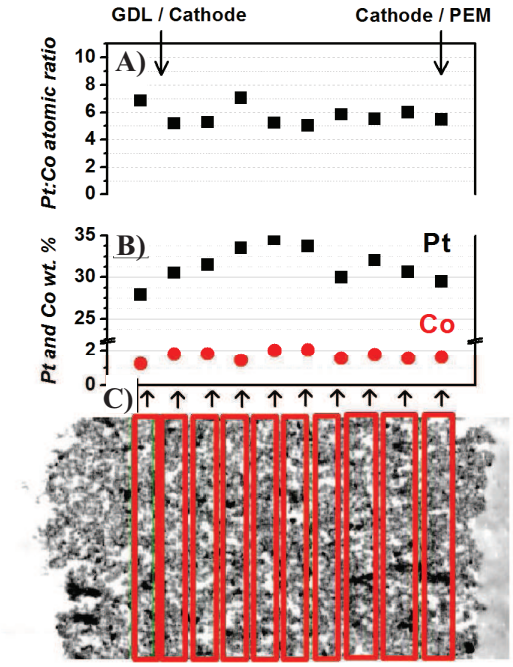

Figure VI-6. (A, B) X-EDS analyses performed locally on ten different positions in the cathode CL imaged in (C). (A) The Pt:Co atomic ratio and (B) the Pt and Co weight percentage (the contribution of carbon to the X-EDS signal was not considered for the calculation in (B)).

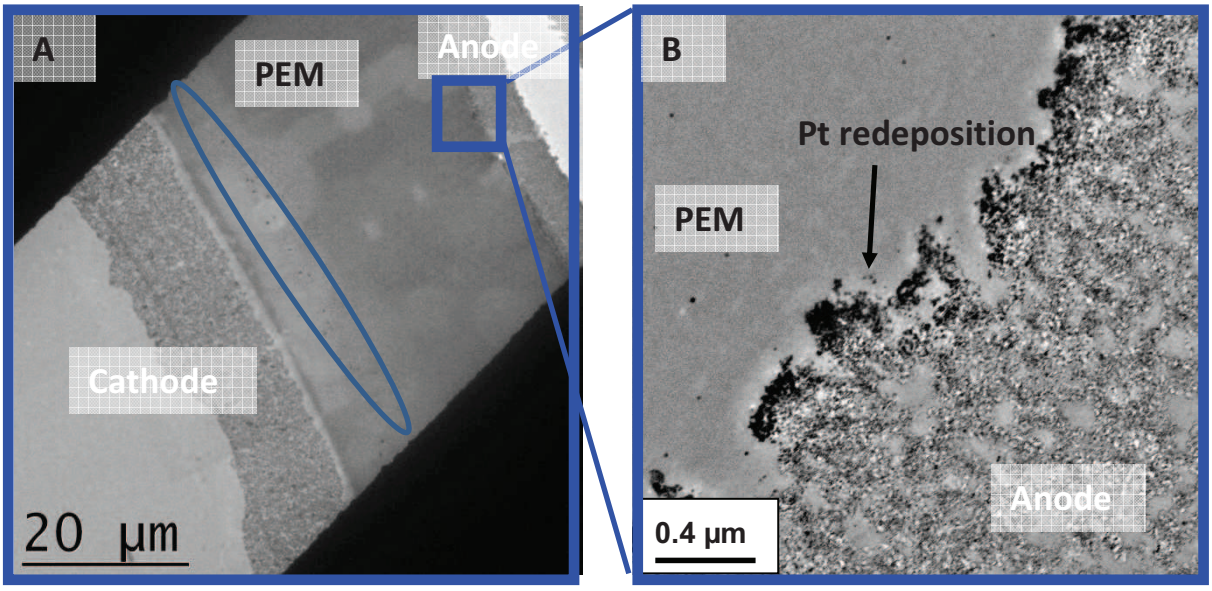

Figure VI-7. TEM images of (A) an ultramicrotomed MEAs aged for t = 1341 h at I = 20 A in the cathode inlet region. Figure (B) is a zoom at the PEM / anode interface.

Through-the-plane degradations of the cathode catalyst are found to appear at a much lower extent than what was observed by Ferreira *et al.* on a Pt /C based CL [5] and Chen *et al.* on a Pt-Co/C based CL [15], the most cited paper dealing with through-the-plane degradations of the cathode catalyst. Their main conclusions are summarized in Figure VI-8. The way the samples are aged in their situation is completely different to our situation: Chen *et al.* worked on a unit-cell PEMFC MEA cycled between 0.650 and 1.050 V *vs.* RHE at v = 100 mV s^{-1} for 24 hours under H_2/N_2 at T = 353 K and 100% RH; Ferreira *et al.* worked on a PEMFC MEA cycled for 110 hours between 0.600 and 1.000 V *vs.* RHE at v = 20 mV s^{-1} under H_2/N_2 at T = 353 K and 100% RH. At variance, in the present study, MEAs were operated at constant current density in real PEMFC operating conditions. Similar as discussed in **Chapter III** regarding the instability of Pt-alloy catalysts, this result tends to show that accelerated aging procedures fail to reproduce real PEMFC aging mechanisms. Moreover, the ultramicrotomed slices were sampled in the cathode inlet region in this work, where the potential across the cathode thickness is more homogeneous compared to the outlet region (due to a higher diffusion gradient in the outlet region), which could have been a plausible reason at the origin of such aging heterogeneities. Unfortunately, the localization where the ultramicrotomed analysis where carried out is not discussed in Ferreira *et al.* [5] and Chen *et al.* [15].

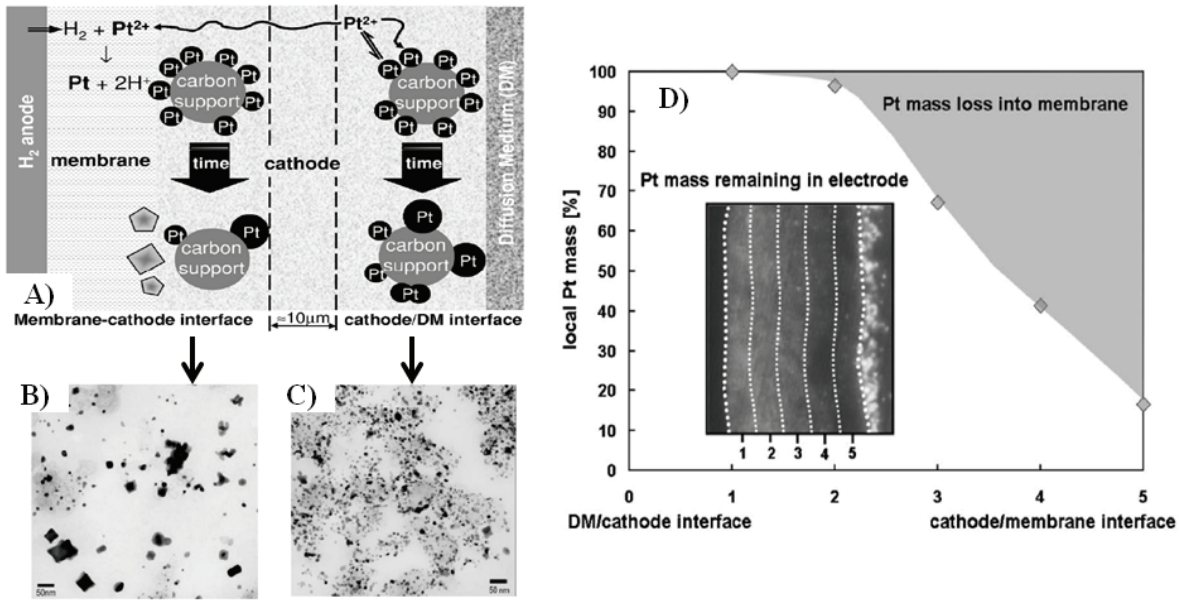

Figure VI-8. Scenario of the cathode catalyst through-the-plane aging in a PEMFC proposed by Ferreira et al. [5] built up on the basis of (B,C) characteristic TEM images obtained at both interfaces. (D) Pt mass remaining in the voltage cycled cathode as a function of position (DM stands for diffusion media i.e. the GDL) reprinted from Chen et al. [15].

III. In-the-plane heterogeneities

1. Presence/absence of Pt particles in the PEM

Figure VI-9 shows representative FEG-SEM images of the MEA aged for t = 1124 h at I = 50A in stationary mode. More specifically, Figure VI-9A shows an image of the whole MEA in the cathode inlet zone. Figure VI-9B is a zoom inside the PEM, *ca.* 5-6 µm away from the interface with the cathode inlet. Figure VI-9C shows the whole MEA in the cathode outlet zone of the cathode (“cathode outlet”) and Figure VI-9D is an image of the PEM taken in the same conditions and distance to the cathode interface as Figure VI-9B. It is obvious that the “platinum-band” inside the PEM is only present in the cathode inlet region of the MEA. This band originates from the chemical reduction of Pt^{z+} ions (produced by the corrosion of the cathode electrocatalyst) by H_2 crossing-over the PEM from the anode to the cathode. As evidenced by previous studies, the position of the “Pt-band” depends on the balance between O_2 and H_2 partial pressures [19, 20]. Its presence in the inlet region highlights that both Pt^{z+} and H_2 are concomitantly present in the PEM in this region of the MEA. On the contrary, its absence in the cathode outlet region implies either that no Pt^{z+} is provided to the PEM at the cathode outlet or that no H_2 crosses over the PEM in this region. Considering that our MEAs were operated in counter-flow configuration, *i.e.* with the anode inlet facing the cathode outlet, the second hypothesis is unlikely. Indeed, the larger H_2 stoichiometry in the fuel in the anode inlet region and the continuous decrease of the local current density upon aging in this region (see for example references [7, 21]), strengthen the effect of the H_2 crossover and should favour the redeposition of Pt^{z+} directly within the cathode CL rather than in the PEM. Conversely, the larger H_2 crossover in the cathode outlet region favours its diffusion up to the cathode, preventing consequent transport of Pt^{z+} species through the PEM and rendering even more unlikely Pt redeposition at the anode CL | PEM interface facing this zone. As stated above, only for longer durations (t = 1341 h) and higher cathode potentials (for the aging at I = 20 A) are some Pt crystallites detected in the PEM at the cathode-outlet, but in much lower extent than in the cathode-inlet region, (Figure VI-10) while none was monitored after t = 1007 h at I = 20 A. We should therefore expect large extent of Pt^{z+} reduction at the cathode/PEM interface in the cathode outlet region, as will be investigated in the following section.

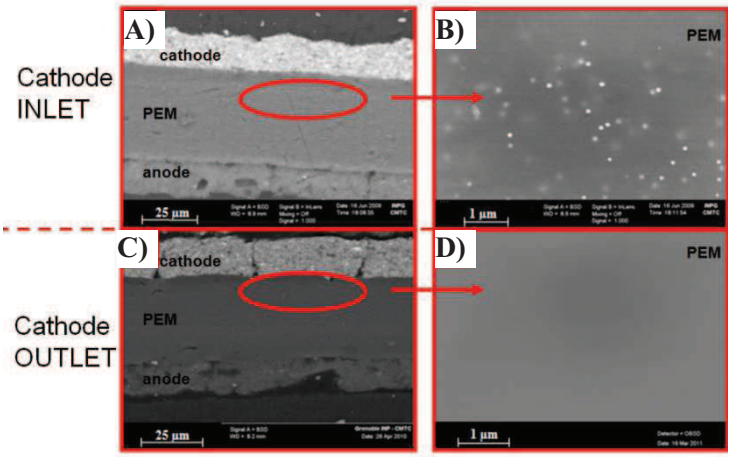

Figure VI-9. FEG-SEM images of MEAs operated for t = 1124 h at j = 0.60 A cm^{-2} in stationary conditions: (A) whole MEA located in the cathode inlet with a special focus (B) in the PEM region facing the cathode, (C) whole MEA located in the cathode outlet with a special focus (D) in the PEM region facing the cathode.

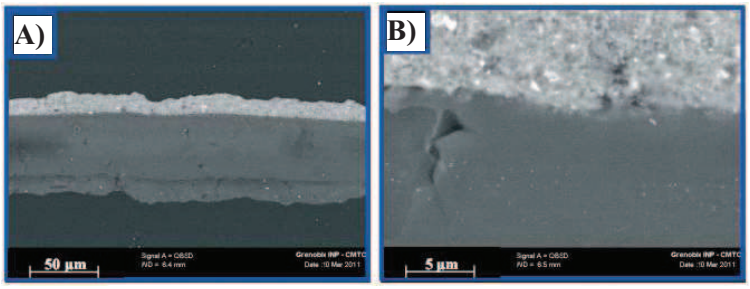

Figure VI-10. FEG-SEM images of MEAs operated for t = 1341 h at I = 20 A in stationary conditions: (A) whole MEA located in the cathode outlet with a special focus (B) in the PEM region facing the cathode.

2. Mean particle size/density (TEM), and mean crystallite size (XRD)

Transmission electron microscopy (TEM) images of the fresh/aged Pt-Co/C cathode electrocatalyst obtained from scraped CL materials are presented in Figure VI-11 for the different operating conditions investigated. The associated densities of isolated and agglomerated particles per µm^2 of carbon established from TEM images are shown in Figure VI-12. The observed trends agree with those obtained by binarization of the TEM images and semi-quantitative estimation of the Pt-Co/C surface coverage (Figure VI-13). Finally, Figure VI-14 presents the volume-averaged mean particle size ($\overline{d}_V$) calculated from transmission electron microscopy (TEM) images and the mean crystallite size estimated by XRD ($\overline{d}_{XRD}$, see Section 2.4). For the determination of the volume-averaged mean particle size (Figure VI-14), only spherical Pt-Co/C nanoparticles were counted, while agglomerated or non-spherical Pt-Co/C particles were disregarded. In XRD, the mean crystallite size was estimated from the width at half-maximum of the (111) and (220) diffraction patterns. TEM and XRD are complementary techniques: the observed changes of $\overline{d}_V$ directly reflect the changes of the isolated and (hemi-)spherically shaped particles, whereas the changes of $\overline{d}_{XRD}$ are representative of the size of the coherently scattering crystallites.

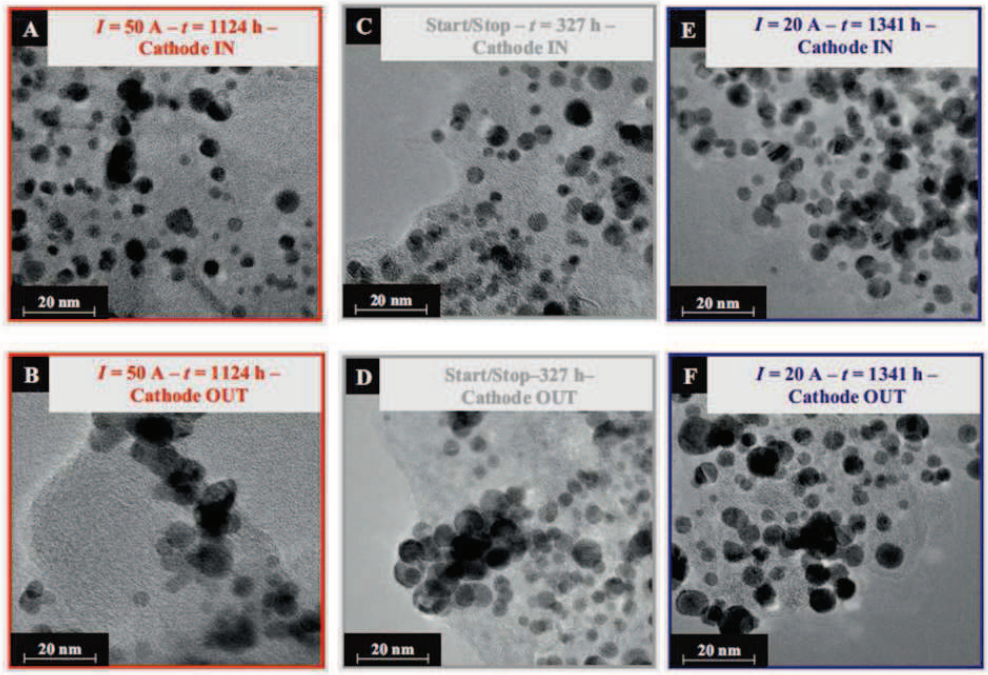

Figure VI-11. Representative TEM images at high magnification (×200,000) of the aging performed at I = 50 A in stationary mode for t = 1124 h (a) cathode inlet (b) cathode outlet, I = 50 A in start/ stop mode t = 327 h (c) cathode inlet (d) cathode outlet and I = 20 A in stationary mode t = 1341 h (e) cathode inlet (f) cathode outlet.

In the cathode inlet zone, the fraction of agglomerated particles expands upon operation, independently of the operating conditions. In parallel, the fraction of isolated particles continuously decreases upon aging (Figure VI-12A). The variations of the fraction of isolated/agglomerated particles are particularly fast during the conditioning step (t = 17 h). These features point towards the occurrence of (i) crystallite migration and (ii) mild Ostwald ripening (growth of large particles at the expense of small ones) in the cathode inlet. Both processes are classical degradation mechanisms of carbon-supported platinum-based materials and have been detailed in **Chapter III** [13, 22]. Interestingly, the scenario is completely different at the cathode outlet zone: the formation of agglomerates at the expense of isolated particles is largely promoted during the conditioning step (and more pronounced than in the inlet region) but the density of isolated and agglomerated particles remains nearly constant during the rest of the aging test (Figure VI-12). In the same time, $\overline{d}_V$ first increases during the conditioning step and then stabilizes (cathode outlet region, Figure VI-14A). These results strongly indicate that the extent of degradation is different in the cathode inlet and outlet regions, which may possibly be linked to differences in local operation conditions. The most likely explanation for the observations of Figure VI-12, Figure VI-13 and Figure VI-14 is that the inlet region of the cathode is a source of Pt^{z+} species that more easily redeposit in the cathode outlet region.

Analysing the mean crystallite size derived from XRD analyses after aging at I = 50 A strengthens this conclusion (Figure VI-14B). Indeed, the variations of $\overline{d}_V$ are comparable in the cathode inlet and outlet regions. Conversely, the variations of $\overline{d}_{XRD}$ are much larger at the cathode outlet than the inlet. These differences agree with the presence of larger single crystalline domains in the cathode outlet region (not necessarily accounted for in $\overline{d}_V$ if the generated particles are not spherical) that are generated by the consequent Pt redeposition in this region. The presence of these agglomerated and non-spherical particles follows a 3D-Ostwald ripening mechanism with the source of Pt^{z+} species being the cathode inlet region. It is also important to stress that the operating current density strongly influences in-the-plane heterogeneities: whereas the differences between the inlet and outlet regions are obvious at high current (I = 50 A in stationary or start-stop modes), almost zero difference is observed on $\overline{d}_{XRD}$ at low current operation (I = 20 A). These results indicate that the MEA is working more homogeneously at low current relative to high current.

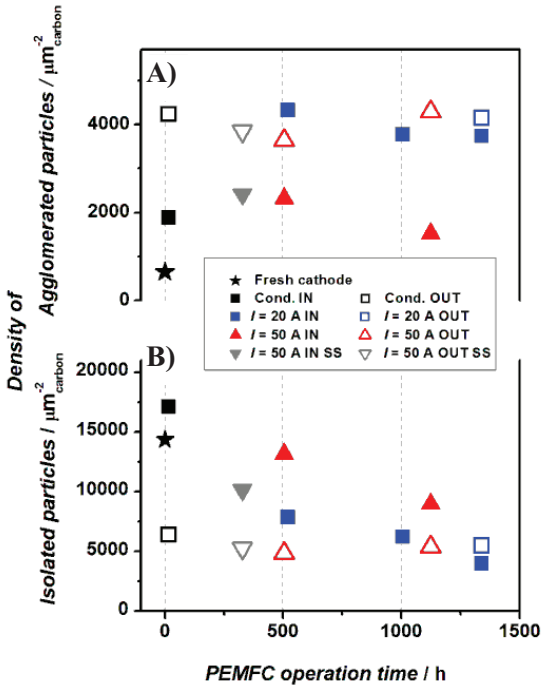

Figure VI-12.Density of (A) agglomerated and (B) isolated particles per µm² of carbon evaluated from TEM images of the fresh/aged cathode electrocatalysts in the different operating conditions investigated in this study.

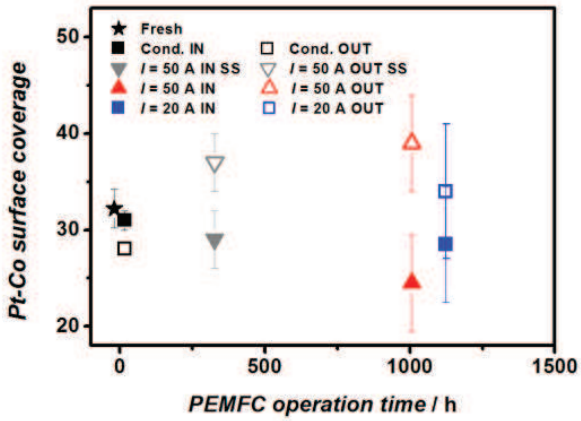

Figure VI-13. Pt-Co surface coverage over the carbon support estimated by binarization of the TEM images and integration of the pixels with ImageJ® (magnification x 200 000). Each point is the averaged value of at least ten measurements; the error bars represent the standard deviation.

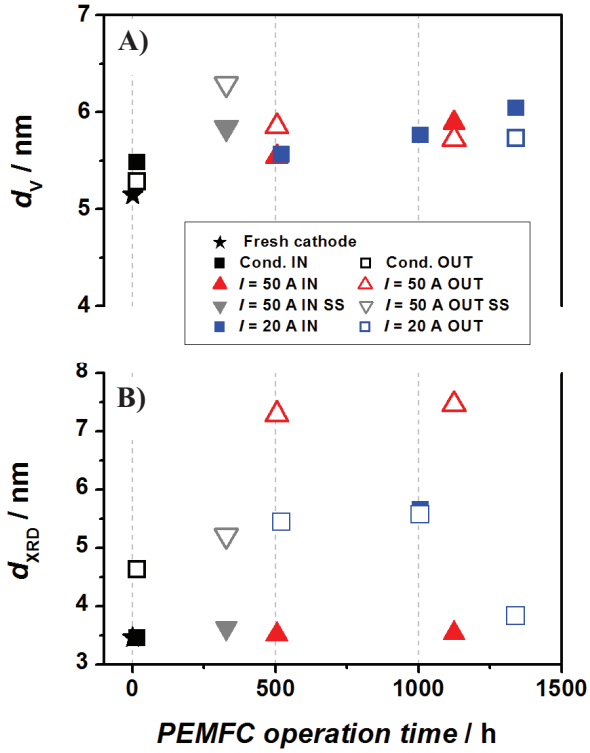

Figure VI-14. (A) Volume-averaged mean particle size of isolated spherical particles estimated from TEM measurements and (B) mean crystallite size estimated from XRD measurements.

The influence of the operating conditions is also clear when comparing the variation of the cathode thickness in the inlet and outlet cathode regions in each operating condition. Table VI-1 shows

that the cathode thickness decrease is more pronounced at low current and when operating in a start/stop mode, signing a faster carbon corrosion (into CO_2) in that case. There are however no major heterogeneities (≤ 1 µm) from the carbon corrosion prospect between the inlet and the outlet regions, meaning that the only parameter that governs the carbon corrosion is the cathode potential (which is homogeneous in the plane of the MEA) and not the local current density. However, even if there are no major changes in the electrode thickness, it is not excluded that the aging induces changes in the porosity (following carbon corrosion) inside the CL when comparing the cathode inlet with the outlet region.

	Thickness / µm
Fresh (cathode inlet)	13.5 ± 1
After conditioning (cathode inlet)	14.0 ± 1
I = 50 A – t = 504 h (cathode inlet)	14.0 ± 1
I = 50 A – t = 1124 h (cathode inlet)	13.0 ± 1
I = 50 A – t = 1124 h (cathode outlet)	14.0 ± 1
I = 20 A – t = 522 h (cathode inlet)	11.5 ± 1
I = 20 A – t = 522 h (cathode outlet)	11.0 ± 1
I = 20 A – t = 1007 h (cathode inlet)	12.5 ± 1
I = 20 A – t = 1007 h (cathode outlet)	12.0 ± 1
I = 50 A start/stop - t = 327h (cathode inlet)	11.5 ± 1
I = 50 A start/stop – t = 327 h (cathode outlet)	10.5 ± 1

Table VI-1. Cathode thicknesses after different life stage in each PEMFC operating condition.

3. Compositional changes

In **Chapter III**, we evidenced that Pt_3Co/C nanoparticles are not stable at the cathode of a PEMFC. In particular, the Gibbs-Thompson relation forecast dynamic evolution of the nm-sized materials, with dissolution of the smallest Pt-Co/C particles and formation of Co^{2+}/Pt^{z+} ions [13, 17, 18, 23]. In addition, because of different standard potentials, only Pt^{z+} ions can redeposit electrochemically onto larger-sized particles [12, 24, 25]. Therefore, the degradation of the fresh Pt_3Co/C particles translates experimentally by an increase of the Pt:Co atomic ratio, making this parameter a structural marker of choice to follow the extent of degradation of the mother Pt_3Co/C electrocatalyst. In this study, the Pt:Co atomic ratio was estimated by ICP and XRD after different life stages (Figure VI-15). Again, differences are observed depending on the analyzed region of the MEA, with the outlet region being less degraded than the inlet region of the cathode CL. In addition, the Co at. % estimated by XRD constantly decreases, while that estimated by ICP-AES remains nearly constant after the conditioning step. These results indicate that the Co^{2+} ions formed by corrosion of

the Pt-Co/C nanoparticles (increase of Pt:Co measured by XRD, signing the dissolution of Co from the crystallized phase) likely remain trapped in the cathode CL ionomer (rather constant overall Pt:Co ratio, including that for non-crystallized Co, *e.g.* Co^{2+}).

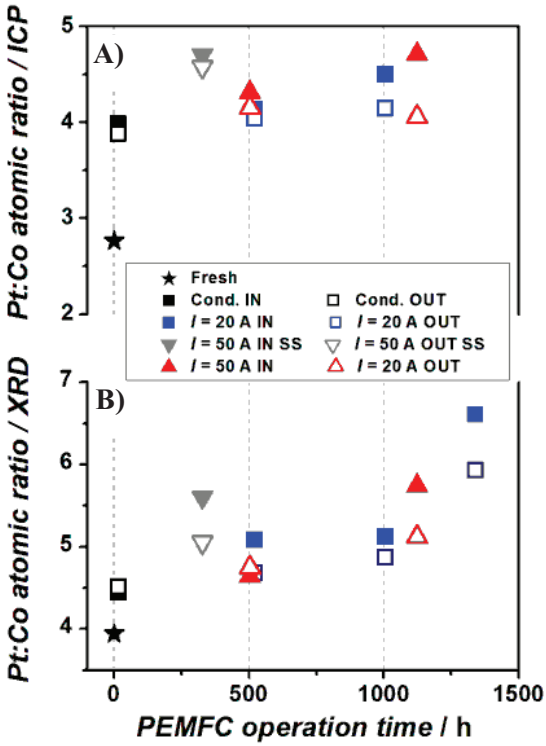

Figure VI-15. Compositional changes of the cathode material during PEMFC operation probed (A) by ICP-AES giving information on the total at% Co of the catalytic layer and (B) by XRD providing the fraction of Co alloyed to Pt.

4. Confirmation of in-the-plane heterogeneities by a segmented cell approach

In the frame of the H2E-OSEO project, the MEAs aged by Axane, have also been subjected to a thorough investigation of their local properties using a segmented fuel cell (at LEMTA). In the last decade, segmented PEMFC have proven to be an excellent *in situ* diagnostic tool to study the factors responsible for the uneven electrochemical response of the MEA “active” area. A segmented fuel cell is similar to an ordinary fuel cell with the exception that one of the electrodes is divided into smaller independent electrodes, having the possibility to be solicited with current, voltage and resistance, independently of the others [26]. Segmented fuel cells are therefore an excellent diagnostic tool to understand local electrochemical performance in single cells and stacks. The integration of various analytical techniques that allow: (i) H_2, O_2, N_2 and H_2O distribution determination, (ii) condensed

water distribution evaluation, (iii) temperature distribution and (iv) local high frequency resistance and local electrochemical impedance spectroscopy (EIS) analysis have been reported. In the approach used at LEMTA, the anodic and cathodic flow fields are the same that have been used by Axane during stack aging tests and the only cathodic bipolar plate has been segmented into 20 regions of equivalent geometric area that basically “follow” the cathode gas channel (Figure VI-16).

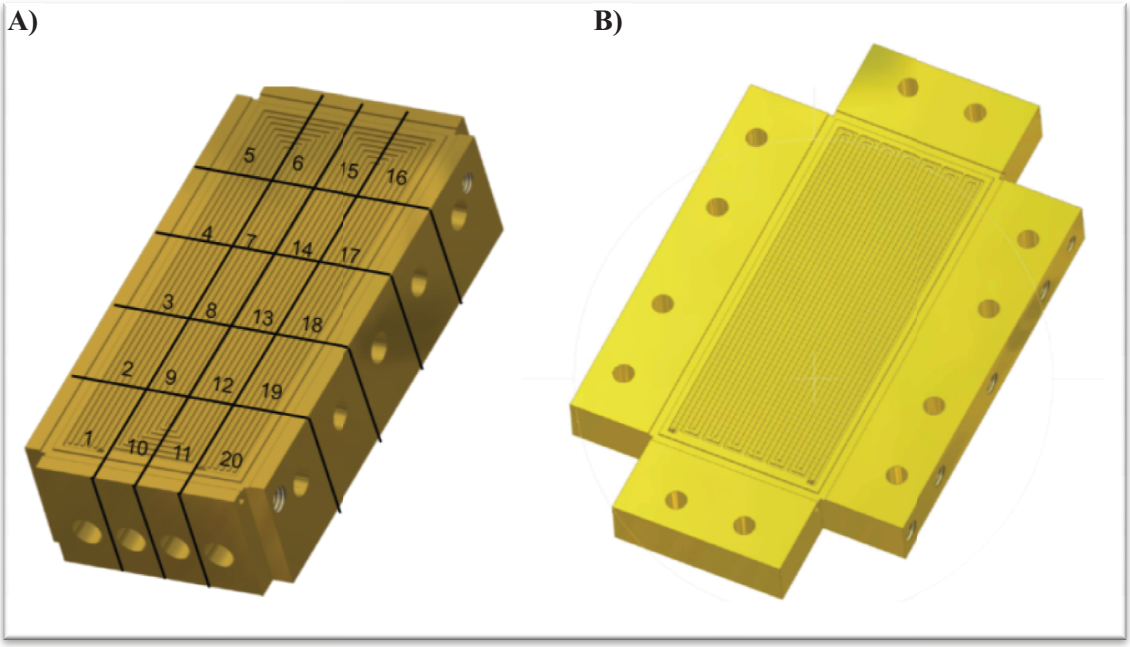

Figure VI-16. (A) Scheme of the 85 cm² segmented cathodic and (B) anodic bipolar plates. Both bipolar plates are gold-plated brass

The current density mapping of five fresh MEAs, similar as those used earlier in this chapter, is given in Figure VI-17. The average current recorded is j = 0.5 A cm^{-2}. Once conditioned, the profile of the current densities within a MEA is not uniform. Differences of more than 30% within the same MEA are recorded (*e.g.* from j = 0.582 A cm^{-2} to j = 0.346 A cm^{-2} on the green curve), with higher current densities measured at the cathode inlet. The decreased performances at the cathode outlet are rationalized by higher oxygen/air mass transport losses in this region. The gradual consumption of oxygen that comes with a gradual production/accumulation of liquid water (that can form water droplets and block the circulation of oxygen) along the air channel are the two main reasons why a lower oxygen concentration is present at the cathode outlet. Therefore, as the cathode outlet is not able to provide the requested current density imposed by the system, the cathode inlet, where the flux of oxygen is not limiting compensates and operates at a higher density than the average. This result is qualitatively confirmed when looking at the local electrochemical impedance spectra (EIS), recorded in a galvanostatic mode (j = 0.5 A cm^{-2}), where larger low frequencies loops, related to mass-transport

phenomena [27, 28], sign higher mass-transport resistances at the cathode outlet with respect to the cathode inlet.

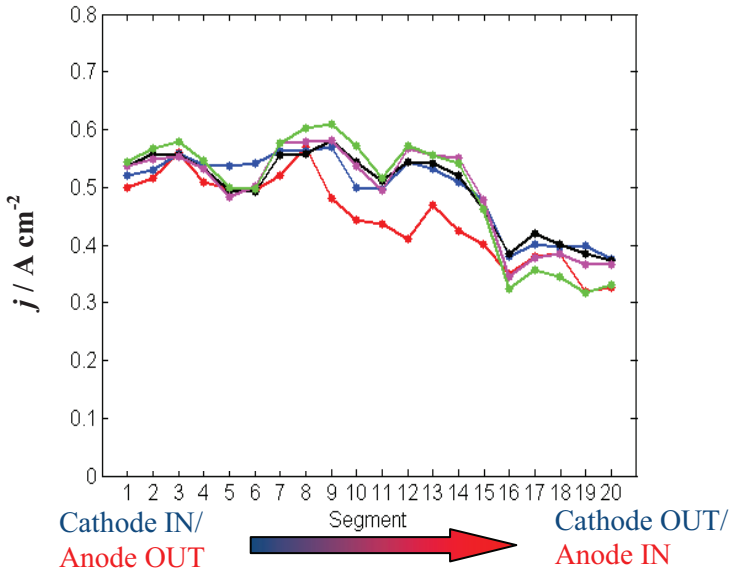

Figure VI-17. Current density distribution as a function of the position at the cathode. For the correspondence segment/position in the cathode, please refer to Figure VI-16. The average current density imposed to the system is set at j = 0.5 A cm^{-2}. H_2 and Air relative humidity are set at 40 % and 75 % respectively. H_2 and Air stoichiometry are set at 1.2 and 2.5 respectively. T = 343 K

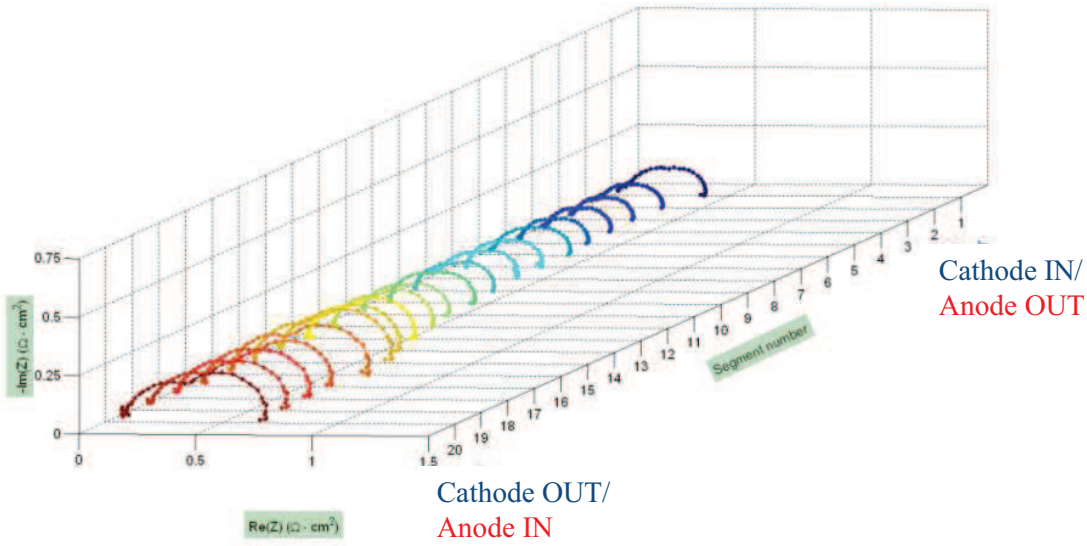

Figure VI-18. EIS spectra distribution recorded in a galvanostatic mode at j = 0.5 A cm^{-2} as a function of the position at the cathode. For the correspondence segment/position in the cathode, please refer at Figure VI-16. Same operating conditions as in Figure VI-17

It is now interesting to study how this irregular current distribution evolves with the aging/degradation of the MEA. In this frame, two aging procedures were performed based on repetitive start and stop cycles (during the start periods, the cell was operated at j = 0.56 A cm^{-2} for t = 30 min under H_2/Air).

In the first aging procedure, repetitive “fuel starvation” events were provoked by purging air at the anode side during each stop event (Figure VI-19). Thus, during each start, the anode is partially exposed to hydrogen and partially exposed to oxygen. As detailed by Reiser *et al.,* this situation generates a flow of current opposite to normal fuel cell mode at the oxygen-exposed region and raises the cathode interfacial potential difference to high values (*ca.* 1.4 V) [29]. Consequently harsh carbon corrosion occurs at the cathode region facing the anode outlet (here the cathode inlet) within the moment where the cell re-operates. Moreover, the analysis of the local internal currents occurring during each start or stop events confirmed that only the start events were harmful to the MEA (because the air purging of the anode compartment was performed at very high flow rate) [30]. Multiplying the number of these events leads to a complete local destruction of the catalyst layer. In the current density distribution in Figure VI-19A, the local and severe degradation of the catalyst layer in the cathode inlet translates by a large decrease of the maximum current density that can be produced locally in this region. To compensate the loss of performances of the cathode inlet region, the outlet region has to produce twice the current than the average, which is possible as long as the cathode outlet region has not been degraded upon aging. The different rates of degradation between the cathode inlet and the outlet are materialized by the behaviours of the local polarization curves (Figure VI-19B for the cathode inlet and Figure VI-19C for the cathode outlet).

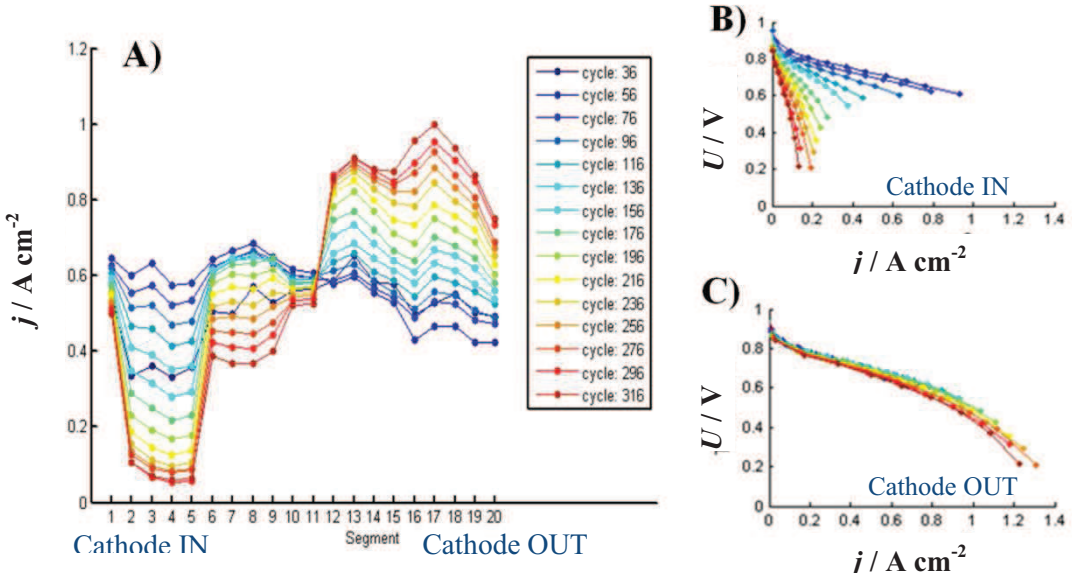

Figure VI-19. (A) Evolution of the current density distribution upon aging of an MEA during an aging mimicking harsh fuel starvation conditions. The representative evolutions of the local

polarization curves upon aging recorded at the cathode inlet (segment 2) and cathode outlet (segment 19) are given respectively in (B) and (C).

During the second aging procedure, the stop events were managed as follows: both gas flows were stopped the 30 min during which a valve sealed the anode and did forbid any air intrusion through the anode gas channel. Therefore, H_2 naturally vented out through the PEM into the cathode. As a result, the composition of the gases at the cathode transiently changed from air to a mixture of air and H_2, inducing transient cathode potential drop to an undetermined value located between the open-circuit potential (OCP) and 0 V *vs.* RHE. This process is accompanied by a transient pressure drop across the MEA, the overall pressure at the anode decreasing fast when H_2 diffuses through the PEM; indeed the diffusion of air in the opposite direction is slower. This way of stopping the cell slows down/ inhibits [31] the issues related to the “fuel starvation” [29]. It is worth mentioning here that the start/stop aging discussed in the beginning of this chapter (from Figure VI-11 to Figure VI-15) was performed in a similar way as the aging presented here, thus without promoting fuel starvation and severe carbon corrosion events at the cathode inlet. As this way of managing start and stop events does not lead to severe degradation of the cathode catalyst layer, which was further confirmed by the local internal currents, the loss of performances that will be discussed below can be mainly attributed to the degradation of the catalyst upon operation under stationary conditions (j = 0.56 A cm^{-2}). When looking at the evolution of the local current densities upon aging (Figure VI-20A), in the light of the corresponding polarization curves (Figure VI-20B for the cathode inlet and Figure VI-20C for the cathode outlet), this current density distribution follows the one obtained on fresh MEA (Figure VI-17). Indeed, the differences between the cathode inlet and outlet are even heightened upon aging, suggesting at least constant mass-transport issues at the cathode outlet. This way of operating the cell engenders loss of performances (degradation of the polarization curve) of the cathode catalyst layer at the cathode outlet, while the cathode inlet remains essentially unaffected. By looking more carefully at the polarization curve recorded at the cathode outlet (Figure VI-20B), its activation overpotential (j < 0.2 A cm^{-2}, related to the ORR overpotential and so to the cathode catalyst) seems more severely affected/ degraded than the rest of the plot, where ohmic losses become non-negligible.

These preliminary results obtained using a segmented cell approach might be enough to rationalize the fact that in-the-plane heterogeneous operating conditions are appearing upon aging (due to the singular design of the flow-field of the cathodic bipolar plate) and impact the rate of degradation of the cathode catalyst layer at the micrometre and the nanometre scales.

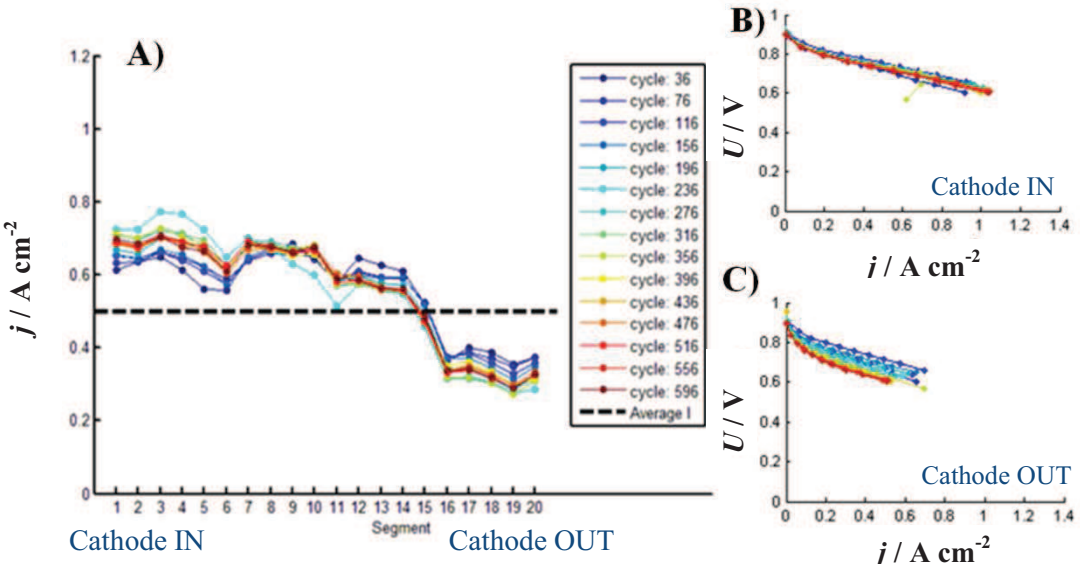

Figure VI-20. (A) Evolution upon aging of the current density distribution of a MEA during a test mimicking stationary aging conditions. The representative evolutions of the local polarization curves upon aging recorded at the cathode inlet (segment 2) and cathode outlet (segment 19) are given respectively in (B) and (C).

IV. Towards a unified spatially-resolved “model” of local degradation within a PEMFC MEA

The results from the two previous sections (through-the-plane and in-the-plane heterogeneities) revealed that the aging of a PEMFC MEA can definitely not be considered homogeneous on the MEA scale: depending on the applied current, one has to take into account the possible differences of aging rate and/or mechanisms at (i) the inlet/outlet regions of the cathode and (ii) within the cathode thickness. We believe that the heterogeneity of operation and aging can be understood as follows:

1- the cathode outlet operates at a lower current density comparing to the inlet, following the larger air mass-transport hindrance of the air-depleted oxidant in the flooded cathode outlet region [7, 21]. Consequently, the flux of protons is likely smaller in the cathode outlet region, which, coupled to the higher presence of liquid water (that accumulates downstream of the air gas channel), locally increases the pH. Conversely, the cathode electrocatalyst is subjected to a higher oxidizing environment at the cathode inlet (lower proton concentration, higher air partial pressure and temperature);

2- as a result, the cathode outlet region that faces the anode inlet region is in a less oxidizing atmosphere than the cathode inlet region, because of the air mass-transport

hindrance mentioned in (1) and the higher H_2 crossover. In addition, the local temperature is also higher in the cathode inlet region (larger heat production at higher current density [32]);

3- the higher temperature and acidity of the cathode inlet as well as the increased local polarization voltage facilitate the dissolution of Pt-Co/C particles, compared to the cathode outlet region;

4- the Pt^{z+} and Co^{y+} formed at the cathode inlet redistribute within the whole MEA (across the PEM and down the cathode gas channel), but only Pt^{z+} species can redeposit for thermodynamical reasons [12, 25]. The Co^{2+} ions are washed and subsequently exhausted in the excess water or retained in the cathode ionomer; the driving force for Pt^{z+} and Co^{2+} redistribution are dual: (i) convection in liquid water in the gas channels or the GDL pores; (ii) diffusion in the hydrated ionomer phase of the catalytic layer. As Co^{2+} ionic species are not consumed by crossover H_2, the diffusion gradient of Co^{2+} species is smaller than for Pt^{z+} species. Consequently, the Co ionic species more likely stay in the ionomer phase within the cathode CL (the migration maintains Co^{2+} at the cathode) or in the PEM (that they may reach by diffusion);

5- the redeposition of Pt is moderate in the inlet region of the cathode CL, where the acid and oxidizing environment is not favourable; therefore Pt^{z+} can diffuse into the PEM facing the cathode inlet region, where its redeposition is possible because of the mild H_2 crossover (the cathode inlet faces the anode outlet, with depleted H_2 in the fuel);

6- on the contrary at the cathode outlet, Pt^{z+} redeposition occurs inside the CL thanks to the more reducing environment in this region (larger H_2 crossover combined with lower air partial pressure); this scenario is supported by the large extent of agglomeration monitored at the cathode outlet (see Figure VI-11 and Figure VI-12), and by the observations of Xie *et al.* of similar agglomeration in high humidity conditions (*i.e.* conditions similar to those of the cathode outlet in the present study) [33];

7- overall, a Pt^{z+} “pump” proceeds between the cathode inlet and outlet, respectively locus of intense generation of Pt^{z+} in the oxidizing environment of the cathode inlet (large air partial pressure and low pH) and locus of intense redeposition in the reducing environment of the cathode outlet (large H_2 crossover; low air partial pressure in the presumably more flooded part of the cathode). Such a Pt^{z+} pump also likely proceeds between the cathode inlet and the anode | PEM interface that faces the cathode inlet favouring the enrichment of the anode | membrane interface in this

particular region of the MEA (the anode | membrane interface that faces the cathode outlet region does not show such Pt enrichment).

These processes are graphically summarized on Figure VI-21. They are extensively supported by the experimental findings presented throughout this chapter and agree with relevant literature data.

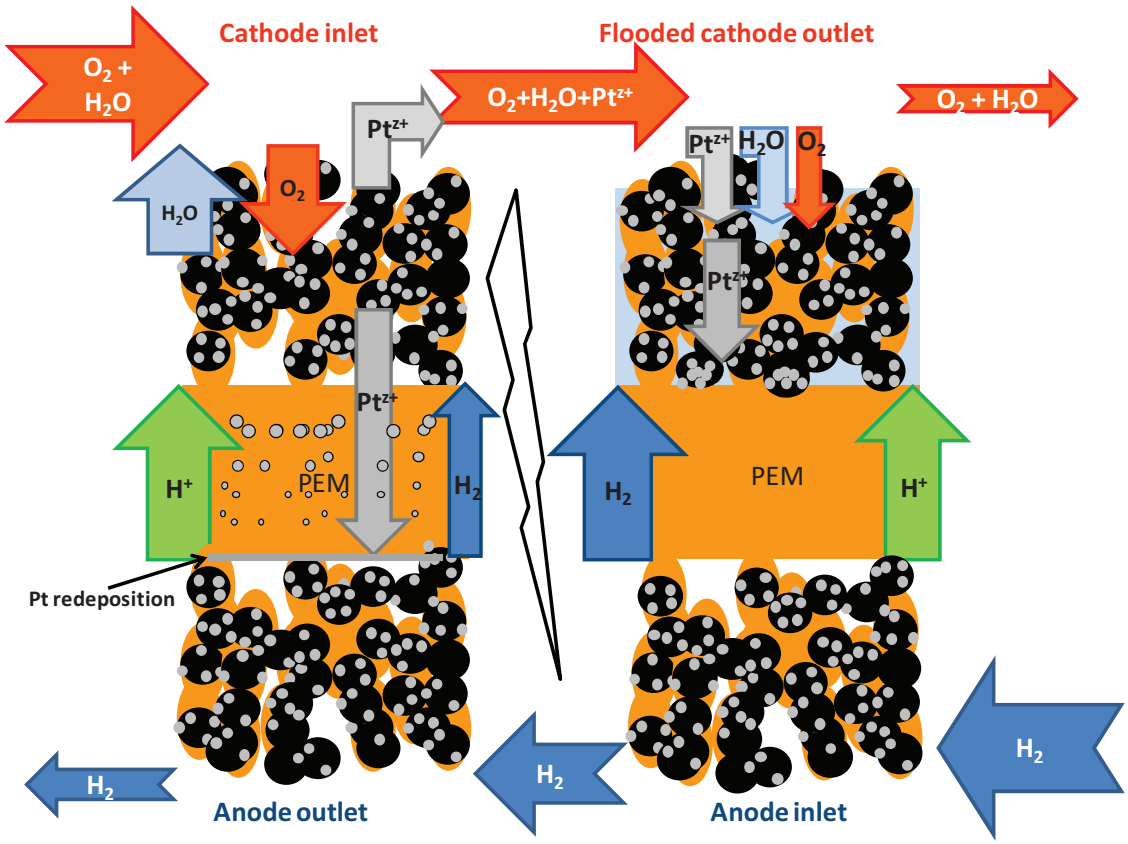

Figure VI-21. Schematic representation of the mass transport fluxes within a PEMFC MEA operating at “high current”, i.e. with an heterogeneous distribution of the current density along the gas channel ($j > j_{average}$ at the inlet and $j < j_{average}$ at the outlet, as a result of the larger air mass-transport hindrance of the air-depleted oxidant in the flooded cathode outlet region). j and $j_{average}$ stand for the localized or average current density, respectively.

V. Conclusion

The present chapter, through the conjunction of several physico-chemical techniques applied to fresh/aged PEMFC MEAs, shows that the degradation of the cathode CL materials cannot be considered as homogeneous. The local analyses indeed put in evidence that the cathode inlet ages much more rapidly than the cathode outlet, when the cell current is high. This likely originates from heterogeneities of local current density and temperature (the inlet works far more than the outlet, essentially because of larger air oxygen mass-transport limitations of the air-depleted-oxidant in the

partially-flooded CL prevent this latter region from operating properly), but the phenomenon levels off upon decrease of the average cell current. As a result, the cells operated at low current (I = 20 A in the present study) operate and age more homogeneously that those operated at high current (I = 50 A) in stationary conditions. Frequent cathode purges and starts/stop steps that enable “de-flooding” of the cathode outlet region, seem also to yield much more homogeneous aging of the cathode CL materials.

VI. References

[1] Shim J., Yoo D. Y. and Lee J. S., Characteristics for electrocatalytic properties and hydrogen-oxygen adsorption of platinum ternary alloy catalysts in polymer electrolyte fuel cell. *Electrochim. Acta*, 45 (2000) 1943-1951.

[2] Sompalli B., Litteer B. A., Gu W. and Gasteiger H. A., Membrane degradation at catalyst layer edges in PEMFC MEAs. *J. Electrochem. Soc.*, 154 (2007) B1349-B1357.

[3] Ohma A., Yamamoto S. and Shinohara K., Analysis of membrane degradation behavior during OCV hold test. *ECS Trans.*, 11 (2007) 1181-1192.

[4] Yu J. R., Matsuura T., Yoshikawa Y., Islam M. N. and Hori M., Lifetime behavior of a PEM fuel cell with low humidification of feed stream. *Phys. Chem. Chem. Phys.*, 7 (2005) 373-378.

[5] Ferreira P. J., La O' G. J., Shao-Horn Y., Morgan D., Makharia R., Kocha S. and Gasteiger H. A., Instability of Pt/C electrocatalysts in proton exchange membrane fuel cells. *J. Electrochem. Soc.*, 152 (2005) A2256-A2271.

[6] Ferreira P. J. and Shao-Horn Y., Formation mechanism of Pt single-crystal nanoparticles in proton exchange membrane fuel cells. *Electrochem. Solid-State Lett.*, 10 (2007) B60-B63.

[7] Chupin S., Colinart T., Didierjean S., Dube Y., Agbossou K., Maranzana G. and Lottin O., Numerical investigation of the impact of gas and cooling flow configurations on current and water distributions in a polymer membrane fuel cell through a pseudo-two-dimensional diphasic model. *J. Power Sources*, 195 (2010) 5213-5227.

[8] Ghosh P. C., Wuster T., Dohle H., Kimiaie N., Mergel J. and Stolten D., *In situ* approach for current distribution measurement in fuel cells. *J. Power Sources*, 154 (2006) 184-191.

[9] Yoon Y. G., Lee W. Y., Yang T. H., Park G. G. and Kim C. S., Current distribution in a single cell of PEMFC. *J. Power Sources*, 118 (2003) 193-199.

[10] Geiger A. B., Eckl R., Wokaun A. and Scherera G. G., An approach to measuring locally resolved currents in polymer electrolyte fuel cells. *J. Electrochem. Soc.*, 151 (2004) A394-A398.

[11] Xie J., Wood D. L., Wayne D. M., Zawodzinski T. A., Atanassov P. and Borup R. L., Durability of PEFCs at high humidity conditions. *J. Electrochem. Soc.*, 152 (2005) A104-A113.

[12] Dubau L., Maillard F., Chatenet M., Guétaz L., André J. and Rossinot E., Durability of Pt_3Co/C cathodes in a 16 cell PEMFC stack: Macro/microstructural changes and degradation mechanisms. *J. Electrochem. Soc.*, 157 (2010) B1887-B1895.

[13] Guilminot E., Corcella A., Charlot F., Maillard F. and Chatenet M., Detection of Pt^{z+} ions and Pt nanoparticles inside the membrane of a used PEMFC. *J. Electrochem. Soc.*, 154 (2007) B96-B105.

[14] Shao-Horn Y., Sheng W., Chen S., Ferreira P., Holby E. and Morgan D., Instability of supported platinum nanoparticles in low-temperature fuel cells. *Topics Catal.*, 46 (2007) 285-305.

[15] Chen S., Gasteiger H. A., Hayakawa K., Tada T. and Shao-Horn Y., Platinum-alloy cathode catalyst degradation in proton exchange membrane fuel cells: Nanometer-scale compositional and morphological changes. *J. Electrochem. Soc.*, 157 (2010) A82-A97.

[16] Holby E. F., Sheng W., Shao-Horn Y. and Morgan D., Pt nanoparticle stability in PEM fuel cells: Influence of particle size distribution and crossover hydrogen. *Energy Environ. Sci.*, 2 (2009) 865-871.

[17] Chatenet M., Guilminot E., Iojoiu C., Sanchez J.-Y., Rossinot E. and Maillard F., Pt redistribution within PEMFC MEAs and its consequence on their performances. *ECS Trans.*, 11 (2007) 1203-1214.

[18] Guilminot E., Corcella A., Chatenet M., Maillard F., Charlot F., Berthome G., Iojoiu C., Sanchez J. Y., Rossinot E. and Claude E., Membrane and active layer degradation upon PEMFC steady-state operation - I. Platinum dissolution and redistribution within the MEA. *J. Electrochem. Soc.*, 154 (2007) B1106-B1114.

[19] Zhang J., Litteer B. A., Gu W., Liu H. and Gasteiger H. A., Effect of hydrogen and oxygen partial pressure on Pt precipitation within the membrane of PEMFCs. *J. Electrochem. Soc.*, 154 (2007).

[20] Yasuda K., Taniguchi A., Akita T., Ioroi T. and Siroma Z., Platinum dissolution and deposition in the polymer electrolyte membrane of a PEM fuel cell as studied by potential cycling. *Phys. Chem. Chem. Phys.*, 8 (2006) 746-752.

[21] Onda K., Araki T., Taniuchi T., Sunakawa D., Wakahara K. and Nagahama M., Analysis of current distribution at PEFCs using measured membrane properties and comparison with measured current distribution. *J. Electrochem. Soc.*, 154 (2007) B247-B257.

[22] Guilminot E., Corcella A., Iojoiu C., Berthomé G., Maillard F., Chatenet M. and Sanchez J.-Y., Membrane and active layer degradation upon proton exchange membrane fuel cell steady-state operation – Part I: Platinum dissolution and redistribution within the membrane electrode assembly. *J. Electrochem. Soc.*, 154 (2007) B1106-B1114.

[23] Dubau L., Durst J., Maillard F., Guétaz L., Chatenet M., André J. and Rossinot E., Further insights into the durability of Pt_3Co/C electrocatalysts: Formation of "hollow" Pt nanoparticles induced by the Kirkendall effect. *Electrochim. Acta*, 56 (2011) 10658-10667.

[24] Dubau L., Durst J., Maillard F., Chatenet M., André J. and Rossinot E., Influence of PEMFC operating conditions on the durability of Pt_3Co/C electrocatalysts. *ECS Trans.*, (2010).

[25] Dubau L., Maillard F., Chatenet M., André J. and Rossinot E., Nanoscale compositional changes and modification of the surface reactivity of Pt_3Co/C nanoparticles during proton-exchange membrane fuel cell operation. *Electrochim. Acta*, 56 (2010) 776-783.

[26] Bender G., Wilson M. S. and Zawodzinski T. A., Further refinements in the segmented cell approach to diagnosing performance in polymer electrolyte fuel cells. *J. Power Sources*, 123 (2003) 163-171.

[27] Antoine O., Bultel Y. and Durand R., Oxygen reduction reaction kinetics and mechanism on platinum nanoparticles inside Nafion®. *J. Electroanal. Chem.*, 499 (2001) 85-94.

[28] Eikerling M. and Kornyshev A. A., Electrochemical impedance of the cathode catalyst layer in polymer electrolyte fuel cells. *J. Electroanal. Chem.*, 475 (1999) 107-123.

[29] Reiser C. A., Bregoli L., Patterson T. W., Yi J. S., Yang J. D. L., Perry M. L. and Jarvi T. D., A reverse-current decay mechanism for fuel cells. *Electrochem. Solid-State Lett.*, 8 (2005) A273-A276.

[30] Lamibrac A., Maranzana G., Lottin O., Dillet J., Mainka J., Didierjean S., Thomas A. and Moyne C., Experimental characterization of internal currents during the start-up of a proton exchange membrane fuel cell. *J. Power Sources*, 196 (2011) 9451-9458.

[31] Maranzana G., Moyne C., Dillet J., Didierjean S. and Lottin O., About internal currents during start-up in proton exchange membrane fuel cell. *J. Power Sources*, 195 (2010) 5990-5995.

[32] Maranzana G., Lottin O., Colinart T., Chupin S. and Didierjean S., A multi-instrumented polymer exchange membrane fuel cell: Observation of the in-plane non-homogeneities. *J. Power Sources*, 180 (2008) 748-754.

[33] Xie J., Wood D. L., More K. L., Atanassov P. and Borup R. L., Microstructural changes of membrane electrode assemblies during PEFC durability testing at high humidity conditions. *J. Electrochem. Soc.*, 152 (2005) A1011-A1020.

Chapter VII.

Conclusion and outlooks

Throughout this manuscript, the multi-scale degradations of the cathode catalyst layer of a PEMFC, key component of such multi-scale system, have been investigated. The special attention paid to the degradation of the cathode catalyst layer was motivated as this component induces most of the voltage losses of a PEMFC system (related to the oxygen reduction reaction and to the oxygen and water transport). Moreover, when considering long-term PEMFC operation under stationary conditions, even if the end of life of a MEA and so of the PEMFC, seems to be dictated by the longevity of the PEM, most of the loss of performances of the PEMFC system can be attributed to (ir)reversible degradations of the cathode catalyst layer. When considering long-term PEMFC operations under transient conditions, representative of the conditions that would sustain the cathode in an automotive application, the impact of the cathode catalyst layer on the longevity of the PEMFC system is even increased. Abundantly commented in the last decade regarding their improved electrocatalytic activity for the ORR with respect to Pt/C catalyst, the presumable stability of nanometer sized Pt_3Co carbon nanoparticles layers has been surveyed and discussed in this manuscript.

First, the fine structure of such Pt-alloy catalysts (chemically and thermally pretreated to form a pure Pt top-surface layer presumably protective toward the dissolution of the non-noble element), was investigated by a detailed EXAFS analysis. The results confirm that the strain effects in Pt-skin surface structures are comprised between those in Pt-skeleton and pure Pt surface structures, which can be rationalized by the intermediate concentration in Pt atoms in Pt-skin surface compared to Pt-skeleton and pure Pt surface structures. As Pt-skin surface structures are performing better for the ORR than the latter, it emphasizes the strong interplay between geometric (modification of the surface strain) and electronic (shift of the d-band vacancy with respect to the Fermi level) effects. Based on EXAFS analysis, the inner core of Pt-skin catalysts largely differs from the inner core of Pt-skeleton catalysts, not only in term of composition but also in term of structure. The singularities evidenced in the Pt-skin inner structure, rarely commented in the literature, was rationalized by different scenario, which could not be verified so far. A more detailed study of the XANES spectra, especially those recorded at the Co edge which appeared to be very sensitive to the catalyst structure, should be done by performing *ab intio* calculations and could be helpful to confirm EXAFS results.

Durability tests followed by physical, chemical and electrochemical characterizations on Pt_3Co/C catalysts, having initially a core-shell structure similar as the Pt-skin catalyst, have shown that the degradation of these PEMFC cathode (electro)catalysts can be divided into two distinct parts. Firstly, these objects are subjected to 3D Ostwald ripening, similar as Pt/C (electro)catalysts, mainly due to their nanometric size. This degradation mechanism results in an increase of the catalyst mean particle size and so to a loss of electrochemical surface area of the cathode catalyst layer. Secondly, Pt_3Co/C catalysts face a decrease of their Co atomic content, which greatly depreciates their surface reactivity for the ORR. Interestingly, under specific aging conditions (high cathode potential) the fast decrease of the Co content over time yields formation of compact spherically shaped “hollow” Pt/C

nanoparticles, free of any Co. These structures perform better for the ORR than both Pt/C and the fresh Pt_3Co/C electrocatalyst. Additional measurements confirmed that the ORR activity increase is clearly attributed to the presence of these Pt-hollow particles within the CL and not to a particle size effect of the remaining Pt-Co nanoparticles. From a fractional viewpoint, the mechanism of Co atoms corrosion from the fresh Pt_3Co catalyst structure seems to be linked to the formation of surface (hydr)oxides, as suggested by electrochemical tests. This result should be confirmed by coupled electrochemical-physical techniques. *In situ* coupled electrochemical/XAS experiments should provide valuable results if performed at the Co edge. This is clearly not possible with the current design of the electrochemical/XAS cell used in this study. A new cell should be built up to allow such measurements.

While Pt-hollow particles are formed upon PEMFC aging, a great amount of cobalt ionic species is redistributed within the whole MEA. Although it is commonly admitted that the produced metal cations do contaminate the ionomer/membrane (contrary to platinum ionic species, which can be chemically or electrochemically reduced), we found that non-covalent interactions between metal cations and the catalyst surface enhance the adsorption of oxygen-containing species and therefore do negatively impact the ORR kinetics. The specific adsorption of sulfonate anions of Nafion® locally modifies the double layer structure and increases the tolerance to metal cations. We also provided evidences that the electrolyte contamination heightens the mass-transport resistance of molecular oxygen for both solid and liquid electrolytes. Even if several interfaces mimicking that encountered in PEMFCs were tested, it could be interesting to confirm these results during single cell PEMFC testing.

Due to the negative effect of cobalt pollution within the MEA, the use of rapid dealloying procedures in PEMFC to generate *in situ* Pt-hollow catalyst from Pt-alloy catalysts is therefore not recommended. It is rather recommended to perform such dealloying procedures on Pt-alloy catalysts prior to their mounting in the MEA, or to find synthesis methods to generate these structures. In particular, a synthesis method that uses Co nanoparticles (electro)deposited on carbon powder support as a template and immerged into deaerated K_2PtCl_4 solution is currently investigated in the laboratory (L. Dubau). This procedure leads to the formation of a pure Pt shell (with controlled thickness, depending on $[K_2PtCl_4]$) surrounding the inner cobalt core which can be removed by electrochemical tests.

Finally, this manuscript has investigated the microscale changes of the cathode catalyst layer upon aging and tackle an issue rarely commented so far: are the rates and mechanisms of degradation homogeneous within a single MEA? Although this manuscript does not debrief all the results obtained in the frame of the H2E project, and more especially those obtained in a close collaboration with LEMTA, interesting prospects have been set up during this PhD. In particular we have shown that heterogeneities of aging can occur in a PEMFC cathode catalyst layer with a segmented cell approach

having a simple 2D geometry (which minimizes mass-transport related issues), 20 segments and a low surface area of *ca.* 30 cm^2. Start-up/shut-down tests were performed and the cathode CL degradation was monitored on-line with the internal currents method coupled to CO_2 measurements of the exhaust gas, localized polarization curves, localized cyclic voltammetry and localized electrochemical impedance spectroscopy measurements. Having in mind the locally resolved information about the cathode CL degradation, the local loss of performances observed in the segmented cell can be correlated to the local degradations of the Pt/C cathode CL. On-going results have put into evidence the heterogeneous rates and mechanisms of degradation in local areas of the MEA, *i.e.* underlying channels and ribs. These results suggest that each specific system design (flow-fields patterns, bipolar plates …), which has a great impact on the initial performance of a PEMFC system, might also induce geometry-related local rates of degradation of the materials. Once again a balance between initial performances and durability of the materials is observed and should be accounted for when designing efficient PEMFC materials/systems.

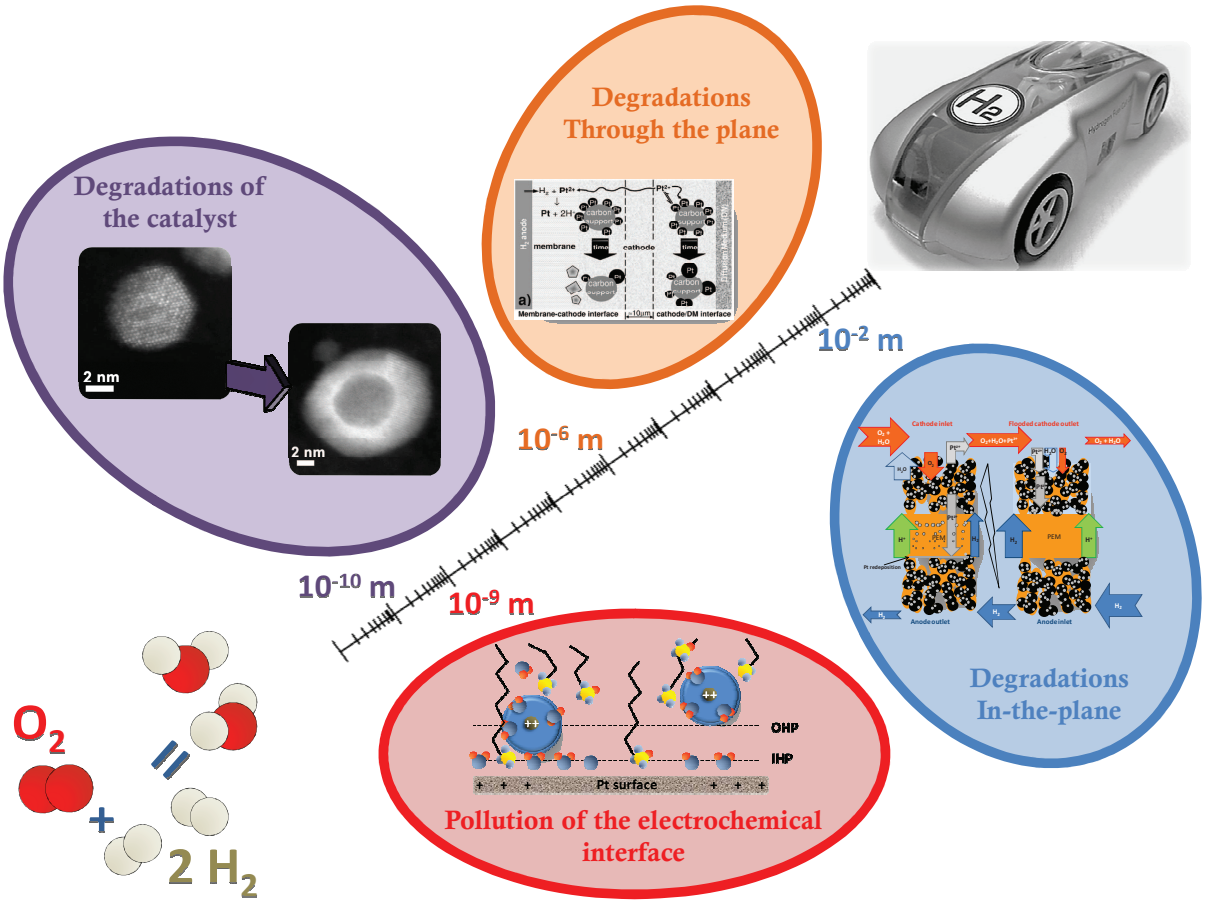

Figure VII-1. Scheme of multi-scale degradations of the cathode catalyst layer of a PEMFC identified and studied in the frame of this PhD thesis

Résumé

Nous avons étudié les mécanismes de dégradation de catalyseurs Pt_3Co/C en conditions réelles (stacks 16 cellules, hydrogène/air, stationnaire et intermittent, t > 1000 heures). Des modifications de la structure atomique, de la morphologie et de la composition chimique des catalyseurs ont été mises en évidence grâce à des techniques à résolution atomique, tels que la microscopie HAADF ou encore la spectroscopie d'absorption de rayons X. En plus d'être sujets à la maturation d'Ostwald 3D, ces catalyseurs perdent continuellement et irréversiblement les atomes de cobalt contenus dans le matériau « natif », ce qui conduit à la formation de nanoparticules « creuses » de Pt. Nous avons montré l'effet d'une contamination de l'électrode par des cations métalliques (Co^{2+}).

Des hétérogénéités de vieillissement de ces électrodes, à la fois « dans le plan » et « à travers le plan », ont été mises en évidence, en utilisant des marqueurs structuraux caractéristiques des électrodes. Des différences locales des cinétiques et des mécanismes de dégradation ont été confirmées grâce à des tests en monocellule PEMFC à cathode segmentée.

Mots clés : pile à combustible à membrane échangeuse de protons, durabilité des matériaux de PEMFC, nanoparticules de Pt/C « creuses », effet d'une contamination cationique des couches catalytiques, hétérogénéités de vieillissement

Abstract

The durability of Pt_3Co/C PEMFC cathode catalysts is investigated under real operating conditions (16-cell short stacks, hydrogen/air, constant current or start/stop, ageing time > 1000 hours). Using atomically resolved physical techniques such as HRSTEM-HAADF, and XAS, a detailed picture of how atomic structure, chemical composition and morphology of these cathode catalysts are changing over time has been drawn. In addition to 3D Ostwald ripening, these Pt-alloy catalysts undergo irreversible decrease of their cobalt content upon aging, yielding formation of "hollow" Pt/C nanoparticles. In the meantime, a great amount of Co^{2+} species is released within the MEA, which influences the catalyst surface reactivity and its ORR activity.

Finally, structural markers of the degradation of the cathode catalyst have been used to unveil aging heterogeneities within the MEA: "through-the-plane" heterogeneities of aging (*i.e.* from the PEM/cathode interface to the cathode/GDL interface), and "in-the-plane" heterogeneities of ageing (*i.e.* from the gas inlet to the gas outlet) have been evidenced. The latter was confirmed using a cathode catalytic layer segmented in 20 segments along the gas flow channel.

Keywords: proton exchange membrane fuel cell, durability of PEMFC materials, "hollow" Pt/C nanoparticles, effect of cation contamination, aging heterogeneities.